Effect of Cochlear Shape and Size on Cochlear Implant Insertion Forces

Filip Hrnčiřík

Department of Clinical Neurosciences
University of Cambridge

This dissertation is submitted for the degree of
Doctor of Philosophy

Girton College August 2023

Preface

This thesis is the result of my own work and includes nothing which is the outcome of work done in collaboration except as declared in the preface and specified in the text. Additionally, I have included a disclosure section on the first page of each chapter to specify what work was done in collaboration. I confirm that this thesis is not substantially the same as any work that has already been submitted before for any degree or other qualification except as declared in the preface and specified in the text. This thesis does not exceed the prescribed word limit for the Clinical Medicine Degree Committee.

Part of Chapter 2 has been published as:

Hrncirik, F., Roberts, I., Sevgili, I., Swords, C. & Bance, M. Models of Cochlea Used in Cochlear Implant Research: A Review. *Ann Biomed Eng* (2023) doi:10.1007/s10439-023-03192-3.

Part of Chapter 3 is in preparation for publication as:

Hrncirik, F., Nagy, L., Grimes, H., Muzaffar, J., & Bance, M. Impact of Insertion Speed, Depth, and Robotic Assistance on Cochlear Implant Insertion Forces and Intracochlear Pressure: A systematic review. *In prep.*

Part of Chapter 4 is in preparation for publication as:

Hrncirik, F., Figar, E., Roberts, I., & Bance, M. Transparent and Accurate Scala Tympani Models via SLA and DLP 3D Printing: A Comparative Study with Nominal-Actual Analysis. *In prep.*

Part of Chapter 5 has been published as:

Hrncirik, F. Roberts, I., Swords, Ch., Christopher, P., Chhabu, A., Gee, A., & Bance, M. Impact of Scala Tympani Geometry on Insertion Forces during Implantation. *Biosensors* 12, 999 (2022).

Abstract

Effect of Cochlear Shape and Size on Cochlear Implant Insertion Forces
Filip Hrnčiřík

This PhD thesis constitutes a comprehensive investigation into the critical factors and parameters influencing cochlear implantation outcomes, with the ultimate aim to enhance surgical practices and patient outcomes.

Chapter 2 offers a detailed overview of the anatomical and physical properties of the cochlea to aid the development of accurate models for improved future cochlear implant (CI) treatments. It highlights the advancements in the development of various physical, animal, tissue engineering, and computational models of the cochlea, along with the challenges and potential future directions.

Chapter 3 performs a systematic review, consolidating and scrutinising the existing literature on cochlear implantation. Firstly, it centres on the determinants of insertion forces (IFs) and intracochlear pressure (IP) during cochlear implantation, focusing on insertion depth, speed, and the role of robotic assistance. The findings underscore the necessity for standardisation across studies and offer critical insights into the factors influencing IFs and IP during cochlear implantation. The second part of the chapter assesses the influence of surgical approach and cochlear implant type on the occurrence and distribution of cochlear trauma, identifying potential areas for improvement. It indicates the significance of implant design and surgical approach in reducing cochlear trauma and enhancing patient outcomes.

Chapter 4 scrutinises the precision and transparency of Stereolithography (SLA) and Digital Light Processing (DLP) 3D printing technologies in creating full cochlea and *scala tympani* models. The most accurate and transparent models were achieved using DLP technology with a 30 µm layer height combined with an acrylic coating. This provides a promising pathway for creating detailed artificial cochlea models for use in cochlear implantation surgery.

Chapter 5 presents a systematic investigation of the influence of different geometrical parameters of the *scala tympani* on the cochlear implant insertion force. This was done using accurate 3D-printed models of the *scala tympani* with geometrical alterations. The results indicate that the insertion force is largely unaffected by the overall size, curvature, vertical trajectory, and cross-sectional area once the forces were normalised to an angular insertion depth. This supports the Capstan model of the cochlear implant insertion force which suggests the major factor in assessing insertion force and associated trauma are the friction, the tip stiffness, and the angular insertion depth, rather than the length of the CI inserted.

This thesis provides novel insights into the dynamics of cochlear implantation, offers a comprehensive appraisal of the current state of research, provides methodologies to fabricate accurate artificial models, and identifies areas for further investigation. It is anticipated that the findings will guide future research and clinical practice to optimise cochlear implantation outcomes.

Acknowledgements

First and foremost, my profound gratitude goes to my supervisor, Prof Manohar Bance. His decision to entrust me with this project catalysed my professional and personal growth. His faith in my capabilities and never ending support inspired me and encouraged me to deliver my best at every stage of this journey.

I would also like to express my heartfelt thanks to my advisor, Prof Sohini Kar-Narayan. Her guidance in the engineering aspects of my work was instrumental in shaping the trajectory of my project. Furthermore, I owe her a debt of gratitude for recommending me to Prof Bance, a decision that led me to embark on this enriching journey.

My colleague and friend, Dr Iwan Roberts, deserves special recognition for his constant assistance and camaraderie. His support in my research was as indispensable as the countless cups of coffee he graciously bought to fuel our brainstorming sessions.

I am thankful to the University of Cambridge, and specifically to the Departments of Clinical Neurosciences and Materials and Metallurgy, for providing me with an intellectually stimulating environment, excellent resources, and opportunities to learn and grow. My gratitude also extends to Girton College for their unwavering support throughout my academic journey.

To my dear friends Aude, Teteu, Fran, Tomi, and Yoya - your companionship made my time away from work enjoyable and stress-free. Each one of you contributed to making my time in Cambridge truly memorable.

My deepest appreciation goes to my parents and my family, whose sacrifices have given me the opportunity to study at one of the world's leading universities. Their unwavering belief in me has been a cornerstone in my academic journey.

Last but certainly not least, I want to express my enduring gratitude to my partner, Tana. Her unwavering support and love carried me through every stage of my PhD. She has been my source of comfort and strength in times of stress and fatigue, and her presence in my life has been a beacon of joy and hope.

In closing, I dedicate this work to every individual who has been part of my journey and contributed to my growth as a researcher. I am profoundly grateful for your roles in helping me reach this significant milestone in my life.

Table of Contents

List of Figures

List of Tables

Glossary

Acronyms / Abbreviations

AB	Advanced Bionics
BDNF	Brain-derived neurotrophic factor
CIs	Cochlear implants
CNC	Computer numerical control
CO	Cochleostomy
CT	Computed tomography
CV	Coefficient of variation
DLP	Digital light processing
eABR	Electrically-evoked auditory brainstem responses
EAS	Electroacoustic stimulation
eCAPS	Electrically-evoked compound action potentials
ECoG	Electrocochleography
ERW	Extended round window
FDM	Fused deposition modelling
HCs	Hair cells
IF	Insertion forces
IHCs	Inner hair cells

IPA	Isopropyl alcohol
IP	Intracochlear pressure
iPSCs	Induced pluripotent stem cells
LCD	Liquid crystal display
LMA	Low-melting-point alloy
LW	Lateral wall
LWT	Lateral wall trauma
micro-CT	Micro-computed tomography
MRI	Magnetic resonance imaging
NP1	Non-planarity 1
NP2	Non-planarity 2
OHCs	Outer hair cells
PANs	Primary auditory neurons
PJP	Polyjet printing
PMMA	Polymethylmethacrylate
PM	Perimodiolar
PTFE	Polytetrafluorethylene
RWM	Round window membrane
RW	Round window
SEM	Scanning electron microscopy
SGNs	Spiral ganglion neurons
SLA	Stereolithography apparatus
SLS	Selective laser sintering

STL	Stereolithography file format
ST	*Scala tympani*
UV	Ultraviolet

Chapter 1

Introduction and General Overview

This dissertation starts with an elucidation of cochlear implants (CIs) and their placement into the inner ear, followed by an overview of their positioning and existing restrictions. As autonomous entities, Chapters 2, 3, 4, and 5 each contain their distinctive introductions and conclusions.

In Chapter 2, I embark upon an extensive review of the various models utilised to study the cochlea, which encompass physical, animal, tissue engineering, and computational models, particularly in relation to cochlear implant research. This chapter delves into the detailed anatomy of the cochlea and its variations in shape. The primary emphasis is on replicating the features of the cochlea and engaging in a discourse on potential future trajectories.

Chapter 3 involves a systematic review of literature, concentrating on the influence of insertion speed, depth, and robotic assistance on the forces and intracochlear pressure during CI insertion. Additionally, I explore the origins of trauma induced by CI insertion and its correlation with the type of CI (perimodiolar or lateral wall) and the insertion technique (round window or cochleostomy).

Chapters 2 and 3 lay the groundwork for the experimental inquiries undertaken in Chapters 4 and 5.

Chapter 4 begins with an exploration of different 3D printing technologies that can be utilised for crafting an accurate cochlear model with a smooth lumen finish. Subsequently, a meticulous examination of two promising 3D printing technologies for the creation of precise and transparent cochlea and *scala tympani* models is carried out, employing nominal-actual analysis.

In Chapter 5, I employ the optimal 3D printing technology from my previous work, fine-tuned through post-processing, to construct *scala tympani* models of varying sizes and shapes. These models are then used to systematically examine the insertion forces that occur during the insertion of a cochlear implant.

1.1 Cochlear implants

CIs are neural prosthetic devices that bypass most of the peripheral auditory system and directly stimulate the cochlear nerve cell bodies and peripheral and central processes. CIs are one of the most mature technologies in the field of chronically implanted electrical stimulating medical devices. Initial attempts started with single-channel stimulation of the cochlear nerve in patients in 1957,[1,2] followed by multichannel implants, which are more extensively reviewed by others.[3–5]

The external component of the CI consists of one or more microphones that receive sound from the environment, a audio processing unit that filters and processes the sound, and a radio-frequency transmitter (external transmitter) that directs processed sound signals and power to the internal parts beneath the skin (see Figure 1.1 (A)). Internal parts are composed of a receiver/stimulator that receives the signal from the external transmitter and converts it into electric impulses, and an electrode array that is introduced into the cochlea (see Figure 1.1 (B)).

The operation of a CI is dependent on the specific spatial stimulation of auditory nerve fibres. In normal hearing, acoustic input is translated spatially into neural stimulation, *i.e.* different frequencies maximally stimulate different regions of the basilar membrane along the cochlea. These stimulations are in turn translated into neurotransmitter release by inner hair cells to stimulate auditory nerve fibres. Note that the base of the cochlea responds best to high frequencies (up to 20 kHz) and the apex to low frequencies (down to 20 Hz).[6] This spatial coding of frequencies along the length of the cochlea is referred to as a tonotopic organisation. CIs bypass the acoustic aspects of hearing and directly stimulate neural activation of the auditory nerve fibres whose cell bodies reside in Rosenthal's canal in the modiolus, the central porous bony portion around which the cochlea turns. The specificity or focusing ability of the implants stimulation is, therefore, largely determined by how far current spreads, which is determined by the electrical properties of the cochlea and its contained fluids.

As CI technology gains ever more impetus, an increasing number of people with residual hearing are receiving implantation. Different countries have differing criteria for implantation, but for instance, in the UK, the National Institute for Health and Care Excellence (NICE) criteria restrict implants for children or adults with diagnosed severe

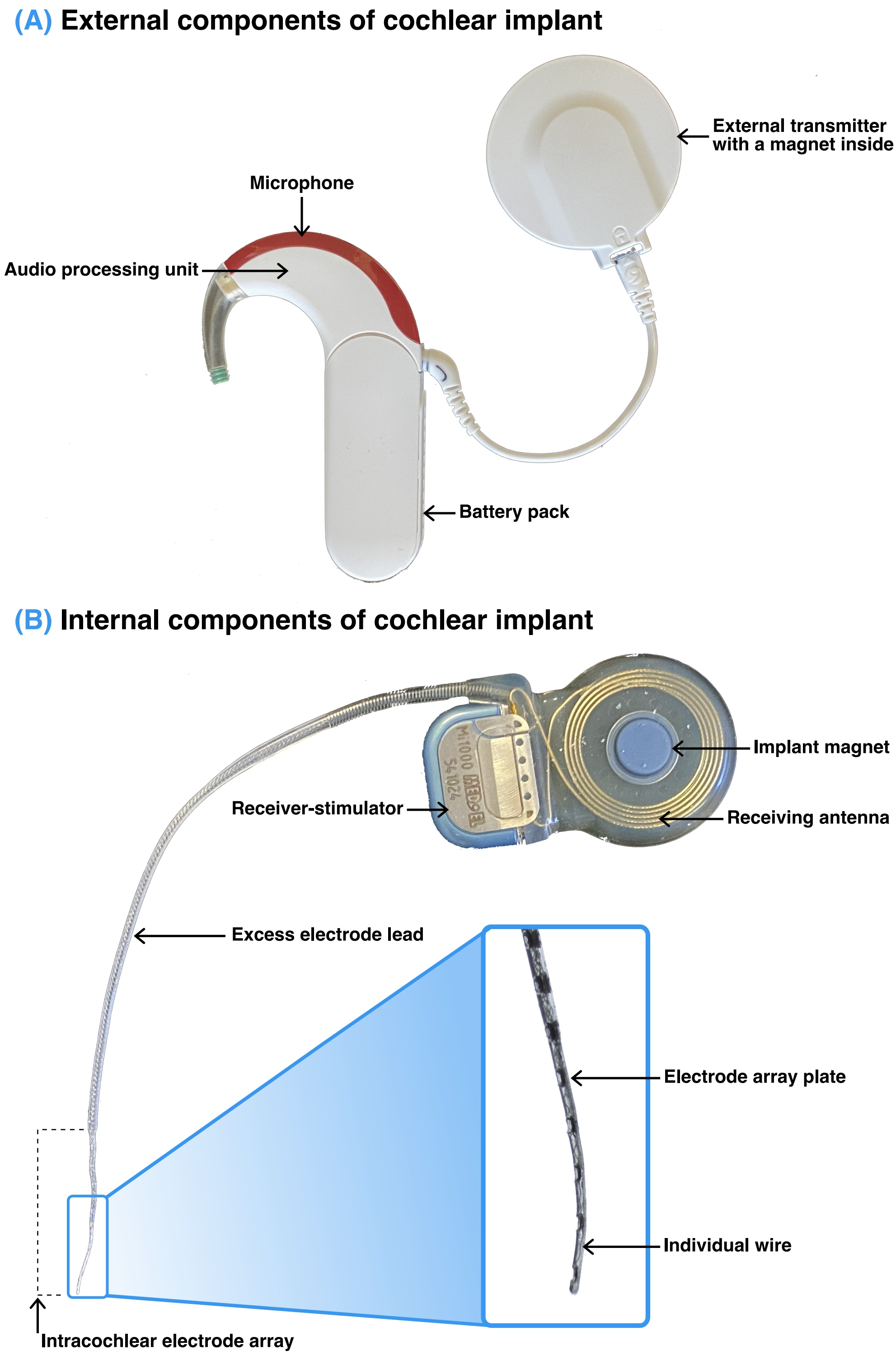

Figure 1.1 External and internal components of a cochlear implant.

to profound deafness. This is defined as hearing only sounds that are louder than 80 dB HL at two or more frequencies bilaterally without any acoustic hearing aids.[7] To a large extent, these criteria are derived from assuring a high probability that the patient will do better with a CI than with hearing aids, as residual hearing is in many people destroyed by the trauma of implantation. Hence, CI decision-making must have a mindset that this is an irreversible procedure, following which the patient cannot go back to their hearing aids if they do not do well with CIs. Reports of partial and total hearing loss vary, but the incidence of patients maintaining *some* residual hearing can be upwards of 90 %,[8–12] particularly at low frequencies. However, 40 – 60 % of patients display a significant decrease compared to their preoperative hearing[10,11,13,14] and a total loss is reported from 8 – 19 % of the time.[8,13,15] Residual hearing has been shown not to have a drastic effect on speech perception outcomes with the CI.[16]

In cases where CI recipients retain some low-frequency hearing, hybrid electric and acoustic stimulation (EAS) CI devices can be beneficial and combine the advantages of acoustic and electrical stimulation.[17,18] In this case, CIs deliver mid-high sound frequencies (as hearing loss is typically more profound at high frequencies), and an amplified acoustic signal covers the low frequencies.[19–21] This is particularly beneficial for better acoustic signal timing information, as CIs perform poorly compared to the acoustic human auditory system.[22] Reducing insertion depth may result in more limited trauma, ensuring better residual hearing preservation. However, this is a trade-off between maximal insertion to increase the range of frequencies that CIs can convey, and reducing trauma during insertion.

Additionally, this irreversible insertion trauma limits these patients from potentially receiving advanced therapies in the future (*e.g.* cell/gene regeneration therapies).

1.2 Insertion of cochlear implants

Various attributes of implantation such as site,[11,14] speed,[23] pressure,[24] angle,[25] and depth of insertion may significantly affect the preservation of the recipient's residual hearing. The following paragraphs briefly introduce these attributes; however, an in-depth analysis of literature is undertaken in Chapter 3.

Regarding the insertion site, two approaches are often taken: introduction of the electrode array through the round window (RW) or by cochleostomy into the *scala tympani*. The first approach penetrates the RW soft membrane, whereas the latter involves drilling into the *scala tympani's* bony wall. The RW technique is frequently and increasingly preferred as it minimises insertional injury compared to cochleostomy, which can introduce bone particles into the intracochlear spaces and negatively impact the patient's acoustic hearing.[21,26] Both can lead to perilymph leakage leading to the theoretical possibility of a perilymph fistula.[27] Nevertheless, cochleostomy may provide better positioning of the electrode array entry point along a vector aligned with the basal turn of the cochlea and, therefore, may, in this aspect, reduce the initial insertion trauma. It is worth noting that RW's orientation and size vary across CI's recipients and may produce difficulties during the insertion process.[28]

Several papers have discussed the implication of insertion speed on the preservation of acoustic hearing.[23,24,29,30] In general, it has been reported that the lower the insertion speed, the lower the insertion forces and, theoretically, less the trauma of implantation. Kesler *et al.* demonstrated that the lowest continuous insertion speed of the electrode array by an experienced surgeon was approximately $867\,\mu\text{m}\,\text{s}^{-1}$.[31] Lower insertion speeds can only be achieved by utilising advanced motorised insertion tools. These can reach speeds as low as $50\,\mu\text{m}\,\text{s}^{-1}$,[24] and can steadily introduce the electrode into the cochlea. The constancy of speed is also of paramount interest as discontinuous movement may result in higher transient intracochlear pressure changes and higher insertion forces which are associated with traumatic implantation.[29,32,33]

Hartl *et al.* argued that measuring insertion forces provides only an indirect projection of cochlear input energy.[24] These measurements can be misleading as other forces, such as internal friction and shear may arise within the device during insertion. However, measurement of intracochlear pressure is a direct way of characterising cochlear input energy and, thus, may more precisely quantify insertion trauma. Intracochlear pressure changes can be attributed to several factors such as the method of entry into the cochlea,[24,34] insertion techniques and velocities,[35] and the shape of the electrode array.[29]

The size of the cochlea duct can significantly vary between patients.[36] Manufacturers produce a range of CIs lengths, from 15 to 31.5 mm, to be able to accommodate individual's needs.[37] However, there has been a general convergence of CI towards about 20 – 25 mm along the lateral wall over the past 20 years.[38] With regards to the depth of insertion, the consensus is that angular insertion depth is superior to the measurement of insertion depth in millimetres as it then compensates for the diversity of cochlear dimensions and CI's trajectories.[39] Deeper insertion of the electrode array into the apical region of the cochlea results in better coverage of low-range frequencies.[40] However, deep insertions are also associated with excessive insertion forces and trauma, and perhaps more loss of residual hearing.[41] This may also lead to a greater risk of translocation of the CI from the *scala tympani* through the *scala media* to the *scala vestibuli*, causing irreparable damage to the basilar membrane and other internal structures of the cochlea.[42] Furthermore, over-inserting the electrode array may contribute to insufficient stimulation of the basal turn region[43] if basal electrodes are pushed past this region. If acoustic hearing preservation is of interest, a smaller electrode length or partial insertion may be considered.

1.3 Cochlear implant positioning

The positioning of CIs within the cochlea is an important factor which determines the induced trauma and detrimental effect on remaining hearing as well as the effectiveness of the implant itself. Auditory nerve fibre degeneration (specifically of the spiral ganglion cells) is strongly associated with duration and severity of hearing loss;[44,45] intra-cochlear inflammation induced via CI insertion trauma can lead to further degeneration and loss of sensitivity of the cochlea.[20] Additionally, long term inflammation and fibrosis can significantly impact the clinical effectiveness of CIs and residual hearing.[46,47]

An essential concept in the positioning of CIs is pitch-place matching. As different parts of the basilar membrane respond to different frequencies, so too do the corresponding spiral ganglion neurons that connect to different regions of the cochlea, at least in post-lingually deafened recipients.[48] CIs aim to compensate for this 'tonotopicity' by allocating lower frequencies to more apical electrodes and higher frequencies to more basal electrodes. However, a substantial mismatch exists between the 'normal' acoustic frequency that would occur at a given cochlear site and the frequency mapped to the electrode in that location. While the brain possesses the ability to reorganise its internal frequency map to a certain extent, there is mounting evidence that more meticulous placement and mapping of frequencies in CIs may offer benefits. Precise alignment, such that the electrodes stimulate the spiral ganglions corresponding to the intended 'natural' frequencies, may expedite improvements in speech recognition. Nevertheless, the evidence supporting this assertion remains in its early stages and continues to emerge.[49] This pitch-place matching, therefore, determines the signal processing and encoding of the stimulation. Although calibration steps in programming (such as pitch ranking) can be used to compensate for initial pitch place mismatch, this is fairly limited especially in the case of electroacoustic and unilateral hearing loss cases using CIs, where the CI stimulation should ideally synchronise with acoustic stimulation in the other ear to prevent conflicting signals.[50]

The lateral to medial positioning of CIs can affect both the implantation-induced trauma and proximity of the electrodes to the spiral ganglion. This has led to the development of two distinct types of CIs which have different mechanical designs: lateral wall and perimodiolar. Lateral wall implants are straight electrodes and use the cochlear lateral wall to guide the insertion. This type is thin and flexible to reduce the insertion forces and trauma that it causes on the lateral wall tissue. Conversely, perimodiolar hugging CIs are pre-curved and generally utilise a metal stylet or insertion tube to keep the array straight during the initial insertion. Once the array reaches the ascending portion of the basal turn, the stylet is removed, or the electrode follows its natural precurved shape as it exits the insertion tube, and the array then follows the perimodiolar wall of the cochlear duct. This approach results in secure positioning of the implant along the modiolus, much closer to the auditory nerve spiral ganglion cell bodies, which may require less power to stimulate the close-by nerve cells and possibly enhancing the hearing performance by reducing the electric spread during stimulation,[38] although this remains to be proven.

1.4 Limitations of current cochlear implants

Two major limitations of CIs are mechanically induced trauma and current spread which limits their clinical effectiveness. Current generations of CIs are not yet optimised for fully atraumatic insertion. As a result, inflammation of intracochlear tissue and trauma occur during insertion. Traumatic insertion can be attributed to numerous issues that arise during the dynamic movement of the implant in the limited space of the cochlear duct.

For instance, high resistance during the insertion process may result in bending or kinking of the electrode array, especially in the basal region as the *scala tympani* diameter is broader towards the base allowing room for buckling.[36] This undesirable motion can elevate the basilar membrane, which may interfere with its standard vibrational mechanics and, therefore, decrease the level of residual hearing preservation. Penetration of the basilar membrane may result in the total loss of residual hearing.[20,26] Continued force on a mechanically blocked electrode array may result in an upwards buckling of the array and an ensuing fracture of the osseous lamina. This fracture would separate dendrites of spiral ganglion cells, lead to local fibrosis and inflammation, and its degeneration in the exposed area.

Partial electrode implantation can be associated with physical obstacles to the insertion trajectory, typically attributed to ossification, fibrosis, irregular cochlear anatomy, or lateral wall friction which also induces lateral wall trauma (LWT).[20,26] LWT is often found at points in the cochlea where there are increased contact forces between the implant and the cochlear lateral wall. In the *scala tympani* (where implants sit), the lateral wall is lined by the spiral ligament, a delicate network of fibres and cells that helps to regulate the inner ear ionic and biologic milieu.[10,20,36] The cochlea's contact points are particularly noticeable in specific regions due to its ascending spiral nature. The first distinct marking is at the point where the basal turn starts to ascend. The next notable marking occurs within the basal turn, where the array tends to buckle if it is either pushed too far or encounters resistance. Finally, significant problems are also seen in the more apical regions of the cochlea, specifically where the structure begins to narrow. Another well-recognised complication is electrode array tip fold-over, in which the tip of the implant reverses direction and partially comes back rather than advancing forwards in the cochlea. This buckling effect has been described in many studies and is affiliated with both straight electrodes (lateral wall),[51] but more commonly with perimodiolar electrodes.[52] The tip fold-over is frequently associated with an obstruction in the cochlear lumen, sub-optimal insertion trajectory, or incorrect application of electrode arrays with pre-curved electrode design (perimodiolar). Furthermore, it may cause significant trauma on the walls of *scala tympani*.[40] Pre-curved perimodiolar electrodes utilise an internal stylet or external sheath to remain straight during insertion. The tool that provides mechanical support during initial insertion is removed at the edge of the first part of the basal turn so that the pre-curved electrode can start to curl up and hug the modiolus. However, this tendency to curl up predisposes this design to tip fold-over.[20,21] Scalar translocation corresponds to an undesired movement of the array between *scala tympani* and *scala vestibuli* through the basilar membrane. Such a disturbance is associated with the loss of residual hearing and may also contribute to a reduction in speech perception[53] as the electrode is further away from spiral ganglion cell bodies. In general, straight electrodes have a lower probability of translocation into the *scala vestibuli* than perimodiolar electrodes.[53–56] 'Electrode migration' is a result of electrodes movement after the surgery and is sometimes thought to be due to ossification or fibrosis of cochlear ducts,[57] but can also be attributed to the inherent 'springiness' of the implant, or external pulling forces from the leads (also discussed in Chapter 5).[20] In this regard, there is a trade-off between the very low friction needed for insertion and the relatively high friction required to retain the implant in the cochlea post-insertion. The range of migration can vary greatly, from nearly undetectable movement to the total migration out of the cochlea, and may take months[58] or longer[59] to be noticed.

Some of the aforementioned positioning and trauma issues can be detected intraoperatively, for instance, by using electrocochleography (ECoG) during insertion, which can detect damage to hearing, allowing the surgeon to change or modify insertion.[60] Surgeons often utilise computerised tomography (CT) or magnetic resonance imaging (MRI) preoperatively to understand the cochlear shape and any abnormalities. It is worth noticing that cochlear shapes and sizes vary significantly between recipients; however, electrodes come in fixed lengths and the actual position of the implant will depend on the size and shape of the cochlea. Even without considering trauma, CIs still face significant challenges and are particularly limited in their capacity to convey speech information. A major limitation with CIs is the severe cross-talk between CI electrodes stimulation and the populations of stimulated neurones due to extensive current spread inside the cochlea. Although electrodes vary between manufacturers, typical CIs include 12 – 22 electrodes. The effective number of information channels is thought to be only 7 – 8 due to this severe cross-talk, resulting in low-fidelity representations of the input acoustic signals as experienced by the recipients.[61] In addition, current shunting in the cochlea results in higher power requirements.

Chapter 2

Models of Cochlea Used in Cochlear Implant Research

Disclosure

This chapter is based on a published paper:

Hrncirik, F., Roberts, I., Sevgili, I., Swords, C. & Bance, M. Models of Cochlea Used in Cochlear Implant Research: A Review. *Ann Biomed Eng* (2023) doi:10.1007/s10439-023-03192-3.

The research and writing of this chapter were conducted by the author unless otherwise stated. The manuscript contains contributions from Dr Roberts (for diagrams, tissue engineering, and computational model sections), Ms Sevgili (for the tissue engineering and animal models sections) and Ms Swords (advising on the anatomy) along with reviewing from all authors listed.

2.1 Introduction

The unique spiral structure of the cochlea is essential to its function as the hearing sensory organ. It transduces physical fluid pressure waves into neural impulses that can be interpreted by the brain to sense and understand the acoustic environment. Although this shell-like structure is vital to one of our most essential senses, relatively little has been done to manufacture an artificial cochlea for research purposes. *In vivo* experiments have provided a wealth of information about the mechanisms of hearing;[21,36,55,62] however, artificial models could provide a platform to further understand and address many of the remaining challenges in repairing hearing impairments.

Hearing impairment is the most prevalent sensory deficit in humans, affecting 466 million people worldwide (World Health Organisation).[63] CIs have been transformative for those suffering from severe-to-profound hearing loss by bypassing normal acoustic hearing mechanisms and directly stimulating the cochlear nerve electrically. However, key limitations still constrain the clinical effectiveness and wider eligibility of these implants. Mechanical trauma generated during CI insertion and the resulting tissue trauma and chronic inflammatory response can damage residual acoustic hearing. Residual acoustic hearing can be beneficial when combined with CI electrical hearing (electro-acoustic hearing), and any interventions to preserve this would increase eligibility for CIs.[17,64–66] Current means for detailed physical examination of the electrode-cochlear interactions involve animal[67–69] and human cadaveric testing.[70–72] However, these models present significant challenges as they cannot be easily instrumented or modified in shape and size to allow systematic testing of performance parameters. Furthermore, animal cochlae are very different anatomically from human cochleae[73] and also have restrictions on the availability and ethical considerations in their use. Only limited progress has been made towards other models, such as engineering realistic artificial cochleae.[74]

A bio-mimetic cochlea has the potential to accelerate both the development of new treatments for hearing loss as well as optimise existing treatments. Therefore, by reviewing the structure and physical properties of the cochlea and its interaction with cochlear implants, I can evaluate requirements for a realistic model and assess current attempts to engineer artificial cochleae and indicate future directions for their development.

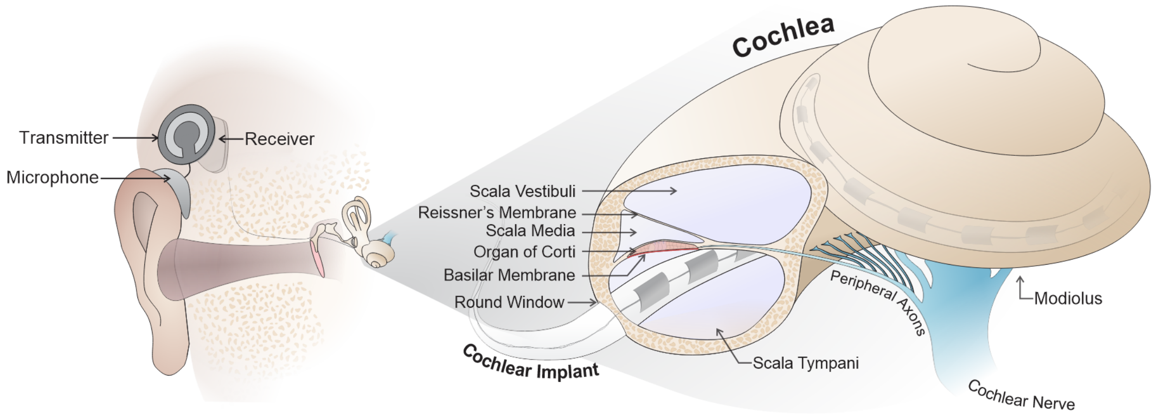

Figure 2.1 Diagram depicting the structure of the cochlea (right) and the insertion of the CI through the round window into the *scala tympani*. This is shown in relation to its position relative to the middle ear and external components of the CI (left). Note that spiral ganglion neurons from the cochlear nerve spiral around the 2.75 turns of the cochlea around the central axis (the modiolus).

2.2 Biological background of cochlea

2.2.1 Anatomy

Embedded in the temporal bone, the cochlea is a fluid-filled structure that is part of the osseous (bony) labyrinth, also referred to as the otic capsule. This consists of the semi-circular canals, responsible for sensing head rotation which is essential for balance, the vestibule, which houses the linear acceleration detectors (the otolith organs), and the cochlea itself (see Figure 2.1).

Neural representation of frequencies in the normal cochlea are structured in a tonotopic manner, primarily by the intrinsic passive and active tuning of the basilar membrane, which maximises vibrations for particular frequencies in a graded manner from apex to base. This results in neurons (specifically spiral ganglion neurons localised in the Rosenthal's canal) along the length of the cochlear spiral encoding low frequencies at the apex and high frequencies towards the base (in a range from 20 Hz to 20 kHz).[75] CIs try to somewhat replicate this tonotopic representation, by presenting lower frequency signals to the apical electrodes and higher frequency ones to the basal electrodes.

A defining feature of the cochlea is its distinct ascending spiral geometry. One reason for the nautilus shell-like structure is thought to be due to spatial constraints in the temporal bone.[76] However, more recent studies have presented evidence suggesting that it also provides functional benefits. For instance, a study by Manoussaki *et al.* indicates that the graded curvature of the cochlea can aid the propagation of low frequencies similar to "whispering gallery nodes" and therefore influence low-frequency hearing limits.[77]

Key parts of the cochlea for surgeons are the bony RW niche and the RW itself, as they are the most common entry portal for CI insertion (see Figure 2.2 (A)). The RW niche is a bony pouch of the tympanic cavity located anterior to the RW which is closed with a membrane. The niche has a width and depth of about 1.66 ± 0.34 mm and 1.34 ± 0.25 mm, respectively.[78] The RW is a small, circular opening with a transverse diameter of about 1.65 ± 0.21 mm positioned inferior and slightly posterior to the oval window at an average distance of 2 to 2.2 mm. It is covered by a thin membrane (69.4 ± 4.3 µm)[79] called the round window membrane (RWM), which enables fluid movement within the cochlea during auditory stimulation.[78,80,81] The oval window is closed by the stapes footplate, a part of one of the three ossicles in the middle ear which transfer vibrations of the eardrum to the inner ear fluids. The oval window is set in the bony vestibule. During auditory stimulation, the stapes footplate vibrates, creating inner ear pressure which is released by the compliant RW membrane.

2.2.2 Variation in cochlear anatomy

Human cochleae display large variations in both size and shape,[36,82] which likely affects the clinical performance of CIs. It is, therefore, crucial to understand this variation when attempting to produce a representative artificial model. Indeed, by developing physical (*i.e.* model made of plastic or similar material that represents anatomically accurate 'mechanical' twin of the human cochlea) or computational models that can represent the variation present in the human cochlea, researchers can try to understand the relationship between different structural features of the cochlea and the effectiveness of CIs. This could reveal possibilities for personalised/stratified medicine within this field by relating different device designs as being optimal for certain types of cochleae, particularly concerning the length of the cochlea, but also to other material properties such as stiffness of the implant in different dimensions for optimal, minimally traumatic full insertion.

Additionally, through a deeper comprehension of these disparities, researchers can enhance the utilisation of animal models by acknowledging the anatomical variations between the human and animal cochlea.

Characterisation of the cochlea size and shape

The cochlea has a characteristic spiral geometry which flares out from a typical Archimedean spiral at the base. This has been characterised by either a piecewise function,[83,84] which separately describes the base and apex or a continuous double exponential function.[85,86] Additionally, a function to determine the height of the cochlea is highly dependent on the reference frame used. For instance, when using a mid-modiolar axis, it is possible to determine that the height of the cochlear centerline increases linearly.[84] This can lead to the observation of three cochlea shape categories: sloping, intermediate, and 'rollercoaster'.[36] A sloping shape has an upward trajectory without any significant downward trend. The intermediate shape follows a slight upward trajectory after the RW, which then follows a slight decrease. Lastly, the 'rollercoaster' shape follows a downward trajectory after the RW, followed by an upward trajectory around 75 to 120°. Nevertheless, Gee *et al.* propose a different perspective. They argue that if a basal plane is defined such that the average height of the first 270° of the basal turn matches the viewpoint of the inserted cochlear implant, then the 'rollercoaster' trajectory is no longer observed.[87] This definition results in a more sigmoidal increase of the cochlear height where the basal turn is rather flat, followed by a sharply defined rising of the cochlear spiral.[87]

Size and shape variation of cochlea

The variability of the cochlea is reflected in the range of cochlear duct lengths ranging from 30.8 to 43.2 mm[88,89] and also, to a lesser extent, with the variable number of turns.[36,90,91] Hence, individual cochleae are not only a scaled-up version of the same basic shape but represent true morphologic variations. Therefore, different shapes and lengths of the electrode arrays should ideally be considered if atraumatic insertion, place-pitch matching (aligning the sound frequencies assigned to electrodes to the natural biologic tonotopic map), and preservation of residual hearing are of interest. Table 2.1 summarises some of the key anatomical features of the cochlea.

Furthermore, the height of the centre part of the *scala tympani* (ST) is larger than in the lateral and modiolar regions. The ST is the lumen into which CIs are placed.[36] Lateral wall height significantly decreases following the second turn (after 450°),[36,92] which can imply a higher possibility of CI translocation through the basilar membrane from the ST (intended site) into the *scala vestibuli* or pushing against the basilar membrane. This likely increases the probability of residual hearing loss and perhaps also worse CI hearing outcomes, if the trauma affects the auditory neurons. Figure 2.2 (C) depicts the changes in the cross-section of the cochlea and the width and thickness of its key membranes at the base and apex. The basilar membrane (excluding Organ of Corti) becomes thinner and wider towards the apex of the cochlea, ranging from 1.26 – 1.92 µm thickness and ∼202 µm width to 0.53 – 0.89 and 475 µm, respectively.[93] However, the thickness and width of the Reissner's membrane remain consistent throughout the cochlear duct length at about 6.4 ± 2.6 µm and 770 ± 180 µm, respectively.[94]

The basal turn represents a large part of the cochlear duct length. Its size variability is, therefore, a significant contributor to the overall CI insertion path and may drastically impact the angular insertion depth of the implant.[80,95] Furthermore, the majority of insertion trauma is observable within this region (180 to 270° from the RW,[96–98] also see Chapter 3) which underlines its importance.

In addition to the major axis change between the first and ascending portions of the basal turn, several smaller anatomical peaks, dips and vertical jumps have been described in the vertical trajectory of the ST.[36,76] These relatively sudden changes in the vertical trajectory of the ST can be critical when calculating the required implant insertion depth in 3D. Therefore, it is essential to replicate them in detail in the physical or computational artificial model as they may play a significant role in determining the insertion interactions between the cochlea and the implant. Each cochlear shape category is unique and, in theory, could require slightly different approaches in terms of insertion site and angle to minimise trauma. However, recent evidence shows a relative independence of the overall friction force experienced by the implant to the cochlea shape,[86] although shape may still play a role in the local stresses and trajectories of the implant, and where this force is concentrated.

Variations of round window

The RW also demonstrates large variability in shapes between implant recipients with majority being of oval-shape (see Table 2.1).[28,99–101] A sharp bony crest called the *crista fenestra*, which occupies an extensive area projecting into the RW, may play a significant role as a barrier to the ST.[101] Different RW niche morphologies produce various sizes of crests.[102] In some situations, removing the crest is necessary to introduce the implant successfully. If the RW is unreachable or the entry angle is not satisfactory, a cochleostomy (separate hole drilled into the ST) is typically considered. Additionally, the surgical view of the RW is limited by the margins of facial recess, *i.e.*, facial nerve posterior, *chorda tympani*, eardrum anterior, and incus buttress superiorly (see Figure 2.2 (A)). Therefore,

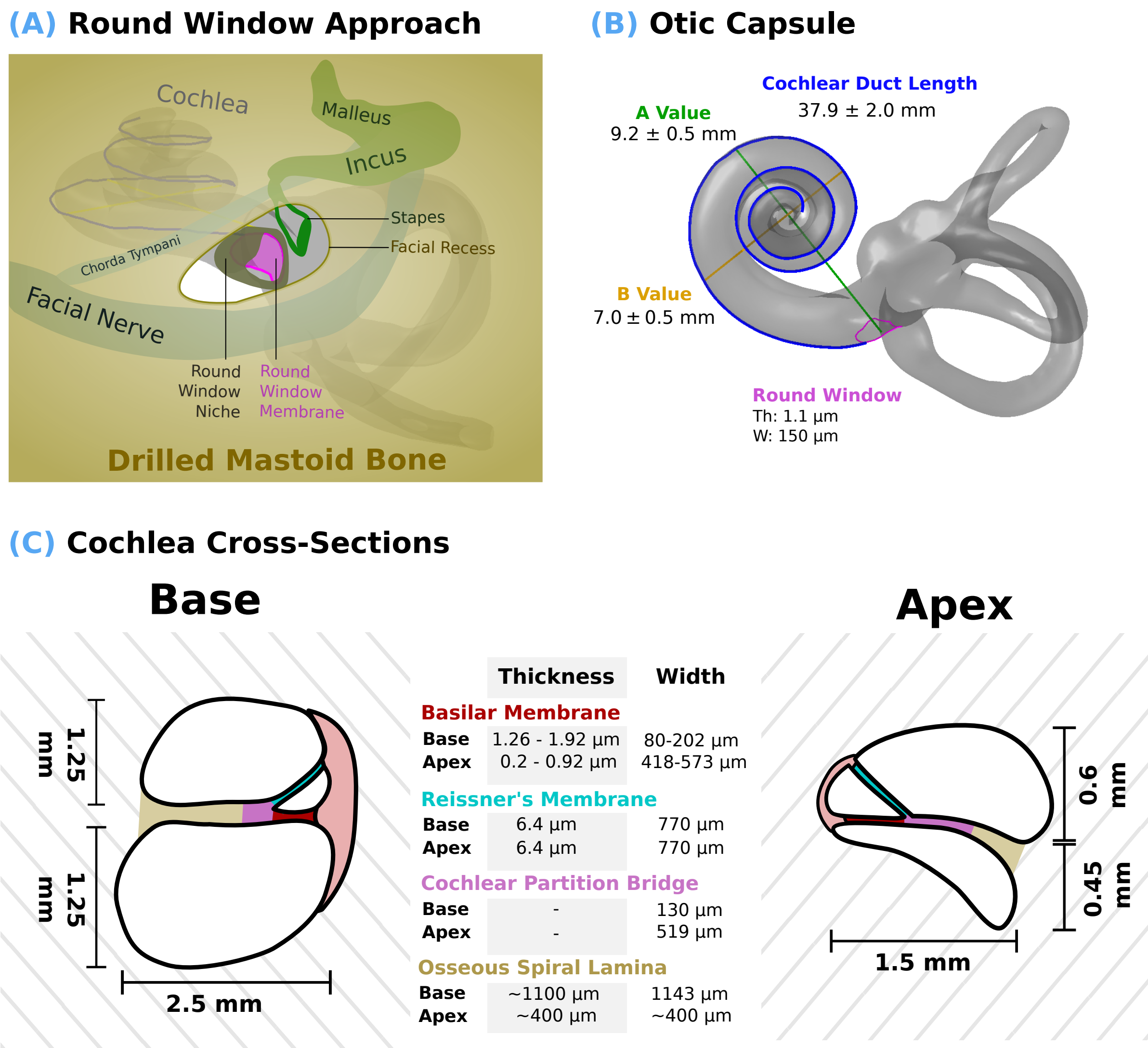

Figure 2.2 Limited surgical view of the round window during implantation (A) and Otic Capsule with cochlear duct length measurement (B). Cross-section of the cochlea at base and apex highlighting key anatomical features (C). Th - thickness; W - width

the surgeon's manoeuvrability is restricted and could benefit from the experience acquired by training on a physical phantom of the human cochlea.

Table 2.1 Summary of the size and shape of various features of human cochleae. SD – Standard Deviation; N - number of samples.

Component of cochlea	Measure		N	Refs
Cochlear duct length	Mean ± SD (range) [mm]			
	37.9 ± 2.0 (30.8 – 43.2)		436	89
	35.8 ± 2.0 (30.7 – 42.2)		310	103
	40.9 ± 2.0 mm angular length 966.7 ± 45.1° (outer wall) number of turns 2.69 ± 0.13		108	76
Number of turns	Number of turns	Percentage [%]	68	90,91
	2.5	1		
	2.5	13		
	2.5 – 2.75	74		
	2.75 – 3	12		
Round window membrane	Height [mm]	Width [mm]		
	1.91 ± 0.78	1.37 ± 0.43	20	99
	0.69 ± 0.25	1.16 ± 0.47	34	81
	1.62 ± 0.77	1.15 ± 0.39	50	100
	Transverse diameter [mm]			
	1.65 ± 0.21		558	78
	Thickness [µm]			
	69.4 ± 4.3		37	79
Round window shape	Oval (60 %), round (25 %) and triangular (15 %)		20	99
	Oval (50 %), round (20 %, triangular (12 %), comma (10 %), quadrangular (6 %), and pear-shaped (2 %)		50	100
Round window niche	Width [mm]	Depth [mm]		
	1.66 ± 0.34	1.34 ± 0.26	541, 460	78
Facial recess	Width [mm]			
	4.01 ± 0.56		356	78
Basilar membrane (excluding Organ of Corti)	Base	Apex		
	Width [µm]			
	~80	498	25	104
	138	573	up to 15	105
	126	418	1	106
	201.9	475.2	up to 14	93
	Thickness [µm]			
	1.26 – 1.92	0.53 – 0.89	up to 13	93
	1.46 – 1.51	0.2 – 0.96	1	106

Continued on the next page

Table 2.1 – continued from the previous page

Component of cochlea	Measure			N	Refs
Organ of Corti		Base	Apex		
		Height [µm]		up to 15	93
		66.02	62.69		
Reissner's membrane	Width (spiral ligament to spiral limbus) [µm]			18	94
	770 ± 180				
	Thickness [µm]				
	6.4 ± 2.6				
Cochlear partition bridge		Base	Apex		
		Width [µm]			
		130	519	up to 15	105
		228.6	499.2	up to 13	93
Osseous spiral lamina		Base	Apex		
		Width [µm]			
		1143	∼400	up to 15	105
		726.6	335.9	up to 13	93
		Thickness [µm]			
		1100	∼400	up to 15	105
Helicotrema	Length (along lateral wall) [mm]			14	107
	1.6 ± 0.9				
Scala tympani		Width [mm]	Height [mm]	9	108
	Base (0°)	2.5 ± 0.3	0.9 ± 0.25		
	Apex (900°)	1.2 ± 0.3	0.4 ± 0.1		
Scala vestibuli		Width [mm]	Height [mm]	9	108
	Base (0°)	2.5 ± 0.2	1.3 ± 0.1		
	Apex (900°)	1.3 ± 0.3	0.5 ± 0.15		

2.3 Reproduction of cochleae

Models of the cochlea can be broadly classified into four categories: physical models, animal models, tissue engineering models, and computational models. Physical models are useful for investigating the mechanical aspects of CI insertion and the electrical properties of the electrode-nerve interface.[29,74,92] These models are often created using materials that mimic the mechanical and electrical properties of the cochlea and can be modified to study the influence of specific parameters on CI behaviour. Animal models, such as guinea pigs[118–120] and chinchillas,[121] are prevalent in CI research due to their ability to replicate physiological responses to stimulation, or damage. Tissue-engineered models are created using living cells and could be potentially used to study the effects of CIs on cells and tissues in more biologically realistic environments than 2D cultures on tissue culture plastic. In general, tissue-engineered models are often constructed using scaffolds that support the growth and organisation of cells into tissues. For cochleae,

Table 2.2 Approximate values for the mechanical properties of different components of the cochlea. Note values were derived from measurements of the specific tissues where possible. OSL - osseus spiral lamina, BM - basilar membrane, RM - Reissner's membrane

Component of cochlea	Rupture load [mN]	Young's modulus [MPa]	Notes	Refs
Basilar membrane	Apical turn: 26 Middle turn: 33 Basal turn: 35	Apical turn: 6.4 Middle turn: 6.0 Basal turn: 9.7	58 yrs, woman	109
Round window membrane	564	9.8	69 yrs, man	109
		Storage modulus (G'): 2.32 to 3.83 Loss Modulus (G"): 0.085 to 0.925		110
Reissner's membrane	4.2	34.2	58 yrs, man	109
Osseus spiral lamina	44 – 122	-	10 cadaveric samples; OSL, BM, RM measured together	111

Table 2.3 Approximate values for the electrical properties of selected anatomical elements of the cochlea. *Based on similar ionic composition of cerebrospinal fluid and **saline.

Anatomical Element	Electrical Conductivity [Sm^{-1}]	Refs
Perilymph	1.43* – 1.78**	112,113
Endolymph	1.68	112
Stria vascularis	0.0053	114
Basilar membrane	0.027 – 0.375	43,114,115
Reissner's membrane	0.0006 – 0.00098	43,114
Temporal bone	0.0156	116,117
Spiral ligament	1.67	114

there have been examples of organoid cultures[122] and decellularised tissues[123] for cochlear tissue engineering although more extensive studies of producing replacement tissues have been discussed for the middle and outer ear.[124–126] Lastly, computational models are increasingly being used to study the electrical and mechanical properties of the cochlea and the effects of CIs on the auditory system.[114,127–129] These models can be used to replicate the complex biological environment of the cochlea in a more controlled and reproducible manner and one that can be easily modified to study specific parameters. Computational models could also be used to predict the performance of CIs in different scenarios, such as differing electrode configurations or stimulation strategies.

The aforementioned models often work in tandem as the acquired data from physical, animal, and tissue-engineered models can be subsequently fed into computational simulation models to accelerate research and examine variables that would otherwise be substantially time-consuming to study. These models play an imperative role in validating computational simulations, as the simulations fail without their tangible data and confirmation.

The following sections discuss various techniques to produce physical artificial cochlea models and the utilisation of animal models, tissue engineering models, and computational simulations.

2.3.1 Physical models

The development of an anatomically accurate model of the human cochlea is of great interest to researchers studying the mechanical aspects of CI insertion (*e.g.*, atraumatic implantation and insertion trajectories) and electrical properties in optimising the electrode-nerve interface (*e.g.*, simulating nerve activation with different stimulation strategies and electrode positions). For example, having a model that can reliably measure insertion forces and can register it with implant position over time (*e.g.*, instantaneous insertion depth) delivers information that can influence surgical practice. Studying the behaviour of electrode arrays within the cochlea can improve CI design and introduce an individualised approach by understanding how a specific implant might behave for a given recipient based on their cochlear shape and size, allowing a personalised selection of implants to possibly minimise insertion forces, optimised electrode position, or avoid basilar membrane contact.

The properties of the artificial cochlea model may vary based on the experiment. For instance, a transparent physical model with a smooth intracochlear lumen with embedded sensors is required to evaluate the intracochlear pressure or insertion forces.[12,29,35,130] The transparency of the model is essential as it allows direct visualisation of the implant behaviour during insertion.[131] The insertion forces can be measured using a force sensor that can be attached to the cochlear model (often multi-axis measurement),[30,131,132] between the electrode array and the insertion device (one-axis).[23,133] Alternatively, in the case of an 'open-channel' artificial model (a model with only the basal turn of the ST fully open at the top surface), the overall force at the location of the basilar membrane/ osseous spiral lamina can be measured with flat force sensor or membrane.[130]

Nevertheless, in order to create these models, it is vital to understand the mechanical and electrical properties of the cochlea. Table 2.2 displays key mechanical data that should be considered when fabricating an artificial cochlea. For instance, the load required to rupture the basilar membrane, which is in the basal turn and apical turn about 35 and 26 mN,[109] respectively, is of great interest when mimicking cochlear implant insertion as its penetration can result in the translocation of the cochlear implant into the *scala media* and *scala vestibuli*, which is frequently associated with the loss of residual hearing, and worse CI function.[26,55,92,134–136]

Additionally, if we are able to replicate the electrical properties (*e.g.*, resistivity) of the cochlear bone and its contained fluids (see Table 2.3), this would greatly help in understanding current spread during cochlear electric stimulation. Having artificial models can very significantly increase the number of repeated experiments that can be performed in a standardised model,[74,86] as opposed to biological tissues, and thus the robustness of any conclusions; these models are mechanically more durable than cadaveric specimens and do not degrade quickly over time. Furthermore, the use of fixed cadaveric tissues may alter the electrical and mechanical properties of the sample, and the availability of fresh cadavers is often limited. Artificial models can also be altered to change one parameter at a time in order to explore the influence of specific parameters (this is further discussed in Chapter 5). However, replicating the electrical properties of a cochlea has proven to be difficult. Artificial cochleae could be created from bone-like material to better mimic *in vivo* tissue; nevertheless, these materials are yet to be fully characterised for high-resolution additive manufacturing. One interesting solution is that 3D printing can be used to fabricate models with an appropriate size of embedded pores filled with a conductive solution that would enable fine-tuning the electrical properties of the material.[74,137,138]

Several methods can be utilised for the development of artificial cochleae (see Figure 2.3 and 2.4).

Casting

For a long time, casting has been the prevalent technique for developing artificial cochleae. Several studies have utilised polymethylmethacrylate (PMMA, often known as acrylic glass or plexiglass) as the casted material for the fabrication of 2D[132,139] and 3D[34,35,131,133,139,140] cochleae models. The advantage of this material is its transparency which provides good visualisation of the array's behaviour during insertion. However, the 2D models offer only limited information as they lack the true three-dimensional form.[84]

Rebscher *et al.* described a multi-casting process exploiting low-melting-point alloy (LMA) and PMMA for the development of an artificial ST (see Figure 2.3).[139] They pro-

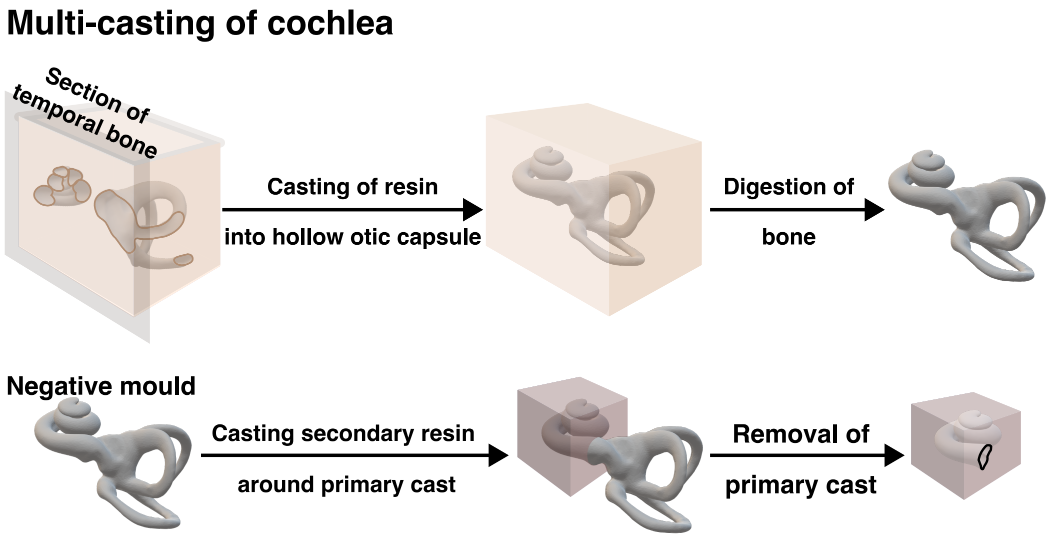

Figure 2.3 Workflow of corrosion casting method. This method uses curable resins that fill the hollow otic capsule within the temporal bone, which is digested to leave the cured resin that replicates the otic capsule space. Negative moulds utilise a double casting method, using the initial cast as a mould which is subsequently removed to leave the hollow lumen of the cochlea.

duced multiple high-accuracy replicas of the same temporal bone by utilising vulcanising silicone rubber, which functioned as a mould. Firstly, the PMMA was injected into a dissected temporal bone and subsequently cooled down. To remove the ST cast from the cadaveric specimen, the temporal bone was decalcified. Following that, the PMMA cast was then covered by vulcanising silicone creating mould. After the curing process of the silicone, the mould was carefully divided into two parts to release the original PMMA cast. In the next step, LMA was poured into the silicone mould to create LMA-casted replicas. Lastly, LMA casts were covered by PMMA. Once PMMA cooled down, the LMA was released (lower melting point than PMMA) to fabricate a 'block' model of the ST.

This process of multi-casting is relatively complicated and time-consuming, in addition to the work needed for the dissection of temporal bones from cadaveric specimens. Moreover, the number of fabricated models using Rebscher's method is limited by the number of dissected samples, and the models' shape cannot be easily modified or adjusted, as it is based on the anatomical specimen itself. Many studies have exploited casted cochlea models from companies such as Advanced Bionics (AB), MED-EL or Cochlear.[84,131,133,141] However, dimensions and anatomic accuracy of these models can be

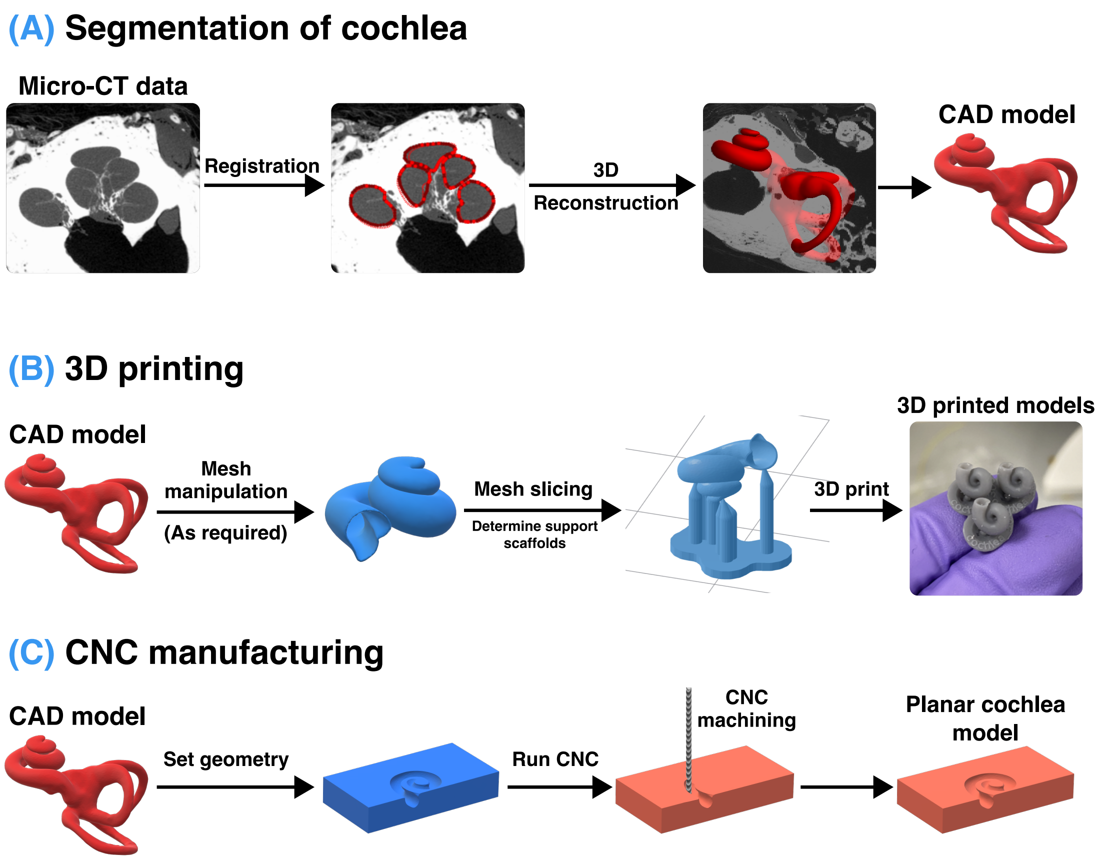

Figure 2.4 Workflow of 3D printing and CNC machining artificial cochlea. (A) Registration and segmentation of the otic capsule from micro-CT scans of the temporal bone can be used to generate CAD files of the cochlear structure. (B) CAD files can be manipulated to make various geometries for 3D printing. For resin-based 3D printing, scaffolding and slicing the model are required prior to printing shape-accurate models. (C) CNC-compatible files can be derived from cochlear CAD models that can be programmed to machine planar cochlear models.

sub-optimal compared to other manufacturing techniques, although this has not been systematically quantified yet.[84,131] As multi-casting involves many steps, each inherently introducing a level of variability, it can be assumed that the anatomic accuracy will suffer as small features could be difficult to reproduce.

In addition to producing cochlear models, corrosion casting has been used to study various anatomical features of the cochlea. For example, Carraro *et al.* have used partial corrosion casting to study the vasculature within the cochlea.[142,143] By perfusing the vasculature with a castable commercial resin, Mercox II, and digesting tissue, it was possible to preserve the vascular structure in mouse cochleae and study it with scanning electron microscopy.

Additive manufacturing

Additive manufacturing, such as 3D printing, is now a well-proven technology that has the potential to develop highly accurate artificial models of human cochleae. Nevertheless, not all 3D printing techniques are suitable for developing such models. Firstly, some 3D printing technologies, such as fused deposition modelling (FDM) or selective laser sintering (SLS), do not produce products with the level of detail required for cochlear research. This is a result of the materials used as well as the nature of the technique. SLS exploits a laser to sinter plastic particles (often nylon-based material) into a solid structure. Although SLS does not require support generation during printing as the powder supports the print, its limitation is the printing resolution, which is suboptimal for prints of the inner ear very small size. FDM may utilise transparent materials (*e.g.*, PLA); however, it fabricates products by heating a filament and building it layer-by-layer, which may generate a step-like finish with a low level of smoothness. The printing resolution is, therefore, significantly dependent on the layer's height. This limitation may further result in suboptimal transparency of the product as each layer scatters light. Secondly, the cochlea anatomy is complex as it contains overhangs, tunnels, and hollow structures, and its fabrication may require temporary supportive scaffolds. If the supports are erected within the cochlea lumen, the smoothness of the inside structure may be compromised. Following that, after the removal of the supportive scaffold, the print is frequently polished to obtain better surface smoothness. However, due to the complex anatomy and inaccessibility; this is not easily achievable in the cochlea.

Some 3D printing techniques such as stereolithography (SLA, see Figure 2.4 (B)),[130,131,140,144,145] digital light processing (DLP),[86] and polyjet printing (PJP)[84,131] have been already exploited for the fabrication of the ST models with much better accuracy (<40 µm).[86] SLA and DLP are photopolymer-based technologies that use ultraviolet light to cure resin (liquid plastics) into 3D prints. In the case of SLA, a system of mirrors focuses the laser into a small spot that is subsequently moved over the printing plane to cure each layer. A single accurate light source provides good smoothness as each printed layer is merged with the previous one. In addition, the layer-merging process also decreases the number of needed supports. DLP uses a projector with UV light to cure the whole layer at once, which enables faster printing but might produce a step-like finish with a too-high layer height. For SLA and DLP, the printed product must be further processed after the printing by washing in isopropanol and curing using a UV-light chamber to obtain the highest possible quality. The optimal printing quality of these techniques comes with a trade-off, as the only supported materials are photopolymer-based. Furthermore, SLA and DLP enable the printing of the product from one material only. However, for example, the material's conductive properties might be tuned by introducing microchannels or pores for modifying the electrical conductivity of the used construct when studying CI stimulation electrical properties.[74]

PJP techniques, on the other hand, allow the printing of multiple materials at once and, thus, fabricating products with various mechanical properties (*e.g.*, flexible and rigid). It exploits thermoplastics that are heated and then deposited on a platform layer-by-layer in the form of droplets using multiple print heads. Moreover, the supportive scaffolds can be printed out of soluble materials, which are easier to remove than SLA and DLP supports which are made of the same materials as the print.

Leon *et al.* used both PJP and SLA printing techniques to fabricate an artificial model of ST and compared them to models from CI companies MED-EL (SLA printed), AB (multi-step casting) and Cochlear (2D planar model).[131] They observed that the measured insertion forces in the SLA model were similar to Cochlear's model, which demonstrates good inner surface smoothness. However, the PJP model demonstrated even lower insertion forces than the SLA printed model, implying an improved internal surface finish. The disadvantage of the PJP model was its semi-transparency which was not optimal for successful visualisation of the implant behaviour during insertion. Hence, they recommend the SLA technique due to its ability to fabricate transparent models. However, PJP technique can achieve enhanced transparency with the use of appropriate material, for example, VeroClear (Stratasys).[146]

It is important to bear in mind that 3D printing capabilities progress rapidly. Several new materials are developed each year, enhancing 3D printing abilities and providing new avenues for prototyping.[147,148] Hence, different 3D printing techniques can be recommended for the fabrication of artificial cochlea each year as the material's selection vary.

Other manufacturing methods

Some studies have used 2D polytetrafluorethylene (PTFE) artificial cochleae.[12,23] This material was used due to its low friction coefficient, which was found to be comparable to the slippery endosteum of the ST.[149,150] These models can be prepared by using computer numerical control (CNC, see Figure 2.4 (C)) machines that carve the material in a 2D plane using precise drills. Although the PTFE material provides optimal smoothness of the internal surface of the model, the lack of the third dimension significantly alters the electrode array's behaviour during insertion.[84,131]

Electro-acoustic models

As there are many aspects of cochlear physiology that are of interest to researchers, there are a variety of different models to replicate these different aspects. In addition to the physical ones mentioned above, some have investigated modelling electro-acoustic aspects of the cochlea. These typically attempt to replicate the sensory epithelium of the cochlea using electro-active materials such as piezoelectric membranes and micromechanical systems.[151–155] Replicating the high-frequency selectivity (20 Hz – 20 kHz) and sensitivity, sound pressure level range (0 – 140 dB SPL) as well as the small size and power requirements of the human cochlea, presents a substantial technical challenge; however, work continues towards the aim of restoring the range and specificity of natural hearing with CIs.[156,157] This may involve atraumatic insertion covering the full extent of cochlear spiral and an increasing specificity of the neural activation. Currently, devices have demonstrated some limited tonotopy within the range of human speech, typically in the $\sim 1.4 - 14$ kHz range with rather high 70 dB+ sound pressure levels.[153,154] Other reports have used alternative methods such as triboelectric devices to detect lower frequency ranges from $\sim 300 - 2000$ Hz in *in vivo* conditions with Guinea pigs[158] with idealised conditions in other studies lowering the minimum frequency to the tens of hertz.[159]

2.3.2 Animal models

Animal models are well established in CI research and have benefits as models in replicating the complex structure of the cochlea and its constituent tissues. By conducting *in vivo* experiments, it is possible to use the features of intact myelinated primary auditory neurons/ spiral ganglion neurons within the cochlea, an immunological response which is important in understanding chronic issues such as fibrosis and ossification,[67,160,161] and potential for conducting some behavioural studies and measuring electrically evoked potentials[162–165] to conduct a wide range of CI studies to understand the CI-nerve interface.

However, there are several considerations in the applicability of different animal models for human CI research in terms of their anatomy and physiology. The cochlea varies in size, shape, and complexity among different species, with differences in the length, width, and number of turns.[73,166,167] Although the overall scalar structure is largely conserved in mammals, the overall shape and size do not scale linearly with overall body size, indicating that factors other than body size determine the cochlea's structure.[166] As most animals have much smaller cochleae than humans, smaller custom-made CIs are required, which increases the complexity of conducting and extrapolating results from animal models.[68,168,169] Furthermore, the structure of the cochlea will determine the spread of the electric field from the CI and, hence, the neural activation which limits their effectiveness in answering some of the key questions in the CI field such as the spread of neural activation to different CI parameters.

Several different animal models have been used for studies that are interested in structure-related parameters and CI implantation. Reiss *et al.* review the extensive use of rodent models–such as mice, rats, gerbils, guinea pigs, ferrets, and chinchillas– in CI research due to their availability, potential for instrumentation, and established gene-editing tools in the case of mice and rats.[73] Guinea pigs, in particular, have been extensively used due to their wide availability, their inner ears being easy to access, and their cochleae being more comparable to the human cochlea in several physiological aspects.[68,118–120,170] Chinchillas have been considered an even better model due to the similarities of their cochlea to humans with regards to its number of turns, hearing range, and sensitivity.[121] Cats are the most popular non-rodent model due to their basal turn being of a similar size to human cochlea,[73] although, the overall shape and size of their cochleae differ significantly from humans. Moreover, the lack of myelin in the soma regions of human type I primary auditory neurons causes a delay in spike conduction compared to cat neurons,[171] which can impact the transmission of temporal fine structure of auditory signals in the human cochlea. Larger animal models include sheep[172] and miniature pigs[69] as well as marmoset[167] and rhesus macaque monkeys.[73,173] These models more closely resemble the size of human cochleae, with the marmoset cochlea demonstrating the highest similarity when scaled up by a factor of 2.5.[167] While this enables partial implantation of clinical electrodes, marmosets and similar models are less readily available than small rodents. Furthermore, they do not effectively reproduce many unique characteristics of human cochleae that are absent even in other primates.[174] For comparison, the ratio of the volume of the human cochlea to different animal cochleae is as follows: mouse $80-100:1$, rat $20-25:1$, gerbil $5-6:1$, cat $2-3:1$, macaque $2-3:1$, and sheep $\sim 1.7:1$.[73]

It is important to consider that the use of animal models is complementary to measures that can be conducted in human patients and cadaveric tissues. For instance, several studies have characterised the electrical properties[70,71] and conducted CI insertion studies[140,175,176] in both fresh-frozen and fixed human cochleae. Furthermore, many electrophysiological and psychoacoustic measures have been developed to test the CI-nerve interface in humans. These include contact impedance and trans-impedance measurements,[177–179] electrically-evoked compound action potentials (eCAPS),[180–182] and electrically-evoked auditory brainstem responses (eABR)[183,184] which enable the evaluation of CI electrical characteristics (including fibrosis, positioning, and electrical faults), cochlear neural activation patterns, and propagation of the CI stimulation to the brain, respectively. However, human studies do not allow us to systematically test numerous parameters in the same experiment, such as electrode position, stimulation parameters, pulse shapes, the geometry of the cochlea, and electrode design, size, and shape, which are much more possible in other models.

In conclusion, animal models are valuable in conducting validation of CI techniques and the systemic responses to CI implantation. However, the limitations of these different models should be considered, especially in light of reducing animal use and used in conjunction with human measures and other models, as will be explored below.

2.3.3 Tissue engineering

Several animal models have been utilised to study the cochlea and develop strategies to improve CI performance. Yet, it remains unclear how to improve electrical stimulation and how different stimulation strategies could affect neural excitation. This necessity led to the use of tissue engineering in the hearing field.

Tissue engineering is a set of methods that can replace or repair damaged or diseased tissues with natural, synthetic, or semi-synthetic tissues which can be fully functional or will grow into the required functionality.[185] These methods could, in theory, be utilised for replicating the complex three-dimensional cellular architecture of the cochlea *in vitro*. Furthermore, they could serve as useful platforms for studying cellular viability and expression in various conditions.

Two important cell types in the cochlea are hair cells (HCs) and primary auditory neurons (PANs), also known as spiral ganglion cells (SGNs). In the mammalian cochlea, HCs serve to sense the mechanical movement, amplify it and transmit this signal to the auditory nerve.[186,187] PANs act as the neural conduit transmitting cochlear HC signals to the brain.[188]

Some research has focused on culturing auditory cells obtained from animals or differentiated from induced pluripotent stem cells (iPSCs). Much work has been conducted *in vitro*, which mostly use mouse, rat, and guinea pig sources for auditory HCs and PANs. Although it has been quite challenging to obtain these cells in significant numbers and maintain them over time, especially when requiring specific purified cell populations, recent studies have demonstrated some success.[189,190] A few studies have progressed to generating human inner ear cells (*e.g.*, IHCs and OHCs) from iPSCs.[191–193] Differentiating PANs has posed a significant challenge due to considerations involving electrical activity, firing potentials, the presence of appropriate ion channels, and gene expression profiles.

While *in vitro* models have facilitated the understanding of cellular mechanisms within the cochlea, they are limited in replicating the complexity of the *in vivo* micro-environment.

By combining data from the flexibility and specificity of *in vitro* experiments, systematic effects and replication of live structures of *in vivo* studies, and the clinical relevance of cadaveric studies, much has been learned about the cochlea and the impact of CIs. However, as all of these approaches have their limitations, there is an unmet need for *in vitro* platforms for hearing research. The cellular and molecular aspects of the cochlea could be integrated into a 3D model, which would complement the limitations of the previous models. This *in vitro* platform could mimic the main functional aspects of the cochlea, including the current spread profile. If incorporated as a host to human iPSC-derived cells, this model would not only reduce the time and cost required for testing but also eliminate the need for animal experiments to study cochlear biology and determine the efficiency and reliability of new drugs or technologies, *e.g.*, CIs, for hearing research.

2.3.4 Computational models

There is a large field of computational audiology that has been used to effectively model several aspects of the cochlea which I will briefly overview in this review. In terms of modelling physical aspects of the cochlea, these can broadly be categorised as electrical and mechanical models.

Electrical models of the cochlea are focused on optimising the electrical implant-nerve interfaces that underlie the function of a cochlear implant and have been reviewed extensively by others.[194–196] These models primarily consist of two main aspects: 1) modelling of the electrical voltage spread within the cochlea, and 2) biophysical and phenomenological models of the neural excitation of auditory nerve fibres.

For the 3D electrical characteristics of the cochlea, there has been extensive work in developing finite element models of the electrical stimulation of cochlear implants that have been established by the groups of Frijns and Rattay.[114,127] These have gradually increased in complexity from simpler parametric representations of the cochlear spiral to micro-CT based models that also incorporate the trajectories of auditory neurons.[116,197,198] As well as understanding the electrical properties of the cochlea, these finite element models have also been utilised for impedance-guided insertion to determine the CI positioning within the cochlea from electrical measurements.[199] These finite element models can be coupled to multi-physics simulations such as thermal safety analyses of intracochlear heating with magnetically steered CIs.[145] As an alternative to finite element models, simpler circuit models of the cochlea have been developed, such as ladder network models, to model specific phenomena.[200]

Biophysical models of neural activation are extensions of the foundational work of Hodgkin and Huxley.[201] As discussed by Bachmaier,[32] the use of multi-compartmental biophysical models of myelinated nerve fibres is able to replicate many phenomena observed in patients such as the sensitivity of the auditory nerves to the polarity of stimulation.[127,202,203]

In contrast to the biophysical approach, phenomenological models do not rely on specific biophysical mechanisms and derive empirical relationships based on neurophysiological and psychophysical observations.[204] Due to the much-reduced parameter space, this approach allows the efficient modelling of complex phenomena that can be adjusted to individual CI patients and has proven effective at predicting and explaining a diverse range of auditory phenomena.[204–206]

Combining the 3D volume conduction models with neuronal models can be a compelling method to investigate the effect of various parameters of the electrode-nerve interface for CIs. These enable the investigation of the effect of different stimulation parameters and positioning on auditory nerve fibre activation.[116,117,197,198] Recent studies have demonstrated the coupling of neural activation from these models to an automatic speech recognition neural network to predict phoneme-level speech perception and information transmission.[85]

The mechanics of the cochlea have been extensively studied since the pioneering work of von Békésy.[115] The extensive work in the mathematical and computational modelling of the basilar membrane micromechanics that underlie the mechanism of acoustic hearing is reviewed by Ni and colleagues.[128] Finally, mechanical models can provide insight into the insertion forces during cochlear implantation, which can lead to significant trauma and inflammatory response, damaging residual hearing.[129]

In conclusion, computational models can be powerful tools to facilitate the understanding of the physical phenomena within the cochlea. However, these models require the correct inputs for measured quantities that can often be difficult to derive and need validation with experimental data to ensure that the model is accurate.

Tables 2.1, 2.2, and 2.3 summarise some of the essential information regarding cochlea physical, electrical, and mechanical attributes that can be used for computational simulations.

Table 2.4 concisely outlines the benefits and drawbacks of the different types of artificial cochlea models examined in this study.

Table 2.4 Advantages and disadvantages of discussed types of artificial cochlea models.

	Advantages	**Disadvantages**
Physical models	Systematically modifiable and reproducible	Limited trauma prediction
Animal models	Suitability for testing physiological and inflammatory responses *in vivo*	Difference in cochlear anatomy and physiology
Tissue engineering	Possibility of manipulation and reproducibility	Limited replication of human cochlear microenvironment
Computational models	Systematic modification, flexibility, integration of multiple models	Requires validation and accurate parameterisation, difficult to model complex non-linear behaviours

2.4 Future perspectives

Future research will focus on developing anatomically accurate artificial cochlea with embedded force and pressure sensors to detect insertion forces that arise during CI implantation. Preserving the residual hearing will aid the further development of EAS implants as natural acoustic stimulation is yet to be exceeded in performance by the electrical stimulation. Additionally, these models could also be utilised for studying inner ear therapeutics and drug delivery systems. Accurate, transparent cochlea models could help precisely determine the pharmacokinetics of drugs delivered inside the inner ear and their spread over time.

Combining cell-based models with animal models can lead to a more comprehensive understanding of CIs and improve the design of safe and effective treatments for auditory disorders. Cell-based models can be used to simulate the electrical and mechanical properties of the cochlea and to study how different stimulation parameters affect the auditory nerve. This information can then be used to guide the design of animal experiments, such as determining the optimal stimulation parameters to use *in vivo*. Animal models can be used to validate and refine the cell-based models and verify their accuracy in replicating the *in vivo* response of the cochlea to CIs. A cell-based 3D model of the cochlea could play an important role in understanding the pathophysiology and aetiology of auditory disorders as well as allowing the interpretation of electric fields of the electrode arrays of CIs in the cochlea by bio-mimicking the true cochlear physiology. Despite the limitations of animal models, they still have advantages in certain areas, such as tracking the systemic response to cochlear implantation and aiding in the development of new therapeutic approaches to mitigate potential adverse effects.

The data from *in vivo* and *in vitro* experiments enables us to validate and inform the design of computational models to understand the mechanisms of the CI-auditory nerve interface. These computational models have increased in complexity over the last 20 years in development to combine finite element models with auditory nerve models to test a variety of clinically relevant parameters and help devise new stimulation strategies. Further development in this field may enable personalised approaches to replicate an individual's specific cochlear anatomy and CI interface to improve their performance rather than generic procedures. Additionally, the dynamic time-dependent component of CI stimulation, rather than purely resistive finite element models, could allow further insights into the validity of using specific stimulation parameters to improve focused auditory nerve stimulation.

Ultimately, by combining the insights from patients, cadavers, animals, *in vitro* experiments, physical models, and computational models it is possible to account for their individual limitations and build a more comprehensive understanding of optimal CI application for patient benefit.

2.5 Conclusion

The elaborate and intricate structure of the human auditory system is a marvel that cannot yet be matched by modern engineering. However, understanding the cochlear structure and how to interact with the delicate system is crucial in addressing huge challenges in otology and audiology. Improving models and understanding the cochlea will lay the foundation for developing the next generation of CIs and future inner ear therapies.

These implants and treatments should address the major challenges of insertion trauma and current spread to preserve cochlear health and residual hearing while conveying high sound fidelity by improving the spatial selectivity of stimulation.

Furthermore, understanding the variability of cochlea's anatomy and its effect on insertion parameters and CI performance could open up the capability of personalised approaches for individual cases to deliver optimal patient outcomes. Addressing these challenges will widen the eligibility for cochlear implants and improve the lives of the growing proportion of people suffering from hearing loss.

Ultimately, a 3D *in vitro* model of the cochlea with integrated auditory cells would revolutionise the study of various features of the inner ear to support the development of new technologies and the validation of computational simulations and drug-based therapies.

Chapter 3

Impact of Insertion Speed, Depth, and Robotic Assistance on Cochlear Implant Insertion Forces and Intracochlear Pressure

Disclosure

Part of Chapter 3 is in preparation for publication as:

Hrncirik, F., Nagy, L., Grimes, H., Muzaffar, J., & Bance, M. Impact of Insertion Speed, Depth, and Robotic Assistance on Cochlear Implant Insertion Forces and Intracochlear Pressure: A systematic review. *In prep.*

The research and writing of this chapter was conducted by the author unless otherwise stated. The manuscript contains contributions from Mr Nagy and Ms Grimes (aid with data collection) along with reviewing from all authors listed.

3.1 Introduction

The World Health Organisation reports that 466 million people worldwide are affected by hearing impairment, which is the most common sensory deficit. The loss of hearing can have a dramatic effect on a person's quality of life, leading to social stigmatisation, isolation, psychological issues, loss of career opportunities, difficulty in relationships and communication, and a higher incidence of depression,[207–209] dementia,[210–212] and overall mortality.[213,214]

CIs have revolutionised the treatment of severe to profound hearing loss by electrically stimulating the cochlear nerve and bypassing normal hearing mechanisms. Despite their benefits, CIs have limitations in terms of their clinical effectiveness and the number of people who can use them. One of the challenges of CI insertion is the mechanical trauma it generates, which can result in intracochlear tissue damage and an ongoing inflammatory response that can harm residual acoustic hearing.[96,176,215] Preservation of this hearing is important, as it can enhance the benefits of combined electro-acoustic stimulation and expand the eligibility of patients for CIs.

Several factors may contribute to the occurrence of cochlear trauma during implantation, including the surgical approach, electrode design, and the interaction between these factors. Two main surgical approaches are utilised for cochlear implant insertion: RW approach and cochleostomy (CO) approach. Additionally, various types of cochlear implants, such as lateral wall (LW) and perimodiolar (PM) implants, can influence the risk of intracochlear trauma during surgery. Understanding the relationship between these factors and cochlear trauma is essential to refining surgical techniques and implant designs, ultimately leading to improved patient outcomes. The Eshraghi *et al.* scale serves as an important tool for categorising trauma levels in cochlear implantation procedures.[216] This scale enables researchers to systematically evaluate the occurrence and severity of trauma and its potential implications for patient outcomes.

To investigate factors such as insertion speed, insertion depth, and the implementation of semi-automated or fully automated insertion techniques, which influence insertion force (IF) and intracochlear pressure (IP) changes, researchers have employed physical artificial models (*e.g.*, *scala tympani* or combined-scalae cochlea models fabricated from plastic or similar materials)[86,141,176,217–225] as well as computational simulations[129] in their studies. These models provide a controlled environment for observing and measuring the IFs and transient IP changes that arise during CI insertion. However, as artificial models do not normally contain the flexible membranes (basilar and Reissner's) separating the individual *scalae*, the findings in these models should be accepted with caution.[226] It is important to consider data from cadaveric specimens and also from histologic examinations in order to correlate insertion trauma location with the rise of IFs and IP.[96,176,215,227] To truly understand the impact of CI insertion on residual hearing preservation, it is crucial to consider both artificial models and cadaveric specimens.

In an effort to improve CI technology and reduce mechanical trauma during the implantation process, researchers have explored using different lubricants[132,219,228–230] and optimising insertion speed.[129,176] By lowering the friction between the implant and the cochlear wall during insertion, it is possible to minimise IFs, thus reducing the potential for tissue damage and, in theory, preserving residual acoustic hearing. Furthermore, optimising insertion speed might help to mitigate transient IP changes, which may be important for both preserving hearing and not damaging the vestibular (balance) structures.[231]

This systematic review aims to provide a comprehensive overview of the current understanding of CI's IFs and IP and their impact on the preservation of residual hearing. An analysis of the existing literature on the measurements of IFs and IP in artificial cochlea models and cadavers, the impact of insertion speed, depth of insertion, and the use of robotic assistance during implantation is performed. Lastly, the review evaluates collected literature concerning cochlear trauma associated with varying surgical methods and types of cochlear implants.

3.2 Materials and methods

The study was prospectively registered in the PROSPERO database of systematic reviews for human (CRD42021246926) and animal studies (CRD42021247348).

3.2.1 Study criteria

Inclusion criteria

The types of studies included: any experimental study describing IFs in cochlear implantation. This includes: case control, case series, randomised controlled trials, animal studies (live, explant, *in vitro*). All animal models (live, explant, *in vitro*, all species, all sexes) implanted with a cochlear implant. All studies (live and cadaveric) assessed the insertion trauma or force resulting from cochlear implantation.

Cochlear implantation – primary outcome assessed will be insertion force measurements (mN) obtained in artificial, cadaveric, and animal models for all brands of cochlear implant with respect to different conditions such as:

- Audiometry measures of hearing preservation
- Evoked potentials in response to auditory stimuli
- Hydrostatic pressures measured in the inner ear during insertion
- Variation in cochlear size
- Variation in cochlear shape
- Speed of insertion (if measured)
- Shape of implant tip (if recorded)

Exclusion criteria

The types of studies excluded: review articles, though reference lists will be searched; case reports and studies with insufficient data.

3.2.2 Search strategy

The search was conducted on 03/04/2021 through the following databases: MEDLINE, Embase, Cochrane, Scopus, and Web of Science. The searches were re-run and confirmed to be up to date on 23/04/2023.

The search strategy for MEDLINE was used as a template on which further strategies were developed for the different listed databases. The literature referenced by identified publications was reviewed to screen for further appropriate studies. The search strategy was as follows:

1. Cochlear Implants/ or Cochlear Implantation/
2. (“cochlear implant*” or “cochlear device*” or “cochlear electrode*” or ”cochlear array*”).ti,ab,kw.
3. “insert*”.ti,ab,kw
4. (“force” or “impact” or “speed” or “pressure”).ti,ab,kw
5. (“insert*” adj2 (“force” or “impact” or “speed” or “pressure”)).ti,ab,kw
6. 1 or 2
7. 5 and 6
8. (“insert*” adj5 (“force*” or “impact*” or “speed*” or “pressure*”)).ti,ab,kw
9. 6 and 8

The MeSH terms used on MEDLINE were ‘Cochlear Implants’ and ‘Cochlear Implantation’.

3.2.3 Study selection

Two authors independently screened the titles and abstracts of all search results generated by the strategy. The full texts were considered by both authors independently with respect to the inclusion and exclusion criteria.

3.2.4 Data extraction and management

A standardised spreadsheet was used to guide data extraction from our included publications. Data was extracted from text, tables and diagrams within the included publications in the following domains:

1. Reference details
2. Study design
3. Intervention details
4. Outcome measurements

3.2.5 Outcome measures

The primary outcome measure was force during cochlear implant insertion. The secondary outcome measures included hearing threshold levels, auditory evoked potentials, histological damage to cochlea.

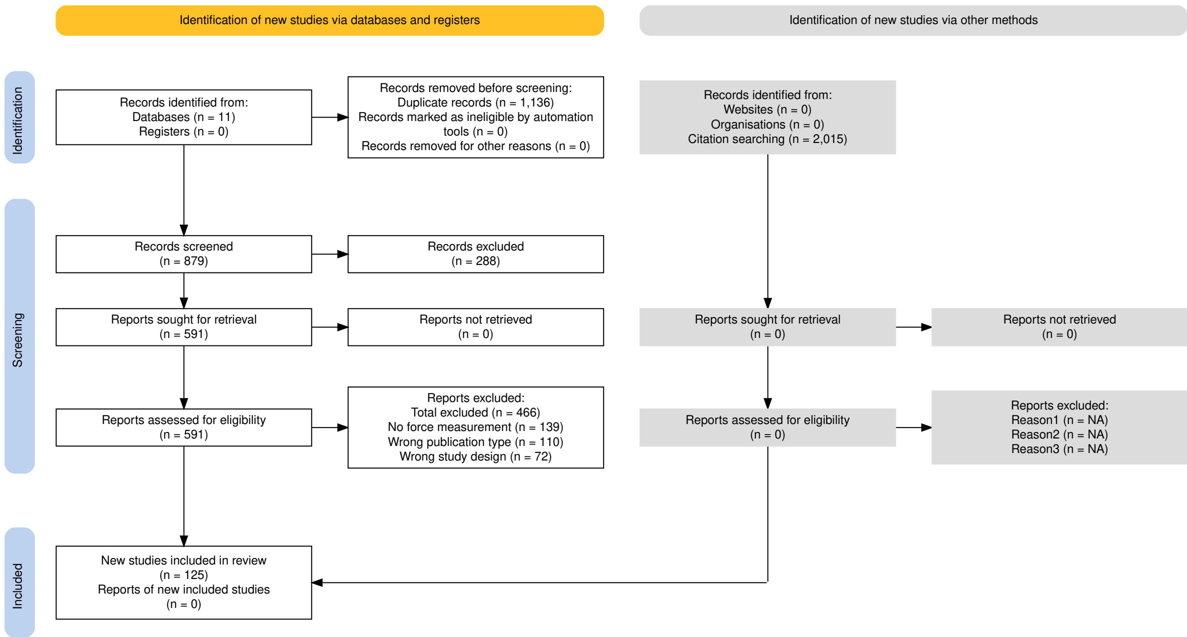

Figure 3.1 PRISMA flowsheet showing number of search results. The figure was generated using the PRISMA Flow Diagram tool.[232]

3.2.6 Statistical processing and meta-analysis

Statistical analyses were performed using MATLAB (MathWorks). An unweighted two-sample t-test was employed when the number of studies in each group was unequal, while a weighted t-test was utilised when the groups had an equal number of data points. The significance level for the data was set at $p < 0.05$. To obtain data at specific insertion depths from diagrams, WebPlotDigitizer[233] was employed.

3.3 Results and discussion

3.3.1 Effect of insertion speed

The analysis of the effect of insertion speed on cochlear implant IFs and IP revealed a trend in studies performed in artificial models: higher insertion speeds are associated with increased IFs and higher IP (Figure 3.2 (B)). However, this effect was not confirmed in cadaveric studies (see Tables 3.1 and 3.2). The variability in results between the cadaveric and artificial studies might be partly attributed to the larger number of studies in artificial category compared to those conducted on cadaveric specimens. Among the latter, only two studies were conducted using fresh temporal bones, one focused on IFs and the other on IP. In the study by Kaufmann *et al.*,[176] insertion speed did not appear to have a substantial effect on the observed maximum forces in either artificial or cadaveric test specimens, likely due to the low speed range tested. The chosen insertion speeds of 0.1 , 0.5 , and $1.0\,\mathrm{mm\,s^{-1}}$ represented the low end and average of typical reported manual insertion speeds, as well as constant, robotics-assisted speeds below human limits. The lack of a strong correlation between insertion speed and insertion forces in this study could be attributed to the limited speed range examined.

Figure 3.2 (B-I) illustrates the relationship between IF and insertion speed in artificial cochlea models using linear regression for each study separately. This approach was chosen because of the numerous variables, such as friction, insertion depth, and cochlear implant type and brand, that contribute to IFs, and are very heterogenous between studies. Consequently, studies could not be directly compared, and the trends were analysed individually for each study rather than creating a single trendline for all studies. The impact of varying insertion speeds on mean intracochlear pressure was investigated by only two studies which were fitted with linear regression to highlight the trend (see Figure 3.2 (B-II)). As with the analysis of IFs, generating a trendline across all studies for mean pressure would not be appropriate, given the differences in artificial cochlea models, round window or cochleostomy openings, and cochlear implant types and brands used in each study.

The pressure measurements in cadaveric specimens for speed analysis were obtained using intracochlear measurements, which included the pressure in the *scala vestibuli* and *scala tympani*. The resulting trans-membrane intracochlear pressure difference was calculated as the difference between the pressure in the *scala vestibuli* and *scala tympani* during insertion. In contrast, measurements in artificial models primarily focused on the mean pressure during insertion. This was measured in the *scala tympani* (or in the lumen where the implant was inserted, as some studies used artificial cochlea models that had all *scalae* fused together), mean amplitude, which was obtained by measuring three to five largest changes and averaging these values, or peak frequency, which represented the number of peaks over the time of insertion (Figure 3.5). As observed by Banakis Hartl and Greene, the dynamic measurement of intracochlear pressure enables the quantification of alterations independent of the fluid volume displaced, while static pressures are directly influenced by the fluid volume displacement resulting from electrode insertion into the intracochlear space.[234] The discrepancy in pressure measurement methodologies between cadaveric and artificial studies may stem from the fact that artificial models lack flexible membranes that adequately replicate fluid dynamics observed in cadaveric specimens.

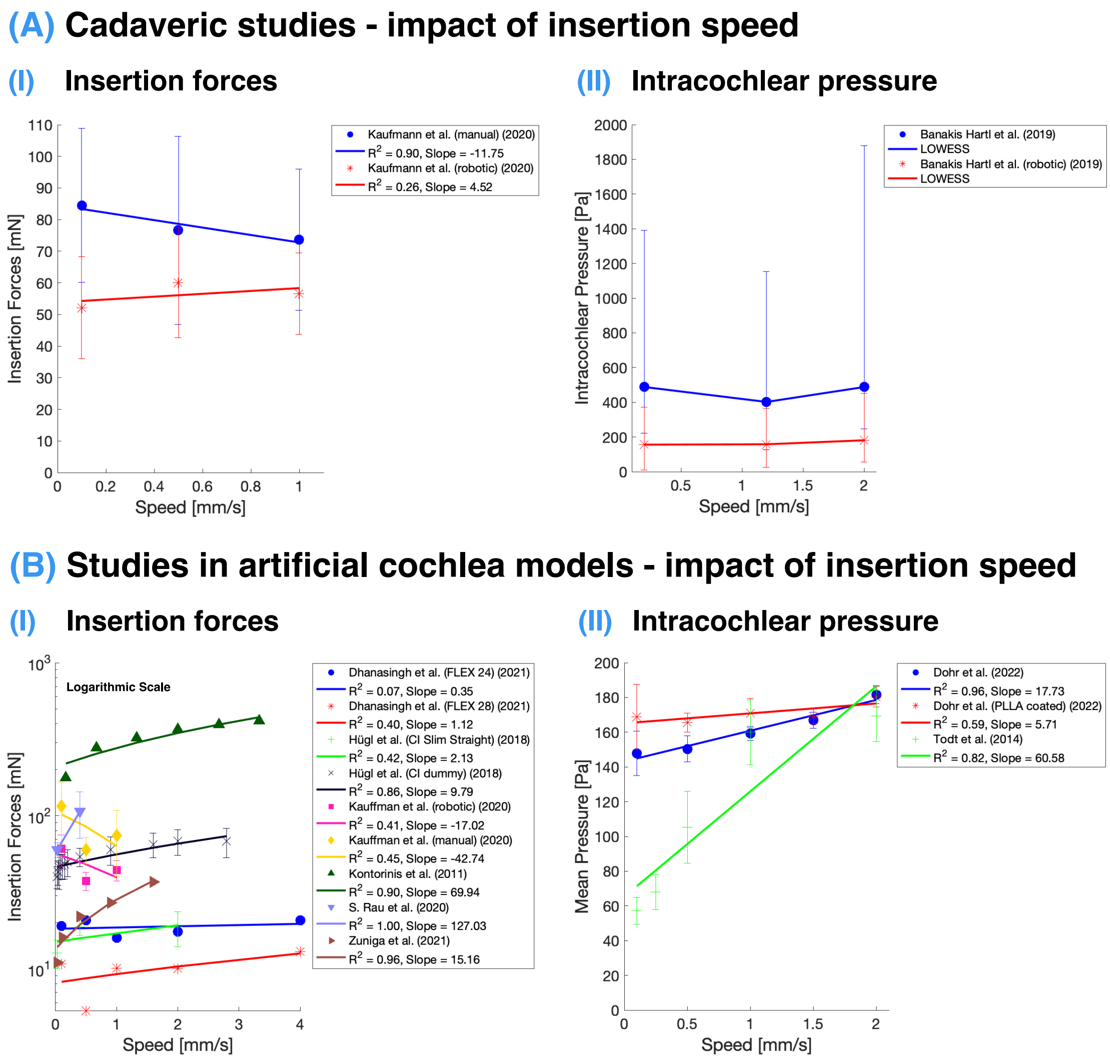

Figure 3.2 Impact of insertion speed on insertion forces and intracochlear pressure. (A) Studies were done in cadaveric specimens. The study of intracochlear pressure was evaluated using a nonparametric regression technique called Locally Weighted Scatterplot Smoothing (LOWESS). (B) Studies done in artificial cochlea models. The impact of insertion speed on insertion force is displayed in the logarithmic y-axis; hence, the linear regression lines appear curved. The colour corresponds with the study, and the points and error bars represent mean and standard deviation., except in the case of cadaveric intracochlear pressure measurement, where these represent the median and interquartile range.

3.3.2 Depth of insertion

Figure 3.3 presents the effects of angular insertion depth and insertion distance on IFs in studies conducted on both cadaveric specimens and artificial cochlea models.

The IFs displayed are the maximum forces reported in these studies at the specified depths/distances. It is essential to note that intracochlear pressure measurements are not included in this analysis, as pressure typically equalises rapidly during insertion. Consequently, changes in pressure with the final implant position within the cochlea are minimal, and such data are often not included in studies. Nevertheless, the rate of pressure equalisation is highly dependent on the size of the round window or cochleostomy opening,[224,235,236] as discussed in the previous section. This factor could lead to slower pressure equalisation during insertion and thus observable IP changes at varying insertion depths.[24] Following this, Ordonez *et al.* reported possible higher pressure levels with deeper insertions, attributed to decreasing volume of *scala tympani* at deeper levels.[237] This effect may be exacerbated if the round window or cochleostomy opening is small and intracochlear fluids cannot escape. Presumably, this will also be influenced by the impedance of the helicotrema. Banakis Hartl *et al.* highlighted the estimated external ear canal pressure values recorded during electrode insertion reached peak levels that would be equivalent to acoustic levels as high as 170 dB sound pressure levels.[24] True acoustic pressures this high would certainly be detrimental to human hearing. However, it is not immediately clear if this conversion is actually a valid measure of the damaging effects, as it also depends partly on the time course of the pressure change. Lastly, Mittmann *et al.* reported that as insertion depth increased, both the number of pressure peaks and the amplitude size diminished.[35] The authors attribute this decrease to the increased stability and reduced intracochlear electrode movement as the depth of insertion increases. The Advanced Bionics IJ electrode array used in the study has a large area of contact with the lateral wall, which could reduce IP changes by providing stabilisation and less movement at the lateral wall. However, the study has limitations due to its artificial cochlear model, which may not accurately represent the *in vivo* situation. The resistance of the artificial model, the size of the round window opening, and the absence of natural pressure equilibration pathways may influence the observed IP. Further research with limited variable factors and different electrode array characteristics is needed to better understand the relationship between insertion depth and intracochlear pressure changes.

Recognising the significance of using angular insertion depth rather than insertion distance in measuring IFs is crucial. Insertion distance is measured based on the cochlear implant position in relation to cochlea's entry point; for example, a fully inserted 20 mm long cochlear implant would have an insertion distance of 20 mm. However, a 20 mm insertion into a small cochlea results in a significantly deeper angular insertion compared to a large cochlea. Angular insertion depth provides insight into the size of the implanted cochlea and offers information about the implant's location relative to the cochlea.[86] By measuring IFs against angular insertion depth, comparisons within the literature become more meaningful.

All studies in Figure 3.3 utilised lateral wall cochlear implants. This is because lateral wall implants generally exhibit a similar IF profile due to the compounding of IFs during insertion. If the cochlear implant follows the lateral wall, the IF profile resembles an exponential function (see Chapter 5).[86] Perimodiolar cochlear implants often do not fully adhere to the contacted wall (in this case, the perimodiolar wall), as they have preformed shapes, resulting in a significantly different insertion profile that cannot be directly compared with lateral wall implants.[141,238] Interestingly, no study adhering to the systematic criteria was found that directly contrasted the IF profiles of perimodiolar and lateral wall cochlear implants.

A trend suggesting an increase in IFs with greater insertion depth is apparent in both cadaveric and artificial studies, as shown in Figure 3.3 (A) and (B). This trend, however, is less evident in artificial cochlea studies considering insertion distance. Although linear regression trendlines were computed for each study category, they do not account for potential influencers such as cochlear implant brand, implant lubrication (or other implant surface modification), steering techniques, or cadaveric specimen freshness. These factors, which can significantly impact IFs, may explain the discrepancy observed in studies.

In the pool of investigated studies, only two have examined alterations to the *scala tympani* environment or modifications to the surface of cochlear implant electrodes, both in artificial cochlea models. Kontorinis *et al.* investigated the effects of modifying the *scala tympani* environment with alginate and the surface of CI (perimodiolar) electrodes with brain-derived neurotrophic factor (BDNF)–producing fibroblasts on insertion forces.[219] Alginate was used as it can serve as an intracochlear drug delivery system, and different concentrations were tested to identify the most effective ones in reducing insertion forces. They found that 50 % alginate/barium chloride gel significantly decreased the insertion forces compared to the control groups. Following that, the BDNF-producing fibroblasts coated CI electrodes resulted in lower insertion forces compared to plain electrodes.

In the study by Hugl *et al.*, two ultra-high viscosity alginate-cell-based drug delivery strategies were tested in artificial cochlea model to improve CI therapy.[239] They found that the alginate created a flexible, mechanically soft surface, shielding the hydrophobic silicone of the CI-electrode. The coating increased the volume of the electrode arrays by about 20 %, which could impact intracochlear pressure and perilymph displacement. Despite variations in coating thickness, the alginate coating appeared to reduce incidences of buckling and tip fold-over during insertion, possibly due to reduced friction and better force distribution. The authors suggest that the hydrophilic nature of the alginate coating may have additional benefits for CI outcomes, such as reduced surgically-induced trauma, decreased foreign body reaction, and protection of inner ear tissue and residual hearing.

Nevertheless, these studies present several limitations, including their limited scope, reliance on artificial models, variation in coating materials and techniques, and a lack of long-term data on implant performance and patient outcomes. Research addressing these limitations is necessary to provide conclusive evidence on the effectiveness and safety of such techniques in clinical practice.

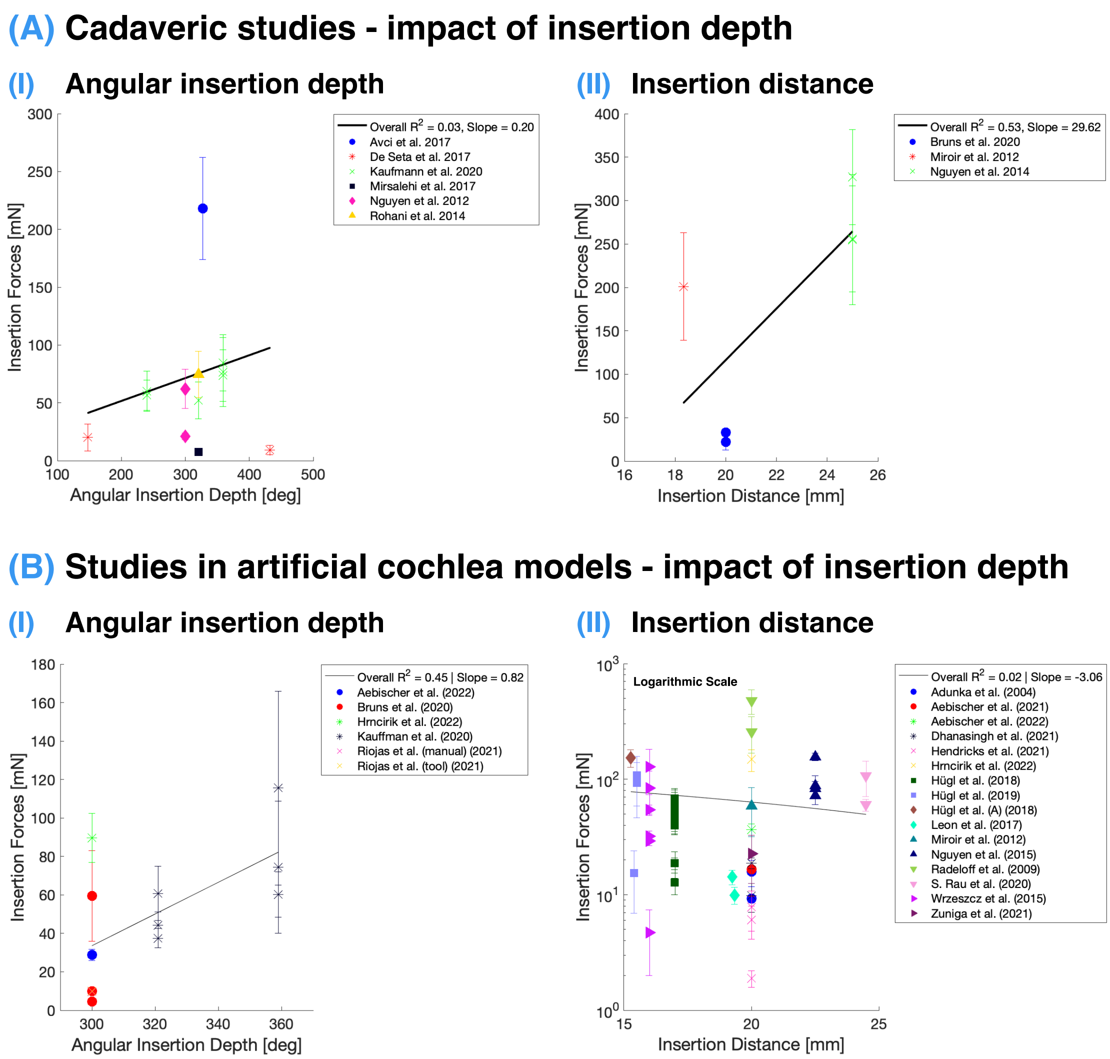

Figure 3.3 Impact of insertion depth on the IFs measured in cadaveric specimens (A) and in artificial cochlea models (B) with angular insertion depth in degrees and insertion distance in mm. (B-II) has y-axis with a logarithmic scale. The colour corresponds with the study, and the points and error bars represent the mean and standard deviation.

Table 3.1 Summary of intracochlear pressure measurements in studies using artificial cochlea models. The primary measurements include mean pressure during CI insertion (measured in the *scala tympani* or in the lumen in cases where the implant was inserted into models with all *scalae* fused together), mean amplitude (calculated by averaging three to five of the largest changes), and peak frequency (indicative of the number of peaks over the course of the insertion). The term 'Robotic?' denotes the use of semi-automatic or automatic systems (*e.g.*, stepper motor) during the insertion process. Term 'Steering?' refers to the regulation or control exerted over the CI during insertion. Values are presented as (mean ± standard deviation) where data allowed. LW - lateral wall CI; PM - perimodiolar wall CI; N - number of insertions.

Author	Mean Pressure [Pa]	Amplitude [Pa]	Peak Frequency [-]	Speed [mm/s]	Robotic?	Steering?	CI Type	CI Brand	N	Model
Dohr *et al.* 2022[240]	(148 ± 13)	-	-	0.1	Y	N	LW	MED-EL	10	Artificial
	(150 ± 7)	-	-	0.5	Y	N	LW	MED-EL	10	Artificial
	(159 ± 4)	-	-	1	Y	N	LW	MED-EL	10	Artificial
	(167 ± 5)	-	-	1.5	Y	N	LW	MED-EL	10	Artificial
	(182 ± 5)	-	-	2	Y	N	LW	MED-EL	10	Artificial
	(169 ± 19)	-	-	0.1	Y	N	LW	MED-EL	10	Artificial
	(165 ± 5)	-	-	0.5	Y	N	LW	MED-EL	10	Artificial
	(171 ± 8)	-	-	1	Y	N	LW	MED-EL	10	Artificial
	(169 ± 4)	-	-	1.5	Y	N	LW	MED-EL	10	Artificial
	(180 ± 6)	-	-	2	Y	N	LW	MED-EL	10	Artificial
Mittmann *et al.* 2018[222]	-	(14 ± 5)	(6.4 ± 0.4)	0.5	N	N	PM	HiFocus Midscalar AB	5	Artificial
	-	(8 ± 1)	(8.2 ± 0.2)	0.5	N	N	LW	LW prototype	5	Artificial
Mittmann *et al.* 2017[35]	-	(35 ± 16)	(18 ± 2)	0.5	Y	N	LW	HiFocus 1J AB	3	Artificial
	-	(27 ± 8)	(14 ± 2)	0.5	Y	N	LW	HiFocus 1J AB	3	Artificial
Mittmann *et al.* (A) 2017[29]	(115 ± 7)	(12 ± 9)	(12 ± 1)	0.48	N	N	LW	Slim Straight Cochlear	5	Artificial
	(149 ± 20)	(51 ± 9)	(12 ± 1)	0.48	N	N	PM	Nucleus 24 Cochlear	5	Artificial
Todt *et al.* 2017[225]	(96 ± 19)	(24 ± 11)	(11 ± 2)	0.5	N	N	LW	HiFocus 1J AB	5	Artificial
	(109 ± 31)	(13 ± 13)	(4 ± 1)	0.5	N	N	PM	AB Helix	5	Artificial
	(80 ± 21)	(21 ± 13)	(13 ± 4)	0.5	N	N	PM	AB HF Midscalar	5	Artificial
	(51 ± 16)	(25 ± 39)	(11 ± 2)	0.5	N	N	LW	AB LW23	5	Artificial
Todt *et al.* 2014[231]	(57 ± 8)	-	-	0.1	Y	N	LW	HiFocus 1J AB	3	Artificial
	(68 ± 10)	-	-	0.25	Y	N	LW	HiFocus 1J AB	3	Artificial
	(105 ± 21)	-	-	0.5	Y	N	LW	HiFocus 1J AB	3	Artificial
	(160 ± 19)	-	-	1	Y	N	LW	HiFocus 1J AB	3	Artificial
	(169 ± 15)	-	-	2	Y	N	LW	HiFocus 1J AB	3	Artificial
Todt *et al.* 2016[224]	-	(87 ± 19)	(21 ± 2)	0.2	N	N	LW	HiFocus 1J AB	3	Artificial
	-	(25 ± 227)	(11 ± 1)	0.2	N	N	LW	HiFocus 1J AB	3	Artificial
	-	(8 ± 4)	(7 ± 1)	0.2	N	N	LW	HiFocus 1J AB	3	Artificial
	-	(20 ± 9)	(9 ± 2)	0.2	Y	N	LW	HiFocus 1J AB	3	Artificial
	-	(12 ± 5)	(8 ± 1)	0.2	Y	N	LW	HiFocus 1J AB	3	Artificial
	-	(4 ± 3)	(3 ± 1)	0.2	Y	N	LW	HiFocus 1J AB	3	Artificial
Todt *et al.* (A) 2016[230]	-	(63 ± 8)	-	0.33	N	N	LW	HiFocus 1J AB	5	Artificial
	-	(64 ± 4400)	-	0.33	N	N	LW	HiFocus 1J AB	5	Artificial
	-	(244 ± 60)	-	0.33	N	N	LW	HiFocus 1J AB	5	Artificial

Table 3.2 Overview of insertion force measurements in studies using cadaveric and artificial cochlea models. The CI insertion length is quantified either as angular insertion depth (in degrees) or as linear insertion distance (in millimetres). The term 'Robotic?' denotes the use of semi-automatic or automatic systems (*e.g.*, stepper motor) during the insertion process. Term 'Steering?' refers to the regulation or control exerted over the CI during insertion. Values are presented as (mean ± standard deviation) where data allowed. LW - lateral wall CI; PM - perimodiolar wall CI; N - number of insertions.

Author	Force [mN]	Depth [deg]	Distance [mm]	Speed [mm/s]	Robotic?	Steering?	CI Type	CI Brand	N	Model
Adunka *et al.* 2004[217]	(16 ± 4)	-	20	-	N	N	LW	C40+ MED-EL	14	Artificial
	(9 ± 1)	-	20	-	N	N	LW	C40+ Flex MED-EL	7	Artificial
Aebischer *et al.* 2022[97]	(36 ± 5)	-	20	0.33	Y	N	LW	Custom	39	Artificial
	(29 ± 3)	300	-	0.33	Y	N	LW	Custom	39	Artificial
Aebischer *et al.* 2021[241]	(17 ± 7)	-	20	0.33	Y	N	LW	Custom	21	Artificial
Avci *et al.* 2017[98]	(218 ± 44)	327	22	0.5	Y	N	LW	HiFocus 1J AB	27	Cadaveric
Bruns *et al.* 2020[140]	(59 ± 24)	300	-	-	N	N	LW	Flex MED-EL	4	Artificial
	(10 ± 2)	300	-	1.25	Y	N	LW	Flex MED-EL	4	Artificial
	(5 ± 1)	300	-	1.25	Y	Y	LW	Flex MED-EL	4	Artificial
	(33 ± 4)	-	20	1.25	Y	N	LW	Flex MED-EL	4	Cadaveric
	(22 ± 9)	-	20	1.25	Y	Y	LW	Flex MED-EL	4	Cadaveric
De Seta *et al.* 2017[96]	(9 ± 4)	240	-	0.8	Y	N	LW	Flex MED-EL	6	Cadaveric
	(20 ± 12)	240	-	0.8	Y	N	LW	Flex MED-EL	6	Cadaveric
Dhanasingh *et al.* 2021[242]	10.73	-	28	0.1	Y	N	LW	Flex 28 MED-EL	9	Artificial
	5.33	-	28	0.5	Y	N	LW	Flex 28 MED-EL	9	Artificial
	10.08	-	28	1	Y	N	LW	Flex 28 MED-EL	9	Artificial
	10.02	-	28	2	Y	N	LW	Flex 28 MED-EL	9	Artificial
	12.91	-	28	4	Y	N	LW	Flex 28 MED-EL	9	Artificial
	19.04	-	24	0.1	Y	N	LW	Flex 24 MED-EL	9	Artificial
	20.67	-	24	0.5	Y	N	LW	Flex 24 MED-EL	9	Artificial
	15.96	-	24	1	Y	N	LW	Flex 24 MED-EL	9	Artificial
	17.53	-	24	2	Y	N	LW	Flex 24 MED-EL	9	Artificial
	20.73	-	24	4	Y	N	LW	Flex 24 MED-EL	9	Artificial
Hendricks *et al.* 2021[130]	(8 ± 3)	-	20	1.3	Y	N	LW	Standard MED-EL	12	Artificial
	(6 ± 2)	-	20	1.3	Y	Y	LW	Standard MED-EL	12	Artificial
	(1.9 ± 0.3)	-	20	1.3	Y	Y	LW	Standard MED-EL	12	Artificial
Hrncirik *et al.* 2022[86]	(90 ± 13)	300	-	0.5	Y	N	LW	Slim straight Cochlear	10	Artificial
	(148 ± 32)	-	20	0.5	Y	N	LW	Slim straight Cochlear	10	Artificial
Hügl *et al.* 2019[239]	(93 ± 47)	-	15.5	0.4	Y	N	LW	Custom	23	Artificial
	(15 ± 9)	0.4	(15.39 ± 0.02)	-	Y	N	LW	Custom with coating	26	Artificial
	(108 ± 49)	-	15.5	0.4	Y	N	LW	Flex MED-EL	60	Artificial
Hügl *et al.* 2018[30]	(40 ± 7)	-	17	0.03	Y	N	LW	Custom	24	Artificial
	(43 ± 8)	-	17	0.045	Y	N	LW	Custom	24	Artificial
	(46 ± 13)	-	17	0.06	Y	N	LW	Custom	24	Artificial
	(47 ± 8)	-	17	0.08	Y	N	LW	Custom	24	Artificial
	(47 ± 9)	-	17	0.11	Y	N	LW	Custom	24	Artificial
	(48 ± 9)	-	17	0.15	Y	N	LW	Custom	24	Artificial
	(50 ± 10)	-	17	0.2	Y	N	LW	Custom	24	Artificial
	(54 ± 8)	-	17	0.4	Y	N	LW	Custom	24	Artificial
	(60 ± 13)	-	17	0.9	Y	N	LW	Custom	24	Artificial
	(65 ± 12)	-	17	1.6	Y	N	LW	Custom	24	Artificial
	(68 ± 13)	-	17	2	Y	N	LW	Custom	24	Artificial
	(68 ± 15)	-	17	2.8	Y	N	LW	Custom	24	Artificial
	(13 ± 3)	-	17	0.03	Y	N	LW	Slim straight Cochlear	9	Artificial
	(19 ± 2)	-	17	0.4	Y	N	LW	Slim straight Cochlear	9	Artificial
	(19 ± 5)	-	17	2	Y	N	LW	Slim straight Cochlear	9	Artificial
Hügl *et al.* (A) 2018[243]	(153 ± 26)	-	(15.3 ± 0.2)	0.4	Y	N	LW	Custom	117	Artificial

Continued on the next page

Table 3.2 – continued from the previous page

Author	Force [mN]	Depth [deg]	Distance [mm]	Speed [mm/s]	Robotic?	Steering?	CI Type	CI Brand	N	Model
Kauffman *et al.* 2020[176]	(116 ± 50)	(359 ± 113)	-	0.1	N	N	LW	Unknown	12	Artificial
	(60 ± 12)	(359 ± 113)	-	0.5	N	N	LW	Unknown	12	Artificial
	(74 ± 34)	(359 ± 113)	-	1	N	N	LW	Unknown	12	Artificial
	(61 ± 14)	(321 ± 84)	-	0.1	Y	N	LW	Unknown	12	Artificial
	(38 ± 5)	(321 ± 84)	-	0.5	Y	N	LW	Unknown	12	Artificial
	(44 ± 7)	(321 ± 84)	-	1	Y	N	LW	Unknown	12	Artificial
	(85 ± 24)	(359 ± 113)	-	0.1	N	N	LW	Unknown	36	Cadaveric
	(77 ± 30)	(359 ± 113)	-	0.5	N	N	LW	Unknown	36	Cadaveric
	(74 ± 22)	(359 ± 113)	-	1	N	N	LW	Unknown	36	Cadaveric
	(52 ± 16)	(321 ± 84)	-	0.1	Y	N	LW	Unknown	36	Cadaveric
	(60 ± 17)	(321 ± 84)	-	0.5	Y	N	LW	Unknown	36	Cadaveric
	(57 ± 13)	(321 ± 84)	-	1	Y	N	LW	Unknown	36	Cadaveric
Kontorinis *et al.* 2011[23]	(177 ± 3)	-	17	0.17	Y	N	PM	Nucleus 24 Cochlear	10	Artificial
	(279 ± 6)	-	17	0.67	Y	N	PM	Nucleus 24 Cochlear	10	Artificial
	(323 ± 4)	-	17	1.33	Y	N	PM	Nucleus 24 Cochlear	10	Artificial
	(366 ± 7)	-	17	2	Y	N	PM	Nucleus 24 Cochlear	10	Artificial
	(394 ± 4)	-	17	2.67	Y	N	PM	Nucleus 24 Cochlear	10	Artificial
	(418 ± 8)	-	17	3.33	Y	N	PM	Nucleus 24 Cochlear	10	Artificial
Leon *et al.* 2017[218]	(14 ± 2)	-	(19 ± 1)	∼0.2	Y	N	LW	Flex MED-EL	29	Artificial
	(10 ± 2)	-	(19 ± 1)	∼0.2	Y	Y	LW	Flex MED-EL	19	Artificial
Majdani *et al.* 2010[141]	36	16	-	0.3	Y	N	PM	Nucleus 24 Cochlear	8	Artificial
	26.3	236	-	0.3	Y	N	PM	Nucleus 24 Cochlear	8	Artificial
	17.7	60	-	-	N	N	PM	Nucleus 24 Cochlear	26	Artificial
	31.4	196	-	-	N	N	PM	Nucleus 24 Cochlear	26	Artificial
Miroir *et al.* 2012[244]	(58 ± 26)	-	20	1.3	Y	N	LW	HiFocus 1J AB	6	Artificial
	(201 ± 62)	-	(18 ± 1)	1.5	Y	N	LW	HiFocus 1J AB	3	Cadaveric
Mirsalehi *et al.* 2017[245]	(8 ± 3)	148	-	-	N	N	LW	Slim straight Cochlear	10	Cadaveric
Nguyen *et al.* 2015[132]	(156 ± 12)	-	(23 ± 4)	1.5	Y	N	LW	Digisonic SP	35	Artificial
	(83 ± 12)	-	(23 ± 4)	1.5	Y	N	LW	Digisonic SP Evo	35	Artificial
	(88 ± 19)	-	(23 ± 4)	1.5	Y	N	LW	Digisonic SP Evo coating 1	35	Artificial
	(72 ± 12)	-	(23 ± 4)	1.5	Y	N	LW	Digisonic SP Evo coating 2	35	Artificial
Nguyen *et al.* 2014[246]	(256 ± 61)	-	25	-	N	N	LW	HiFocus 1J AB	39	Cadaveric
	(327 ± 55)	-	25	-	N	N	LW	HiFocus 1J AB	39	Cadaveric
	(255 ± 75)	-	25	0.6	Y	N	LW	HiFocus 1J AB	39	Cadaveric
Nguyen *et al.* 2012[227]	(62 ± 17)	300	-	0.5	Y	N	LW	Digisonic SP	8	Cadaveric
	(21 ± 3)	300	-	0.5	Y	N	LW	Custom	15	Cadaveric
Radeloff *et al.* 2009[247]	(479 ± 116)	-	20	0.5	Y	N	LW	C40+ MED-EL	8	Artificial
	(257 ± 89)	-	20	0.5	Y	N	LW	C40+ MED-EL and coating	8	Artificial
Riojas *et al.* 2021[248]	9.71	300	-	-	N	N	LW	MED-EL	4	Artificial
	9.97	300	-	-	N	N	LW	MED-EL	4	Artificial
Rohani *et al.* 2014[249]	(75 ± 20)	(432 ± 75)	-	-	N	N	LW	Unknown	5	Cadaveric
S. Rau *et al.* 2020[221]	(60 ± 7)	-	24.5	0.03	Y	N	LW	Standard MED-EL	10	Artificial
	(107 ± 36)	-	24.5	0.4	Y	N	LW	Standard MED-EL	10	Artificial
Schurzig *et al.* 2010[238]	(86 ± 3)	-	17	-	Y	N	PM	Freedom Advance CI	4	Artificial
	(17 ± 7)	-	17	-	Y	N	PM	Freedom Advance CI	4	Artificial
Smetak *et al.* 2023[250]	(140 ± 80)	(428 ± 40)	-	0.65	Y	N	PM	Cochlear	15	Cadaveric
Wrzeszcz *et al.* 2015[229]	(128 ± 54)	-	16	2	Y	N	LW	Custom	5	Artificial
	(29 ± 3)	-	16	2	Y	N	LW	Slim straight Cochlear	5	Artificial
	(5 ± 3)	-	16	2	Y	N	LW	Custom	5	Artificial
	(54 ± 5)	-	16	2	Y	N	LW	Custom	5	Artificial
	(84 ± 34)	-	16	2	Y	N	LW	Custom	5	Artificial
	(32 ± 3)	-	16	2	Y	N	LW	Slim straight Cochlear	5	Artificial
Zuniga *et al.* 2021[251]	11	-	16	0.03	Y	N	LW	Custom	11	Artificial
	16	-	16	0.11	Y	N	LW	Custom	11	Artificial
	22	-	16	0.4	Y	N	LW	Custom	11	Artificial
	27	-	16	0.9	Y	N	LW	Custom	9	Artificial
	37	-	16	1.6	Y	N	LW	Custom	9	Artificial

3.3.3 Controlled robotic insertion

Both cadaveric specimen and artificial cochlea model measurements indicate no statistically significant difference ($p > 0.05$) in mean maximal IFs when employing controlled robotic assistance for insertion (Figure 3.4). The analysis utilised an unweighted t-test, as the number of studies for each group (manual or robotic) was not equal. It is essential to note that the data are plotted regardless of any other variables that might have contributed to the lack of significant difference between IFs measured using manually and automatically inserted cochlear implants. Only three studies[140,176,246] have investigated the use of robotic insertion and compared it to standard manual insertion performed by a surgeon. Among these, only the group of Kaufmann *et al.* had an adequate sample size.[176] According to their data, there was a significant difference ($p < 0.001$) between the IFs measured with manual and robotic insertion for both cadaveric specimens and artificial cochlea model insertions.

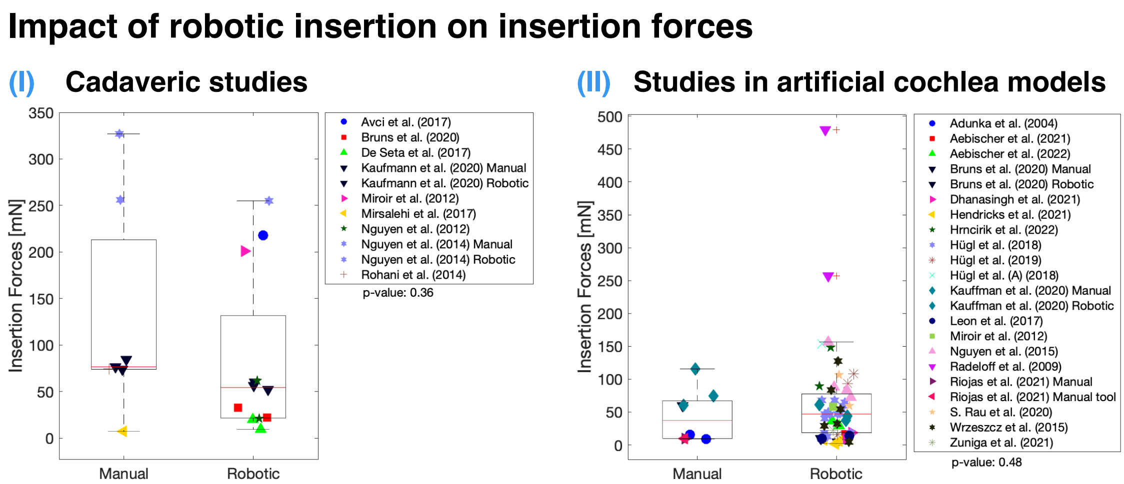

Figure 3.4 Impact of robotic insertion on mean maximal IFs measured in cadaveric specimens (I) and artificial cochlea models (II). Unweighted two-sample t-tests were used for both diagrams with no significant difference found (box charts not weighted). Red line - median; black box - interquartile range; red crosses - outliers

Figure 3.5 presents studies conducted on artificial cochlea models that demonstrate various pressure parameters, namely, frequency of pressure peaks, mean pressure amplitudes, and mean pressure, which could be affected by robotic insertion. Similar to the IF measurements, the difference between manually inserted and robotically assisted insertion was not found to be significant ($p > 0.05$) for most of these parameters when compared across different studies except for the mean pressure ($p < 0.001$). This might partly be attributed to the fact that authors Dohr *et al.* used a linear artificial *scala tympani* model, which might have contributed to the higher observed pressures, and this study provide a large number of the data points.[252] Additionally, they focused on measuring maximum pressure during the insertion process, which might potentially differ from the mean pressure. A broader issue in pressure-measurement studies in the cochlea is the varying definitions of variables, contributing to inconsistencies across findings.

A single study by Todt *et al.* directly contrasted robotic and manual insertion techniques from the standpoint of sudden pressure changes.[224] They observed a significant difference for both the number of pressure peaks ($p = 0.011$, when all manual and robotic insertion data points were compared together, see Figure 3.5 (II)) and the mean amplitude ($p = 0.027$) size that arose during implant insertion into the artificial cochlea model. They noted that manual insertion introduced hand tremor, which increased the pressure peak frequency and amplitude. The tremor and sudden movements during insertion could be minimised by supporting the surgeon's hand and by using semi-automated or fully automatic insertion systems.[224] Nonetheless, implant volume is an important factor, as larger implants displace greater amounts of fluid within the cochlea, resulting in increased pressure.[225,235] This effect is particularly evident when comparing lateral wall and perimodiolar wall implants.[234]

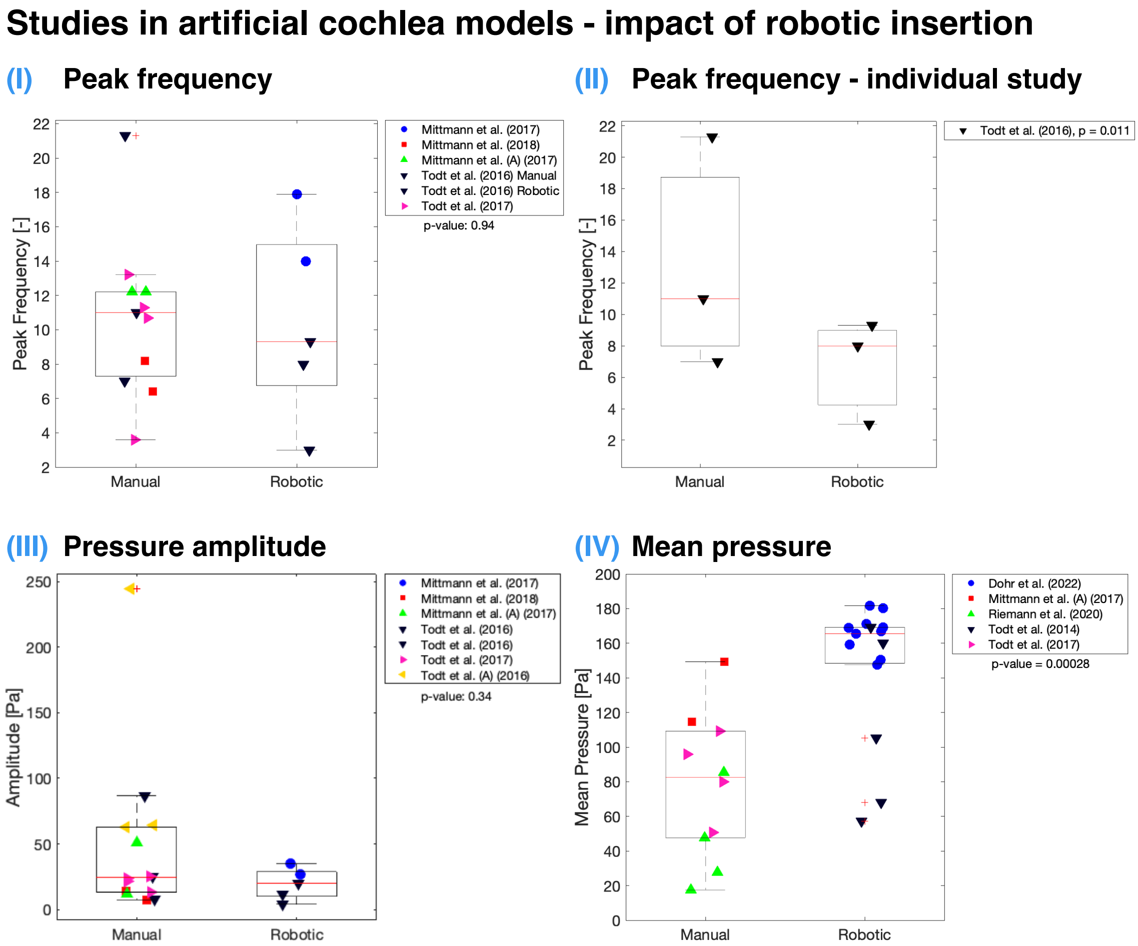

Figure 3.5 Impact of robotic insertion on pressure measurements in artificial cochlea models. Four diagrams compare manual and robotic insertion methods: (I) Peak frequency, (II) Peak frequency for a specific study, (III) Pressure amplitude, and (IV) Mean pressure. Unweighted two-sample t-tests were used for (I), (III), and (IV), with significant differences found in mean pressure measurements (box charts not weighted, $p < 0.001$). A weighted t-test was used for (II), highlighting a significant difference between manual and robotic insertion ($p = 0.011$). Red line - median; black box - interquartile range; red crosses - outliers

3.3.4 Analysis of trauma distribution by cochlear implantation approach and implant type

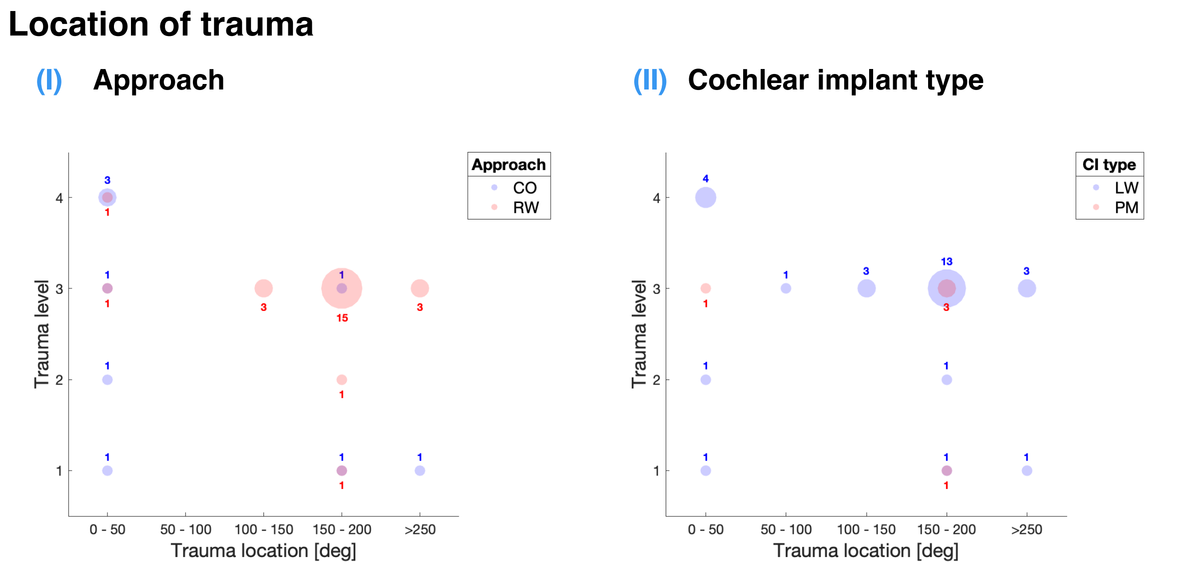

Figure 3.6 Distribution of trauma occurrences by angular insertion depth, surgical approach, and cochlear implant type in cochlear implantation studies: (I) Comparison of cochleostomy (CO) and round window (RW) approaches. (II) Evaluation of lateral wall (LW) and perimodiolar (PM) cochlear implants. Trauma locations are categorised by angular insertion depth in degrees: 0 – 50; 50 – 100; 100 – 150; 150 – 200; 200 – 250; above 250 degrees. Trauma levels follow the Eshraghi *et al.* scale.[216] Bubble size and accompanying number indicate the number of trauma occurrences.

Figure 3.6 offers an in-depth analysis of the data gathered from the selected studies, presenting a depiction of the association between the location and level of trauma in relation to different cochlear implant insertion approaches and implant types. The systematic review paid particular attention to two main insertion approaches: entry through the RW and CO. Table 3.3 shows that the majority of the analysed papers (5 out of 6) employed the RW approach for cochlear implant insertion, which suggests a preference for this method within the studies evaluated.

For the RW approach, the most commonly observed insertion trauma was at level 3 (see Figure 3.6 (I)), which corresponds to the rupture of the basilar membrane as defined by the Eshraghi *et al.* scale.[216] This trauma level can have significant implications for the patients, as it may result in reduced hearing performance and hinder the overall effectiveness of the cochlear implant. The preponderance of trauma instances for this approach were found at 150° to 200° of angular insertion depth, amounting to 15 occurrences. Furthermore, there were three instances each at 100° to 150° and more than 250° of angular insertion depth. The distribution of these instances may indicate potential areas for improvement in the RW approach to minimise the occurrence of insertion trauma.

In contrast, the CO approach exhibited a higher number of trauma instances at 0° to 50° of angular insertion depth. This finding is particularly intriguing, as these instances might be ascribed to the trauma stemming from the location and angle of the cochleostomy site, rather than being explicitly related to the electrode carrier. This observation raises questions about the surgical technique employed in the CO approach and its potential to inadvertently cause trauma.

Group of Adunka *et al.* emphasised that in four bone samples, grade 2 to 4 trauma was only discernible in the region of the cochleostomy.[217] This discovery suggests that the observed trauma is more likely a result of the surgical procedure itself, as opposed to being directly induced by the electrode array. Consequently, it raises concerns about the need for refining the CO approach to mitigate the risks associated with the surgical process.

The trauma location is in good accordance with the findings of Ishiyama *et al.*, that performed a histopathological study of human temporal bones from CI patients who exhibited intracochlear injury related to translocation (trauma level 4).[253] The authors found that nearly all cases of electrode translocation or migration occurred near the same angular insertion, which was at or near 180° of angular insertion depth, with the junction between the descending and ascending basal turn of the cochlea appearing to be the area susceptible to translocation from *scala tympani* to *scala vestibuli*. The authors suggest that the triggering of osteoneogenesis from the site of cochleostomy due to endosteal damage may play a role in the increased severity of intracochlear damage when translocation occurs in the setting of cochleostomy. They recommend using the round window approach with careful drilling of the operculum for the placement of CI to minimise intracochlear trauma.

Similarly to the Ishiyama *et al.* study, group of Fayad *et al.* also did histopathological study which investigated the CI insertion damage, the relationship between dendrite and spiral ganglion cell populations, and the structures stimulated by CI.[254] The study revealed that the primary site of trauma was the anterior part of the basal turn, where the electrode made contact with the outer wall of the cochlea before bending towards the modiolus. This led to disruption of the spiral ligament and stria vascularis, resorption of the organ of Corti, ossification from the damaged endosteum, fracture of the osseous spiral lamina, and degeneration of dendrites. The study also found that the structures stimulated by cochlear implants are primarily the spiral ganglion cells or axons, and not the dendrites. Furthermore, the research suggested that response to stimulation could occur with as little as 10 % of the normal population of ganglion cells, highlighting that fewer ganglion cells than previously thought might be necessary for successful stimulation.

Figure 3.6 (II) and Table 3.3 demonstrate that LW cochlear implants were predominantly used in the analysed studies. The highest occurrence of trauma for LW implants was observed at level 3, which corresponds to the rupture of the basilar membrane, a critical structure for hearing. This trauma was primarily found at approximately 150° to 200° of angular insertion depth. Additionally, a considerable level of trauma (level 4) was observed at 0° to 50° insertion depths, corresponding to the translocation of the CI from *scala tympani* to *scala vestibuli.* The study by Adunka *et al.* indicated that this trauma is likely attributable to the surgical procedure rather than the specific cochlear implant type.[217]

Regarding PM CI insertion, Figure 3.6 (II) indicates five occurrences of trauma, primarily at 150° to 200° insertion depths and level 3 insertion trauma. These findings were derived from a study conducted by Briggs *et al.*, which introduced a novel, thin perimodiolar prototype electrode array.[215] The study employed a multi-center collaborative approach with a large cohort of surgeons, emphasising that the cochlear implant's size and shape are crucial factors in minimising trauma during implantation. A thin and flexible electrode array was shown to reduce the risk of intracochlear trauma, highlighting the importance of considering size and shape in cochlear implant design to optimise patient outcomes and minimise surgical complications.

Table 3.3 Summary of trauma incidences related to cochlear implantation, detailing the trauma location (in degrees of angular insertion depth) and level (according to Eshraghi *et al.*),[216] the surgical approach and implant type used, and the cochlear implant brand, as reported in various literature studies. CO - cochleostomy; RW - round window; LW - lateral wall CI; PM - perimodiolar wall CI.

Author	Trauma location	Trauma level	Approach	CI Type	CI Brand
Adunka *et al.* 2004[217]	0 – 50	4	CO	LW	C40+ Flex MED-EL
	0 – 50	4	CO	LW	C40+ Flex MED-EL
	0 – 50	4	CO	LW	C40+ Flex MED-EL
	0 – 50	2	CO	LW	C40+ Flex MED-EL
	0 – 50	1	CO	LW	C40+ Flex MED-EL
	250	1	CO	LW	C40+ Flex MED-EL
Kaufmann *et al.* 2020[176]	0 – 50	4	RW	LW	Unknown
	150 – 200	1	RW	LW	Unknown
	150 – 200	3	RW	LW	Unknown
Briggs *et al.* 2011[215]	0 – 50	3	CO	PM	Custom
	150 – 200	1	CO	PM	Custom
	150 – 200	3	CO	PM	Custom
	150 – 200	3	RW	PM	Custom
	150 – 200	3	RW	PM	Custom
De Seta *et al.* 2017[96]	150 – 200	3	RW	LW	Flex 28 MED-EL
	150 – 200	3	RW	LW	Flex 28 MED-EL
	150 – 200	3	RW	LW	Flex 28 MED-EL
	150 – 200	3	RW	LW	Flex 28 MED-EL
	150 – 200	3	RW	LW	Flex 28 MED-EL
	150 – 200	2	RW	LW	Flex 28 MED-EL
Mirsalehi *et al.* 2017[245]	100 – 150	3	RW	LW	Slim Straight Cochlear
	150 – 200	3	RW	LW	Slim Straight Cochlear
	100 – 150	3	RW	LW	Slim Straight Cochlear
	100 – 150	3	RW	LW	Slim Straight Cochlear
Nguyen *et al.* 2012[227]	50 – 100	3	RW	LW	Digisonic SP
	150 – 200	3	RW	LW	Digisonic SP
	150 – 200	3	RW	LW	Digisonic SP
	150 – 200	3	RW	LW	Digisonic SP
	150 – 200	3	RW	LW	Custom
	150 – 200	3	RW	LW	Custom
	150 – 200	3	RW	LW	Custom
	<250	3	RW	LW	Custom
	<250	3	RW	LW	Custom
	<250	3	RW	LW	Custom

Limitations and future research

It is important to acknowledge the limitations of the selected studies for the trauma distribution, as none directly compared LW and PM cochlear implants within the same investigation. As a result, definitive conclusions regarding the superiority of one implant type over the other cannot be drawn based on the existing data. Nevertheless, the findings underscore the significance of implant design and surgical approach in reducing cochlear trauma and enhancing patient outcomes.

A few studies not included in this review investigated the synergistic impact of implant design and insertion approach. Wanna *et al.* conducted a comprehensive study examining 100 postlingually deafened adult patients with a total of 116 implants, comprising both

LW and PM designs.[255] The surgical approaches employed were CO, extended round window (ERW), and RW. The study found that LW electrodes had a higher rate of complete ST insertion compared to PM designs (89 % vs. 58 %). Both ERW and RW procedures resulted in higher rates of complete ST insertion compared to CO procedures. A statistically significant difference in consonant-nucleus-consonant word recognition was identified, with the group with electrode placement entirely within the ST exhibiting higher mean consonant-nucleus-consonant scores than the group with placement outside the ST (48.9 % vs. 36.1 %; $p < 0.045$). Interestingly, no statistically significant differences were observed among the three device manufacturers regarding the rate of complete ST-electrode insertion or audiometric performance when comparing LW electrodes.

Jwair *et al.* conducted a systematic review and meta-analysis to investigate scalar translocation in cochlear implantation and its relationship with speech perception scores and residual hearing.[92] The authors discovered a significantly lower scalar translocation rate for LW electrode arrays compared to PM electrode arrays, which is consistent with Wanna *et al.* group's findings.[255] Furthermore, similar to our results, the study found that translocations predominantly occurred at an angular insertion depth of approximately 180°, primarily with PM arrays. The researchers posited that the primary reason for the occurrence of translocations at this specific depth could be attributed to a steep decrease in the dimensions of the *scala tympani*, and the cochlear hook region, situated at the base of the cochlea, exhibits a complex and heterogeneous shape, which could increase the likelihood of trauma. Lastly, increased intracochlear friction might also play a role in the occurrence of translocations at this depth.

The potential influence of implant type on the level and location of trauma warrants further consideration. Future research endeavours could benefit from a more in-depth exploration of the effects of implant design and materials on insertion trauma, as well as an examination of the possible synergistic impact resulting from the combination of insertion approach and implant type. By investigating these factors, researchers may be able to identify crucial elements that contribute to reduced cochlear trauma and improved patient outcomes in cochlear implantation procedures.

3.4 Conclusion

This systematic review provides a comprehensive analysis of the factors affecting IFs and IP during cochlear implantation, with particular emphasis on insertion depth, cochlear implant design, and robotic assistance. Alongside these considerations, the review also offered key insights into the occurrence and distribution of cochlear trauma in relation to different cochlear implant insertion approaches and implant types.

While the collective analysis of the studies included in this review presented variability in the relationship between IFs and different metrics of insertion (both distance and angular depth) due to a myriad of variables across research groups, the study by Kaufmann et al.[176] distinctly demonstrated the correlation between IFs and angular insertion depth. Their data showed that with an increase in angular insertion depth, there was a corresponding increase in IFs. This insight underscores the importance of evaluating IFs specifically against angular insertion depth for a more nuanced and meaningful comparison within the literature.

In terms of cochlear trauma, the findings highlight that the RW approach is the preferred insertion method among the studies analysed, with the majority of trauma instances occurring at an angular insertion depth of 150° to 200°. In contrast, the CO approach showed a higher incidence of trauma at 0° to 50° of angular insertion depth. This raises questions about the surgical technique used in the CO approach and its potential to inadvertently cause trauma.

The majority of studies in this review focused on lateral wall cochlear implants, which exhibit a consistent IF profile. A parallel trend was found in the assessment of cochlear trauma, with LW implants being predominantly used in the analysed studies. The highest occurrence of trauma was found at level 3 on the Eshraghi *et al.* scale, corresponding to the rupture of the basilar membrane. Although the existing data does not allow for a definitive comparison between LW and PM cochlear implants, these findings underscore the significance of implant design and surgical approach in determining both IFs and trauma levels.

Perimodiolar implants were not included in the IF analysis due to their distinct insertion profile, and no study directly contrasted the IF profiles of perimodiolar and lateral wall cochlear implants. Additionally, no studies in the trauma review directly compared LW and PM cochlear implants within the same investigation. Future research should address these gaps by investigating the differences in IF and trauma profiles between these implant types, to inform clinicians about the most appropriate implant type for specific patient cases and potentially enhance patient outcomes.

Regarding robotic assistance, the analysis revealed no statistically significant difference in mean maximal IFs between manually and robotically inserted cochlear implants. However, robotic assistance may offer potential benefits, such as reduced hand tremor and more controlled insertion. The impact of robotic assistance on cochlear trauma remains an open question, and future studies should address this by focusing on its potential impact on patient outcomes and residual hearing preservation.

The reviewed studies exhibited considerable variability in methodology, implant type, and measurement techniques. Future research should aim to develop more standardised and accurate models that closely mimic the *in vivo* situation, and a standardisation of methods and reporting across studies would facilitate better comparisons. This holds true for both IF and cochlear trauma research, contributing to a more robust understanding of the factors influencing IFs, IP, and cochlear trauma during cochlear implantation.

In conclusion, this systematic review has emphasised the importance of insertion depth, cochlear implant design, and robotic assistance in determining IFs and IP during cochlear implantation, as well as in understanding the occurrence and distribution of cochlear trauma. Future research should focus on addressing the identified limitations and knowledge gaps to optimise cochlear implant surgery, improve patient outcomes, and preserve residual hearing. Through this endeavour, researchers and clinicians can collaborate to improve the overall effectiveness of cochlear implant procedures and enhance the quality of life for patients with hearing loss.

Chapter 4

Fabrication of Transparent and Accurate Cochlea Models

Disclosure

Part of Chapter 4 is in preparation for publication as:

Hrncirik, F., Figar, E., Roberts, I., & Bance, M. Transparent and Accurate Scala Tympani Models via SLA and DLP 3D Printing: A Comparative Study with Nominal-Actual Analysis *In prep.*

The research and writing of this chapter was conducted by the author unless otherwise stated. The manuscript contains contributions from Mr Figar (aid with nominal-actual analysis and micro-CT scanning) along with reviewing from all authors listed.

4.1 Introduction

The intricate structure of the human cochlea plays an essential role in the complex process of hearing, making it of great significance for scientific research and clinical applications. Efforts to address hearing impairment, which currently affects over 466 million people worldwide, has led to the development and widespread use of CIs. Despite the transformative impact of these devices, there remain substantial challenges in optimising their performance and minimising the risk of complications. One such challenge lies in the insertion process itself, as mechanical trauma and tissue damage caused during implantation can have detrimental consequences on residual acoustic hearing, which, if preserved, can significantly enhance electro-acoustic hearing capabilities. Consequently, it is imperative to investigate innovative approaches to deepen our understanding of the interaction between CIs and the cochlea, in order to optimise the design and implantation process of these devices.

Artificial cochlea models present a promising avenue for such investigations, providing a controlled and customisable platform for examining electrode-cochlear interactions, including the measurement of insertion forces. The development of accurate and transparent artificial cochlea models facilitates a more comprehensive and precise analysis of the underlying factors influencing CI performance, by allowing us to visualise the implant position relative to the cochlear walls. Moreover, these models hold potential applications beyond CI research, extending to the study of inner ear therapeutics and drug delivery systems, which can contribute to the development of new treatments for auditory disorders.

While in vivo experiments involving animal and cadaveric models have yielded valuable insights into the mechanics of hearing and CI functionality (see Chapter 2), artificial cochlea models offer several advantages, including increased experimental control, repeatability, and a broader scope for testing. In addition to transparency, artificial cochlea models allow integration of advanced sensors for measuring insertion forces and other parameters critical for optimising CI design and implantation techniques.

Harnessing the potential of innovative additive manufacturing, this chapter aims to elucidate methods for fabricating precise, transparent models that facilitate controlled experimentation. The valuable insights derived from these models have the capacity to transform cochlear implant design, refine implantation processes, and ultimately contribute to an improved quality of life for countless individuals affected by hearing impairments.

In the preliminary research, detailed in Appendix A, a comprehensive evaluation of several 3D printing technologies was conducted to develop and fabricate an artificial cochlea for implant insertion studies. This work utilised 3D CAD models derived from micro-CT scans of cadaveric temporal bones. Briefly, the investigation carefully evaluated five varied 3D printers, finding that the Cadworks3D (M-50, CADworks3D microfluidics) and Form 3 (Formlabs) devices, utilising DLP and SLA technologies respectively demonstrated superior surface smoothness and geometric accuracy. The Form 3 printer was subsequently utilised to fabricate three distinct artificial cochlea designs: the 'shell,' 'open-top,' and 'block' models. The 'shell' model, constructed with a 100 µm wall thickness, represented an optimal balance between print quality and wall size. The 'open-top' model offered excellent visualisation, notwithstanding certain limitations (*e.g.*, CI sliding out of the model during insertion), while the 'block' model efficiently addressed these constraints. The latter was executed in a range of sizes, further substantiating the printer's versatility. The model transparency was significantly enhanced through a post-processing procedure we developed, specifically the application of acrylic and pluronic coating. This improvement facilitated direct observation of implant positioning dynamics, although potential deviations introduced by the coating process were not assessed. Collectively, the study emphasises the promising role that SLA and DLP 3D printing technologies could play in the development of precise and transparent cochlea and *scala tympani* models.

SLA utilises a liquid resin which is deposited layer by layer and simultaneously polymerised by ultraviolet (UV) laser or other source of light.[256] The laser is a single beam source of light which is rastered across the printing layer using a system of mirrors and lenses.[257] The resin is made of photopolymers that react with the UV light – a typical resin for laser with a wavelength of 355 nm is a mixture of monomers that polymerised by the combination of free radical and cationic mechanisms. When a layer is cured, it adheres onto the building platform which moves to a defined position after polymerisation to allow photo-crosslinking of the following layer. SLA printers such as Formlabs uses a laser with 405 nm wavelength with resin that polymerised by free radical reaction. The superiority of a 405 nm laser relative to a 355 nm one lies in its obviation of the necessity for a cationic photoinitiator.[256] On the other hand, the resins that utilise 405 nm lasers provide sub-optimal mechanical properties and lower accuracy which restricts their application as functional materials.

DLP is essentially very similar printing technology to SLA. It utilises a liquid photosensitive resin which is cured by UV light. However, the printed layer is not treated

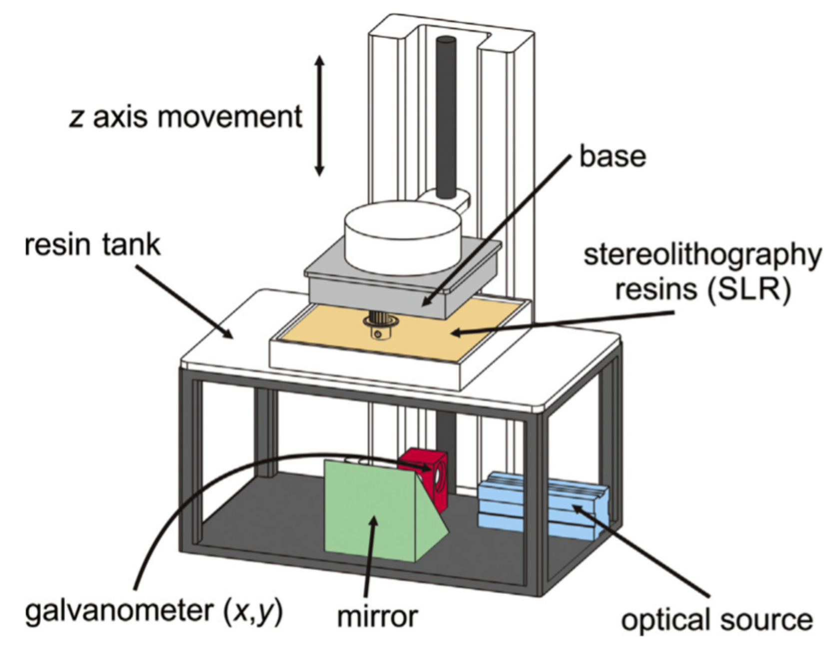

Figure 4.1 SLA printer with core components. The print is located at the bottom of the base (upside down) after the printing process is finished.[258]

by a single light beam that cures limited spot at a time, but the whole layer is exposed to UV light at once by projecting it onto a micromirror array or by using liquid crystal display (LCD). An entire 2D pattern of the object cross-section is projected for each layer, enabling faster printing comparing to SLA. The disadvantage of this technology is visible voxel artefacts that arise when the resolution of the projector or LCD screen is sub-optimal, as described in Figure 4.2). DLP printers frequently use a light source with 405 nm wavelength; nevertheless, some can be purchased with shorter wavelength, *e.g.* 365 or 385 nm wavelength.

The following section provides an in-depth exploration of SLA and DLP technologies, employing micro-CT scanning for precise nominal-actual analysis.

4.2 Materials and methods

4.2.1 Fabrication and optimisation of CAD model

High-resolution scans of cochlear structures, including the *scala tympani*, were obtained from a human cadaver sample using a Nikon XT 225 ST micro-CT operating at 160 kV and 180 µA with a voxel resolution of 27 µm (see Figure 4.3 (A)). The reconstruction of

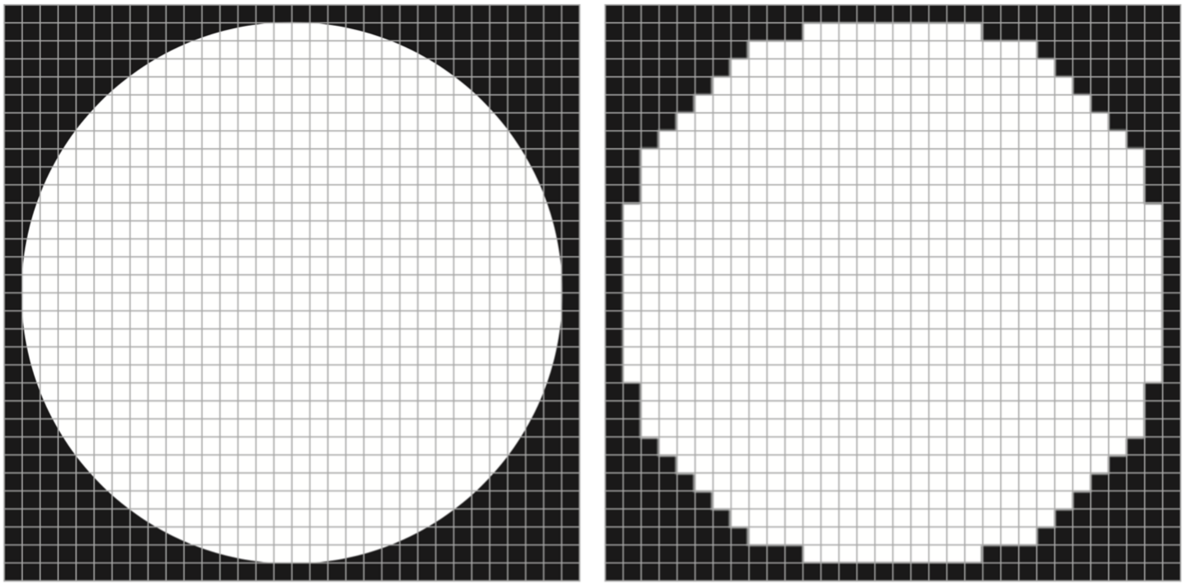

Figure 4.2 Demonstration of DLP technology limitation. Desired pattern (left) and rasterisation based on the resolution of the projector or screen.[259]

the cochlea was completed using Stradview software (version 7.0, accessed on 10 March 2022), which was integrated into a semi-automated workflow, enabling swift segmentation via template otic capsule (statistical shape model from 18 human temporal bones)[87] fitting.

Cochlea models were derived from the reconstructed cochlea scan through a process of solid embedding and subtraction within a volumetric matrix (boolean operations), implemented via Fusion 360 software (Autodesk, USA). The entry point of the cochlea, located at the basal section, was aligned with the matrix perimeter to establish a viable opening. The opening was approximately at the location of the round window, which is frequently used as an entry point for CI insertion. In addition, the models had a narrow 1 mm in diameter opening at the apex (end of the cavity) to flush out resin residues after printing.

4.2.2 3D printers and materials

DLP technology was represented by the CADworks3D printer (M-50, CADworks3D microfluidics, Toronto, ON, Canada), which was set to a resolution of 30 µm across all axes, with an exploration of 5 µm resolution on the z-axis (see Figure 4.3 (B)). This was facilitated by configuring parameters for the stepper motor, which controlled the build plate movement, along with the fixed x and y-axis resolution. The latter resolution

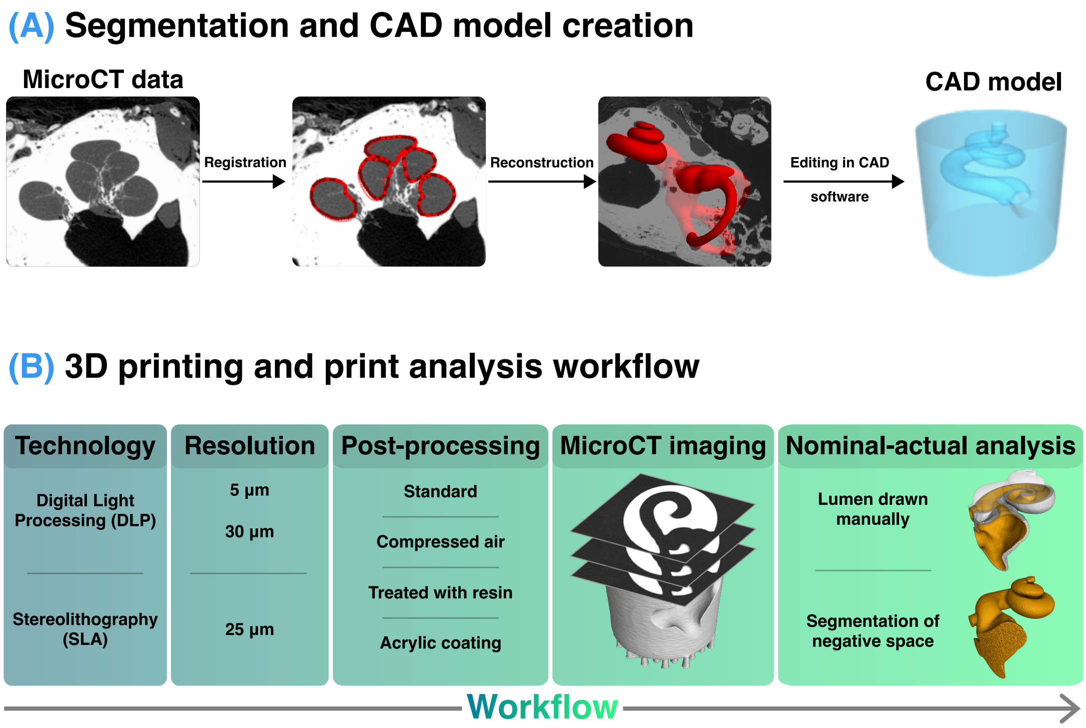

Figure 4.3 Complete workflows for creating and analysing fabricated models. (A) A schematic illustrating the methodology for generating 3D printable files from micro-CT scans of cadaveric specimen. (B) Workflow diagram detailing the process of 3D printing, post-processing, and print analysis.

was dictated by the projector resolution, as each projected pixel was set by its x and y size. The selected printing material was Clear Microfluidics Resin (V7.0a, CADworks3D microfluidics, Toronto, ON, Canada).

On the other hand, SLA technology, as demonstrated by the Formlabs Form 3B (Formlabs, MA, USA), operated with preset settings of 25 µm across all x, y, and z axes. In this instance, the resolutions were determined by the galvanic components (galvanometers and galvo mirrors), main mirror, and the size of the laser spot (85 µm).[260] Clear V4 resin (Formlabs, MA, USA) was used for the model fabrication.

In both DLP and SLA instances, the models were printed directly on the build platform.

4.2.3 Optimisation of print transparency and post-processing methods

Post-printing, the models were treated with 99.9 % isopropyl alcohol (SLS Ltd., Nottingham, UK), followed by curing three times for 10 s with a one-minute break between each run using a CureZone UV chamber (CADworks3D microfluidics, Toronto, ON, Canada) for the DLP printed samples. SLA samples were cured in Form Cure (Formlabs, MA, USA) for 15 min at 60 °C.

To maximise transparency, various coating methods were examined. Prints referred to as 'standard' in the Results and discussion section were not subjected to any further treatment beyond the processes outlined in the preceding paragraph.

Prints labelled as post-processed with 'compressed air' exclusively underwent a variation of standard post-processing. Instead of the IPA wash used in standard post-processing, surplus resin was removed solely by deploying compressed air.

The third option was to treat prints with a resin coating following a distinct process. Initially, these prints underwent standard post-processing, including IPA washing, after which the excess resin was eliminated using compressed air. Subsequently, the same resin used for model fabrication was sampled and infused into the lumen of the print with a syringe. This was succeeded by another application of compressed air to expel excess resin, leaving a thin resin coating within the print's lumen. The treated models were then cured using the CureZone UV chamber for DLP prints, and the Form Cure chamber for SLA prints.

The fourth tested option was to treat prints with an acrylic coating. Firstly, standard post-processing was applied, including IPA washing and full curing in the relevant chambers. Thereafter, an acrylic coating (Pro-cote Clear Lacquer, Aerosol Solution) was used to coat the lumen of the models. This coating was injected into the lumen of the model, allowed to rest for 10 s, and then surplus coating was removed using compressed air to leave a thin, smooth layer and achieve a clear finish.

4.2.4 Water resistance

Both the DLP-printed samples treated with resin and acrylic coatings underwent testing to evaluate their resistance to damage caused by water exposure. The resin coated samples underwent curing three times for 10 s, 20 s, and 40 s with a one-minute intermission between each run. In contrast, samples treated with the acrylic coating were cured three times for 10 s with a one-minute break between each run prior to the coating. Subsequently, distilled water was injected into the samples' cavity and the samples were submerged in beakers filled with distilled water. These beakers were then placed in an ultrasonic bath (VWR, Ultrasonic Cleaner USC-T) for a period of 480 s. After this, the water was replaced, and the samples underwent a second ultrasonic bath for another 480 s.

4.2.5 Examination of prints' surface quality

All measurements were performed using a CT machine GE Phoenix (type v|tome|x L240) operating at an ambient temperature of 21 °C, with the sole exception being the preliminary evaluation of diverse post-processing methods, wherein a Nikon XT 225 ST micro-CT with a voxel resolution of 28 µm was deployed. Initial samples with resin coating were scanned as groups of six, where CT data were obtained with 16 µm voxel resolution. In order to improve the resolution, the samples with acrylic coating were scanned as groups of two, providing a higher resolution of 10 µm per voxel. Obtained data were reconstructed per group using software for reconstruction Datos (version 2.6.1.18128) where no additional filtration was applied. Reconstructed groups were split into data sets containing individual samples.

To further scrutinise the surface quality of the printed models, a desktop Scanning Electron Microscope (SEM, Hitachi TM3030Plus) was utilised. Preceding the SEM analysis, the samples were subject to a coating of gold particles using a metal sputter coater (Quorum Emitech K550). This preparation step ensured optimal conditions for SEM analysis, facilitating the detailed examination of the surface quality of the 3D-printed objects.

4.2.6 Nominal-actual analysis and deviation compensation

Each data set with individual samples was processed in software VGStudio Max (version 3.5, Volume Graphics, Hegagon). The surface of the samples was first determined by 'isosurface' method applying a global gray value threshold, calculated as 50 % of the mean material and mean air value.

This contour was subsequently used as the initial contour for an advanced algorithm within the 'Advanced Surface Determination' function of VGStudio. This algorithm detects local gray value differences to determine the surface more accurately (refer to Figure 4.4 (A) and (B)).

The surface obtained by the advanced surface determination method is subvoxel-accurate, meaning it precisely captures details smaller than a voxel (see Figure 4.4 (C)).

The surface obtained from each sample was aligned onto a nominal object of the cochlea using the 'best-fit' algorithm in order to perform the nominal-actual analysis and evaluate the deviations between the print and the nominal object. This analysis provides both a graphical representation of deviations that are colour-coded based on their deviation values and statistical data.

Furthermore, the compensation mesh function was performed on the entire sample. By utilising the analysed deviations and mirroring them, a new mesh was generated. This newly generated mesh was then used during the subsequent printing, employing identical parameters for optimal comparison.

4.2.7 Statistical analysis

The statistical significance of deviation across 90 % of the surface area was evaluated using MATLAB (Mathworks). This analysis incorporated one-way and two-way Analysis of Variance (ANOVA) functions and a post-hoc Tukey-Kramer test for multiple comparisons between group means. A p-value of less than 0.05 was deemed statistically significant, indicating a non-random difference between the groups under investigation.

4.3 Results and discussion

4.3.1 Segmentation techniques and nominal-actual analysis

Figure 4.5 (A) displays the two distinct segmentation techniques implemented for the nominal-actual analysis. The nominal-actual analysis did not discern any differences

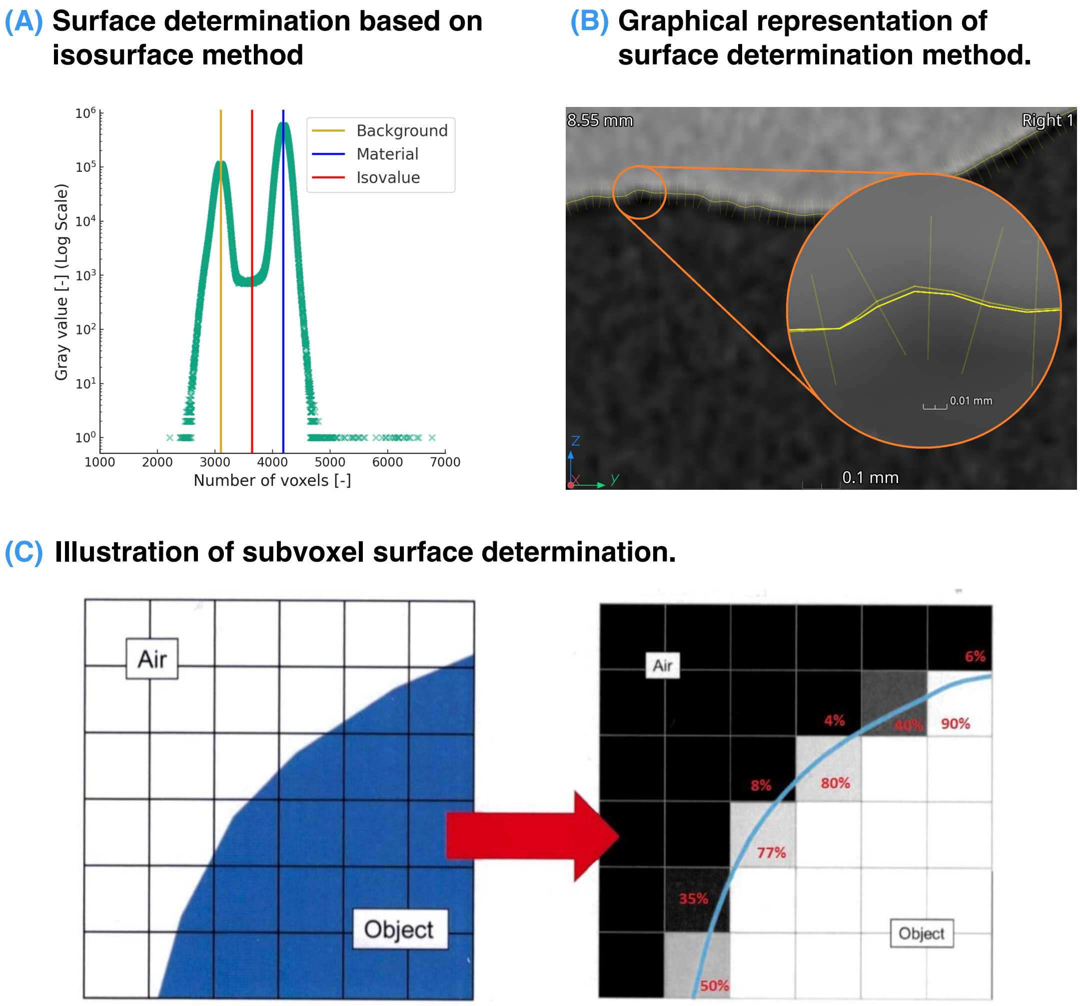

Figure 4.4 Depiction of the grey value analysis and surface determination process: (A) Logarithmic scatter plot illustrating the distribution of grey values versus voxel count, with notable data demarcations highlighted: the dominant background intensity peak (dark yellow), the calculated isovalue midpoint (red), and the peak of material intensity (blue). (B) Visualisation of surface refinement utilising an advanced method and an initial contour. (C) Demonstration of subvoxel surface determination, showcasing the ability to accurately capture details finer than a voxel's resolution.

between these segmentation methods. However, the approach of manually drawing the lumen was found to be less suitable for investigating internal lumen deviations since a plane cut was necessary to visualise the heat spots indicating deviation from the original CAD model. Conversely, the segmentation of the negative space within the printed model rendered the heat map directly onto the model's surface, thereby simplifying the observation of surface deviations from the original CAD model. Nevertheless, interpreting the results of the negative space segmentation method proved slightly more challenging as it represented the inverse of the printed model. Figure 4.6 (A) provides an example of a nominal-actual analysis performed using negative space segmentation, complete with a heat-map scale bar on the left. In this analysis, a positive deviation (leaning towards the red end of the spectrum) indicates a larger quantity of negative space than that in the original CAD model, while a negative deviation (tending towards the blue end) suggests the opposite. An examination of a printed model revealed a slight excess of material in the initial cochlear turn at the upper part of the lumen (see Figure 4.6 (A), middle), marked by light blue spots, which corresponded to a reduction in negative space and hence a negative deviation. Due to its superior capability of visualising surface deviation, negative space segmentation technique was utilised for all samples analysed in this study.

Figure 4.5 (B) presents two techniques employed in the nominal-actual analysis: the 'complete' and the 'cut' options. The 'complete' analysis encompasses the entire inner space of the printed model, including the entrance, whereas the 'cut' technique focuses only on a selected portion. In this study, it was found that the entrance component introduced significant deviations, which skewed the analysis results. As the primary focus of this research was on the accuracy of printing the *scala tympani* lumen, the 'cut' technique was deemed more suitable and was consequently preferred. This method facilitated a more accurate representation of the lumen printing accuracy, free from the confounding influence of entrance deviations.

As shown in Figure 4.6 (B), a histogram was used to quantify the heat-map of deviation. In an ideal circumstance – where there is a 100 % match between the original CAD and evaluated print – the peak would be centred at 0 deviations with minimal width. The position of the peak provides an indication of whether there is an excess (negative numbers) or deficit (positive numbers) of material inside the lumen. All prints in this study showed peaks shifted towards the negative spectrum, suggesting that the printed lumens are slightly smaller due to the presence of more material inside. Figure 4.6 (C) underlines this observation by computing the absolute cumulative deviation across 90 % of the surface, a metric employed for comparison among different samples.

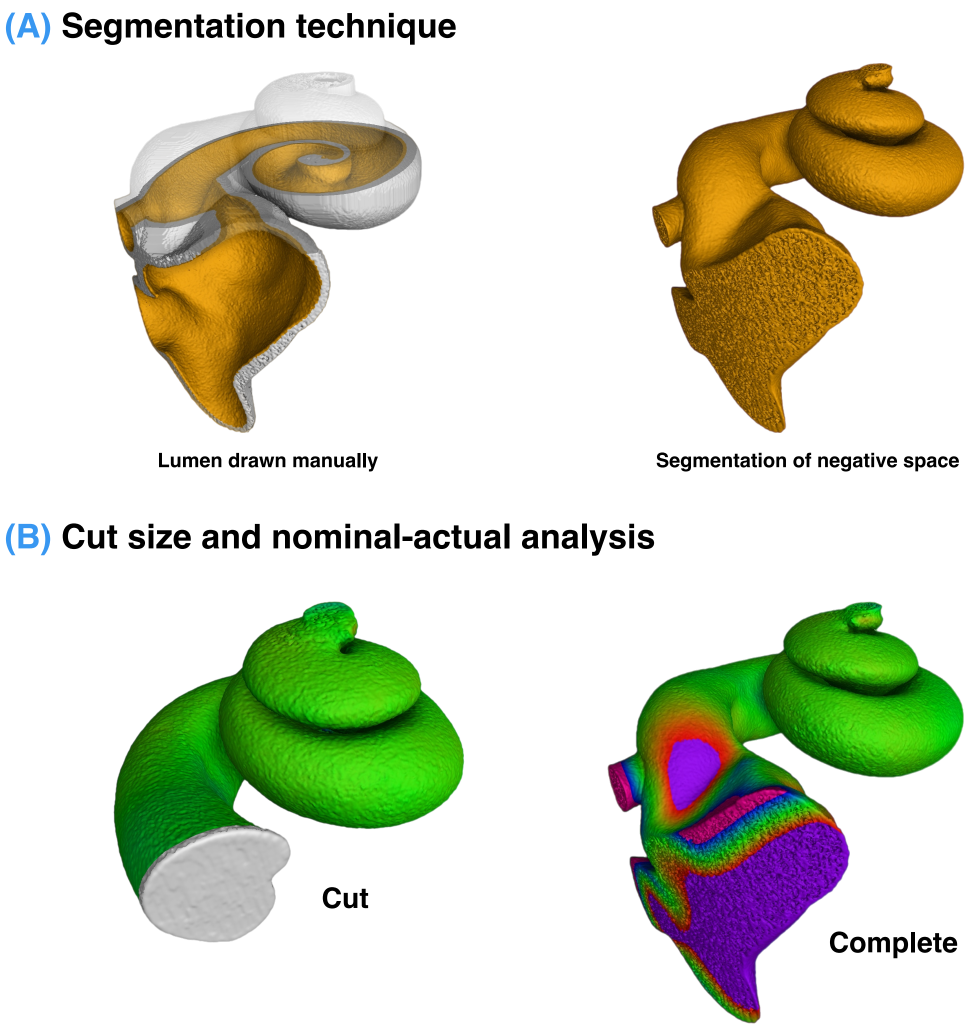

Figure 4.5 Methods of nominal-actual analysis with segmentation techniques and analysis options. (A) Comparative display of two segmentation techniques for nominal-actual analysis: manually drawing the lumen and negative space segmentation within the printed model. (B) Illustration of 'complete' and 'cut' options used in nominal-actual analysis, highlighting the preference for 'cut' technique to avoid entrance-induced deviations.

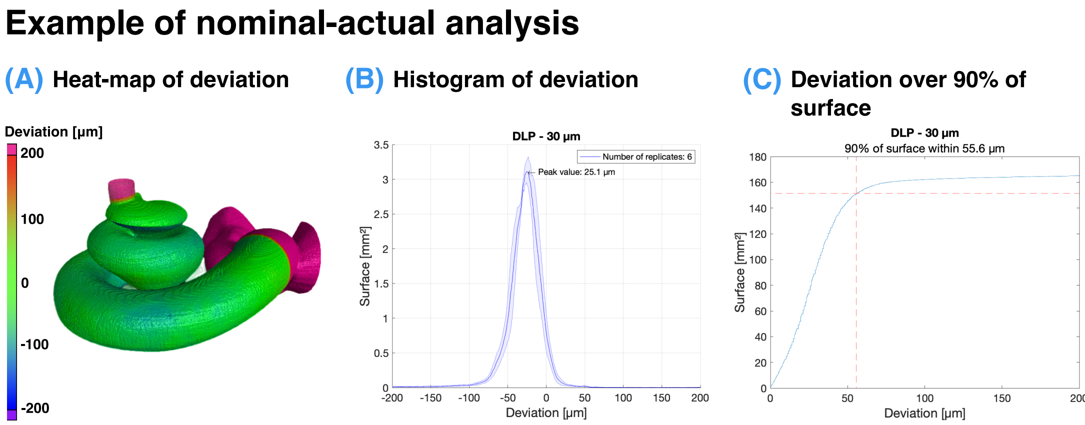

Figure 4.6 Analysis of printed models' deviation from the original CAD model using negative space segmentation, deviation quantification, and comparative cumulative deviation calculation. (A) Nominal-actual analysis of a printed model using negative space segmentation. Heat-map scale bar illustrates the deviation from the original CAD model with positive values (red) indicating larger negative space and negative values (blue) indicating a reduction. (B) Histogram quantifying the heat-map of deviation, with the peak position indicative of material excess or deficit inside the lumen. (C) Computed absolute cumulative deviation across 90 % of the surface area, utilised as a comparative metric among different samples.

4.3.2 Surface analysis of standardly post-processed 3D printed models

Figure 4.7 presents models which were subjected to plane-cut during the CAD preparation phase (refer to Figure 4.7 (A)). This allowed for the inner section of the cavity to be coated with a 10 μm layer of gold for the visualisation under SEM. These models underwent 'standard' post-processing. It is evident that the DLP method with a layer height of 30 μm yielded a stepped finish corresponding to the layer-by-layer process, a characteristic commonly associated with DLP technology (see Figure 4.7 (B)). The measured layer height for these models was found to be 28.28 ± 1.695 μm ($n = 15$).

In contrast, when the same printer was utilised with a layer height of 5 μm, a smooth lumen surface was achieved without any discernible steps, with the measured layer height being 4.15 ± 0.340 μm ($n = 15$).

In terms of overall surface quality, SLA technology notably outperformed DLP with 30 μm layer height and was on par with 5 μm setting, producing a consistently smooth surface finish devoid of visible steps and a smooth lumen (with a measured layer height of 24.19 ± 1.812 μm, $n = 15$). The enhanced smoothness observed in SLA can be associated

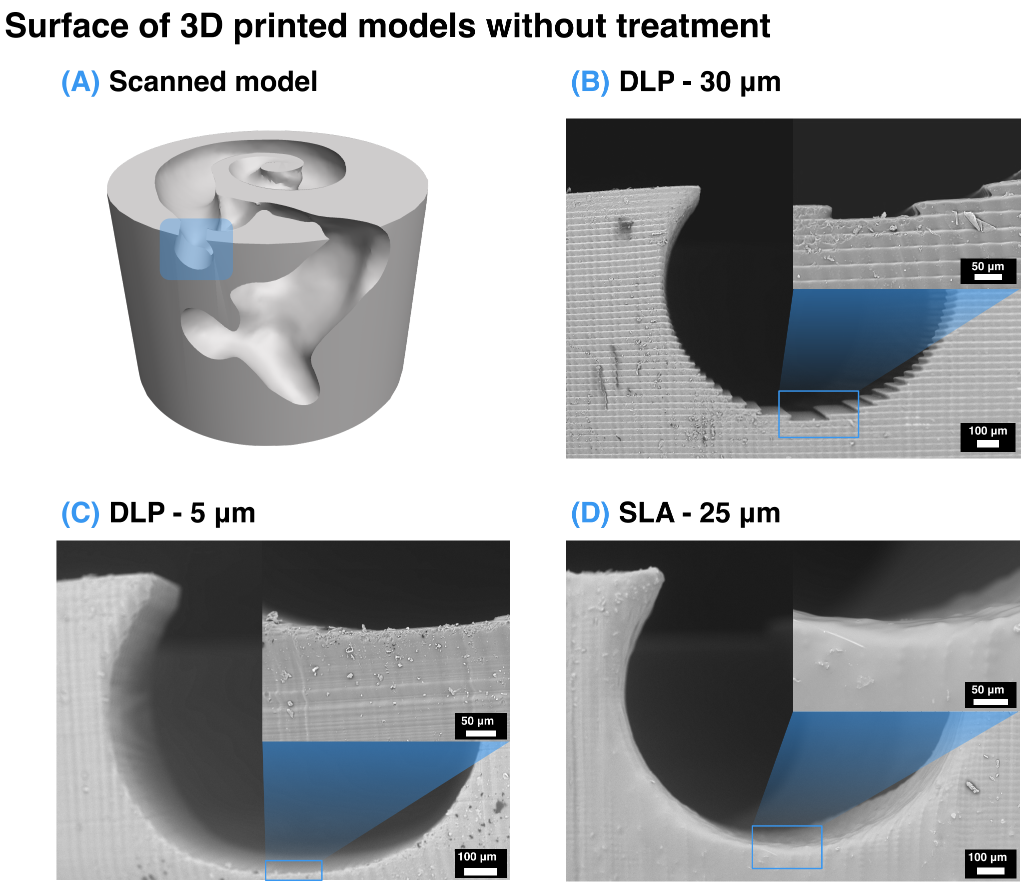

Figure 4.7 Scanning electron microscopy of samples printed with DLP and SLA printers. (A) Preparation of models via plane-cutting for SEM analysis of lumen surface quality. (B and C) Demonstrates the stepped finish associated with DLP printing at a layer height of 30 µm, contrasted by the smooth finish obtained at 5 µm layer height. (D) Illustration of good surface quality achieved with SLA printing, characterised by the absence of detectable steps and smooth lumen, attributed to the laser-curing process of the resin.

with the unified nature of all layers in the x, y, and z directions, attributable to the laser-curing process of the resin, which employs a spot size of approximately 85 µm.[260]

4.3.3 Post-processing impact on print accuracy

A comprehensive evaluation of various post-processing techniques was conducted with the aim of maintaining high print transparency without compromising their accuracy, applicable to both DLP and SLA (refer to Figure 4.8). Among the methods tested, post-processing utilising only compressed air resulted in the highest deviation for both printers. Although prints treated with resin coating exhibited higher deviation than those without coating (designated as 'standard'), the uncoated models offered only semi-transparency, which was deemed insufficient as the aim was to produce anatomically accurate and optically transparent models. Therefore, post-processing treatments involving resin were selected for subsequent analysis.

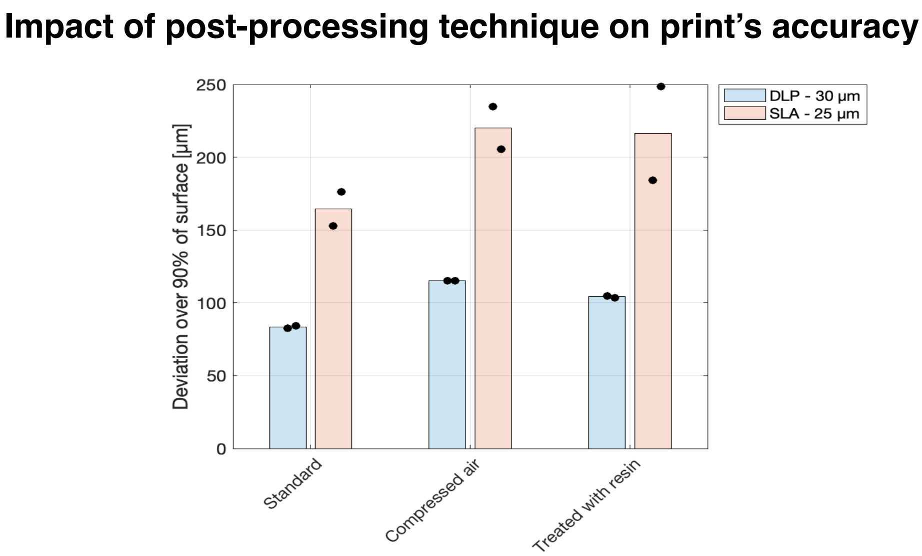

Figure 4.8 Comparative assessment of post-processing methodologies' impact on the accuracy of DLP and SLA printed cochlea models. The techniques studied include 'standard' (usage of isopropyl alcohol (IPA) and compressed air without additional coating), 'compressed air' (exclusive use of compressed air without isopropyl alcohol), and 'treated with resin' (similar to 'standard' processing, but with a final resin coating applied within the print lumen). Notably, DLP demonstrated superior model accuracy compared to SLA. The 'standard' post-processing approach exhibited the smallest deviations. The bar chart displays the mean values derived from individual data points. Lumen size: full cochlea; Micro-CT voxel size: 28 µm.

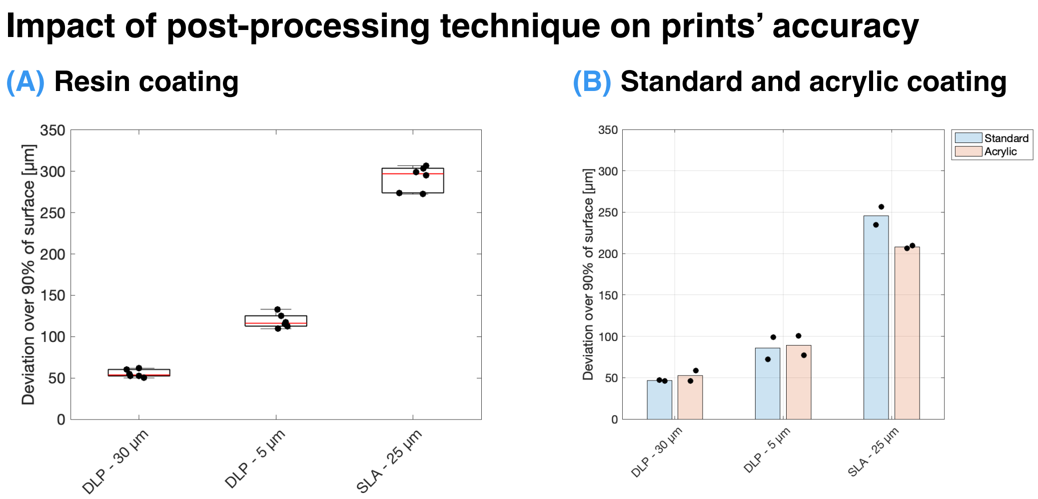

Figure 4.9 Analysis of the influence of resin and acrylic coatings on DLP and SLA 3D printed models' accuracy. (A) Comparative analysis of the impact of resin coating on prints fabricated with DLP at layer heights of 30 and 5 µm, and with SLA, demonstrating significant deviation in resin-treated SLA prints compared to DLP samples. Boxplot: red line - median, box - interquartile range ($n = 6$ replicates). Lumen size: full cochlea; Micro-CT voxel size: 16 µm. (B) Evaluation of acrylic coating as an alternative to resin, with full transparency achieved and minimal impact on the accuracy of DLP printed samples irrespective of layer height. Bar chart represents mean of the individual datapoints. Lumen size: full cochlea; Micro-CT voxel size: 10 µm.

Figure 4.9 (A) delineates the impact of resin coating on prints fabricated with DLP at layer heights of 30 and 5 µm, as well as with the SLA technology. Notably, SLA prints treated with resin coating displayed a significantly higher deviation than DLP printed samples ($p < 0.001$, $n = 6$). Intriguingly, DLP prints with 30 µm layer height manifested significantly lower deviation compared to those with 5 µm layer height ($p < 0.001$, $n = 6$). Despite seeming contradictory at first, it should be noted that the resin used was optimised by the manufacturer for printing at a 30 µm resolution in all directions.

As a potential alternative to resin coating, acrylic coating was examined, considering the semi-transparent finish of prints without coating. With the application of acrylic coating, the resultant models exhibited full transparency. Figure 4.9 (B) showcases the impact of acrylic coating in comparison to untreated samples. Once again, SLA prints displayed the highest deviation, with DLP prints with 30 µm layer height showing the smallest deviation among the acrylic-treated and untreated samples. Importantly, the acrylic coating appeared to have no significant influence on the accuracy of samples printed with DLP regardless of layer height, with results remaining comparable to untreated samples.

4.3.4 Water exposure impact on print transparency

To optimise print transparency entailed exploring various coatings and assessing their resilience in a wet environment, mimicking the *in vivo* condition where the cochlear lumen is filled with perilymph. This was important as the potential dissolution of the coating could reduce print transparency. Figure 4.10 documents an experiment wherein samples printed with DLP and coated with resin and acrylic were subjected to an ultrasonic water bath. Resin-coated samples underwent three different durations of curing, as prolonged UV exposure enhances the curing process of the applied resin. Conversely, samples treated with acrylic coating were post-processed, fully cured, and then coated with acrylic, eliminating the need for extended UV exposure testing. A cochlear implant was inserted in the models under scrutiny to monitor transparency changes correlating with prolonged water exposure.

This qualitative investigation revealed that a longer UV exposure contributed to superior resin curing within the lumen. However, despite quadrupling the curing duration, the resin eventually began to dissolve, rendering the prints 'cloudy' and less transparent than at the experiment's inception. In contrast, acrylic coating demonstrated good water resistance, maintaining initial transparency even after 960 s of exposure. Given the observed failure of resin coating under wet conditions, acrylic coating was chosen for subsequent analysis.

4.3.5 Effects of acrylic coating and DLP z-axis printing resolution on print accuracy

Building on insights from the water exposure experiment, in which the acrylic coating maintained transparency without dissolving in water, further exploration was conducted into the potential trade-off between transparency and precision. This specifically involved investigating whether extended exposure of the print lumen to the acrylic coating could compromise its accuracy. Figure 4.11 illustrates the results from assessing the same print subjected to varying durations of acrylic coating exposure, specifically 10 , 30 , 60 , and 120 s. The prints were fabricated in two batches, with each batch comprising six prints.

Interestingly, prints exposed for 120 s exhibited the highest mean deviation over 90 % of the surface. This was captured in the bar chart, which hinted at a subtle trend towards decreased accuracy with increased duration of acrylic coating exposure. However, given the limited sample size, this observation remains a speculative trend rather than a statistically substantiated conclusion. The deviation between prints exposed to acrylic for 10 and 60 s was minimal, underscoring the negligible impact of acrylic coating duration on print accuracy within this exposure range.

In summary, while acrylic coating did marginally compromise the precision of the printed models, this effect was relatively minor. It is also crucial to note that the observed deviation might equally be attributable to the error inherently associated with the micro-CT scanning process (see Figure 4.13). Therefore, the benefits of enhanced transparency offered by the acrylic coating, coupled with its minimal impact on print accuracy, underscore its viability for the intended application.

Figure 4.12 presents a comprehensive experiment delineating the effects of acrylic coating and printing resolution on the accuracy of samples produced through DLP technology. A total of 24 prints were fabricated and analysed. A one-way ANOVA indicated significant disparities among the groups assessed, and a post-hoc Tukey-Kramer test revealed no significant difference between samples printed at a 30 µm layer height, whether treated with acrylic or untreated ($p = 0.373$). However, a significant difference was observed for samples printed at 5 µm layer height ($p = 0.014$). Moreover, a two-way ANOVA examining the influence of printing resolution and the post-processing technique

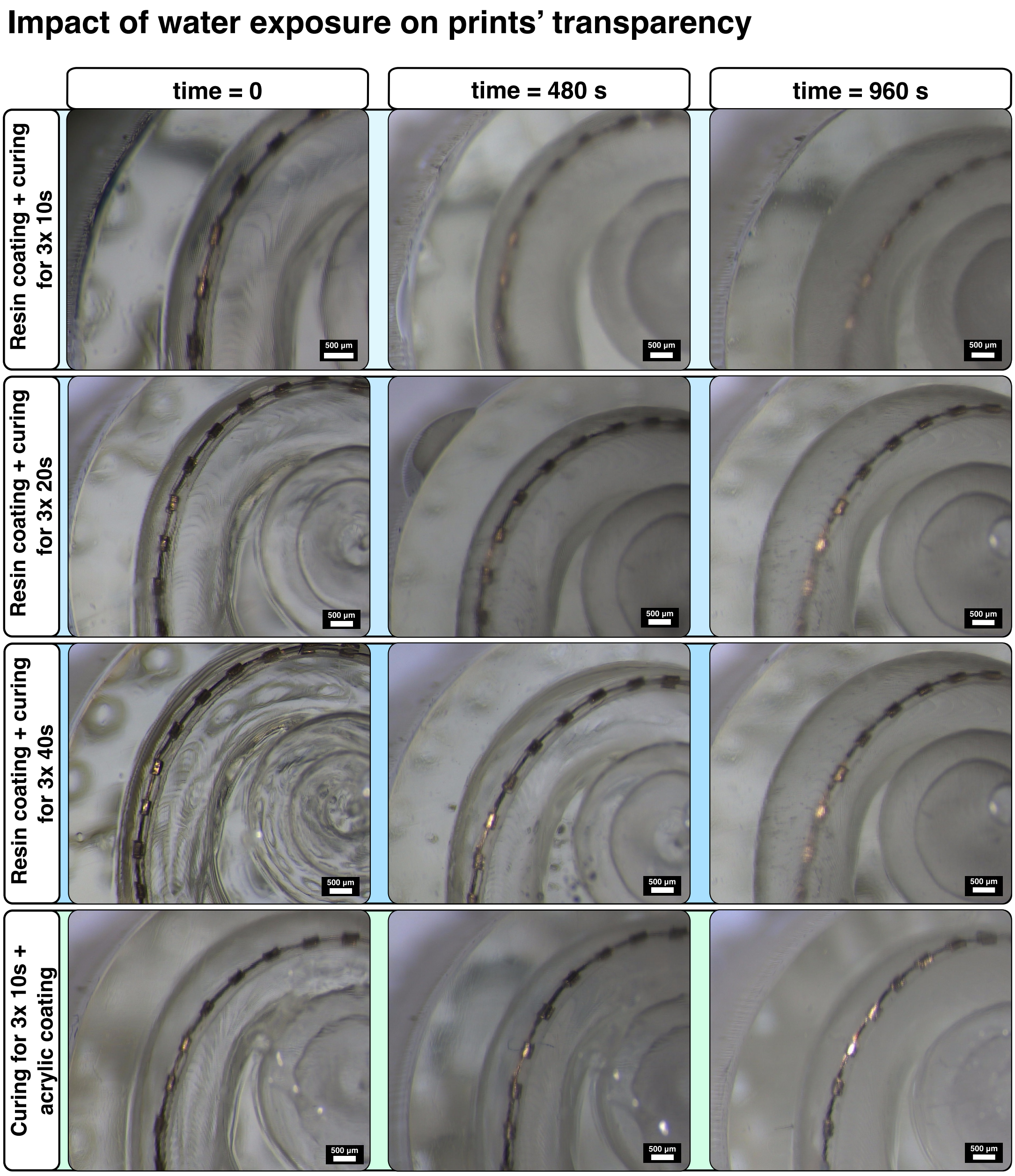

Figure 4.10 Assessment of resin and acrylic coated DLP printed samples subjected to ultrasonic water bath. The impact of different curing durations on resin-coated samples and the effect of water exposure on transparency were studied. While resin-coated samples demonstrated increased curing with prolonged UV exposure, eventual dissolution resulted in decreased transparency. Acrylic-coated samples, on the other hand, maintained initial transparency throughout the experiment.

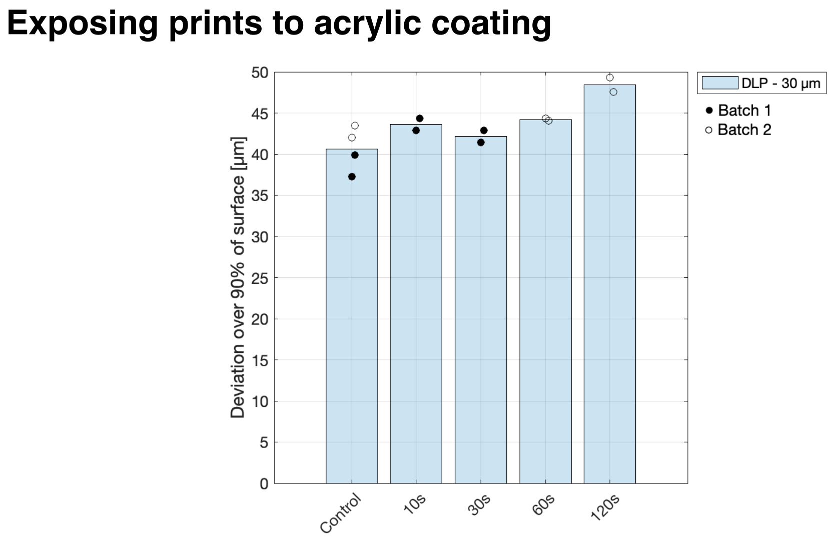

Figure 4.11 Effect of acrylic coating duration on DLP-printed model accuracy. The figure compares prints exposed to acrylic coating for 10 , 30 , 60 , and 120 s. Highest mean deviation was observed in 120 s exposure. Minimal difference was noted between 10 s to 60 s exposures, highlighting the minor impact of coating duration on print precision within this range. Despite the marginal precision compromise, the enhanced transparency justifies acrylic coating use. The bar chart displays the mean values derived from individual data points. Lumen size: *scala tympani*; Micro-CT voxel size: 10 µm.

revealed that the post-processing method's effect on the 'mean deviation over 90 % of surface' is not statistically significant ($p = 0.053$).

Table 4.1 Summary of statistical analysis for combined batches, comparing different printing layer height (30 vs 5 µm) and post-processing techniques (standard vs acrylic). Note: p-values indicate statistically significant interactions between printing layer height and post-processing. $Mean_{90\%}$ - mean deviation over 90 % of surface; SD - standard deviation

Layer height (µm)	Post-processing	$Mean_{90\%}$	SD	$p_{\text{layer height}}$	$p_{\text{post-processing}}$	$p_{\text{interaction}}$
30	standard	33.4	2.0	< 0.001	0.053	0.007
	acrylic	31.8	3.2			
5	standard	60.5	1.2			
	acrylic	67.3	0.8			

Table 4.1 summarises the statistical analysis for combined batches one and two. With respect to printing resolution, the trend observed is an increase in the 'mean deviation over 90 % of surface' as the printing layer height decreases (from 30 to 5 µm). For both post-processing techniques, measurements with a layer height of 5 µm are significantly larger than those with 30 µm ($p < 0.001$). This pattern, consistently observed throughout the

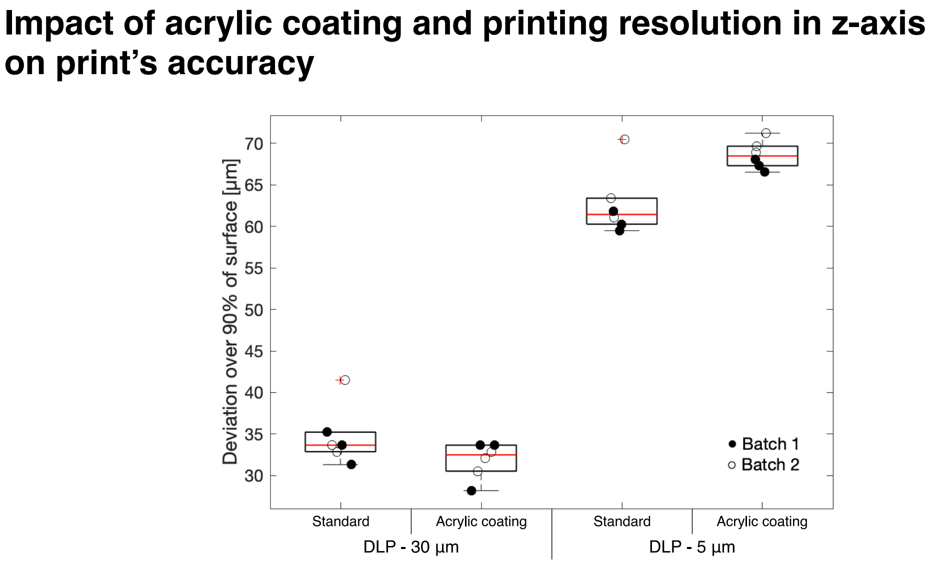

Figure 4.12 Comprehensive experiment illustrating the impacts of acrylic coating and printing resolution on DLP printed sample accuracy. One-way ANOVA demonstrates significant differences among groups, with post-hoc Tukey-Kramer tests showing no significant variance between 30 µm layer height prints with or without acrylic treatment ($p = 0.373$), but significant disparities for 5 µm layer height samples ($p = 0.014$). Two-way ANOVA underlines that the post-processing technique's effect on the 'mean deviation over 90 % of surface' is not statistically significant ($p = 0.053$). Boxplot: red line - median, box - interquartile range ($n = 6$ replicates). Lumen size: *scala tympani*; Micro-CT voxel size: 10 µm.

study, could be attributable to the DLP printer's resin (Clear Microfluidics), optimised for printing at 30 µm. The resin's viscosity may not be sufficiently low to support successful printing at 5 µm layer height. The low-viscosity resin's rapid flow in and out of print cavities prevents inappropriate curing sites. Although the printer can technically fabricate with a layer height of 5 µm, the material requires further optimisation. Regarding post-processing, for a given printing resolution, there appears to be a slight difference in mean deviation between the two post-processing techniques. For a printing resolution of 30 µm, the 'acrylic' post-processing displays a marginally lower mean deviation compared to the 'standard' technique. However, for a printing resolution of 5 µm, 'acrylic' post-processing shows a higher mean deviation than the 'standard' method. Despite this, as previously discussed, the post-processing does not have a statistically significant impact on the 'mean deviation over 90 % of surface' ($p = 0.053$). Table 4.1 also underscores a statistically significant interaction between the used resolution and post-processing, at approximately $p = 0.007$. This suggests that the effect of printing resolution on the outcome variable depends on the level of post-processing, and vice versa.

It is important to also acknowledge that the process of micro-CT scanning introduces an absolute measurement error of approximately 10 µm. This can be attributed to the absence of calibration between each measurement, primarily due to cost and time efficiency considerations (as illustrated in Figure 4.13 (A)). The relative measurement error of the scanning process, which amounted to roughly 2.8 µm, was determined by thrice measuring the same sample and juxtaposing the results with the initial measurement (see Figure 4.13 (B)).

Table 4.2 Repeatability analysis of the 3D printing process across varied layer heights, post-processing conditions, and batches. Mean deviations within the 10 µm threshold suggest influences from the micro-CT scanning process rather than the printing process. $Mean_{90\%}$ - mean deviation over 90 % of surface; SD - standard deviation; CV - coefficient of variation.

Layer height (µm)	Post-processing	Batch	$Mean_{90\%}$	SD	CV (%)
30	standard	1	33.4	1.97	5.9
		2	36.0	4.76	13.2
	acrylic	1	31.8	3.16	9.9
		2	31.8	1.20	3.8
5	standard	1	60.5	1.20	2.0
		2	65.0	4.89	7.5
	acrylic	1	67.3	0.78	1.2
		2	69.9	1.20	1.7

The repeatability analysis of the 3D printing process, as summarised in Table 4.2, takes into account factors such as layer height, post-processing conditions, and batch

Figure 4.13 Measurement errors in micro-CT scanning process. (A) illustrates the absolute error of approximately 10 µm, resulting from lack of calibration. (B) highlights the relative error of about 2.8 µm, calculated from three repeated measurements of the same sample. The bar chart displays the mean values derived from individual data points. Lumen size: *scala tympani*; Micro-CT voxel size: 10 µm.

number ($n = 3$ per batch). Across both 'standard' and 'acrylic' post-processing conditions, at layer heights of 30 µm and 5 µm, mean deviations between batches were within the 10 µm measurement deviation threshold associated with the micro-CT scanning process. This suggests that the observable differences in both instances might be influenced by the scanning process rather than variations in the printing process itself. Notably, the coefficient of variation (CV) increased from 5.9 % to 13.22 % between batches under the 'standard' post-processing condition (as indicated by one outlier in Figure 4.12), which could also be attributed to this measurement deviation. Overall, these findings highlight that the differences in mean deviations that fall below the 10 µm threshold may not be reflective of the actual performance of the printing process, but could instead be influenced by the inherent measurement deviation introduced by the micro-CT scanning process.

4.3.6 Optimisation of SLA accuracy using nominal-actual analysis and mesh compensation

The optimisation of SLA printer accuracy was accomplished through a methodical application of nominal-actual analysis paired with mesh compensation. In this analysis, the preliminary print, as depicted in Figure 4.14 (A), served as the 'actual' model. This was then juxtaposed with the 'nominal' model in a nominal-actual analysis, elucidating the disparities between the examined models, as evidenced in the cross-section analysis of Figure 4.14 (B). This examination was instrumental in fabricating a 'compensated' mesh.

Significant deviations were observed in the upper segment of the cavity in the initial print. This can potentially be attributed to the higher viscosity of the resin used (Clear V4 by Formlabs). Due to the pronounced surface tension, an excessive amount of the resin was trapped inside the cavity, resulting in an overly abundant resin curing at a given time. Consequently, there was a surplus of material at the top part of the print, taking into account the fact that the print is being created 'upside down' as the build platform is being immersed into the resin tank.

The implementation of the compensated model led to a notable reduction in the deviation over 90 % of surface, in comparison with the original model ($n = 4$, $p < 0.001$, refer to Figure 4.14 (C)). The derived improvement in accuracy was approximately 49 %, an intriguing finding given that a singular iteration of the compensation process yielded such significant improvement in SLA printer accuracy. Future research may consider employing multiple iterations of compensation, with the goal of achieving the saturation point of possible improvement.

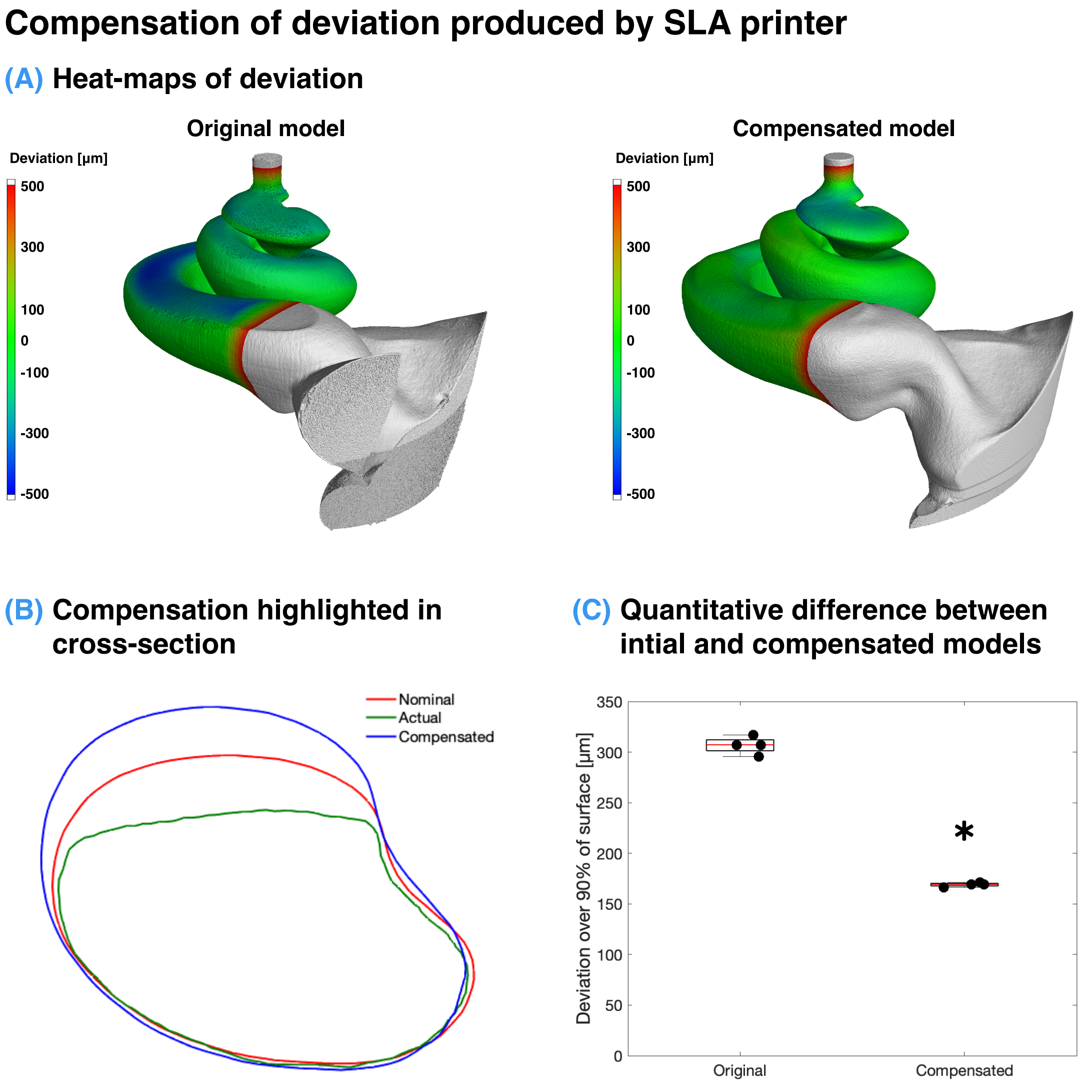

Figure 4.14 An improvement of SLA printer accuracy through nominal-actual analysis and mesh compensation. (A) Depicts the original 'actual' print model and the 'compensated' printed model. (B) Shows the nominal-actual cross-section analysis highlighting deviations in the models. (C) Demonstrates the significantly improved 'compensated' model ($p < 0.001$, highlighted with *) with a notable reduction in deviation over 90 % of the surface, providing approximately 49 % improvement in print accuracy. Boxplot: red line-median, box-interquartile range ($n = 4$ replicates). Lumen size: full cochlea; Micro-CT voxel size: 10 µm.

4.3.7 Comparison with previous work

To the best of my knowledge, this study stands as a significant milestone in cochlear modelling, successfully fabricating the most accurate and transparent cochlea model to date. Empirical evidence supports this claim, with a nominal-actual analysis indicating that 90 % of the printed surface of the *scala tympani* lumen remained within a 32 µm deviation.

When considering the current literature, as discussed in Chapter 2, several studies have attempted the fabrication of an artificial cochlea model utilising additive manufacturing.[84,131,242] However, the precision of these models remains unverified. Notably, these studies typically resort to upscaling the *scala tympani* cavity in order to compensate for discrepancies in their 3D printed models.

This study demonstrates a substantial leap forward, not only in the fabrication of a highly accurate cochlea model, but also in setting a measurable benchmark for the verification of model accuracy, without resorting to such modifications.

4.4 Conclusion

This study affirms the applicability of SLA and DLP 3D printing technologies in fabricating precise and transparent cochlea and *scala tympani* models. Comparative evaluation of segmentation techniques underlined the superiority of negative space segmentation, augmented by the 'cut' technique and histogram quantification to enhance precision. Experimental findings corroborate the merit of SLA and DLP (5 µm layer height) technologies, offering a superior surface finish.

Post-processing plays a pivotal role in model accuracy and transparency, with 'compressed air' post-processing resulting in significant deviations. Resin-coated models demonstrated improved transparency compared to 'standard' post-processing, but larger deviations, whereas the use of acrylic coating maintained full transparency with minor effects on accuracy.

Environmental influence on model transparency was assessed, revealing the robustness of acrylic-coated prints under wet conditions, highlighting the superiority of acrylic coating under differing environmental conditions. A nuanced interaction between the acrylic coating and printing resolution affected overall model precision, albeit minor in practical implications.

Notably, DLP technology with a 30 µm layer height excelled in terms of model accuracy, irrespective of post-processing methods used. A recognition of measurement errors induced by micro-CT scanning was noted – an important factor in 3D printing accuracy and repeatability interpretations.

This study also demonstrates the use of nominal-actual analysis and mesh compensation for enhancing SLA printer accuracy. A significant improvement of approximately 49 % was observed from a single compensation iteration, indicating a potential for further enhancements. Future work could explore repeated compensation iterations to identify the maximal accuracy potential, thus progressing the field of 3D printing, especially when working with SLA technology and high-viscosity resins.

In conclusion, the combination of DLP with 30 µm layer height and acrylic coating produced transparent, accurate *scala tympani* models. Nevertheless, it is vital to highlight the balance required between ensuring transparency while preserving precision. Future research should endeavour improved precision at lower layer heights and explore alternate 3D-printing technologies for the creation of models with flexible membranes. Despite limitations, this study's findings underpin further research within cochlear implantation surgery by providing methods to fabricate transparent, accurate artificial cochlea models.

Chapter 5

Impact of Scala Tympani Geometry on Insertion Forces During Implantation

Disclosure

This chapter is based on a published paper:

Hrncirik, F. Roberts, I., Swords, Ch., Christopher, P., Chhabu, A., Gee, A., & Bance, M. Impact of Scala Tympani Geometry on Insertion Forces during Implantation. *Biosensors* 12, 999 (2022).

The research and writing for this study were primarily conducted by the author with help from Dr Roberts and contributions from other authors as specified. Ms Swords, Dr Gee, and Dr Roberts contributed to micro-CT segmentation, validation, and characterisation of cochlea geometry. Dr Roberts also aided with the manipulation of the *scala tympani* shape. Dr Christopher contributed to the Capstan model mathematics. All authors have reviewed and approved the final version of the manuscript.

5.1 Introduction

There are over 466 million people worldwide that suffer from disabling hearing loss and is expected to rise to 700 million by 2050.[261] As the second leading disability worldwide,[262] hearing loss can be severely debilitating and has been linked to depression,[207,209,263–265] dementia,[266–269] and living discomfort.[270–272]

Those suffering from severe to profound sensorineural hearing loss can benefit from CIs, a transformative technology that helps people regain their hearing. However, a key limitation in increasing the eligibility of CIs is the damage caused to the cochlea during the insertion of these implants as well as the resulting chronic inflammatory response. This insertion trauma has been shown to reduce or destroy the residual acoustic hearing in up to 50 % of implantations;[273–277] therefore, only those with the most severe hearing loss are currently implanted.

A CI consists of a linear array of 12 – 22 platinum-based electrodes insulated by silicone connected via a lead to a processor placed on the skull. The electrode array is typically inserted into the ST chamber of the cochlea, in the inner ear, which is a hollow spiral-shaped chamber within the mastoid bone, filled with perilymph fluid. In order to be implanted, patients must undergo surgery where the skin is opened behind the pinna, and the skull and mastoid bone are drilled until the facial nerve, *chorda tympani*, and *incus* are visible. These landmarks are used to find the round window, an opening to the ST covered with a membrane that can be easily penetrated and which provides an entry point for the CI insertion. The common approach is to implant through the round window niche and round window where possible rather than through a cochleostomy,[278–283] which requires surgeons to create a new entry to the ST by drilling into the cochlea. Implanted CIs can then electrically stimulate the auditory nerves in the modiolus (the inner part of the cochlea spiral) and facilitate 'electronic hearing'.

Furthermore, by avoiding key auditory structures (*i.e.*, the eardrum and the middle ear) during implantation, patients can retain some residual hearing and benefit from some limited auditory cues. Furthermore, EAS, which is a combination of CI electrically stimulated hearing and low-frequency acoustic amplification, has been shown to improve the listening performance.[17,64–66] Additionally, destroying the residual hearing eliminates the possibility of a patient potentially being eligible for future therapies to restore the acoustic hearing, such as gene therapies.[284] Therefore, it is necessary to protect patients' residual hearing whenever possible.

The loss of natural hearing is often associated with the mechanical trauma that arises during the CI insertion,[21,275–277,285] which might result in fibrosis and neural degeneration, further limiting the CI performance.[176,276,286] Generally, there are two types of CI: (1) straight, which follows the lateral wall of the ST, and (2) perimodiolar, which is pre-curved and follows the modiolar (inner) wall of the ST. Although perimodiolar electrodes can, in theory, be placed closer to the target neural population, their placement can also risk more insertion trauma.[55] For straight electrodes, the initial contact is with the lateral wall of the ST, which is lined with soft tissue, and the CI slides along the lateral wall throughout the insertion. The basilar membrane, located along the top part of the lateral wall, accommodates the organ of Corti, which facilitates acoustic hearing. It is crucial to avoid damaging, or penetrating in some circumstances, this membrane as it can result in the permanent loss of hearing in that region.[96,287]

Although CIs are a triumphant story of permanently implantable devices, there are still limitations in the implantation process. For instance, CIs are commonly inserted manually by a skilled surgeon; however, it has been shown that the stable, slow insertion speeds achieved with a robotic and a semi-robotic insertion setup could lower IFs significantly.[130,176,288,289] Furthermore, there has been uncertainty about the effect of the CI size and its influence on the IFs. Historically, there has been a trade-off between making longer implants that could electrically stimulate a larger proportion of the cochlea, and convey a larger range of frequencies,[290,291] and preventing large IFs at deeper insertions. The higher IF and related mechanical trauma have led the CI industry to converge to a 'one size fits all' approach where newer CI electrode arrays are typically around 20 mm in length.[292,293] Additionally, few studies investigated how the ST size may affect IFs;[84,131,241,242] however, these either used artificial models with combined *scalae* (not a true ST model) or they did not investigate the individual parameters that might contribute to higher IFs.

This study aims to investigate the impact of the ST geometry on IFs. By systematically adjusting the key parameters of the ST, such as the volume, vertical trajectory, curvature, and cross-section area, it is possible to determine the influence of these individual components on the IFs. Furthermore, this can inform the optimal CI insertion strategies to improve patient outcomes by creating a mechanistic model from the acquired insights that match our experimental observations.

5.2 Materials and methods

5.2.1 Micro-CT segmentation of scala tympani

A cadaveric specimen was imaged with a Nikon XT 225 ST micro-computed tomography (micro-CT) scanner with an accelerating voltage of 160 kV, current of 180 µA, and a voxel resolution of 27 µm. The specimen was reconstructed using Stradview software (version 7.0, https://mi.eng.cam.ac.uk/Main/StradView, accessed on 10 March 2022). Important landmarks highlighting 68 points along the basilar membrane on the ST surface were added, so complete parametrisation using a custom-built MATLAB script was possible.

5.2.2 Characterisation of scala tympani

The 3D PLY files exported from the segmentation were imported into a custom MATLAB script for analysis together with the coordinates of landmarks along the cochlear trajectory. This workflow used the gptoolbox[294] and geom3D[295] libraries available on the MathWorks FileExchange. Using a similar methodology to Gee *et al.*,[87] a best-fit plane was determined for the landmark point coordinates along the first 270° of the basal turn of the basilar membrane. This enabled the separation of the cochlear trajectory's vertical (height) and radial (spiral) components. The cross-sections of the ST model were determined by producing planes along the cochlear trajectory perpendicular to the cochlear lumen according to the landmarks placed along the ST and calculating the closest intersection of the plane and cochlear mesh to that landmark (to eliminate intersections through multiple turns of the cochlea). This spiral, represented by the centroids of the cross-sections, was fitted to the following equation defining the radius of the curve, R, in terms of angle, θ, in degrees:

$$R(\theta) = R_{scale} \times (e^{\frac{-\theta}{\theta_1}} + e^{\frac{-\theta}{\theta_2}}) \tag{5.1}$$

where R_{scale} parametrises the overall scale of the cochlea, and θ_1 and θ_2 characterise the tightness of the basal turn and central spiral, respectively. This is a modification of previous piecewise definitions[83,296,297] of the cochlear spiral in favour of a continuous double exponential function,[85] which fits the whole cochlea while accounting for the 'flaring out' of the base. Using a continuous function offers several advantages in the mathematical modelling and shape manipulation when compared to a piecewise function. Note, for the conversion of electrode insertion distance to degrees, Equation 5.1 was applied to the basilar membrane landmarks for each ST model as the CI would follow the lateral wall rather than the middle of the ST which was confirmed/adjusted according to the actual maximal insertion angle manually measured from the video of each insertion.

5.2.3 Manipulation of scala tympani shape

In order to manipulate the shape of the cochlea, the extracted cross-sections described in Section 5.2.2 were positioned according to the required shape manipulation, as detailed below.

A custom lofting function was created in MATLAB to re-connect the cross-sections into a 3D mesh geometry from individual cross-sections. This involved sorting the vertices of the cross-sections in a clockwise direction (with respect to the base), interpolating the cross-sections to have 100 points each, triangulating the vertices between each cross-section in turn, and capping the ends to produce a fully enclosed mesh.

5.2.4 Cochlear size manipulation

Volumetric scaling of the ST was conducted by directly multiplying the coordinates of the vertices of the original ST mesh by a constant factor to produce 'large' (110 % volumetric scaling) and 'small' (90 % volumetric scaling) models.

5.2.5 Vertical trajectory manipulation

For vertical trajectory manipulation experiments, the z-component of the ST cross-sections was altered without changing the radial trajectory of the ST. For the 'flat' models, the z-component of each cross-section was subtracted from each vertex so that the ST centreline would be a two-dimensional spiral along the basal plane.

In order to simulate non-planarity, a sinusoidal function was added to the mean z-component of each cross-section from $0° - 270°$. The amplitude of the sinusoidal change was set at 200 µm, and the period was set at either 270° or 135° for conditions of artificial non-planarity 1 (NP1) and artificial non-planarity 2 (NP2), respectively.

5.2.6 Curvature manipulation

In order to manipulate the curvature of the ST models, the parameters of the fitted spiral Equation 5.1 were manipulated. Specifically, θ_2 was doubled for the loose model and halved for the tight one to either decrease or increase the curvature of the inner spiral, respectively. The ST cross-sections were projected along this new spiral and lofted into a 3D structure ready to produce a 3D print.

5.2.7 Uniform cross-section models

Uniform cross-section models used a consistent cross-section (from 1 mm from the round window) projected onto the original ST centreline to build models with the same trajectory as the original ST but with a uniform cross-section.

5.2.8 3D printing an artificial scala tympani

A custom MATLAB script, utilising Boolean operations from the gptoolbox library, was used to generate 3D printable stereolithography (STL) files for 3D printing. *Scala tympani* orientation was controlled to be consistent for all models where the first 10 – 20° of the ST were orientated along the x-axis of insertion. In addition, the basal end of the ST remained open to provide a consistent entry trajectory, and an access hole was produced at the ST apex to allow for flushing of the models with solutions prior to insertion.

Prepared models were then printed at 30 µm resolution on a CADworks3D printer (M-50, CADworks3D Microfluidics, Toronto, ON, Canada) with Clear Microfluidics Resin (V7.0a, CADworks3D Microfluidics, Toronto, ON, Canada). The printed models were then post-processed using 99.9 % isopropyl alcohol (SLS Ltd., Nottingham, UK). Lastly, the models were cured three times for 10 s with a one-minute break between the runs using a CureZone UV chamber (CADworks3D Microfluidics, Toronto, ON, Canada).

In order to achieve the transparent finish of the models, acrylic coating (Pro-cote Clear Laquer, Aerosol Solution) was used for coating the lumen (inner part) of the models. The coating was injected into the ST model, left for 10 s, and excess was then removed using compressed air to leave a thin layer to smooth the surface and achieve a clear finish. In addition, 5 % solution of Pluronic (F-127, Merck KGaA, Germany) and distilled water was used for coating the lumen of the models 24 h prior to insertion to lower friction coefficient of the printed models.

5.2.9 Insertion setup

A custom-built insertion setup used in this study was assembled using several components, namely a one-axis force sensor (500 mN Load Cell, 402B, Aurora Scientific Europe), a six-axis force sensor (NANO 17Ti transducer, ATI Industrial Automation, Apex, NC, USA), a one-axis motorised translation stage (PT1/M-Z8, Thorlabs, UK) with a K-Cube brushed DC servo motor controller (KDC101, Thorlabs, UK), a high-precision rotation mount (PR01/M, Thorlabs, UK), a large dual-axis goniometer (GNL20/M, Thorlabs, UK), an XYZ translation stage (LT3/M, Thorlabs, UK), a high-sensitivity CMOS camera (DCC3240C, Thorlabs, UK), a ring illumination lamp (Kern OBB-A6102, RS Components, UK), and a Nexus breadboard (B6090A, Thorlabs, UK). The data acquisition was facilitated by a DAQ (USB-6210 Bus-powered, National Instruments Ltd., UK) and a connected laptop (DELL, Austin, TX, USA). A Form 3B 3D printer (Formlabs, Somerville, MA, USA) with Grey Pro resin (Formlabs, Somerville, MA, USA) was utilised to fabricate the necessary parts for attaching the aforementioned components. A custom C# program was used to synchronise the stepper motor insertion with force measurements and video recording.

The one-axis sensor was attached to the motorised translation stage with a custom adapter to facilitate the insertion movement. The six-axis sensor was attached to the dualaxis goniometer, located on the top of the rotation mount and the XYZ translation stage. The camera and the ring light were attached above the six-axis sensor to illuminate the model correctly to observe the implant behaviour during the insertion (see Figure 5.1).

A practice cochlear implant electrode (Cochlear Slim Straight CI422, Cochlear Europe Ltd., UK) was attached to the one-axis sensor, and a 3D-printed artificial ST model was connected to the six-axis sensor. A 1 % solution of sodium dodecyl sulfate (SDS, Sigma Aldrich) in distilled water was injected into the model prior to the insertion for lubricating the lumen of the model.[228,252] The insertion speed, facilitated by the motorised translation stage, was set to $0.5\,\mathrm{mm\,s^{-1}}$, and the insertion depth from the artificial model opening was set to 20 mm (only 'small' and 'tighter spiral' models were inserted to 17 mm). After the full insertion, a 5 s long pause was introduced, and then the electrode was retracted. Each model was implanted ten times combined over two identical CIs that were re-straightened by hand after every insertion.

To eliminate bubbles, the ST model was periodically filled with solution up until a point where no leakage of the fluid would occur due to surface tension at the ST basal opening.

5.2.10 Fitting of insertion forces to a Capstan model

It has been shown before[97,133] that the forces on the implant can be modelled similarly to a classical Capstan problem. The Capstan problem is a statics problem Figure 5.2 (A)–

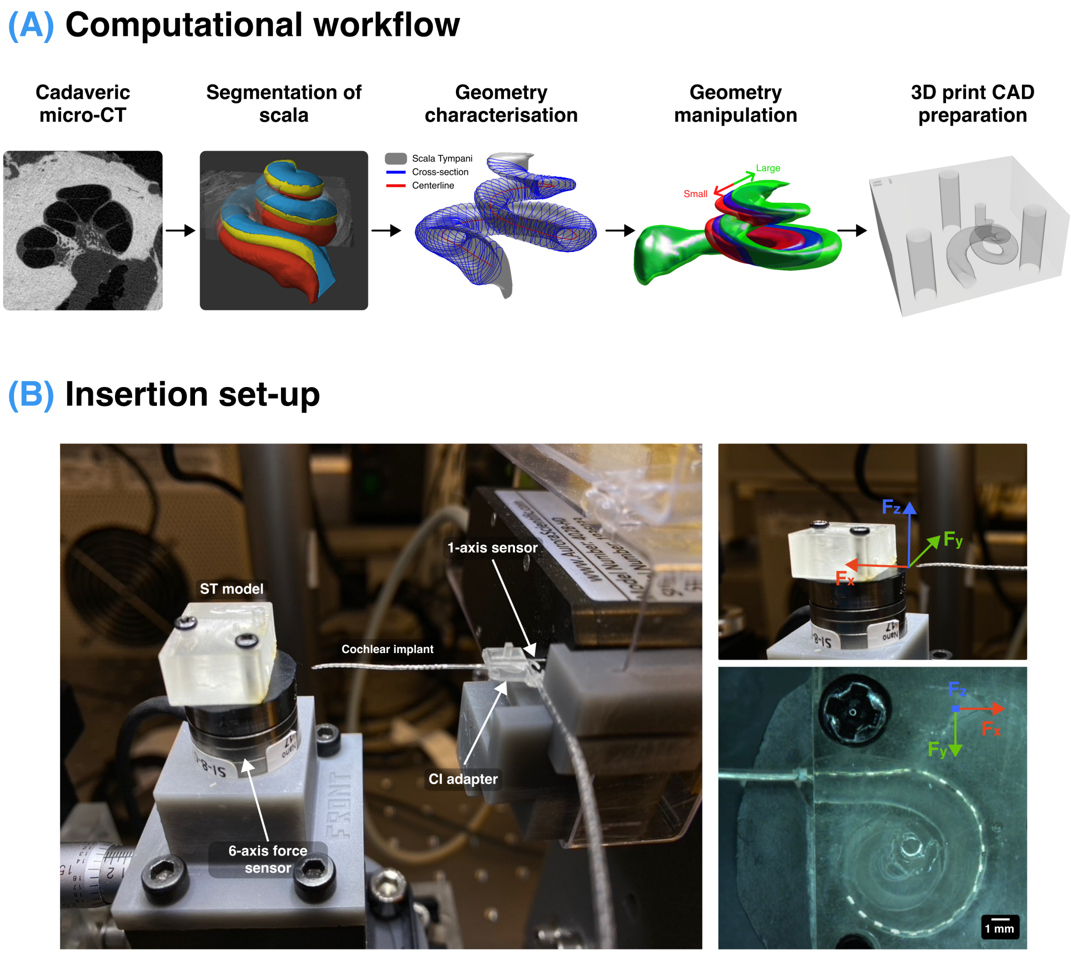

Figure 5.1 Computational workflow and the custom insertion setup. (A) A cadaveric specimen was micro-CT scanned and segmented using Stradview software. The 3D geometry was then characterised in terms of its spiral trajectory and cross-sections using a custom MATLAB script which was used to manipulate the geometry according to each experiment. This generated a 3D file of the ST which was prepared for 3D printing using another custom MATLAB script. (B) Insertion setup consists of transparent 3D-printed ST models affixed with screws to a six-axis force sensor placed on a six-axis positioning stage and a CI secured with 3D-printed adapters to a one-axis force sensor placed on a stepper motor that moved the CI into the ST model at a defined speed. The setup measures the force on the ST model in the direction of implantation (x), perpendicular in the left and right directions (y), and vertically (z), shown on the right. The one-axis force sensor measured the reaction force on the implant.

encountered when attempting to pull a rope around a rigid bollard. For a non-elastic, flexible, thin line on the verge of sliding around a rigid bollard, the problem can be modelled as

$$T_2 = T_1 e^{\mu\theta} \tag{5.2}$$

where T_1 is the tension on the side of the rope that is being pulled on (it is the 'input' or 'applied' force), T_2 is the tension on the side that is being wrapped around the bollard or object (it is the 'output' or 'held' force), θ is the total angle subtended by the contact region of the rope, and μ is the coefficient of friction. Notably, the Capstan equation acts as a 'force multiplier', with the ratio between T_2 and T_1 being fixed for a given position on the verge of sliding. The exponential nature of this relationship is such that theoretically, for a coefficient of friction of 0.7, approximately that of steel on steel, a 1 kg restraining force would be capable of holding over 3.5 million tonnes with only five full turns.

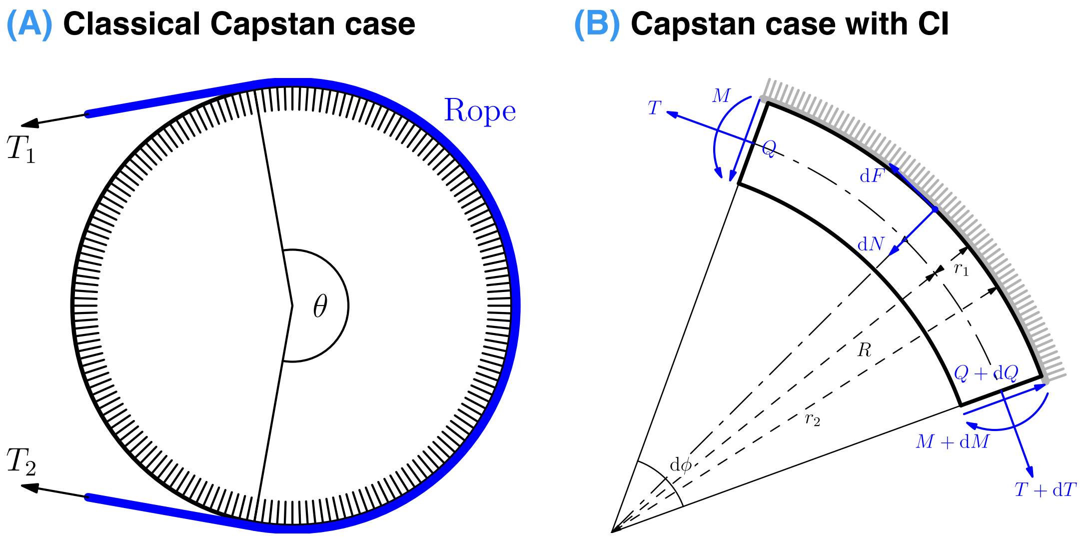

Figure 5.2 (A) Capstan problem showing the classical case of rope being secured around a circular bollard and (B) the case with an cochlear implant being inserted inside of a spiral structure.

In this case, the Capstan equation can be expressed as an overall force on the implant during insertion, $F_{implant}(\theta)$, being related to the angular insertion along the ST wall, θ, according to:

$$F_{implant}(\theta) = F_{tip} e^{\mu' \theta} \tag{5.3}$$

where F_{tip} is the tip force of the electrode, μ' is the exponential coefficient that is linearly correlated to the coefficient of friction but includes other factors, including surface roughness and the spiral nature of the ST. Note that θ, in this case, is related to the angle relative to the initial contact point of the CI with the ST lateral wall rather than to the round window, measured in degrees.

When fitting the exponential growth of the insertion force exhibited on the implant with respect to insertion angle, F_{tip} was fixed per tested condition (e.g. volume scaling, as the tip force during initial contact between the CI and ST wall was observed to be very similar for all insertions within each experiment.

5.2.11 Statistical analysis

MATLAB (Mathworks) ANOVA 1 with Multcompare function was used to study the statistical significance of exponential coefficients between the measurements. Data were found significant if $p < 0.05$. Each condition was replicated $n = 5$ times for two separate, but identical, Cochlear Slim straight electrodes for a total of 10 experimental repeats for each ST model.

5.3 Results

5.3.1 Insertion setup with accurate scala tympani model

A workflow for creating the 3D printable CAD models of the ST was generated (see Figure 5.1 (A)), which included the characterisation of the micro-CT segmented cochlea and the manipulation of the ST shape before generating an STL file suitable for printing. The 3D-printed ST model and cochlear implant were secured to a six-axis and one-axis force sensor, respectively, to monitor the forces through the insertion (Figure 5.1 (B)).

Using DLP 3D printing, it was possible to produce highly accurate 3D models of the *scala tympani* cavity (Figure 5.3). Furthermore, through the addition of an acrylic coating after the standard post-processing on the inside and outside surfaces of the model, it was possible to significantly improve the transparency of the models, as seen in Figure 5.3 (A). The accuracy of these 3D prints was validated using a nominal–actual analysis to quantify the surface deviation of the 3D-printed ST with the original STL

CAD file. This determined that 90 % of the surface was within 32.1 µm of the original file, with the highest deviation occurring at the top surface of the basal and apical ends of the ST (Figure 5.3 (B)). The localised deviation at the top surface of the ST is likely due to the printing of a free-standing surface without support structures. However, as the CI will not be in contact with these regions, they do not influence the CI insertion.

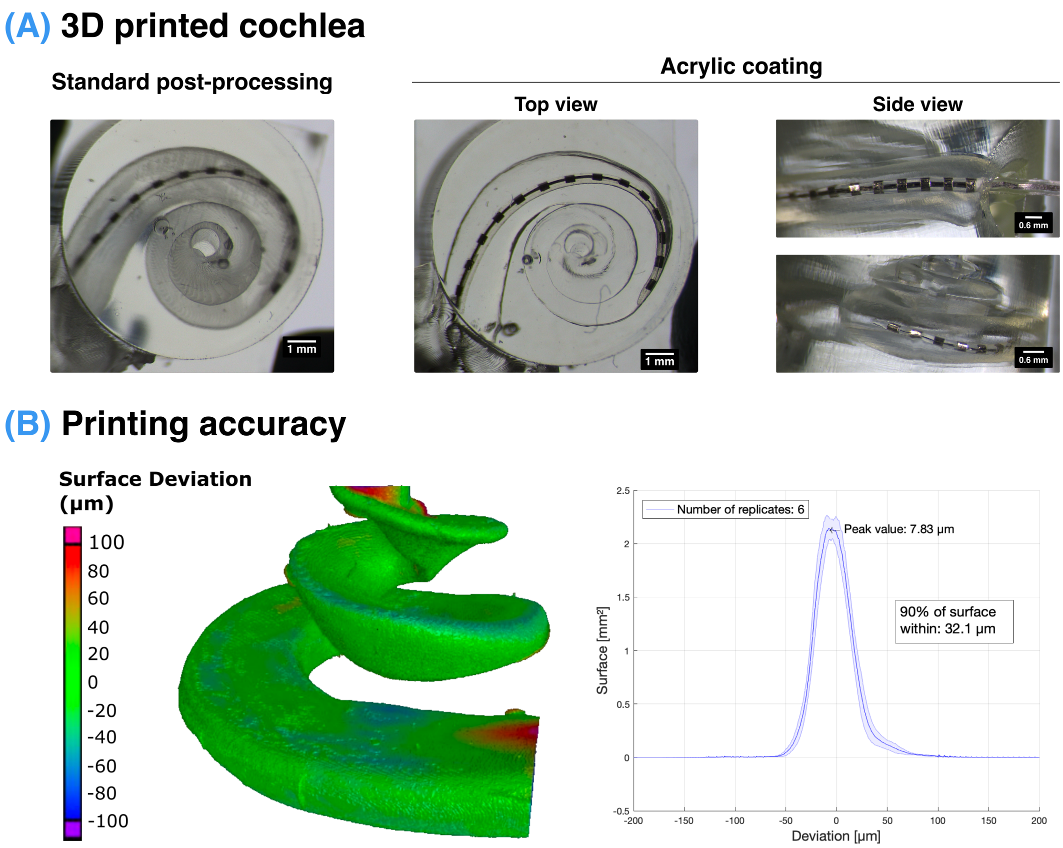

Figure 5.3 (A) Implantation of a CI in ST models with manufacturer-recommended post-processing (left) and an additional acrylic coating (right). This demonstrates the clear imaging of the CI electrodes, vertically and horizontally, to investigate CI positioning and validate the angular insertion depth. (B) Quantification of 3D-printing accuracy using nominal–actual analysis demonstrating the 3D map (left) and histogram of surface deviation (right) compared to the original CAD file used for printing.

5.3.2 Influence of overall size on insertion force

Although some studies have found some relation between the overall size of the cochlea and the CI insertion force,[242] as well as residual hearing preservation,[82] a systematic study into the force dependence on size has not been previously conducted.

This study measured the forces exerted on both the implant and the cochlea. A six-axis force sensor provided the reactive force of the implant insertion in the x, y, and z axes (as depicted in Figure 5.1) which correspond to the forces in the direction of the implant insertion and perpendicular on the horizontal and vertical axes, respectively, as well as the torque around these axes. The overall force on the implant shows good agreement with the reaction force measured on the implant ($R^2 = 0.999$), which acts as a good cross-validation of the two independent sensors (Figure 5.4). As expected, the overall force on the cochlea is dominated by the force in the direction of the CI insertion (along the x-axis), and the force along the perpendicular directions is approximately 10 % of the magnitude of that primary force; see Figure 5.5.

As seen in Figure 5.6, the insertion force on the implant increased exponentially with the depth of the insertion. Additionally, the increase in this force was highly dependent on the size of the model, where a 10 % increase or decrease in the overall volume (respectively, for the 'large' and 'small' models) of the model significantly impacts the insertion force. However, when normalising these profiles to the angular insertion depth rather than the length of the electrode inserted, the profiles overlap. This is as predicted by the Capstan model (described in Section 5.2.10) and is based on the perhaps unintuitive fact that the friction force is independent from the contact area between sliding objects and depends only on the total normal force and the coefficient of friction. For instance, in a 'large' model, a longer length of the CI is in contact with the cochlear wall for a given angle when compared to a 'small' model, but this just distributes the same overall normal force on a larger area. However, this suggests that there would be higher local stresses in a smaller cochlea due to the same overall force being distributed along a smaller contact area.

It should be noted that the 'small' model was inserted only to a 17 mm insertion distance to preserve the structural integrity of the implant as a deeper insertion might damage the implant and change the forthcoming measurements.

The tip force (F_{tip}) was determined as the force to bend the CI tip during the initial contact between the CI and the cochlear wall, at 100° depth relative to the round window. This force remained relatively consistent (at (2.60 ± 0.37) mN, (3.10 ± 0.35) mN, (3.10 ± 0.38) mN, and (3.00 ± 0.49) mN, for the volume scaling, manipulation of ST

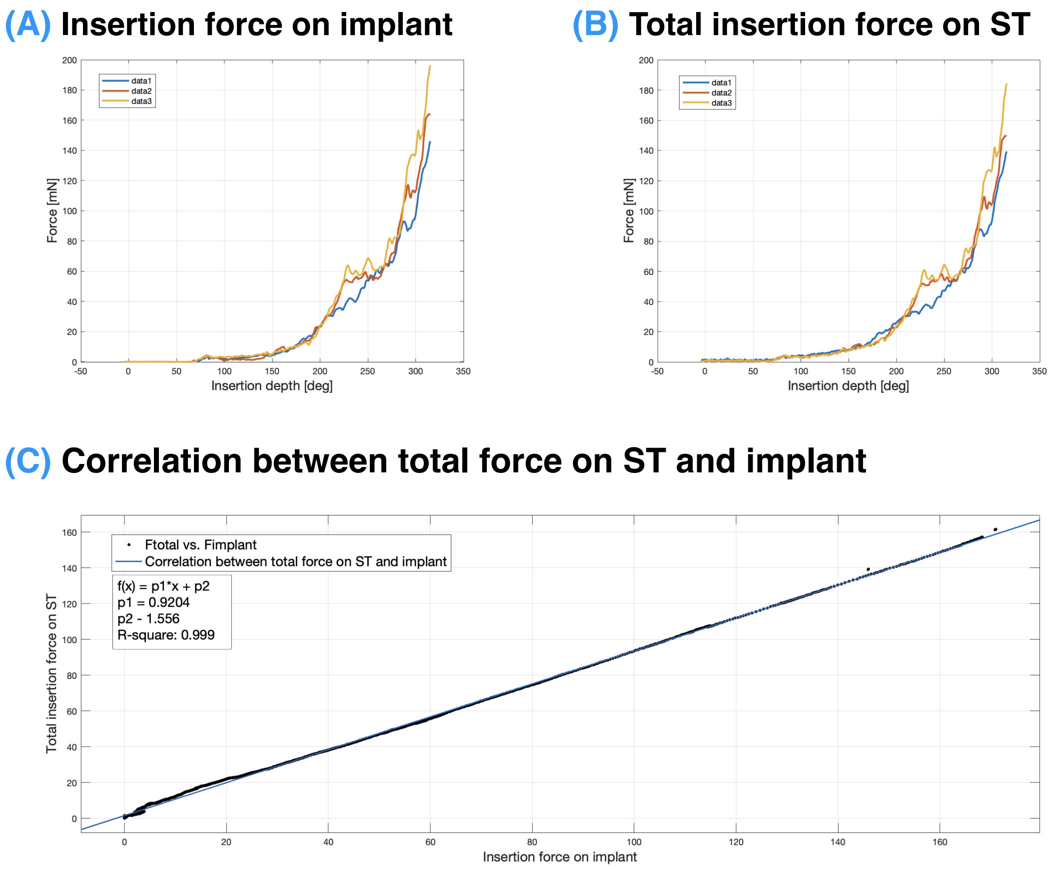

Figure 5.4 Cross-validation of insertion force measurements. (A) and (B) show three measurements of insertion forces on the implant and ST model measured by the one-axis sensor and the six-axis sensor, respectively. The total insertion force was calculated following equation: $F_{total} = \sqrt[2]{F_x^2 + F_y^2 + F_z^2}$. (C) illustrates the correlation between measurements with one-axis and six-axis sensors with an $R^2 = 0.999$.

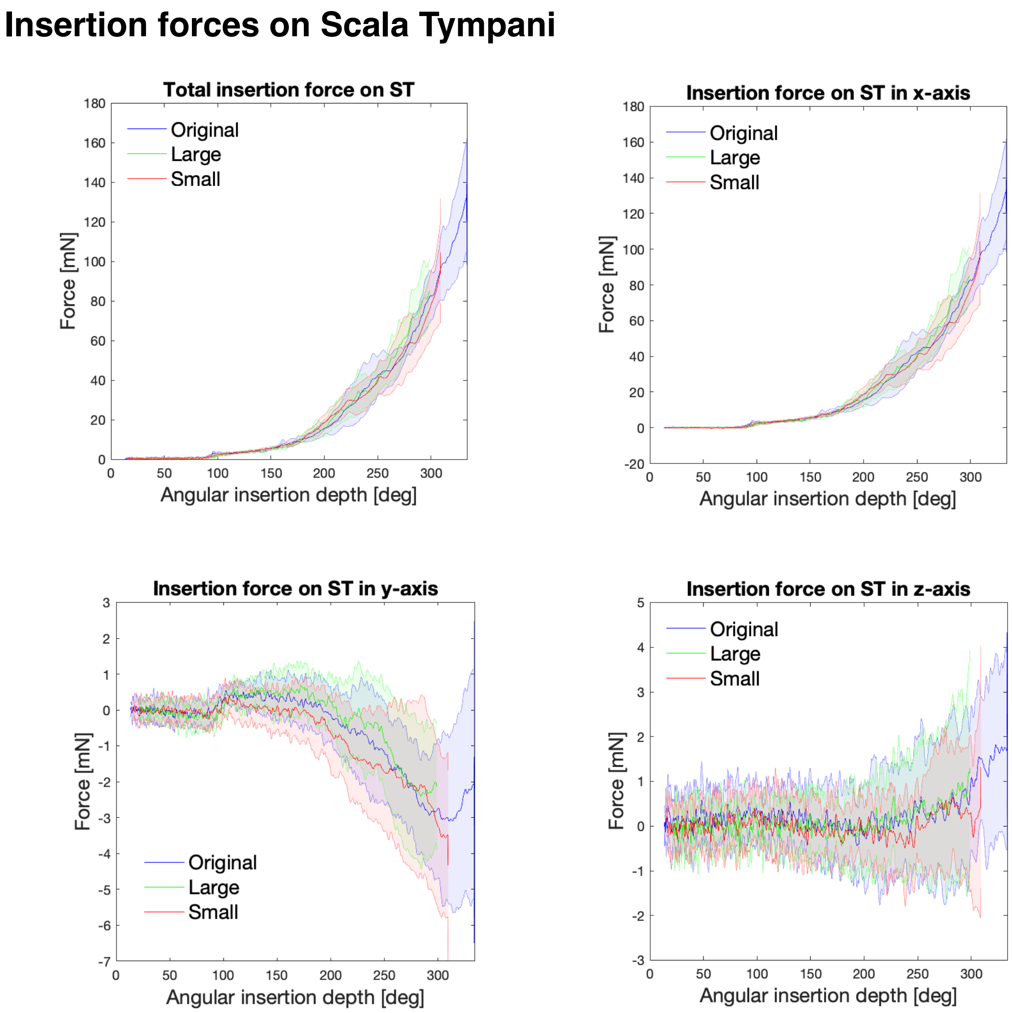

Figure 5.5 Total insertion forces measured on ST model (top-left) consisted of three components: insertion forces in x-axis (top-right), y-axis (bottom-left), and z-axis (bottom-right). The total insertion force was calculated following equation: $F_{total} = \sqrt[2]{F_x^2 + F_y^2 + F_z^2}$. Insertion forces measured on the 'original' (no alteration of size or shape), the 'large' (110 % scale of the original model volume), and the 'small' (90 % scale of the original model volume) model overlay once normalised for a correct angular insertion depth. Mean and standard deviation ($n = 10$) are highlighted by solid line and shaded area, respectively.

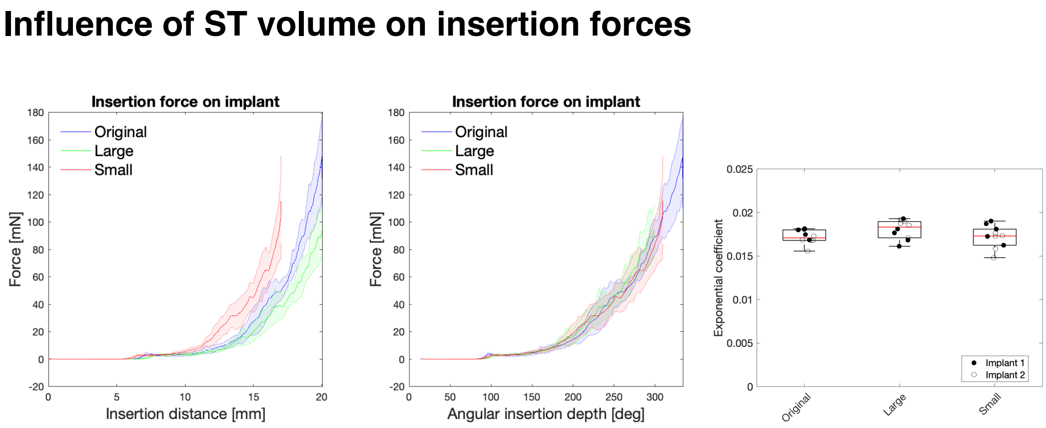

Figure 5.6 Influence of ST overall size on insertion forces. A volumetric scaling of the ST model was conducted to produce a ‘large’ (110 % the volume of the ‘original’) and ’small’ (90 % of the ‘original’ model) models. Whereas a significant difference is seen when plotting force exerted on the CI (mean-solid line; shaded area-standard deviation) with respect to insertion distance (left), these force profiles overlap when plotting relative to angular insertion depth of the round window (middle). The exponential coefficients (right) of the Capstan model fitting to the force on the implant with respect to the angular insertion depth illustrate no significant difference ($p > 0.05$) between the insertion force profiles. Boxplot: red line-median, box-interquartile range ($n = 10$ replicates combined over $N = 2$ implants).

vertical trajectory, curvature, and cross-sectional area experiments, respectively) and was fixed in fitting the Capstan model (Equation 5.3) to the force exerted on the implant for each experiment. The fitting of the force profile to the exponential Capstan model then determined the exponential coefficient μ' (see Table 5.1 for the R^2 error of the fitting and Figure 5.7 (A) for an example of the fitting).

Figure 5.7 (B) presents the average insertion force profiles for all conditions under examination, with the y-axis rendered in a logarithmic scale to better visualise force magnitudes. Notably, the 'loose' and 'flat C-A' models exhibit engagement with the cochlea's lateral wall at a lower angular insertion depth of approximately 80°, in contrast to the remaining samples which conform to the wall at about 100°. This observation is consistent with the anatomical configuration of these models, which are characterised by a less pronounced curvature of the ST outer wall, facilitating earlier contact.

In a further analysis depicted in Figure 5.7 (C), the average insertion profiles of all tested conditions ($n = 10$) are meticulously fitted. The parallel nature of the fitted lines across the graph suggests a uniform exponential correlation between the insertion force and the angular insertion depth, irrespective of the experimental condition. This consistent pattern, quantitatively summarised in Table 5.1, underscores a predictable increase in force as the implant advances deeper into the cochlea. Additionally, the diagram reveals variability in the initial force, F_{tip}, necessary for bending the implant's tip. Such discrepancies in F_{tip} could be ascribed to an array of factors including minor variations in insertion trajectories, the mechanical impact of repeated straightening on the implants, and inherent differences in the tip-to-lateral wall interaction. These findings underscore the importance of factoring in the initial deformations at the implant's tip, which introduce a critical, albeit variable, component to the insertion force profile.

The exponential coefficients were not significantly different between the samples, suggesting that the insertion force is related to the angle of the CI insertion rather than the overall length of the CI in contact with the ST wall.

As the overall size influences many aspects of the cochlear geometry, as depicted in Table 5.2, a systematic variation in the different aspects of the cochlear geometry and their effect on the cochlear implant insertion force was conducted. These three main factors included (1) the vertical trajectory of the ST, (2) the horizontal trajectory of the ST (*i.e.*, curvature), and (3) the cross-sectional area of the ST.

Table 5.1 Summary of the mean R^2 error of the force profile fitting to the exponential Capstan model, determined exponential coefficient μ', and p value compared to control within the experiment. $n = 10$ replicates combined over $N = 2$ implants; STD - standard deviation.

Experiment	**Sample**	**Error of Fitting R^2 (Mean ± STD)**	**Exponential Coefficient μ' (Mean ± STD)**	**p-Value**
Volume scaling	Original	0.97 ± 0.011	0.017 ± 0.0008	Control
	Large	0.96 ± 0.035	0.018 ± 0.0011	0.187
	Small	0.96 ± 0.038	0.017 ± 0.0013	0.997
Manipulation of ST vertical trajectory	Original	0.97 ± 0.011	0.017 ± 0.0008	0.986
	Flat	0.97 ± 0.023	0.017 ± 0.0010	Control
	NP1	0.96 ± 0.027	0.017 ± 0.0007	0.994
	NP2	0.94 ± 0.044	0.016 ± 0.0008	0.01
Manipulation of ST curvature	Flat	0.97 ± 0.012	0.017 ± 0.0008	Control
	Flat - loose	0.96 ± 0.018	0.017 ± 0.0004	0.972
	Flat - tight	0.98 ± 0.014	0.018 ± 0.0009	0.201
Manipulation of ST cross-sectional area	Flat	0.97 ± 0.013	0.017 ± 0.0008	Control
	Flat - uniform CS	0.98 ± 0.006	0.016 ± 0.0011	0.315

Table 5.2 Summary of manipulation of ST size/shape and its impact on ST height of the lateral wall, and trajectory of the CI in the vertical axis and horizontal plane.

		IMPACT ON		
		Height of LW	Trajectory in vertical axis	Trajectory in horizontal plane
MANIPULATION OF MODEL	Volume	✓	✓	✓
	Basal planarity and rising spiral	✗	✓	✗
	Curvature	✗	✗	✓
	Cross-section area	✓	✗	✗

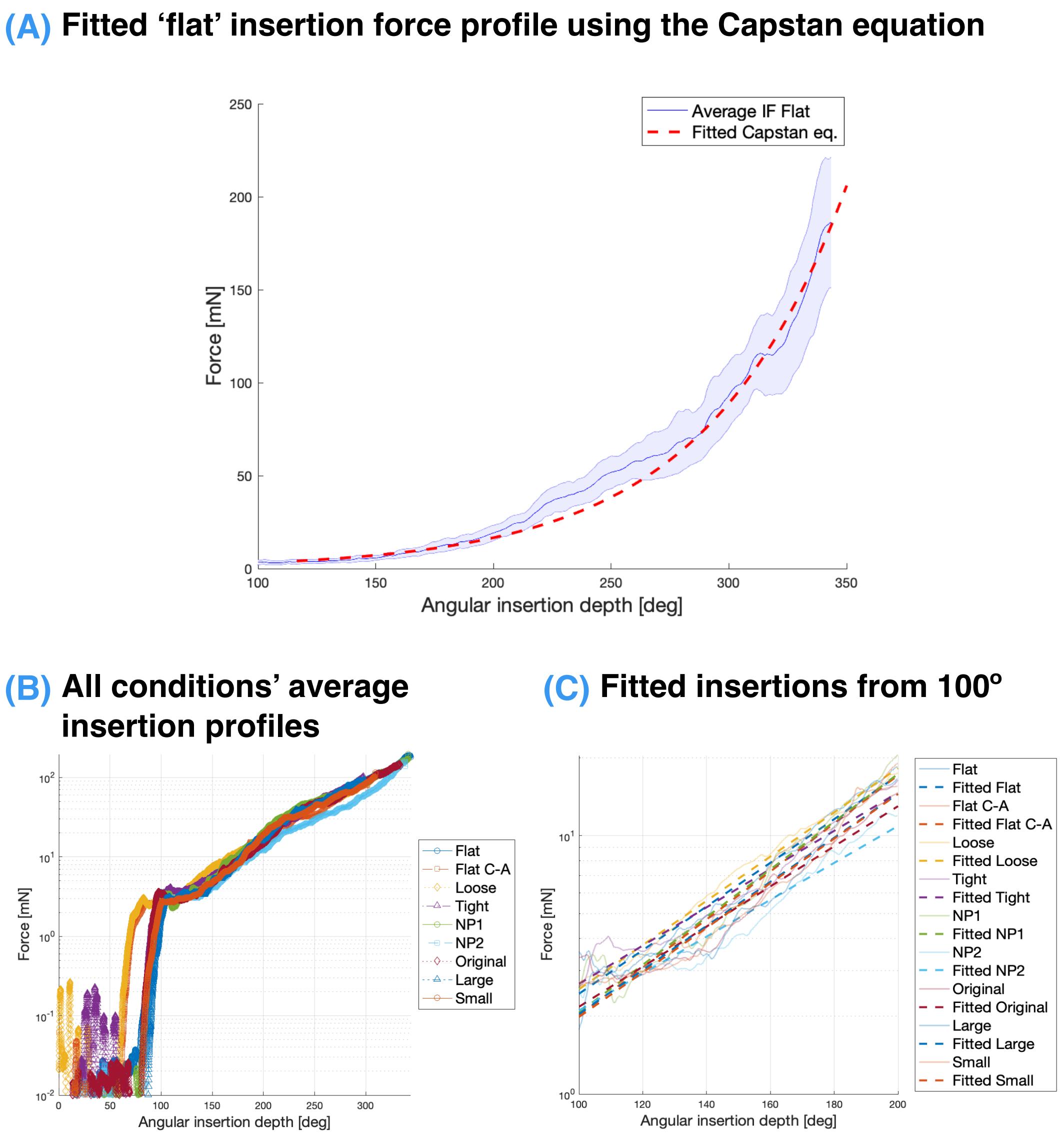

Figure 5.7 (A) Fitting of 'flat' condition insertion force profile using the Capstan equation. (B) Logarithmic representation of average insertion force profiles across all conditions. The 'loose' and 'flat C-A' models engage with the cochlea's lateral wall at approximately 80° of angular insertion depth, as opposed to the approximate 100° observed in other models, reflecting the anatomical variance in the curvature of the cochlea's outer wall. (C) Detailed fitting of average insertion profiles ($n = 10$) to the exponential Capstan model, demonstrating a consistent relationship between force and angular insertion depth and elucidating some variability in the initial force F_{tip}.

5.3.3 Influence of scala tympani vertical trajectory on insertion forces

Firstly, the manipulation of the ST vertical trajectory was conducted wherein the centreline of the ST cross-sections was unaltered except for their vertical position, as depicted in Figure 5.8. This included producing a 'flat' model where the centreline of all the cross-sections lay along the same x-y plane. The non-planar models introduced a sinusoidal variation in the vertical trajectory in the first 270°, with conditions NP1 and NP2 having a consistent amplitude of 0.2 mm but a period of 270° and 135°, respectively. This replicates the 'rollercoaster' vertical trajectories observed in several studies.[36,76,87] The overall vertical trajectory (or rising spiral) of the ST centreline did not have a significant effect on the insertion force when considering the flat model versus the original ascending model. However, an increased non-planarity (condition NP2) led to a small but statistically significant decrease ($p = 0.024$ relative to the 'original' model) in the insertion force on the implant and along the z-axis of the model, whereas the decreased frequency of the non-planarity led to a slightly higher force along the z-axis.

5.3.4 Influence of scala tympani curvature on insertion forces

The curvature of the ST models was changed by adjusting the parameter influencing the curvature of the inner spiral of the cochlea (θ_2), as seen in Figure 5.9. This was conducted on flat models; therefore, only the curvature was influencing the force profiles. As the curvature affected the angular insertion of the implant, this was a significant factor in determining the total insertion force for a given length of the inserted CI. Once normalised for the angular insertion depth, the IF profiles of all three ('flat', 'loose' spiral, and 'tighter' spiral models) models overlapped and there was no statistically significant difference in their exponential coefficients ($p > 0.05$; see Table 5.1). Similar to the 'small' model, the 'tighter' spiral model was also inserted to only a 17 mm insertion distance to preserve the structural integrity of the CI.

5.3.5 Influence of scala tympani cross-sectional area on insertion forces

Finally, the effect of the ST cross-sectional area was investigated (see Figure 5.10). Typically, there is a decrease in the cross-sectional area with an angle as the ST tapers from the base to the apex (see Figure 5.11). However, in this experiment, this was

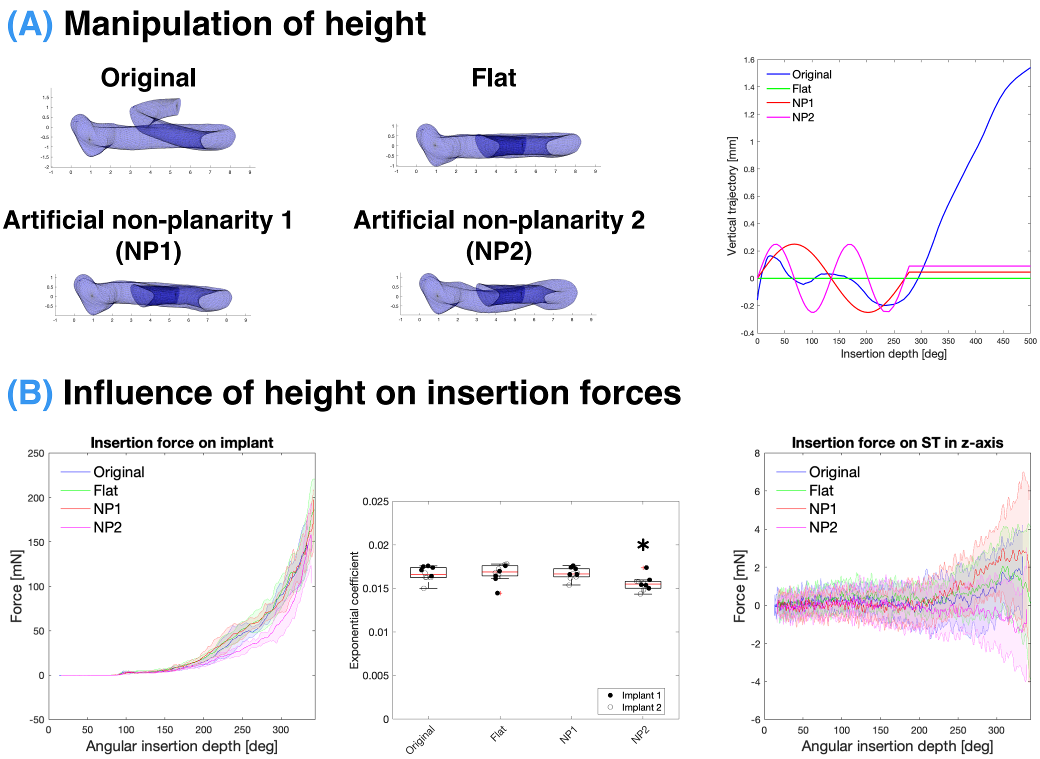

Figure 5.8 Manipulation of the vertical trajectory of the ST and its influence on CI insertion forces. (A) Representation of the 3D geometry (left) and the centreline z-component relative to the basal plane (right) of the different ST models, only varying in the vertical trajectories of their centrelines; these consist of the original geometry (cut off at 500° for comparison), a flat model where all centrelines are on the same horizontal plane, and two artificial non-planarities (NP1 and NP2). (B) Insertion force on the implant with respect to angular insertion depth (left; solid line-mean, shaded area-standard deviation) and respective fitting of the Capstan model exponential coefficient (middle; red line-median, box-interquartile range) for models with different vertical trajectories. Data represent $n = 10$ replicates per condition over $N = 2$ implants. Only NP2 showed a statistically significant difference (p values of 0.024, 0.010, and 0.020 compared to 'original', 'flat', and NP1 models, respectively). Vertical forces, along the z-axis, on the ST model due to CI insertion (right). Note, altering the vertical trajectory made little difference to the angular insertion depth per mm of length.

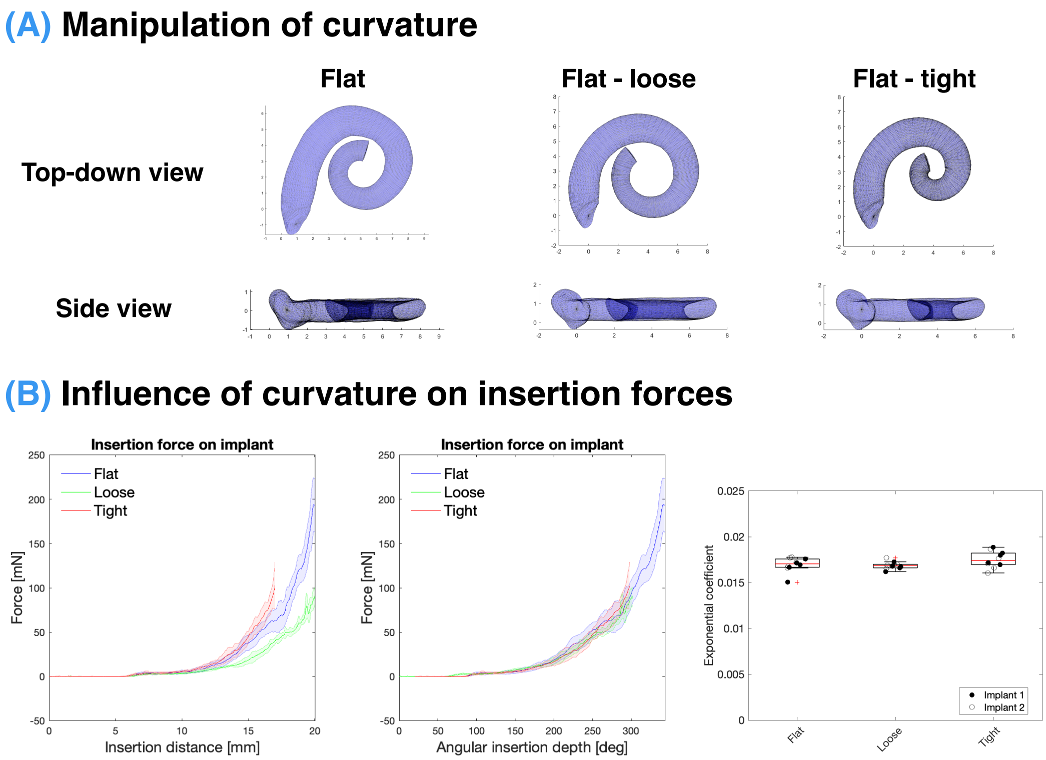

Figure 5.9 Influence of ST curvature on the CI insertion force. (A) Representations of the shape manipulation of the ST models. (B) Insertion force experienced by the implant for models with altered curvatures with respect to insertion distance (left) and angular insertion depth (middle; solid line-mean, shaded area-standard deviation). Statistical analysis of the exponential coefficients, which are acquired by fitting the insertion force profiles, shows no statistical significance between the models ($p > 0.05$; boxplot: red line-median, box-interquartile range). Data represent $n = 10$ replicates per condition combined over $N = 2$ implants.

compared to a uniform cross-section where the cross-section of 1 mm depth from the round window was used along the whole spiral. Similar to the curvature experiment, the vertical trajectory was controlled for in this experiment by comparing to a 'flat' model. When comparing the uniform cross-section model ('flat—uniform CS') to the tapered cross-section model ('flat'), the insertion force is seemingly much smaller for a given insertion distance. However, when normalising for the angular insertion depth, the forces overlap as with other alterations of the ST geometry. When comparing the average exponential coefficient in the growth of the force with respect to the angle, there is no statistically significant difference ($p > 0.05$; see Table 5.1) between these models.

5.4 Discussion

5.4.1 Comparison with previous work

This study represents a thorough analysis of the different contributions of the selected geometrical features, namely the basal planarity, vertical trajectory, overall scaling, curvature, and cross-section area of the ST on the CI insertion. The study demonstrates a method for systematically manipulating the different features of the ST shape by taking the cross-sections of a single ST segmentation, changing their position, and reconstructing them into a 3D mesh. Although others have used a cross-section analysis to characterise the ST shape,[108] none have reconstructed these cross-sections into a 3D structure to investigate their effect on physical properties.

As far as I am aware, the shape manipulation algorithm developed for this study is the first implementation of a generalised lofting function in MATLAB for arbitrary cross-section shapes. This algorithm performed more reliably for this task than the lofting functions in established 3D design software, such as Autodesk Fusion 360. Furthermore, using a nominal–actual analysis, it was determined that the reconstruction was highly accurate to the shape of the original CAD model of the ST (90 % of the surface with $<7.24\,\mu m$ deviation), as seen in Figure 5.12. At the apex of the cochlea, some meshing errors could occur due to the tight curvature of the cochlea, although this region was not of interest for the CI insertions and was not included in the manipulated ST 3D prints. Note that in the 'flat' models, the ST was cut off at the point where one turn of the cochlea would intersect another due to being on the same plane but would always be beyond the level of the full CI insertion.

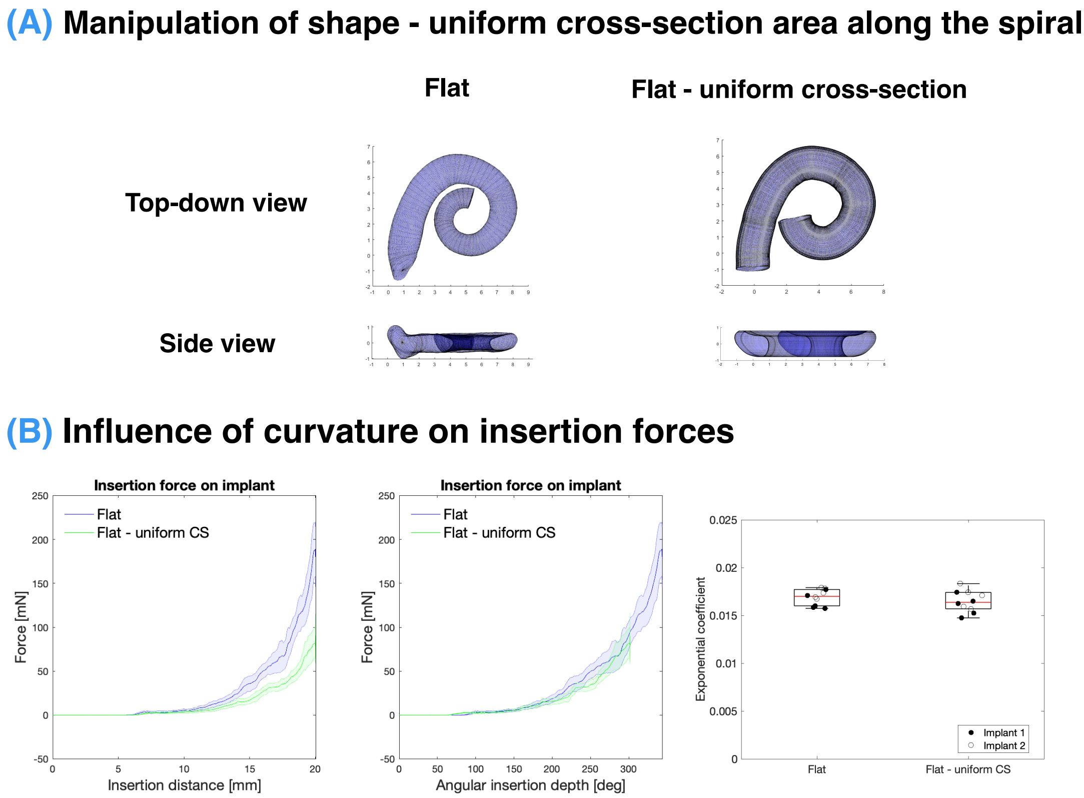

Figure 5.10 Influence of ST cross-sectional area on insertion forces. (A) Manipulation of the ST geometry demonstrating the tapered cross-sectional area of the 'flat' model versus the 'flat-uniform cross-sectional area' model where the cross-section at 1 mm depth from the round window was used along the same horizontal trajectory. (B) Force exerted on the CI during insertion as a function of insertion distance (left) and angular insertion depth (middle; solid line-mean, shaded area-standard deviation) along with the exponential coefficient of the fitting of the force profiles (right; red line-median, box-interquartile range) demonstrates no significant effect ($p > 0.05$) of the uniform cross-section area on insertion force. Data represent $n = 10$ replicates per condition combined over $N = 2$ implants.

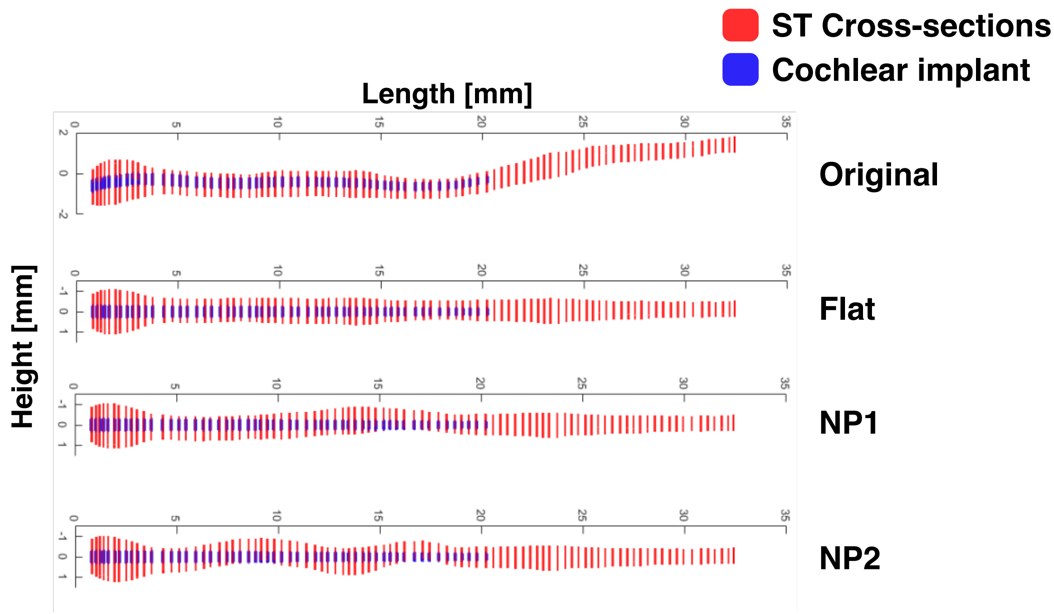

Figure 5.11 Size demonstration of CI (blue) and *scala tympani* (red) with cross-sections aligned into a straight line for the 'original', 'flat', and artificial non-planarity models 'NP1' and 'NP2'.

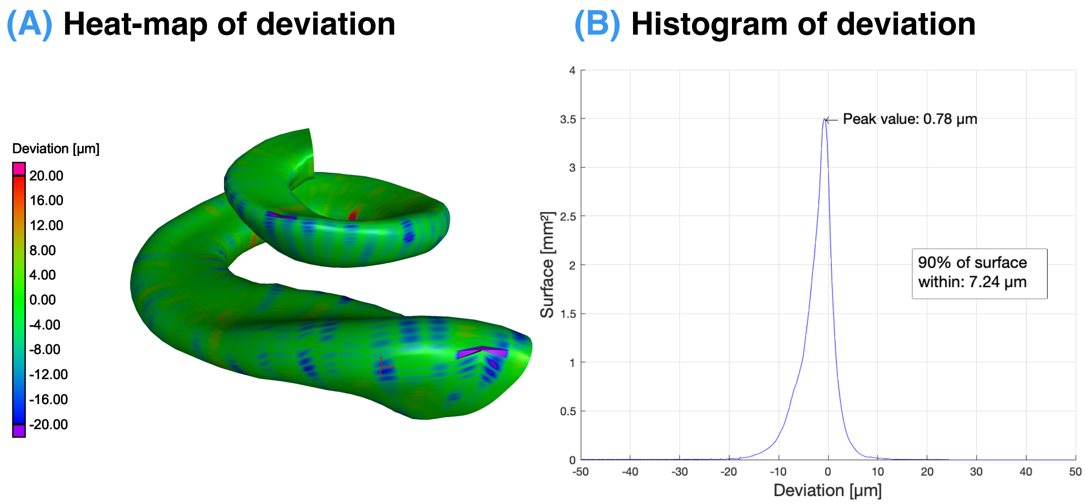

Figure 5.12 Accuracy of reconstructed models from shape manipulation using nominal–actual analysis. (A) The heat-map represents the overlay of ST reconstructed from cross-section lofting with the original ST segmentation mesh demonstrating good overall shape preservation. (B) The histogram manifests the deviation of 90 % of the surface within 7.24 µm which highlights relatively low surface deviation when considering the low number of cross-sections (80 included in this example) relative to the original mesh.

Furthermore, this study demonstrates the fabrication of directly 3D-printed models with a transparent finish and validated accuracy (90 % of the surface within <32 µm deviation; see Figure 5.3). In contrast, the previous studies have either employed scaling ratios of the ST to accommodate for mismatches in their 3D-printed models[84,131,242] or used direct casting, which results in models that combine all three *scalae* and which does not allow for flexibility in manipulating its shape.[139]

5.4.2 Impact of scala tympani shape on insertion forces

Overall, it can be seen that the insertion force on the CI is determined by the angular insertion depth and is rather resilient to other factors. Although the overall volume affected several parameters, as detailed in Table 5.2, the changes in the force were accommodated for by controlling for the angular insertion depth rather than considering the length of the implant inserted. All the changes in the ST geometry did not cause a statistically significant difference in the force relative to the angle; this provides strong evidence for the Capstan model. The only exception is when a large non-planarity is added to the base where the implant trajectory may be altered to a point that it does not follow the Capstan model, as discussed below. As the force increases exponentially with an angular insertion depth, it is very sensitive to changes in the angle, which were confirmed manually using the videos of each insertion.

Effect of scala tympani vertical trajectory

When controlling for the vertical trajectory of the ST, the ascending portion of the cochlea did not affect the force when comparing the 'flat' and 'original' models, both in terms of the overall force and the force in the vertical direction, as seen in Figure 5.8.

Introducing a high non-planarity to the basal turn (as with NP2) led to a small statistically significant decrease in the force on the implant. This somewhat counterintuitive result may be due to the CI having less contact with the lateral wall as it travels through the centre of the cochlear lumen. NP2 also had a lower overall z-force. However, this may be due to the implant being in contact with both the top and bottom walls of the ST and the sum of the vertical forces cancelling each other out. The CI diameter relative to the ST cross-section is demonstrated in Figure 5.11. Although statistically significant, this rather extreme case of non-planarity only results in a small difference in the insertion force which will not likely be clinically significant.

A typical amplitude of the non-planarity and fixed angle of the insertion was used in this study, as the non-planarity can be highly dependent on the coordinate system used to define the vertical trajectory of the cochlea.[87]

Effect of curvature

The effect of the ST curvature on the insertion force was accommodated for by controlling for the angular insertion depth. In this study, only θ_2, which varied the curvature of the inner spiral, was altered and the basal turn of the ST remained unaffected. Therefore, the insertion forces were similar in this region. As with the 'small' model, a full insertion was not possible with the 'tight' ST model as there was a significant risk of kinking the CI at deeper insertion depths.

Effect of cross-sectional area

The cross-sectional area of the ST was determined to have a minimal effect on the CI insertion force. The 'original' ST varies from 2.6 to 1.0 mm^2 across the extent of the CI insertion, whereas the 'uniform cross-sectional' model was fixed at 2.5 mm^2, as seen in Figure 5.13. It is worth noting that the 'uniform cross-section' ST represents a rather extreme difference in the cross-sectional area between the models, which is beyond anatomical variation found in humans. The alteration in the cross-sectional area in the volume-scaled models (as illustrated in Figure 5.13), however, does not demonstrate a significant influence on the force with respect to the angular insertion depth.

As predicted by the Capstan model, the insertion force is determined by the angular insertion depth of the CI into the ST. Therefore, this finding reinforces the fact that it is the CI contact with the wall that determines the force rather than the overall space within the ST. At the depths inserted in this study, the cross-sectional area and the height of the lateral wall are significantly larger than the CI, as illustrated in Figures 5.13 and 5.14, respectively. For instance, at a 20 mm insertion, the height of the lateral wall in the 'original' model varies from 1.6 to 0.9 mm (Figure 5.14), whereas the CI diameter varies from 0.6 to 0.3 mm from the base to the apex.[82] The size of the CI within the ST is illustrated more directly in Figure 5.11 within a straightened ST. However, when the CI diameter would match the height of the ST, the insertion force and mechanical trauma are expected to increase significantly as the CI would be constrained by the top and bottom surfaces of the ST, deviating from the Capstan model.

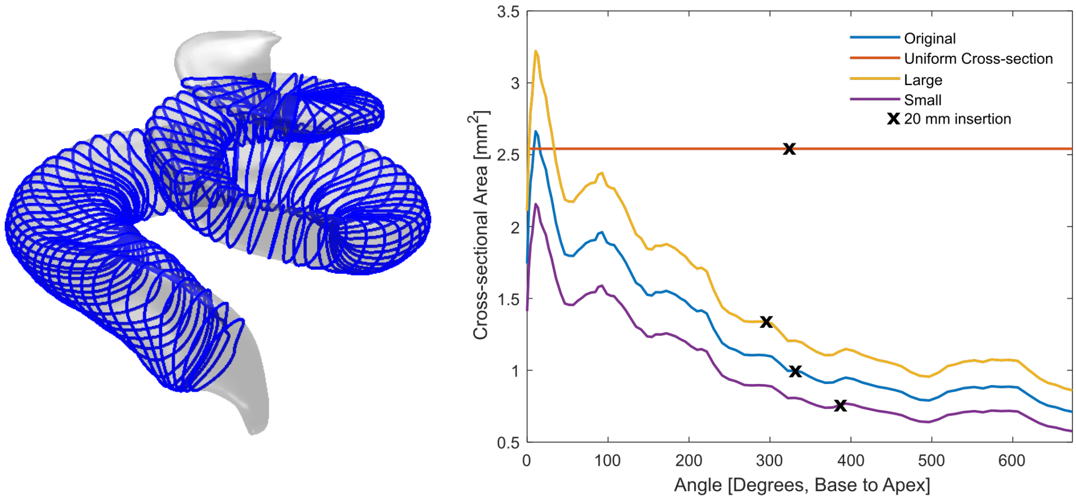

Figure 5.13 Cross-sectional area of selected ST models. Representation of the cross-sections on the 'original' model (left) and quantification of the cross-sectional area along the ST spiral (right). Black cross displays 20 mm insertion distance of CI and its corresponding angular insertion depth.

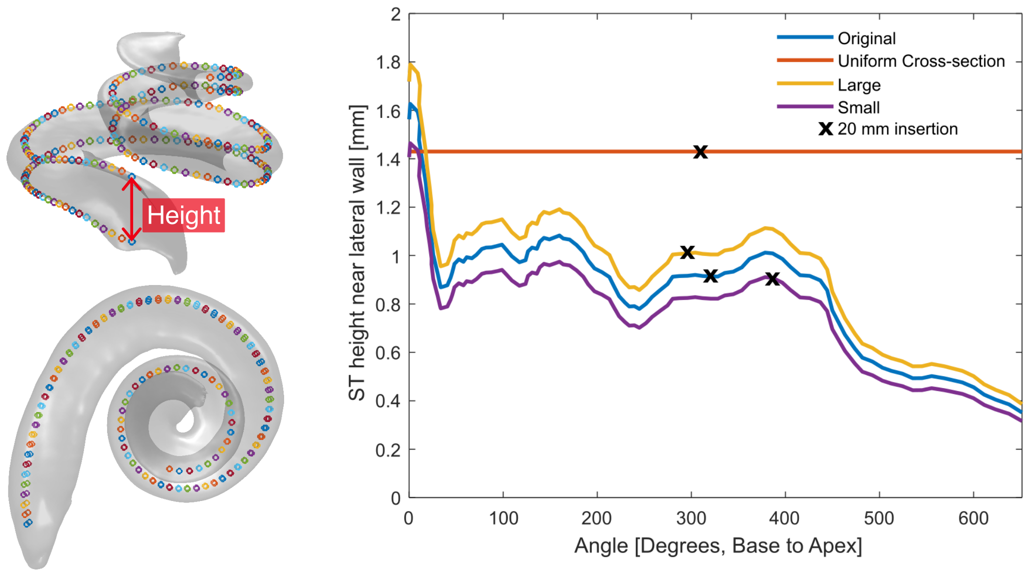

Figure 5.14 Height of selected ST models near the lateral wall. Representation of the points used to determine the height along the lateral wall (left) and quantification of the height in different models (right). Black cross represents 20 mm insertion distance with CI and its corresponding angular insertion depth in selected models.

5.4.3 Comparison with surgical approach

It should be noted that these experiments consisted of an insertion through a *scala tympani* with a fully open base rather than through a simulated round window or cochleostomy approach. Although not exactly the clinical approach, the round window anatomy can be very variable[101] and alters the angle of approach for the insertion. Therefore, by having a consistent insertion trajectory with an open base, it was possible to determine the influence of the ST size and shape on the insertion forces. This allowed the systematic determination of the contributors to the insertion force due to the ST shape. Future studies could focus on the angle approach of the CI insertion and the influence of many different segmentations of the cochlea and surgical approach rather than manipulating a single cochlea shape.

The amplitude range of the insertion forces measured in this study (approximately 50 – 200 mN) were within the range measured in the cadaveric specimen listed in the literature.[98,140,217,218,247] However, these forces strongly depend on the angular insertion depth, which is often not reported; the treatment of the cadaveric specimen (*e.g.*, a reduction in the endosteum – the soft tissue covering the inside of the ST lumen); and other parameters that might affect the coefficient of friction. Hence, it is difficult to compare the data with the published studies. Furthermore, no studies found used a Cochlear Slim Straight electrode as used in this study, which makes comparisons to the existing literature with different implants difficult. This supports the need for reporting insertion forces as a function of the angular insertion to ensure a fair comparison between studies (as discussed in Chapter 3).

5.4.4 Impact of vertical forces

The vertical forces exerted on the ST are important as they present a risk of damaging the basilar membrane and *organ of Corti* structures that are crucial in providing residual acoustic hearing. Therefore, measuring the effect of the force on the vertical z-axis could help determine the conditions of the increased risk of the basilar membrane damage and CI translocation between the *scala*, which can occur in up to 20 % of lateral wall electrode implantations.[92] The results show that the spatial frequency of the variation in the non-planarity of the basal turn seemed to have differing effects on the insertion force. However, there was a significant variation in the force measured, as the range of the forces was reaching the limit of the used sensor (a sensitivity of 1.5 mN for the z-axis). The vertical forces measured within this study are significantly lower (<5 mN) than those measured to rupture the partition, ranging from 42 to 122 mN,[111] which included the bony osseous spiral lamina as well as the basilar membrane. However, the scalar translocation will largely depend on the localised stress applied to the cochlear partition, with the basilar membrane being significantly less stiff than the bony osseous spiral lamina and, therefore, being damaged at much lower forces (see Chapter 2, Table 2.2).

5.4.5 Stress relaxation of cochlear implants

Another factor that is related to the overall insertion forces is the elastic stress held in the CI, which can cause the CI to extrude due to stress relaxation. Due to the stepper motor-assisted insertion, a force relaxation could be observed when the CI was held in position at maximum insertion. The ratio of the force at a fixed distance to the maximum force was consistent across the conditions with a median value of 0.69, except for the ‘small’ and ‘tight’ models where a full insertion could not be achieved and therefore not fully comparable, and the results were more valid (see Figure 5.15). This is likely related to the inherent elasticity of the implant, which refers to the natural resilience of the implant material that allows it to deform under stress and then return to its original shape when the stress is removed. This elasticity may vary across implant brands; hence, the same CI brand was used throughout this study to be consistent and eliminate the variability due to the implant mechanical properties. However, it was shown that there was no significant variability in the insertion force on the same model with repeated insertion (see Figure 5.16).

5.4.6 Consequences of capstan model

The basic Capstan equation has been used with significant success to understand the observed exponential behaviour of the cochlea insertion forces.[133] There are two particularly unintuitive observations, however, that have not been made.

The first consideration is that, for portions of the implant in contact with the ST wall, the bending stiffness does not affect the forces in that region. To see this, remember that

$$M = EI\kappa \tag{5.4}$$

where M is the bending moment, E is the elastic modulus, I is the second moment of the area, and κ is the local curvature. The equilibrium conditions for the infinitesimal body section when $d\phi \to 0$ in Figure 5.2 (B) can be given by balancing forces parallel

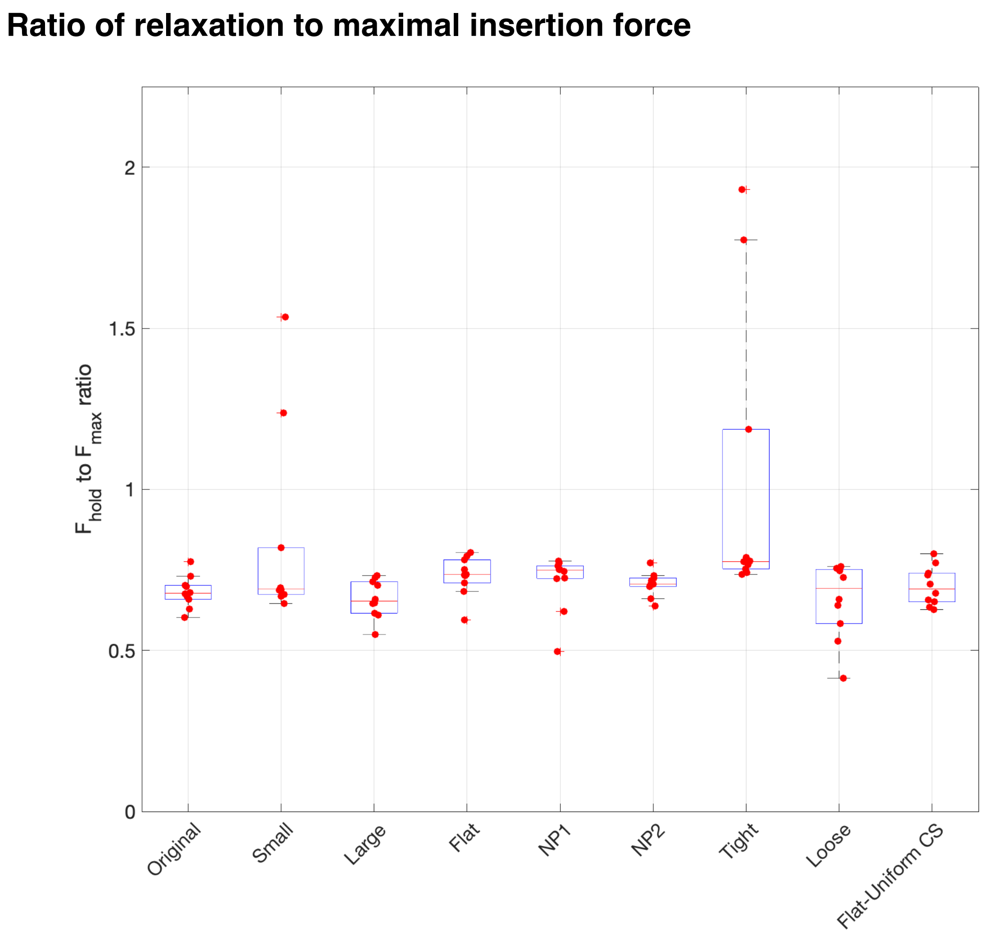

Figure 5.15 Ratio of relaxation for when CI held static post insertion (F_{hold}) to the maximal insertion force during insertion (F_{max}) for all models. Note that 'small' and 'tight' models were not fully inserted and have significant outliers and therefore are not comparable to other conditions.

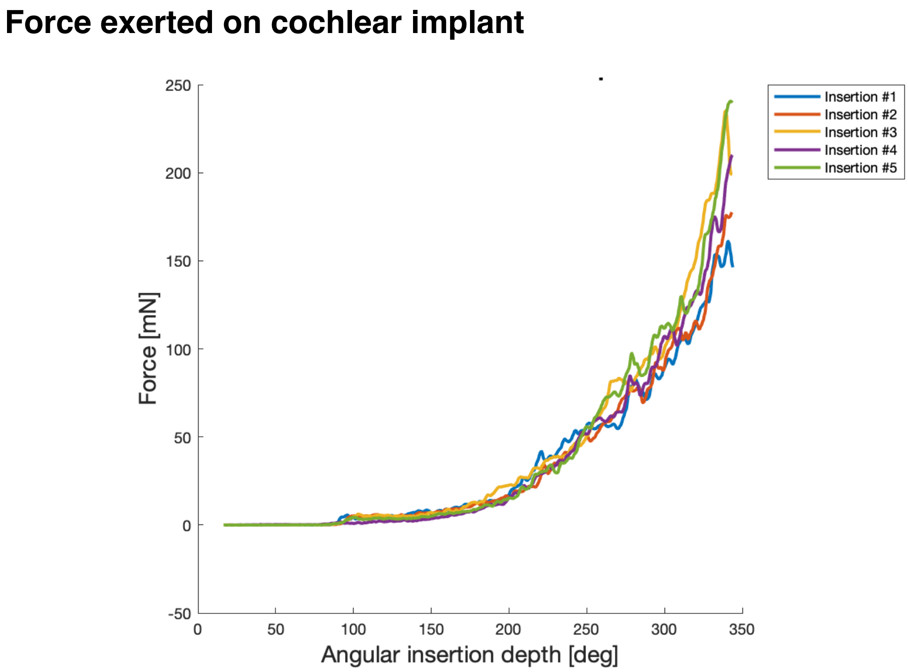

Figure 5.16 Example of the force exerted on the CI with five repeated insertions shows no trend indicating a significant change in implant intensity over repeated insertions. Note, plot displays the 'flat' condition which was randomly sampled throughout all 45+ measurements with this implant in the study.

(F) and normal (N) to the implant as well as the sum of the moments around the centre of the implant section.

$$dT + Qd\phi - dF = 0 \tag{5.5}$$

$$dQ - Td\phi - dN = 0 \tag{5.6}$$

$$dM - QRd\phi - rdF = 0 \tag{5.7}$$

where T is the tension in the implant ('tension' is being used rather than compression in order to remain consistent with the classical versions of the problem; note that tension and compression forces can be obtained from each other by changing a sign), Q is the shear force in the implant, R is the distance to the centroid of the implant, and r is the implant radius.

It can be seen from these equilibrium conditions that this term has no effect on the system solution as dM is zero for the locations of constant curvature. This counterintuitive fact was first noticed by Stuart *et al.*[298] for the classical Capstan problem and suggests that cochlea implant stiffness is not necessarily a limiting factor in the design. This comes with two major caveats, however.

Firstly, the bending moment does have a significant effect on the non-contact regions, such as at the base of the implant, and a stiffer implant may require a lateral constraint within a supportive stiff sheath.

Secondly, the bending moment does change which parts of the implant may be in contact. If the local tension/shear forces are not sufficient to hold the implant against the ST lateral wall, the forces will change.

Taken together, this suggests that the optimum implant stiffness profile is for a 'pyramid of stiffness', chosen to always be less than required to pull the implant away from the wall but great enough to maximise the steering control.

In the discussion above, we have made an implicit assumption based on the capstan model that the curvature remains constant throughout the interaction of the implant with the ST wall. However, the anatomical structure of the cochlea is a rising spiral, with the curvature being tighter towards the apical regions. This non-uniform curvature throughout the cochlea will lead to varying bending moments along different segments of the implant. It's crucial to acknowledge that as the curvature tightens, the insertion forces could vary, potentially resulting in increased friction or resistive forces in those regions. This variability could also influence the actual regions of the implant that come in contact with the ST wall. Understanding this non-constant curvature becomes essential when designing cochlear implants to ensure optimal interaction with the cochlear anatomy without causing damage. In light of this, while the capstan model provides invaluable insights, for more refined predictions, it might be necessary to incorporate the variable curvature of the cochlea.

Within the scope of the modified Capstan model, the role of the initial force, denoted as F_{tip}, is paramount. Variations in this parameter can alter the behaviour of the force curves due to its multiplicative effect, as formalised in Equation 5.3. As evidenced in Figure 5.7 (C), some level of variability in F_{tip} is observed across different experimental conditions. This variability could potentially stem from the repeated mechanical stress and consequent re-straightening of the implant between insertions. The tip of the implant is particularly delicate; composed of a single wire and electrode plate, it not only has a reduced diameter – narrowing from 0.6 mm to 0.3 mm – but also exhibits a heightened vulnerability to damage after successive insertions. During the critical juncture of the CI making initial contact with the ST lateral wall, the pliability of the tip leads to pronounced non-linearities in this region. While our model accounts for the interaction between F_{tip} and the lateral wall in a multiplicative fashion, it underscores the necessity to consider these variabilities when interpreting the forces during the initial stages of implantation.

Nevertheless, the second consideration is just as significant: the angular insertion depth, coefficient of friction, and tip forces are the only significant factors affecting the implant forces. Features such as the ST size, flatness, and profile are only minor in their impact. Particularly surprising is that the spiral geometry makes no difference at all in the model relative to the classical circular geometry used for a Capstan model. This suggests that the majority of the refinement effort in implant design should target the tip profiles and developing materials with low coefficients of friction.

In an intricate analysis of cochlear implant insertion dynamics, the force exerted on the implant adheres to an exponential trend in relation to the angular insertion depth, akin to the classical capstan problem. The adapted coefficient, denoted as μ', extends beyond the conventional coefficient of friction, encapsulating additional variables such as surface texture and the cochlear structure's complex geometry. Notably, the initial force at the implant's tip, F_{tip}, is approximately 3 mN, observed at the critical moment of contact with the cochlear wall. The exponential coefficient μ' is discerned to be around 0.017, indicating a subtler interaction than that implied by frictional components alone.

The mathematical examination juxtaposes the initial frictional moment against the bending moment requisite for the implant to align with the cochlea's curvature. The initial frictional moment, estimated using F_{tip} and the radius of the implant's tip r, is given by:

$$M_{f,initial} = F_{tip} \cdot r = 3 \times 10^{-3} \cdot 0.15 = 4.5 \times 10^{-4}\,\mathrm{N\,mm} \tag{5.8}$$

Simultaneously, the bending moment $M_{bending}$ necessary for the implant to conform to the cochlea's curvature was determined by the product of the implant's elastic modulus E, the second moment of area I, and the curvature κ (see Equation 5.4). Assuming the elastic modulus E to be approximately 182 MPa at the tip of the implant[299] and the second moment of area I for a cylindrical rod with a radius of 0.15 mm, the bending moment is expressed as:

$$M_{bending} = E \cdot I \cdot \kappa = 182 \cdot \frac{\pi \cdot 0.15^4}{4} \cdot \kappa \tag{5.9}$$

For the curvature κ, assumed as the reciprocal of a typical cochlear turn radius of 3.3 mm,[84] the resultant bending moment to match the cochlear curvature is:

$$M_{bending} = 2.19 \times 10^{-2}\,\mathrm{N\,mm} \tag{5.10}$$

In the initial stage of insertion, the cochlear implant encounters a minimal frictional moment, contrasted by a significantly larger bending moment necessitated by the cochlea's curvature. This disparity, with the frictional moment being two orders of magnitude lower, highlights the bending resistance as a primary design consideration. Nonetheless, a pivotal shift occurs as insertion depth increases: frictional resistance escalates exponentially, as evidenced in graphical data. This trend necessitates careful attention in the design process.

At a critical juncture during insertion, the frictional moment, increasing with depth, equals and eventually surpasses the bending moment. This transition, where frictional resistance becomes predominant, is crucial in cochlear implant design, marking the depth at which frictional forces become the primary challenge.

The design implications of these findings are complex. Initially, the implant tip must have a minimal bending moment; however, it should have a sufficient structural integrity to resist tip fold-over. Furthermore, as with the deeper insertion the frictional moment dominates, indicating the need for methods to lower the frictional coefficient. This could involve enhancing implant's surface properties with biocompatible lubricants or modifying material properties to balance stiffness and force exerted against cochlear walls. Furthermore, this transition point offers surgical insights, indicating when adjustments in insertion speed might be beneficial to counter increasing friction.

As the implant advances deeper into the cochlea, the frictional moment follows an exponential trajectory, as described by the modified Capstan equation. On the other hand, the bending moment increases only marginally due to the cochlea spiral shape. Figure 5.17 conceptually contrasts bending and frictional moments as functions of angular insertion depth, underscoring the growing significance of frictional forces in deeper insertion stages.

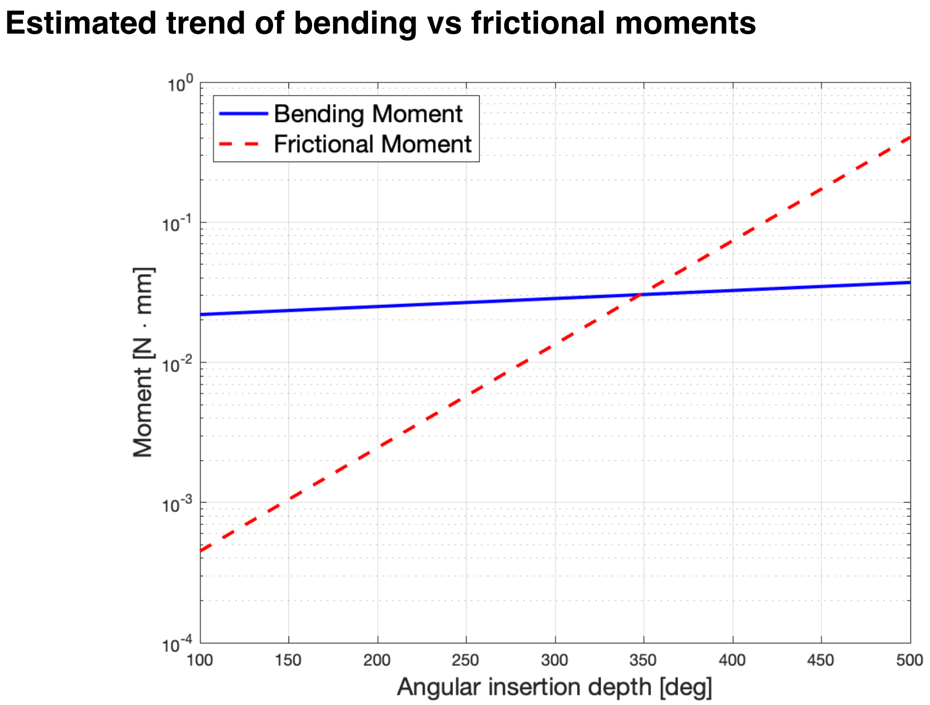

Figure 5.17 Estimated trend of bending vs frictional moments with angular insertion depth. The bending moment (blue) represents the moment required to maintain conformity with the cochlea's curvature, while the frictional moment (red dashed) depicts the exponentially increasing resistance based on the modified Capstan model. These estimates highlight the initial dominance of bending moments and the subsequent increasing importance of frictional moments as insertion depth progresses.

Overall, both graphical and mathematical analyses highlight the initial dominance of bending moments and the increasing relevance of frictional moments with deeper insertion. This emphasises the need for cochlear implants to be designed to manage both types of resistance, ensuring ease of insertion and structural integrity throughout the procedure.

5.4.7 Limitations of this study

Although this study represents one of the more detailed studies of cochlear implant forces to date, there are still limitations to this setup. The conclusions of the Capstan model and overall forces on the cochlea do not let us investigate the local stresses on the cochlea and the identification of the local 'hotspots' which could lead to localised insertion trauma. Therefore, there is a need for high-density force sensors that could be placed along the cochlea that could measure these localised forces. For instance, the buckling of the implant may push on the top and bottom surface of the ST and, therefore, cancel out forces measured with this setup.

5.5 Conclusion

In conclusion, after studying the parameters determining the CI insertion force, it is clear that accommodating for angular insertion depths accounts for most of the variation between the different ST geometries. Although the spatial frequency in the vertical trajectory of the basal turn may have a statistically significant effect on the insertion force, its small influence is unlikely to have a significant effect in surgery. These observations are summarised in Table 5.3.

Table 5.3 Summary of the effect of ST shape manipulation on cochlear insertion forces.

Manipulation of model	**Impact on insertion forces with respect to angular insertion depth**
Volume scaling	No statistically significant difference ($p > 0.05$)
Overall vertical trajectory/ rising spiral	No statistically significant difference ($p > 0.05$)
Basal turn non-planarity	Higher non-planarity may decrease insertion force due to less contact ($p > 0.01$)
Curvature	No statistically significant difference ($p > 0.05$)
Cross-section area	No statistically significant difference ($p > 0.05$)

This is promising in the pre-surgical planning of a CI insertion as even a basic analysis of the cochlear shape could feed into a predictive model of the insertion force and inform the decision of which CI and approach to use for a particular patient. Common measures such as the cochlear duct length and number of turns could be used to determine this angular insertion depth-to-distance relationship. Furthermore, to reduce insertion trauma, surgeons should consider implanting a CI to the same angular insertion depth rather than to a certain length of the implant. However, this comes with a trade-off between reducing trauma and achieving optimal CI electrode positioning to achieve effective neural stimulation. Additionally, the considerations within this paper relate to conventional straight electrodes that are positioned along the lateral wall rather than pre-curved electrodes which rely on the pre-tension to achieve a perimodiolar positioning.

By appreciating the consequences of the Capstan model that the tip force and coefficient of friction are the major determinants of the insertion force for a given angular insertion depth, it is clear that developing new CI tip designs and surface coatings to reduce friction will likely be most effective in reducing insertion trauma. Furthermore, the Capstan model shows that an increased stiffness of the implants may not increase the insertion forces so long as they do not affect the implant following the lateral wall.

By combining these insights to further understand the intracochlear forces during insertion, it may be possible to improve the CI insertion to provide an optimal electrical stimulation while minimising the trauma. This could improve CI users' outcomes by retaining more of their residual hearing that provides acoustic cues to improve their hearing. Additionally, by reducing the risks of the CI insertion, it could be possible to widen the eligibility of CIs to include those with less severe hearing loss to provide these benefits to a much wider patient population.

Chapter 6

Discussion

Cochlear implants have been a groundbreaking solution to severe-to-profound hearing loss, marking a significant stride in the field of medical technology. Yet, despite their transformative potential, these devices present certain challenges that limit their broader application. Throughout this research, I have delved into these challenges with a focus on how to produce accurate 3D printed models for research purposes, understanding the extent of hearing damage, studying the forces involved in insertion, and exploring the physical and anatomical properties of the cochlea. The aim of my research is to improve the effectiveness and reduce risks associated with cochlear implantation.

Cochlear implants require careful and precise placement to mitigate cochlear structure trauma and preserve any residual auditory function. The variables associated with implantation, such as insertion speed and depth, as well as the potential benefits of robotic assistance, were examined in a systematic review of existing literature (see Chapter 3). The analysis revealed that higher insertion speeds tend to increase insertion forces and intracochlear pressure in artificial cochlea models. Interestingly, this trend was absent in cadaveric studies. It is not clear if this is due to the differences in accuracy of measurements, where and how these variables were studied, and study volume. Clearly more work needs to be done in this area. Furthermore, robotic assistance did not significantly reduce maximal insertion forces compared to manual methods, suggesting that the benefits of robotic assistance may be limited to specific contexts (*e.g.*, hand tremor). These findings underscore the need for further investigation and standardisation in research methodologies to better understand the factors affecting cochlear implantation.

The surgical approach and implant type play an important role in mitigating intracochlear trauma during cochlear implantation. A systematic review of literature examining the round window and cochleostomy surgical approaches, as well as lateral wall and perimodiolar cochlear implant types, revealed useful insights. The round window approach was preferred in most studies, with trauma typically observed as a rupture of the basilar membrane, primarily found at 150° to 200° of angular insertion depth. The cochleostomy approach raised concerns due to a higher number of trauma instances at 0° to 50° of angular insertion depth. The majority of studies employed lateral wall cochlear implants, with the highest occurrence of trauma at level 3 (Eshraghi *et al.* scale)[216] and insertion depths of 150° to 200°. These findings highlight the significance of implant design and surgical approach in reducing cochlear trauma and enhancing patient outcomes.

A comprehensive literature review was carried out prior to the fabrication of the cochlear models, focusing also on the construction of artificial cochlea models and delving into the intricate anatomy of the cochlea (refer to Chapter 2). This review identified fundamental features of cochlear anatomy that should be accurately replicated in the artificial models. The insights gathered from this review were instrumental in guiding the fabrication process of the next generation of artificial cochlea models fabricated using SLA and DLP 3D printing technologies, a process which is detailed in Chapter 4. DLP technology with a 30 µm layer height, combined with acrylic coating, produced the most accurate and transparent models. These will be used as a training tool for surgeons and could also be used for R&D purposes for researchers and by major cochlear implant companies. Future research should aim to enhance the accuracy of the fabrication process and explore alternate 3D-printing technologies such as two-photon polymerisation for creating cochlea models with flexible membranes separating *scalae*.

Building on the success of fabricating accurate, transparent cochlear models, these were subjected to specific geometric alterations (see Chapter 5). The aim was to thoroughly probe the influence of distinct geometric parameters on the force exerted during cochlear implant insertion. Analysis revealed that certain factors, including overall size, curvature, vertical trajectory, and cross-sectional area, had minimal influence on the insertion force when the forces were normalised to an angular insertion depth. In addition to this, a Capstan-based model was established to characterise the cochlear implant insertion forces, presenting satisfactory alignment with the empirical data.

Unveiling the key implications of this research, several crucial points surfaced. Firstly, a comprehensive understanding of forces during CI insertion and their interaction with cochlear anatomy was gleaned. This provides valuable information in refining CI design and insertion methodologies, with the potential to minimise procedural damage and significantly improve patient outcomes. Secondly, the study's revelations on the primary factors influencing the implant forces – namely, angular insertion depth, coefficient of friction, and tip forces – together with the information about the trauma location during cochlear implant insertion (refer to Chapter 3), can collectively inform the design and fabrication process of cochlear implants. Notably, a positive correlation between the angular insertion depth and insertion force was also highlighted in Chapter 3. This advocates for design and implantation strategy endeavours to focus on optimising depth of insertion, tip profiles, and developing materials with lower coefficients of friction.

These insights could expedite the development of safer, more efficient cochlear implantation procedures, thereby reducing risks associated with structural damage to the ear and improving post-operative hearing outcomes. The study also offered a re-evaluation of cochlear implant stiffness, challenging the prevalent belief of it being an absolute design constraint. This finding could guide manufacturers towards a more focused allocation of resources during product development. Lastly, the research introduced a novel perspective on determinants of CI insertion forces, propelling a new trajectory for future research and development in this crucial area of audiology.

In conclusion, the research underscores the complex interplay of factors influencing the success and safety of cochlear implantation. The intertwined roles of insertion speed, depth, surgical approach, and implant design each have their part in mitigating cochlear trauma and optimising patient outcomes. The advent of accurate cochlear models using advanced 3D-printing technologies, coupled with a more profound understanding of geometrical parameters influencing insertion force, opens up promising avenues for future research and innovation in cochlear implantation procedures.

Chapter 7

Conclusion

This thesis presents promising results that explore and inform future avenues within the field of cochlear implantation, particularly relating to implantation procedures, research methodologies, and technological prospects, along with the theoretical foundations that guide them.

The comprehensive understanding achieved through this research, regarding the factors that influence the success of cochlear implantation, carries potential clinical significance. This work has shed light on the potential impact of various elements such as insertion speed, depth, surgical approach, and implant design on minimising cochlear trauma and enhancing surgical outcomes. Specifically, insights gained on the round window surgical approach and certain implant designs could serve as a catalyst for improvements in current clinical practices, offering a potentially optimised and more standardised procedure to benefit patients worldwide.

The thesis's emphasis on the importance of research standardisation is an echo of a wider recognition within the scientific community. The variability in implant types and measurement methodologies amongst research endeavours underscores the pressing need for consistent research parameters. This standardisation is crucial in facilitating accurate comparisons, thereby bolstering the comprehensive understanding of cochlear implantation procedures.

Furthermore, the exploration of 3D-printing technologies and their role in improving the healthcare sector opens a promising avenue for future investigations. The effectiveness of Digital Light Processing and Stereolithography Apparatus technologies in creating intricate cochlear models highlights the potential of these technologies to enhance pre-operative planning and surgical outcomes, not only in cochlear implantation but in a broader spectrum of surgical procedures.

In addition to these practical implications, the development of a novel theoretical framework – the Capstan-based model – offers a unique perspective on the relationship between cochlear implant insertion forces and cochlear trauma. This theoretical proposition sets a platform for the conception of new surgical techniques and opens opportunities for future research and development of new refined cochlear implants for atraumatic insertion.

In retrospect, this thesis underscores the importance of interdisciplinary collaboration between medical and technological research. Future endeavours in this field are encouraged to continue the exploration of 3D-printing technologies, to foster standardisation of research methodologies, and to delve further into the optimal techniques for cochlear implantation. Through this, it is anticipated that the field will move closer to the goal of improving patient outcomes in cochlear implantation, thereby enhancing the quality of life for individuals with hearing impairments.

References

1. Djourno, A. & Eyries, C. [Auditory prosthesis by means of a distant electrical stimulation of the sensory nerve with the use of an indwelt coiling]. *La Presse Medicale* **65,** 1417 (1957).
2. Djourno, A., Eyries, C. & Vallancien, B. [Electric excitation of the cochlear nerve in man by induction at a distance with the aid of micro-coil included in the fixture]. *Comptes Rendus Des Seances De La Societe De Biologie Et De Ses Filiales* **151,** 423–425 (1957).
3. Mudry, A. & Mills, M. The Early History of the Cochlear Implant: A Retrospective. *JAMA Otolaryngology–Head & Neck Surgery* **139,** 446–453 (2013).
4. Eshraghi, A. A., Nazarian, R., Telischi, F. F., Rajguru, S. M., Truy, E. & Gupta, C. The cochlear implant: Historical aspects and future prospects. *Anatomical record (Hoboken, N.J. : 2007)* **295,** 1967–1980 (2012).
5. Zeng, F.-G., Rebscher, S., Harrison, W. V., Sun, X. & Feng, H. Cochlear Implants:System Design, Integration and Evaluation. *IEEE reviews in biomedical engineering* **1,** 115–142 (2008).
6. Robles, L. & Ruggero, M. A. Mechanics of the Mammalian Cochlea. *Physiological reviews* **81,** 1305–1352 (2001).
7. NICE - Cochlear implants for people with severe to profound deafness https://www.nice.org.uk/guidance/ta566/chapter/1-Recommendations (2020).
8. Khoza-Shangase, K. & Gautschi-Mills, K. Exploration of factors influencing the preservation of residual hearing following cochlear implantation. *The South African Journal of Communication Disorders* **66** (2019).
9. Moteki, H., Nishio, S.-Y., Miyagawa, M., Tsukada, K., Noguchi, Y. & Usami, S.-I. Feasibility of hearing preservation for residual hearing with longer cochlear implant electrodes. *Acta Oto-Laryngologica* **138,** 1080–1085 (2018).
10. Gautschi-Mills, K., Khoza-Shangase, K. & Pillay, D. Preservation of residual hearing after cochlear implant surgery: an exploration of residual hearing function in a group of recipients at cochlear implant units. *Brazilian Journal of Otorhinolaryngology* **85,** 310–318 (2019).
11. Miranda, P. C., Sampaio, A. L. L., Lopes, R. A. F., Ramos Venosa, A. & Oliveira, C. A. C. P. d. Hearing Preservation in Cochlear Implant Surgery International Journal of Otolaryngology. https://www.hindawi.com/journals/ijoto/2014/468515/ (2020).

12. Roland, J. T. A Model for Cochlear Implant Electrode Insertion and Force Evaluation: Results with a New Electrode Design and Insertion Technique: *The Laryngoscope* **115,** 1325–1339 (2005).

13. Skarzyński, H., Lorens, A., D'Haese, P., Walkowiak, A., Piotrowska, A., Sliwa, L. & Anderson, I. Preservation of residual hearing in children and post-lingually deafened adults after cochlear implantation: an initial study. *ORL; journal for oto-rhino-laryngology and its related specialties* **64,** 247–253 (2002).

14. Balkany, T. J., Connell, S. S., Hodges, A. V., Payne, S. L., Telischi, F. F., Eshraghi, A. A., Angeli, S. I., Germani, R., Messiah, S. & Arheart, K. L. Conservation of Residual Acoustic Hearing After Cochlear Implantation. *Otology & Neurotology* **27,** 1083–1088 (2006).

15. Kopelovich, J. C., Reiss, L. A., Etler, C. P., Xu, L., Bertroche, J. T., Gantz, B. J. & Hansen, M. R. Hearing loss after activation of hearing preservation cochlear implants might be related to afferent cochlear innervation injury. *Otology & neurotology : official publication of the American Otological Society, American Neurotology Society [and] European Academy of Otology and Neurotology* **36,** 1035–1044 (2015).

16. Cosetti, M. K., Friedmann, D. R., Zhu, B. Z., Heman-Ackah, S. E., Fang, Y., Keller, R. G., Shapiro, W. H., Roland, J. T. & Waltzman, S. B. The Effects of Residual Hearing in Traditional Cochlear Implant Candidates After Implantation With a Conventional Electrode: *Otology & Neurotology* **34,** 516–521 (2013).

17. Irving, S., Gillespie, L., Richardson, R., Rowe, D., Fallon, J. B. & Wise, A. K. Electroacoustic Stimulation: Now and into the Future. *BioMed Research International* **2014,** e350504 (2014).

18. Li, C., Kuhlmey, M. & Kim, A. H. Electroacoustic Stimulation. *Otolaryngologic Clinics of North America.* Implantable Auditory Devices **52,** 311–322 (2019).

19. Gifford, R. H., Davis, T. J., Sunderhaus, L. W., Menapace, C., Buck, B., Crosson, J., O'Neill, L., Beiter, A. & Segel, P. Combined Electric and Acoustic Stimulation With Hearing Preservation: Effect of Cochlear Implant Low-Frequency Cutoff on Speech Understanding and Perceived Listening Difficulty. *Ear and Hearing* **38,** 539–553 (2017).

20. Ishiyama, A., Risi, F. & Boyd, P. Potential insertion complications with cochlear implant electrodes. *Cochlear Implants International,* 1–14 (2020).

21. Roland, P. S. & Wright, C. G. Surgical Aspects of Cochlear Implantation: Mechanisms of Insertional Trauma. *Cochlear and Brainstem Implants* **64,** 11–30 (2006).

22. Talbot, K. & Hartley, D. Combined electro-acoustic stimulation: a beneficial union? *Clinical Otolaryngology* **33,** 536–545 (2008).

23. Kontorinis, G., Lenarz, T., Stöver, T. & Paasche, G. Impact of the Insertion Speed of Cochlear Implant Electrodes on the Insertion Forces: *Otology & Neurotology* **32,** 565–570 (2011).

24. Banakis Hartl, R. M., Kaufmann, C., Hansen, M. R. & Tollin, D. J. Intracochlear Pressure Transients During Cochlear Implant Electrode Insertion: Effect of Micromechanical Control on Limiting Pressure Trauma. *Otology & Neurotology* **40,** 736–744 (2019).

25. Landsberger, D. M., Svrakic, S., Roland, J. T. & Svirsky, M. The Relationship between Insertion Angles, Default Frequency Allocations, and Spiral Ganglion Place Pitch in Cochlear Implants. *Ear and hearing* **36,** e207–e213 (2015).

26. Wright, C. G. & Roland, P. S. Vascular Trauma During Cochlear Implantation: A Contributor to Residual Hearing Loss? *Otology & Neurotology* **34,** 402–407 (2013).

27. Robey, A. B., Craig, C. A., Lyden, E. R. & Lusk, R. P. Effect of cochleostomy size on perilymph fistula control. *The Laryngoscope* **120,** 373–376 (2010).

28. Mancheño, M., Aristegui, M. & Sañudo, J. R. Round and Oval Window Anatomic Variability: Its Implication for the Vibroplasty Technique. *Otology & Neurotology* **38,** e50–e57 (2017).

29. Mittmann, P., Mittmann, M., Ernst, A. & Todt, I. Intracochlear Pressure Changes due to 2 Electrode Types: An Artificial Model Experiment. *Otolaryngology–Head and Neck Surgery* **156,** 712–716 (2017).

30. Hügl, S., Rülander, K., Lenarz, T., Majdani, O. & Rau, T. S. Investigation of ultra-low insertion speeds in an inelastic artificial cochlear model using custom-made cochlear implant electrodes. *European Archives of Oto-Rhino-Laryngology* **275,** 2947–2956 (2018).

31. Kesler, K., Dillon, N. P., Fichera, L. & Labadie, R. F. Human Kinematics of Cochlear Implant Surgery: An Investigation of Insertion Micro-Motions and Speed Limitations. *Otolaryngology–Head and Neck Surgery* **157,** 493–498 (2017).

32. Bachmaier, R., Encke, J., Obando-Leitón, M., Hemmert, W. & Bai, S. Comparison of Multi-Compartment Cable Models of Human Auditory Nerve Fibers. *Frontiers in Neuroscience* **13** (2019).

33. Torres, R., Jia, H., Drouillard, M., Bensimon, J.-L., Sterkers, O., Ferrary, E. & Nguyen, Y. An Optimized Robot-Based Technique for Cochlear Implantation to Reduce Array Insertion Trauma. *Otolaryngology–Head and Neck Surgery* **159,** 900–907 (2018).

34. Mittmann, P., Ernst, A. & Todt, I. Intracochlear Pressure Changes due to Round Window Opening: A Model Experiment. *The Scientific World Journal* **2014,** 1–7 (2014).

35. Mittmann, M., Ernst, A., Mittmann, P. & Todt, I. Insertional depth-dependent intracochlear pressure changes in a model of cochlear implantation. *Acta Oto-Laryngologica* **137,** 113–118 (2017).

36. Avci, E., Nauwelaers, T., Lenarz, T., Hamacher, V. & Kral, A. Variations in microanatomy of the human cochlea: Variations in microanatomy of the human cochlea. *Journal of Comparative Neurology* **522,** 3245–3261 (2014).

37. Heutink, F., de Rijk, S. R., Verbist, B. M., Huinck, W. J. & Mylanus, E. A. M. Angular Electrode Insertion Depth and Speech Perception in Adults With a Cochlear Implant: A Systematic Review. *Otology & neurotology : official publication of the American Otological Society, American Neurotology Society [and] European Academy of Otology and Neurotology* **40,** 900–910. PMID: 31135680 (2019).

38. Risi, F. Considerations and Rationale for Cochlear Implant Electrode Design - Past, Present and Future. *The Journal of International Advanced Otology* **14,** 382–391 (2019).

39. Verbist, B. M., Skinner, M. W., Cohen, L. T., Leake, P. A., James, C., Boëx, C., Holden, T. A., Finley, C. C., Roland, P. S., Roland, J. T., Haller, M., Patrick, J. F., Jolly, C. N., Faltys, M. A., Briaire, J. J. & Frijns, J. H. M. Consensus Panel on a Cochlear Coordinate System Applicable in Histologic, Physiologic, and Radiologic Studies of the Human Cochlea: *Otology & Neurotology* **31,** 722–730 (2010).

40. O'Connell, B. P., Cakir, A., Hunter, J. B., Francis, D. O., Noble, J. H., Labadie, R. F., Zuniga, G., Dawant, B. M., Rivas, A. & Wanna, G. B. Electrode Location and Angular Insertion Depth Are Predictors of Audiologic Outcomes in Cochlear Implantation: *Otology & Neurotology* **37,** 1016–1023 (2016).

41. Adunka, O. & Kiefer, J. Impact of electrode insertion depth on intracochlear trauma. *Otolaryngology–Head and Neck Surgery* **135,** 374–382 (2006).

42. Radeloff, A., Mack, M., Baghi, M., Gstoettner, W. K. & Adunka, O. F. Variance of angular insertion depths in free-fitting and perimodiolar cochlear implant electrodes. *Otology & Neurotology: Official Publication of the American Otological Society, American Neurotology Society [and] European Academy of Otology and Neurotology* **29,** 131–136 (2008).

43. Finley, C. C., Holden, T. A., Holden, L. K., Whiting, B. R., Chole, R. A., Neely, G. J., Hullar, T. E. & Skinner, M. W. Role of Electrode Placement as a Contributor to Variability in Cochlear Implant Outcomes: *Otology & Neurotology* **29,** 920–928 (2008).

44. Nadol, J. B., Young, Y.-S. & Glynn, R. J. Survival of Spiral Ganglion Cells in Profound Sensorineural Hearing Loss: Implications for Cochlear Implantation. *Annals of Otology, Rhinology & Laryngology* **98,** 411–416 (1989).

45. Lang, H. in The Primary Auditory Neurons of the Mammalian Cochlea (eds Dabdoub, A., Fritzsch, B., Popper, A. N. & Fay, R. R.) 229–262 (New York, NY, 2016).

46. Foggia, M. J., Quevedo, R. V. & Hansen, M. R. Intracochlear fibrosis and the foreign body response to cochlear implant biomaterials. *Laryngoscope Investigative Otolaryngology* **4,** 678–683 (2019).

47. Wilk, M., Hessler, R., Mugridge, K., Jolly, C., Fehr, M., Lenarz, T. & Scheper, V. Impedance Changes and Fibrous Tissue Growth after Cochlear Implantation Are Correlated and Can Be Reduced Using a Dexamethasone Eluting Electrode. *PLoS ONE* **11** (2016).

48. Stakhovskaya, O., Sridhar, D., Bonham, B. H. & Leake, P. A. Frequency Map for the Human Cochlear Spiral Ganglion: Implications for Cochlear Implants. *Journal of the Association for Research in Otolaryngology* **8,** 220–233 (2007).

49. Canfarotta, M. W., Dillon, M. T., Buss, E., Pillsbury, H. C., Brown, K. D. & O'Connell, B. P. Frequency-to-Place Mismatch: Characterizing Variability and the Influence on Speech Perception Outcomes in Cochlear Implant Recipients. *Ear & Hearing* **Publish Ahead of Print** (2020).

50. Adel, Y., Nagel, S., Weissgerber, T., Baumann, U. & Macherey, O. Pitch Matching in Cochlear Implant Users With Single-Sided Deafness: Effects of Electrode Position and Acoustic Stimulus Type. *Frontiers in Neuroscience* **13** (2019).

51. Briggs, R. J., Tykocinski, M., Xu, J., Risi, F., Svehla, M., Cowan, R., Stöver, T., Erfurt, P. & Lenarz, T. Comparison of Round Window and Cochleostomy Approaches with a Prototype Hearing Preservation Electrode. *Audiology and Neurotology* **11,** 42–48 (2006).

52. Zuniga, M. G., Rivas, A., Hedley-Williams, A., Gifford, R. H., Dwyer, R., Dawant, B. M., Sunderhaus, L. W., Hovis, K. L., Wanna, G. B., Noble, J. H. & Labadie, R. F. Tip Fold-over in Cochlear Implantation: Case Series. *Otology & Neurotology* **38,** 199–206 (2017).

53. O'Connell, B. P., Hunter, J. B. & Wanna, G. B. The importance of electrode location in cochlear implantation: Electrode Location in Cochlear Implantation. *Laryngoscope Investigative Otolaryngology* **1,** 169–174 (2016).

54. Huddle, M. G., Goman, A. M., Kernizan, F. C., Foley, D. M., Price, C., Frick, K. D. & Lin, F. R. The Economic Impact of Adult Hearing Loss: A Systematic Review. *JAMA otolaryngology– head & neck surgery* **143,** 1040–1048 (2017).

55. Holden, L. K., Finley, C. C., Firszt, J. B., Holden, T. A., Brenner, C., Potts, L. G., Gotter, B. D., Vanderhoof, S. S., Mispagel, K., Heydebrand, G. & Skinner, M. W. Factors Affecting Open-Set Word Recognition in Adults With Cochlear Implants: *Ear and Hearing* **34,** 342–360 (2013).

56. Durakovic, N., Kallogjeri, D., Wick, C. C., McJunkin, J. L., Buchman, C. A. & Herzog, J. Immediate and 1-Year Outcomes with a Slim Modiolar Cochlear Implant Electrode Array. *Otolaryngology–Head and Neck Surgery,* 019459982090733 (2020).

57. Connell, S. S., Balkany, T. J., Hodges, A. V., Telischi, F. F., Angeli, S. I. & Eshraghi, A. A. Electrode Migration After Cochlear Implantation: *Otology & Neurotology* **29,** 156–159 (2008).

58. Dietz, A., Wennström, M., Lehtimäki, A., Löppönen, H. & Valtonen, H. Electrode migration after cochlear implant surgery: more common than expected? *European Archives of Oto-Rhino-Laryngology* **273,** 1411–1418 (2016).

59. Rader, T., Baumann, U., Stöver, T., Weissgerber, T., Adel, Y., Leinung, M. & Helbig, S. Management of Cochlear Implant Electrode Migration: *Otology & Neurotology* **37,** e341–e348 (2016).

60. Adunka, O. F., Giardina, C. K., Formeister, E. J., Choudhury, B., Buchman, C. A. & Fitzpatrick, D. C. Round window electrocochleography before and after cochlear implant electrode insertion: Round Window Electrocochleography. *The Laryngoscope* **126,** 1193–1200 (2016).

61. Friesen, L. M., Shannon, R. V., Baskent, D. & Wang, X. Speech recognition in noise as a function of the number of spectral channels: Comparison of acoustic hearing and cochlear implants. *The Journal of the Acoustical Society of America* **110,** 1150–1163 (2001).

62. Helbig, S., Settevendemie, C., Mack, M., Baumann, U., Helbig, M. & Stöver, T. Evaluation of an Electrode Prototype for Atraumatic Cochlear Implantation in Hearing Preservation Candidates: Preliminary Results From a Temporal Bone Study. *Otology & Neurotology* **32,** 419–423 (2011).

63. WHO | Estimates WHO. http://www.who.int/deafness/estimates/en/ (2020).

64. Spitzer, E. R., Waltzman, S. B., Landsberger, D. M. & Friedmann, D. R. Acceptance and Benefits of Electro-Acoustic Stimulation for Conventional-Length Electrode Arrays. *Audiology and Neurotology* **26,** 17–26 (2021).
65. Dorman, M. F., Gifford, R. H., Spahr, A. J. & McKarns, S. A. The benefits of combining acoustic and electric stimulation for the recognition of speech, voice and melodies. *Audiology & Neuro-Otology* **13,** 105–112 (2008).
66. Incerti, P. V., Ching, T. Y. C. & Cowan, R. A systematic review of electric-acoustic stimulation: device fitting ranges, outcomes, and clinical fitting practices. *Trends in Amplification* **17,** 3–26 (2013).
67. Claussen, A. D., Quevedo, R. V., Mostaert, B., Kirk, J. R., Dueck, W. F. & Hansen, M. R. A mouse model of cochlear implantation with chronic electric stimulation. *PLOS ONE* **14,** e0215407 (2019).
68. Kretzmer, E. A., Meltzer, N. E., Haenggeli, C.-A. & Ryugo, D. K. An animal model for cochlear implants. *Archives of Otolaryngology–Head & Neck Surgery* **130,** 499–508 (2004).
69. Yi, H., Guo, W., Chen, W., Chen, L., Ye, J. & Yang, S. Miniature pigs: a large animal model of cochlear implantation. *American Journal of Translational Research* **8,** 5494–5502 (2016).
70. Jiang, C., de Rijk, S. R., Malliaras, G. G. & Bance, M. L. Electrochemical impedance spectroscopy of human cochleas for modeling cochlear implant electrical stimulus spread. *APL Materials* **8,** 091102 (2020).
71. De Rijk, S. R., Tam, Y. C., Carlyon, R. P. & Bance, M. L. Detection of Extracochlear Electrodes in Cochlear Implants with Electric Field Imaging/Transimpedance Measurements:: A Human Cadaver Study. *Ear and Hearing* **41,** 1196–1207 (2020).
72. Mittmann, P., Lauer, G., Ernst, A., Mutze, S., Hassepass, F., Arndt, S., Arweiler-Harbeck, D. & Christov, F. Electrophysiological detection of electrode fold-over in perimodiolar cochlear implant electrode arrays: a multi-center study case series. *European archives of oto-rhino-laryngology: official journal of the European Federation of Oto-Rhino-Laryngological Societies (EUFOS): affiliated with the German Society for Oto-Rhino-Laryngology - Head and Neck Surgery* **277,** 31–35 (2020).
73. Reiss, L. A., Kirk, J., Claussen, A. D. & Fallon, J. B. Animal Models of Hearing Loss after Cochlear Implantation and Electrical Stimulation. *Hearing Research* **426,** 108624 (2022).
74. Lei, I. M., Jiang, C., Lei, C. L., de Rijk, S. R., Tam, Y. C., Swords, C., Sutcliffe, M. P. F., Malliaras, G. G., Bance, M. & Huang, Y. Y. S. 3D printed biomimetic cochleae and machine learning co-modelling provides clinical informatics for cochlear implant patients. *Nature Communications* **12,** 6260 (2021).
75. Hallowell, D. & Silverman, R. Hearing and Deafness, 4th ed. *The Journal of the Acoustical Society of America* **65,** 867–867 (1979).
76. Pietsch, M., Aguirre Dávila, L., Erfurt, P., Avci, E., Lenarz, T. & Kral, A. Spiral Form of the Human Cochlea Results from Spatial Constraints. *Scientific Reports* **7,** 7500 (2017).

77. Manoussaki, D., Chadwick, R. S., Ketten, D. R., Arruda, J., Dimitriadis, E. K. & O'Malley, J. T. The influence of cochlear shape on low-frequency hearing. *Proceedings of the National Academy of Sciences of the United States of America* **105,** 6162–6166 (2008).

78. Su, W. Y., Marion, M. S., Hinojosa, R. & Matz, G. J. Anatomical measurements of the cochlear aqueduct, round window membrane, round window niche, and facial recess. *The Laryngoscope* **92,** 483–486 (1982).

79. Sahni, R. S., Paparella, M. M., Schachern, P. A., Goycoolea, M. V. & Le, C. T. Thickness of the Human Round Window Membrane in Different Forms of Otitis Media. *Archives of Otolaryngology - Head and Neck Surgery* **113,** 630–634 (1987).

80. Singla, A., Sahni, D., Gupta, A. K., Aggarwal, A. & Gupta, T. Surgical Anatomy of the Basal Turn of the Human Cochlea as Pertaining to Cochlear Implantation: *Otology & Neurotology* **36,** 323–328 (2015).

81. Jain, S., Gaurkar, S., Deshmukh, P. T., Khatri, M., Kalambe, S., Lakhotia, P., Chandravanshi, D. & Disawal, A. Applied anatomy of round window and adjacent structures of tympanum related to cochlear implantation. *Brazilian Journal of Otorhinolaryngology* **85,** 435–446 (2019).

82. Takahashi, M., Arai, Y., Sakuma, N., Yabuki, K., Sano, D., Nishimura, G., Oridate, N. & Usami, S.-i. Cochlear volume as a predictive factor for residual-hearing preservation after conventional cochlear implantation. *Acta Oto-Laryngologica* **138,** 345–350 (2018).

83. Yoo, S., Wang, G., Rubinstein, J. & Vannier, M. Three-dimensional geometric modeling of the cochlea using helico-spiral approximation. *IEEE Transactions on Biomedical Engineering* **47,** 1392–1402 (2000).

84. Clark, J. R., Warren, F. M. & Abbott, J. J. A Scalable Model for Human Scala-Tympani Phantoms. *Journal of Medical Devices* **5,** 014501 (2011).

85. Brochier, T., Schlittenlacher, J., Roberts, I., Goehring, T., Jiang, C., Vickers, D. & Bance, M. From Microphone to Phoneme: An End-to-End Computational Neural Model for Predicting Speech Perception With Cochlear Implants. *IEEE transactions on bio-medical engineering* **69,** 3300–3312 (2022).

86. Hrncirik, F., Roberts, I. V., Swords, C., Christopher, P. J., Chhabu, A., Gee, A. H. & Bance, M. L. Impact of Scala Tympani Geometry on Insertion Forces during Implantation. *Biosensors* **12,** 999 (2022).

87. Gee, A. H., Zhao, Y., Treece, G. M. & Bance, M. L. Practicable assessment of cochlear size and shape from clinical CT images. *Scientific Reports* **11,** 3448 (2021).

88. Koch, R. W., Ladak, H. M., Elfarnawany, M. & Agrawal, S. K. Measuring Cochlear Duct Length – a historical analysis of methods and results. *Journal of Otolaryngology - Head & Neck Surgery* **46,** 19 (2017).

89. Würfel, W., Lanfermann, H., Lenarz, T. & Majdani, O. Cochlear length determination using Cone Beam Computed Tomography in a clinical setting. *Hearing Research* **316,** 65–72 (2014).

90. Biedron, S., Westhofen, M. & Ilgner, J. On the Number of Turns in Human Cochleae: *Otology & Neurotology* **30,** 414–417 (2009).

91. Hardy, M. The length of the organ of Corti in man. *American Journal of Anatomy* **62,** 291–311 (1938).

92. Jwair, S., Prins, A., Wegner, I., Stokroos, R. J., Versnel, H. & Thomeer, H. G. X. M. Scalar Translocation Comparison Between Lateral Wall and Perimodiolar Cochlear Implant Arrays - A Meta-Analysis. *The Laryngoscope* **131,** 1358–1368 (2021).

93. Meenderink, S. W. F., Shera, C. A., Valero, M. D., Liberman, M. C. & Abdala, C. Morphological Immaturity of the Neonatal Organ of Corti and Associated Structures in Humans. *Journal of the Association for Research in Otolaryngology* **20,** 461–474 (2019).

94. De Fraissinette, A., Felix, H., Hoffmann, V., Johnsson, L.-G. & Gleeson, M. J. Human Reissner's Membrane in Patients with Age-Related Normal Hearing and with Sensorineural Hearing Loss. *ORL* **55,** 68–72 (1993).

95. Escudé, B., James, C., Deguine, O., Cochard, N., Eter, E. & Fraysse, B. The Size of the Cochlea and Predictions of Insertion Depth Angles for Cochlear Implant Electrodes. *Audiology and Neurotology* **11,** 27–33 (2006).

96. De Seta, D., Torres, R., Russo, F. Y., Ferrary, E., Kazmitcheff, G., Heymann, D., Amiaud, J., Sterkers, O., Bernardeschi, D. & Nguyen, Y. Damage to inner ear structure during cochlear implantation: Correlation between insertion force and radio-histological findings in temporal bone specimens. *Hearing Research* **344,** 90–97 (2017).

97. Aebischer, P., Mantokoudis, G., Weder, S., Anschuetz, L., Caversaccio, M. & Wimmer, W. In-Vitro Study of Speed and Alignment Angle in Cochlear Implant Electrode Array Insertions. *IEEE Transactions on Biomedical Engineering* **69,** 129–137 (2022).

98. Avci, E., Nauwelaers, T., Hamacher, V. & Kral, A. Three-Dimensional Force Profile During Cochlear Implantation Depends on Individual Geometry and Insertion Trauma: *Ear and Hearing* **38,** e168–e179 (2017).

99. Seliet, A., El Hamshary, A., El Refai, A., Ali, A. & Gabal, S. Human round window: morphometry and topographical anatomy and their effect on cochlear implantation. *Benha Medical Journal* **35,** 246 (2018).

100. Singla, A., Sahni, D., Gupta, A., Loukas, M. & Aggarwal, A. Surgical anatomy of round window and its implications for cochlear implantation: Surgical Anatomy of Round Window. *Clinical Anatomy* **27,** 331–336 (2014).

101. Cornwall, H. L., Marway, P. S. & Bance, M. A Micro-Computed Tomography Study of Round Window Anatomy and Implications for Atraumatic Cochlear Implant Insertion. *Otology & Neurotology: Official Publication of the American Otological Society, American Neurotology Society [and] European Academy of Otology and Neurotology* **42,** 327–334 (2021).

102. Angeli, R., Lavinsky, J., Setogutti, E. & Lavinsky, L. The Crista Fenestra and Its Impact on the Surgical Approach to the Scala Tympani during Cochlear Implantation. *Audiology and Neurotology* **22,** 50–55 (2017).

103. Meng, J., Li, S., Zhang, F., Li, Q. & Qin, Z. Cochlear Size and Shape Variability and Implications in Cochlear Implantation Surgery. *Otology & Neurotology: Official Publication of the American Otological Society, American Neurotology Society [and] European Academy of Otology and Neurotology* **37,** 1307–1313 (2016).

104. Wever, E. G. II The Width of the Basilar Membrane in Man. *Annals of Otology, Rhinology & Laryngology* **47,** 37–47 (1938).

105. Raufer, S., Idoff, C., Zosuls, A., Marino, G., Blanke, N., Bigio, I. J., O'Malley, J. T., Burgess, B. J., Nadol, J. B., Guinan, J. J. & Nakajima, H. H. Anatomy of the Human Osseous Spiral Lamina and Cochlear Partition Bridge: Relevance for Cochlear Partition Motion. *Journal of the Association for Research in Otolaryngology* (2020).

106. Liu, W., Atturo, F., Aldaya, R., Santi, P., Cureoglu, S., Obwegeser, S., Glueckert, R., Pfaller, K., Schrott-Fischer, A. & Rask-Andersen, H. Macromolecular organization and fine structure of the human basilar membrane - Relevance for cochlear implantation. *Cell and Tissue Research* **360,** 245–262 (2015).

107. Helpard, L., Li, H., Rask-Andersen, H., Ladak, H. M. & Agrawal, S. K. Characterization of the human helicotrema: implications for cochlear duct length and frequency mapping. *Journal of Otolaryngology - Head & Neck Surgery* **49,** 2 (2020).

108. Demarcy, T., Vandersteen, C., Guevara, N., Raffaelli, C., Gnansia, D., Ayache, N. & Delingette, H. Automated analysis of human cochlea shape variability from segmented micro CT images. *Computerized Medical Imaging and Graphics* **59,** 1–12 (2017).

109. Ishii, T., Takayama, M. & Takahashi, Y. Mechanical Properties of Human Round Window, Basilar and Reissner's Membranes. *Acta Oto-Laryngologica* **115,** 78–82 (sup519 1995).

110. Zhang, X. & Gan, R. Z. Dynamic Properties of Human Round Window Membrane in Auditory Frequencies. *Medical engineering & physics* **35,** 310–318 (2013).

111. Schuster, D., Kratchman, L. B. & Labadie, R. F. Characterization of Intracochlear Rupture Forces in Fresh Human Cadaveric Cochleae. *Otology & Neurotology* **36,** 657–661 (2015).

112. Baumann, S. B., Wozny, D. R., Kelly, S. K. & Meno, F. M. The electrical conductivity of human cerebrospinal fluid at body temperature. *IEEE transactions on bio-medical engineering* **44,** 220–223 (1997).

113. Pile, J., Sweeney, A. D., Kumar, S., Simaan, N. & Wanna, G. B. Detection of modiolar proximity through bipolar impedance measurements: Bipolar Electrical Impedance. *The Laryngoscope* **127,** 1413–1419 (2017).

114. Briaire, J. J. & Frijns, J. H. M. Field patterns in a 3D tapered spiral model of the electrically stimulated cochlea. *Hearing Research* **148,** 18–30 (2000).

115. Von Békésy, G. & Peake, W. T. *Experiments in Hearing. The Journal of the Acoustical Society of America* **88,** 2905–2905 (1990).

116. Potrusil, T., Heshmat, A., Sajedi, S., Wenger, C., Johnson Chacko, L., Glueckert, R., Schrott-Fischer, A. & Rattay, F. Finite element analysis and three-dimensional reconstruction of tonotopically aligned human auditory fiber pathways: A computational environment for modeling electrical stimulation by a cochlear implant based on micro-CT. *Hearing Research* **393,** 108001 (2020).

117. Malherbe, T. K., Hanekom, T. & Hanekom, J. J. The effect of the resistive properties of bone on neural excitation and electric fields in cochlear implant models. *Hearing Research* **327,** 126–135 (2015).

118. Albuquerque, A. A. S., Rossato, M., de Oliveira, J. A. A. & Hyppolito, M. A. Understanding the anatomy of ears from guinea pigs and rats and its use in basic otologic research. *Brazilian Journal of Otorhinolaryngology* **75,** 43–49 (2009).

119. Honeder, C., Ahmadi, N., Kramer, A.-M., Zhu, C., Saidov, N. & Arnoldner, C. Cochlear Implantation in the Guinea Pig. *Journal of Visualized Experiments : JoVE* (2018).

120. Heffner, H. E. & Heffner, R. S. Hearing ranges of laboratory animals. *Journal of the American Association for Laboratory Animal Science* **46,** 20–22 (2007).

121. Trevino, M., Lobarinas, E., Maulden, A. C. & Heinz, M. G. The chinchilla animal model for hearing science and noise-induced hearing loss. *The Journal of the Acoustical Society of America* **146,** 3710–3732 (2019).

122. Koehler, K. R., Nie, J., Longworth-Mills, E., Liu, X.-P., Lee, J., Holt, J. R. & Hashino, E. Generation of inner ear organoids containing functional hair cells from human pluripotent stem cells. *Nature Biotechnology* **35,** 583–589 (2017).

123. Mellott, A. J., Shinogle, H. E., Nelson-Brantley, J. G., Detamore, M. S. & Staecker, H. Exploiting decellularized cochleae as scaffolds for inner ear tissue engineering. *Stem Cell Research & Therapy* **8,** 41 (2017).

124. Chang, B., Cornett, A., Nourmohammadi, Z., Law, J., Weld, B., Crotts, S. J., Hollister, S. J., Lombaert, I. M. & Zopf, D. A. Hybrid 3D-Printed Ear Tissue Scaffold with Autologous Cartilage Mitigates Soft Tissue Complications. *The Laryngoscope* **131,** 1008–1015 (2021).

125. Aleemardani, M., Bagher, Z., Farhadi, M., Chahsetareh, H., Najafi, R., Eftekhari, B. & Seifalian, A. Can Tissue Engineering Bring Hope to the Development of Human Tympanic Membrane? *Tissue Engineering Part B: Reviews* **27,** 572–589 (2021).

126. Al-Qurayshi, Z., Wafa, E. I., Rossi Meyer, M. K., Owen, S. & Salem, A. K. Tissue Engineering the Pinna: Comparison and Characterization of Human Decellularized Auricular Biological Scaffolds. *ACS Applied Bio Materials* **4,** 7234–7242 (2021).

127. Rattay, F., Leao, R. N. & Felix, H. A model of the electrically excited human cochlear neuron. II. Influence of the three-dimensional cochlear structure on neural excitability. *Hearing Research* **153,** 64–79 (2001).

128. Ni, G., Elliott, S. J., Ayat, M. & Teal, P. D. Modelling Cochlear Mechanics. *BioMed Research International* **2014,** 150637 (2014).

129. Areias, B., Parente, M. P. L., Gentil, F. & Natal Jorge, R. M. Finite element modelling of the surgical procedure for placement of a straight electrode array: Mechanical and clinical consequences. *Journal of Biomechanics* **129,** 110812 (2021).

130. Hendricks, C. M., Cavilla, M. S., Usevitch, D. E., Bruns, T. L., Riojas, K. E., Leon, L., Webster, R. J., Warren, F. M. & Abbott, J. J. Magnetic Steering of Robotically Inserted Lateral-wall Cochlear-implant Electrode Arrays Reduces Forces on the Basilar Membrane In Vitro. *Otology & Neurotology* **Publish Ahead of Print** (2021).

131. Leon, L., Cavilla, M. S., Doran, M. B., Warren, F. M. & Abbott, J. J. Scala-Tympani Phantom With Cochleostomy and Round-Window Openings for Cochlear-Implant Insertion Experiments. *Journal of Medical Devices* **8,** 041010 (2014).

132. Nguyen, Y., Bernardeschi, D., Kazmitcheff, G., Miroir, M., Vauchel, T., Ferrary, E. & Sterkers, O. Effect of Embedded Dexamethasone in Cochlear Implant Array on Insertion Forces in an Artificial Model of Scala Tympani: *Otology & Neurotology* **36,** 354–358 (2015).

133. Kobler, J.-P., Dhanasingh, A., Kiran, R., Jolly, C. & Ortmaier, T. Cochlear Dummy Electrodes for Insertion Training and Research Purposes: Fabrication, Mechanical Characterization, and Experimental Validation. *BioMed Research International* **2015,** 1–9 (2015).

134. Wanna, G. B., Noble, J. H., Gifford, R. H., Dietrich, M. S., Sweeney, A. D., Zhang, D., Dawant, B. M., Rivas, A. & Labadie, R. F. Impact of Intrascalar Electrode Location, Electrode Type, and Angular Insertion Depth on Residual Hearing in Cochlear Implant Patients: Preliminary Results. **36,** 6 (2015).

135. Nordfalk, K. F., Rasmussen, K., Hopp, E., Greisiger, R. & Jablonski, G. E. Scalar position in cochlear implant surgery and outcome in residual hearing and the vestibular system. *International Journal of Audiology* **53,** 121–127 (2014).

136. Knoll, R. M., Trakimas, D. R., Wu, M. J., Lubner, R. J., Nadol, J. B., Ishiyama, A., Santos, F., Jung, D. H., Remenschneider, A. K. & Kozin, E. D. Intracochlear New Fibro-Ossification and Neuronal Degeneration Following Cochlear Implant Electrode Translocation: Long-Term Histopathological Findings in Humans. *Otology & Neurotology* **43,** e153–e164 (2022).

137. Cooperstein, I., Layani, M. & Magdassi, S. 3D printing of porous structures by UV-curable O/W emulsion for fabrication of conductive objects. *Journal of Materials Chemistry C* **3,** 2040–2044 (2015).

138. Mu, X., Bertron, T., Dunn, C., Qiao, H., Wu, J., Zhao, Z., Saldana, C. & Qi, H. J. Porous polymeric materials by 3D printing of photocurable resin. *Materials Horizons* **4,** 442–449 (2017).

139. Rebscher, S. J., Talbot, N., Bruszewski, W., Heilmann, M., Brasell, J. & Merzenich, M. M. A transparent model of the human scala tympani cavity. *Journal of Neuroscience Methods* **64,** 105–114 (1996).

140. Bruns, T. L., Riojas, K. E., Ropella, D. S., Cavilla, M. S., Petruska, A. J., Freeman, M. H., Labadie, R. F., Abbott, J. J. & Webster, R. J. Magnetically Steered Robotic Insertion of Cochlear-Implant Electrode Arrays: System Integration and First-In-Cadaver Results. *IEEE Robotics and Automation Letters* **5,** 2240–2247 (2020).

141. Majdani, O., Schurzig, D., Hussong, A., Rau, T., Wittkopf, J., Lenarz, T. & Labadie, R. F. Force measurement of insertion of cochlear implant electrode arrays in vitro: comparison of surgeon to automated insertion tool. *Acta Oto-Laryngologica* **130,** 31–36 (2010).

142. Carraro, M., Negandhi, J., Kuthubutheen, J., Propst, E. J., Kus, L., Lin, V. Y. W. & Harrison, R. V. Attenuating Cardiac Pulsations within the Cochlea: Structure and Function of Tortuous Vessels Feeding Stria Vascularis. *ISRN Otolaryngology* **2013,** 1–7 (2013).

143. Carraro, M., Park, A. H. & Harrison, R. V. Partial corrosion casting to assess cochlear vasculature in mouse models of presbycusis and CMV infection. *Hearing Research* **332,** 95–103 (2016).

144. Narasimhan, N., Riojas, K. E., Bruns, T. L., Mitchell, J. E., Webster, R. J. & Labadie, R. F. A Simple Manual Roller Wheel Insertion Tool for Electrode Array Insertion in Minimally Invasive Cochlear Implant Surgery. in. 2019 Design of Medical Devices Conference (Minneapolis, Minnesota, USA, 2019), V001T06A003.

145. Esmailie, F., Francoeur, M. & Ameel, T. Experimental Validation of a Three-Dimensional Heat Transfer Model Within the Scala Tympani With Application to Magnetic Cochlear Implant Surgery. *IEEE Transactions on Biomedical Engineering* **68,** 2821–2832 (2021).

146. Patpatiya, P., Chaudhary, K., Shastri, A. & Sharma, S. A review on polyjet 3D printing of polymers and multi-material structures. *Proceedings of the Institution of Mechanical Engineers, Part C: Journal of Mechanical Engineering Science* **236,** 7899–7926 (2022).

147. Chen, X., Chen, G., Wang, G., Zhu, P. & Gao, C. Recent Progress on 3D-Printed Polylactic Acid and Its Applications in Bone Repair. *Advanced Engineering Materials* **22,** 1901065 (2020).

148. Prendergast, M. E. & Burdick, J. A. Recent Advances in Enabling Technologies in 3D Printing for Precision Medicine. *Advanced Materials* **32,** 1902516 (2020).

149. Todd, C., Naghdy, F. & Svehla, M. Force Application During Cochlear Implant Insertion: An Analysis for Improvement of Surgeon Technique. *IEEE Transactions on Biomedical Engineering* **54,** 1247–1255 (2007).

150. Kha, H. N. & Chen, B. K. Determination of frictional conditions between electrode array and endosteum lining for use in cochlear implant models. *Journal of Biomechanics* **39,** 1752–1756 (2006).

151. İlik, B., Koyuncuoğlu, A., Şardan-Sukas, Ö. & Külah, H. Thin film piezoelectric acoustic transducer for fully implantable cochlear implants. *Sensors and Actuators A: Physical* **280,** 38–46 (2018).

152. Inaoka, T., Shintaku, H., Nakagawa, T., Kawano, S., Ogita, H., Sakamoto, T., Hamanishi, S., Wada, H. & Ito, J. Piezoelectric materials mimic the function of the cochlear sensory epithelium. *Proceedings of the National Academy of Sciences* **108,** 18390–18395 (2011).

153. Jang, J., Lee, J., Woo, S., Sly, D. J., Campbell, L. J., Cho, J.-H., O'Leary, S. J., Park, M.-H., Han, S., Choi, J.-W., Jang, J. H. & Choi, H. A microelectromechanical system artificial basilar membrane based on a piezoelectric cantilever array and its characterization using an animal model. *Scientific Reports* **5,** 12447 (2015).

154. Zhao, C., Knisely, K. E., Colesa, D. J., Pfingst, B. E., Raphael, Y. & Grosh, K. Voltage readout from a piezoelectric intracochlear acoustic transducer implanted in a living guinea pig. *Scientific Reports* **9,** 3711 (2019).

155. Tsuji, T., Nakayama, A., Yamazaki, H. & Kawano, S. Artificial Cochlear Sensory Epithelium with Functions of Outer Hair Cells Mimicked Using Feedback Electrical Stimuli. *Micromachines* **9** (2018).

156. Mukherjee, N., Roseman, R. D. & Willging, J. P. The piezoelectric cochlear implant: concept, feasibility, challenges, and issues. *Journal of Biomedical Materials Research* **53,** 181–187 (2000).

157. Calero, D., Paul, S., Gesing, A., Alves, F. & Cordioli, J. A. A technical review and evaluation of implantable sensors for hearing devices. *BioMedical Engineering OnLine* **17,** 23 (2018).

158. Jang, J., Lee, J., Jang, J. H. & Choi, H. A Triboelectric-Based Artificial Basilar Membrane to Mimic Cochlear Tonotopy. *Advanced Healthcare Materials* **5,** 2481–2487 (2016).

159. Liu, Y., Zhu, Y., Liu, J., Zhang, Y., Liu, J. & Zhai, J. Design of Bionic Cochlear Basilar Membrane Acoustic Sensor for Frequency Selectivity Based on Film Triboelectric Nanogenerator. *Nanoscale Research Letters* **13,** 191 (2018).

160. Simoni, E., Gentilin, E., Candito, M., Borile, G., Romanato, F., Chicca, M., Nordio, S., Aspidistria, M., Martini, A., Cazzador, D. & Astolfi, L. Immune Response After Cochlear Implantation. *Frontiers in Neurology* **11** (2020).

161. Claussen, A. D., Quevedo, R. V., Kirk, J. R., Higgins, T., Mostaert, B., Rahman, M. T., Oleson, J., Hernandez, R., Hirose, K. & Hansen, M. R. Chronic cochlear implantation with and without electric stimulation in a mouse model induces robust cochlear influx of CX3CR1+/GFP macrophages. *Hearing Research* **426,** 108510 (2022).

162. DeMason, C., Choudhury, B., Ahmad, F., Fitzpatrick, D. C., Wang, J., Buchman, C. A. & Adunka, O. F. Electrophysiological Properties of Cochlear Implantation in the Gerbil Using a Flexible Array. *Ear and hearing* **33,** 534–542 (2012).

163. Hartley, D. E. H., Vongpaisal, T., Xu, J., Shepherd, R. K., King, A. J. & Isaiah, A. Bilateral cochlear implantation in the ferret: A novel animal model for behavioral studies. *Journal of Neuroscience Methods* **190,** 214–228 (2010).

164. King, J., Shehu, I., Roland, J. T., Svirsky, M. A. & Froemke, R. C. A physiological and behavioral system for hearing restoration with cochlear implants. *Journal of Neurophysiology* **116,** 844–858 (2016).

165. Guo, W., Yi, H., Ren, L., Chen, L., Zhao, L., Sun, W. & Yang, S.-M. The Morphology and Electrophysiology of the Cochlea of the Miniature Pig. *The Anatomical Record* **298,** 494–500 (2015).

166. Keppeler, D., Kampshoff, C. A., Thirumalai, A., Duque-Afonso, C. J., Schaeper, J. J., Quilitz, T., Töpperwien, M., Vogl, C., Hessler, R., Meyer, A., Salditt, T. & Moser, T. Multiscale photonic imaging of the native and implanted cochlea. *Proceedings of the National Academy of Sciences* **118,** e2014472118 (2021).

167. Johnson, L. A., Della Santina, C. C. & Wang, X. Temporal bone characterization and cochlear implant feasibility in the common marmoset (Callithrix jacchus). *Hearing Research* **290,** 37–44 (2012).

168. Lu, W., Xu, J. & Shepherd, R. K. Cochlear implantation in rats: A new surgical approach. *Hearing Research* **205,** 115–122 (2005).

169. Rebscher, S. J., Hetherington, A. M., Snyder, R. L., Leake, P. A. & Bonham, B. H. Design and fabrication of multichannel cochlear implants for animal research. *Journal of Neuroscience Methods* **166,** 1–12 (2007).

170. Usevitch, D. E., Park, A. H., Scheper, V. & Abbott, J. J. Estimating the Pose of a Guinea-pig Cochlea Without Medical Imaging. *Otology & Neurotology* **42,** e1219–e1226 (2021).
171. Rattay, F., Potrusil, T., Wenger, C., Wise, A. K., Glueckert, R. & Schrott-Fischer, A. Impact of Morphometry, Myelinization and Synaptic Current Strength on Spike Conduction in Human and Cat Spiral Ganglion Neurons. *PLoS ONE* **8,** e79256 (2013).
172. Schnabl, J., Glueckert, R., Feuchtner, G., Recheis, W., Potrusil, T., Kuhn, V., Wolf-Magele, A., Riechelmann, H. & Sprinzl, G. M. Sheep as a large animal model for middle and inner ear implantable hearing devices: a feasibility study in cadavers. *Otology & Neurotology: Official Publication of the American Otological Society, American Neurotology Society [and] European Academy of Otology and Neurotology* **33,** 481–489 (2012).
173. Marx, M., Girard, P., Escudé, B., Barone, P., Fraysse, B. & Deguine, O. Cochlear Implantation Feasibility in Rhesus Macaque Monkey: Anatomic and Radiologic Results. *Otology & Neurotology* **34,** e76–e81 (2013).
174. West, C. D. The relationship of the spiral turns of the cochlea and the length of the basilar membrane to the range of audible frequencies in ground dwelling mammals. *The Journal of the Acoustical Society of America* **77,** 1091–1101 (1985).
175. Jwair, S., Versnel, H., Stokroos, R. J. & Thomeer, H. G. X. M. The effect of the surgical approach and cochlear implant electrode on the structural integrity of the cochlea in human temporal bones. *Scientific Reports* **12,** 17068 (2022).
176. Kaufmann, C. R., Henslee, A. M., Claussen, A. & Hansen, M. R. Evaluation of Insertion Forces and Cochlea Trauma Following Robotics-Assisted Cochlear Implant Electrode Array Insertion. *Otology & Neurotology* **41,** 631–638 (2020).
177. Hoppe, U., Brademann, G., Stöver, T., Miguel, A. R. d., Cowan, R., Manrique, M., Falcón-González, J. C., Hey, M., Baumann, U., Huarte, A., Liebscher, T., Bennett, C., English, R., Neben, N. & Macías, A. R. Evaluation of a Transimpedance Matrix Algorithm to Detect Anomalous Cochlear Implant Electrode Position. *Audiology and Neurotology* **27,** 347–355 (2022).
178. Leblans, M., Sismono, F., Vanpoucke, F., van Dinther, J., Lerut, B., Kuhweide, R., Offeciers, E. & Zarowski, A. Novel Impedance Measures as Biomarker for Intracochlear Fibrosis. *Hearing Research* **426,** 108563 (2022).
179. Swaddiwudhipong, N., Jiang, C., Landry, T. G. & Bance, M. Investigating the Electrical Properties of Different Cochlear Implants. *Otology & Neurotology* **42,** 59–67 (2021).
180. Garcia, C., Goehring, T., Cosentino, S., Turner, R. E., Deeks, J. M., Brochier, T., Rughooputh, T., Bance, M. & Carlyon, R. P. The Panoramic ECAP Method: Estimating Patient-Specific Patterns of Current Spread and Neural Health in Cochlear Implant Users. *Journal of the Association for Research in Otolaryngology: JARO* **22,** 567–589 (2021).
181. Garcia, C., Deeks, J. M., Goehring, T., Borsetto, D., Bance, M. & Carlyon, R. P. SpeedCAP: An Efficient Method for Estimating Neural Activation Patterns Using Electrically Evoked Compound Action-Potentials in Cochlear Implant Users. *Ear and Hearing* (2022).

182. Cohen, L. T., Richardson, L. M., Saunders, E. & Cowan, R. S. C. Spatial spread of neural excitation in cochlear implant recipients: comparison of improved ECAP method and psychophysical forward masking. *Hearing Research* **179,** 72–87 (2003).

183. Brown, C. J., Hughes, M. L., Luk, B., Abbas, P. J., Wolaver, A. & Gervais, J. The relationship between EAP and EABR thresholds and levels used to program the nucleus 24 speech processor: data from adults. *Ear and Hearing* **21,** 151–163 (2000).

184. Di Stadio, A., Dipietro, L., De Lucia, A., Trabalzini, F., Ricci, G., Martines, F., Pastore, V. & Volpe, A. d. E-ABR in Patients with Cochlear Implant: A Comparison between Patients with Malformed Cochlea and Normal Cochlea. *The Journal of International Advanced Otology* **15,** 215–221 (2019).

185. Tissue engineering - Latest research and news | Nature https://www.nature.com/subjects/tissue-engineering (2020).

186. Souza, P. Compression: From Cochlea to Cochlear Implants. *Ear and Hearing* **25,** 510–511 (2004).

187. Groves, A. K. & Fekete, D. M. in Understanding the Cochlea (eds Manley, G. A., Gummer, A. W., Popper, A. N. & Fay, R. R.) 33–73 (Cham, 2017).

188. The Primary Auditory Neurons of the Mammalian Cochlea (eds Dabdoub, A., Fritzsch, B., Popper, A. N. & Fay, R. R.) (New York, NY, 2016).

189. Meas, S. J., Nishimura, K., Scheibinger, M. & Dabdoub, A. In vitro Methods to Cultivate Spiral Ganglion Cells, and Purification of Cellular Subtypes for Induced Neuronal Reprogramming. *Frontiers in Neuroscience* **12** (2018).

190. Radotić, V., Bedalov, A., Drviš, P., Braeken, D. & Kovačić, D. Guided growth with aligned neurites in adult spiral ganglion neurons cultured *in vitro* on silicon micro-pillar substrates. *Journal of Neural Engineering* **16,** 066037 (2019).

191. Gunewardene, N., Crombie, D., Dottori, M. & Nayagam, B. A. Innervation of Cochlear Hair Cells by Human Induced Pluripotent Stem Cell-Derived Neurons *In Vitro*. *Stem Cells International* **2016,** 1–10 (2016).

192. Hosoya, M., Fujioka, M., Sone, T., Okamoto, S., Akamatsu, W., Ukai, H., Ueda, H. R., Ogawa, K., Matsunaga, T. & Okano, H. Cochlear Cell Modeling Using Disease-Specific iPSCs Unveils a Degenerative Phenotype and Suggests Treatments for Congenital Progressive Hearing Loss. *Cell Reports* **18,** 68–81 (2017).

193. Jeong, M., O'Reilly, M., Kirkwood, N. K., Al-Aama, J., Lako, M., Kros, C. J. & Armstrong, L. Generating inner ear organoids containing putative cochlear hair cells from human pluripotent stem cells. *Cell Death & Disease* **9,** 1–13 (2018).

194. Hanekom, T. & Hanekom, J. J. Three-dimensional models of cochlear implants: A review of their development and how they could support management and maintenance of cochlear implant performance. *Network (Bristol, England)* **27,** 67–106 (2016).

195. Kalkman, R. K., Briaire, J. J. & Frijns, J. H. M. Stimulation strategies and electrode design in computational models of the electrically stimulated cochlea: An overview of existing literature. *Network: Computation in Neural Systems* **27,** 107–134 (2016).

196. Agrawal, V. & Newbold, C. Computer modelling of the cochlea and the cochlear implant: A review. *Cochlear Implants International* **13,** 113–123 (2012).

197. Bai, S., Encke, J., Obando-Leitón, M., Weiß, R., Schäfer, F., Eberharter, J., Böhnke, F. & Hemmert, W. Electrical Stimulation in the Human Cochlea: A Computational Study Based on High-Resolution Micro-CT Scans. *Frontiers in Neuroscience* **13,** 1312 (2019).

198. Heshmat, A., Sajedi, S., Johnson Chacko, L., Fischer, N., Schrott-Fischer, A. & Rattay, F. Dendritic Degeneration of Human Auditory Nerve Fibers and Its Impact on the Spiking Pattern Under Regular Conditions and During Cochlear Implant Stimulation. *Frontiers in Neuroscience* **14,** 599868 (2020).

199. Salkim, E., Zamani, M., Jiang, D., Saeed, S. R. & Demosthenous, A. Insertion Guidance Based on Impedance Measurements of a Cochlear Electrode Array. *Frontiers in Computational Neuroscience* **16** (2022).

200. Vanpoucke, F., Zarowski, A., Casselman, J., Frijns, J. & Peeters, S. The Facial Nerve Canal: An Important Cochlear Conduction Path Revealed by Clarion Electrical Field Imaging. *Otology & Neurotology* **25,** 282–289 (2004).

201. Hodgkin, A. L. & Huxley, A. F. A quantitative description of membrane current and its application to conduction and excitation in nerve. *The Journal of Physiology* **117,** 500–544 (1952).

202. Briaire, J. J. & Frijns, J. H. Unraveling the electrically evoked compound action potential. *Hearing Research* **205,** 143–156 (2005).

203. Smit, J. E., Hanekom, T., van Wieringen, A., Wouters, J. & Hanekom, J. J. Threshold predictions of different pulse shapes using a human auditory nerve fibre model containing persistent sodium and slow potassium currents. *Hearing Research* **269,** 12–22 (2010).

204. Takanen, M., Bruce, I. C. & Seeber, B. U. Phenomenological modelling of electrically stimulated auditory nerve fibers: A review. *Network: Computation in Neural Systems* **27,** 157–185 (2016).

205. Tabibi, S., Boulet, J., Dillier, N. & Bruce, I. C. Phenomenological model of auditory nerve population responses to cochlear implant stimulation. *Journal of Neuroscience Methods* **358,** 109212 (2021).

206. Takanen, M. & Seeber, B. U. A Phenomenological Model Reproducing Temporal Response Characteristics of an Electrically Stimulated Auditory Nerve Fiber. *Trends in Hearing* **26,** 23312165221117079 (2022).

207. Mener, D. J., Betz, J., Genther, D. J., Chen, D. & Lin, F. R. Hearing loss and depression in older adults. *Journal of the American Geriatrics Society* **61,** 1627–1629 (2013).

208. Kim, S. Y., Kim, H.-J., Park, E.-K., Joe, J., Sim, S. & Choi, H. G. Severe hearing impairment and risk of depression: A national cohort study. *PLOS ONE* **12,** e0179973 (2017).

209. Li, C.-M., Zhang, X., Hoffman, H. J., Cotch, M. F., Themann, C. L. & Wilson, M. R. Hearing impairment associated with depression in US adults, National Health and Nutrition Examination Survey 2005-2010. *JAMA otolaryngology– head & neck surgery* **140,** 293–302 (2014).

210. Lin, F. R., Metter, E. J., O'Brien, R. J., Resnick, S. M., Zonderman, A. B. & Ferrucci, L. Hearing loss and incident dementia. *Archives of Neurology* **68,** 214–220 (2011).

211. Neff, R., Jicha, G., Westgate, P., Hawk, G., Bush, M. & McNulty, B. Neuropathological Findings of Dementia Associated With Subjective Hearing Loss. *Otology & Neurotology* **40** (2019).

212. Leverton, T. Resistant behaviour in dementia might be due to hearing loss. *Bmj* **368** (2020).

213. Contrera, K. J., Betz, J., Genther, D. J. & Lin, F. R. Association of Hearing Impairment and Mortality in the National Health and Nutrition Examination Survey. *JAMA otolaryngology– head & neck surgery* **141,** 944–946 (2015).

214. Kim, S. Y., Min, C., Kim, H.-J., Lee, C. H., Sim, S., Park, B. & Choi, H. G. Mortality and Cause of Death in Hearing Loss Participants: A Longitudinal Follow-up Study Using a National Sample Cohort. *Otology & Neurotology* **41,** 25–32 (2020).

215. Briggs, R. J. S., Tykocinski, M., Lazsig, R., Aschendorff, A., Lenarz, T., Stöver, T., Fraysse, B., Marx, M., Roland, J. T., Roland, P. S., Wright, C. G., Gantz, B. J., Patrick, J. F. & Risi, F. Development and evaluation of the modiolar research array – multi-centre collaborative study in human temporal bones. *Cochlear Implants International* **12,** 129–139 (2011).

216. Eshraghi, A. A., Yang, N. W. & Balkany, T. J. Comparative Study of Cochlear Damage With Three Perimodiolar Electrode Designs: *The Laryngoscope* **113,** 415–419 (2003).

217. Adunka, O., Kiefer, J., Unkelbach, M. H., Lehnert, T. & Gstoettner, W. Development and Evaluation of an Improved Cochlear Implant Electrode Design for Electric Acoustic Stimulation: *The Laryngoscope* **114,** 1237–1241 (2004).

218. Leon, L., Warren, F. M. & Abbott, J. J. An In-Vitro Insertion-Force Study of Magnetically Guided Lateral-Wall Cochlear-Implant Electrode Arrays. *Otology & Neurotology: Official Publication of the American Otological Society, American Neurotology Society [and] European Academy of Otology and Neurotology* **39,** e63–e73 (2018).

219. Kontorinis, G., Scheper, V., Wissel, K., Stöver, T., Lenarz, T. & Paasche, G. In vitro modifications of the scala tympani environment and the cochlear implant array surface. *The Laryngoscope* **122,** 2057–2063 (2012).

220. Lo, J., Bester, C., Collins, A., Newbold, C., Hampson, A., Chambers, S., Eastwood, H. & O'Leary, S. Intraoperative force and electrocochleography measurements in an animal model of cochlear implantation. *Hearing Research* **358,** 50–58 (2018).

221. Rau, T. S., Zuniga, M. G., Salcher, R. & Lenarz, T. A simple tool to automate the insertion process in cochlear implant surgery. *International Journal of Computer Assisted Radiology and Surgery* (2020).

222. Mittmann, P., Ernst, A. & Todt, I. Electrode design and insertional depth-dependent intra-cochlear pressure changes: a model experiment. *The Journal of Laryngology & Otology* **132,** 224–229 (2018).

223. Riemann, C., Sudhoff, H. & Todt, I. Effect of Underwater Insertion on Intracochlear Pressure. *Frontiers in Surgery* **7,** 546779 (2020).

224. Todt, I., Ernst, A. & Mittmann, P. Effects of Different Insertion Techniques of a Cochlear Implant Electrode on the Intracochlear Pressure. *Audiology and Neurotology* **21,** 30–37 (2016).

225. Todt, I., Mittmann, M., Ernst, A. & Mittmann, P. Comparison of the effects of four different cochlear implant electrodes on intra-cochlear pressure in a model. *Acta Oto-Laryngologica* **137,** 235–241 (2017).

226. Hrncirik, F., Roberts, I., Sevgili, I., Swords, C. & Bance, M. Models of Cochlea Used in Cochlear Implant Research: A Review. *Annals of Biomedical Engineering* (2023).

227. Nguyen, Y., Miroir, M., Kazmitcheff, G., Sutter, J., Bensidhoum, M., Ferrary, E., Sterkers, O. & Bozorg Grayeli, A. Cochlear Implant Insertion Forces in Microdissected Human Cochlea to Evaluate a Prototype Array. *Audiology and Neurotology* **17,** 290–298 (2012).

228. Kontorinis, G., Paasche, G., Lenarz, T. & Stöver, T. The Effect of Different Lubricants on Cochlear Implant Electrode Insertion Forces. *Otology & Neurotology* **32,** 1050–1056 (2011).

229. Wrzeszcz, A., Steffens, M., Balster, S., Warnecke, A., Dittrich, B., Lenarz, T. & Reuter, G. Hydrogel coated and dexamethasone releasing cochlear implants: Quantification of fibrosis in guinea pigs and evaluation of insertion forces in a human cochlea model: Dex/Hydrogel CI in Guinea Pig and Insertion Forces in Human Model. *Journal of Biomedical Materials Research Part B: Applied Biomaterials* **103,** 169–178 (2015).

230. Todt, I., Ernst, A. & Mittmann, P. Effects of Round Window Opening Size and Moisturized Electrodes on Intracochlear Pressure Related to the Insertion of a Cochlear Implant Electrode. *Audiology and Neurotology Extra* **6,** 1–8 (2016).

231. Todt, I., Mittmann, P. & Ernst, A. Intracochlear Fluid Pressure Changes Related to the Insertional Speed of a CI Electrode. *BioMed Research International* **2014,** 1–4 (2014).

232. Haddaway, N. R., Page, M. J., Pritchard, C. C. & McGuinness, L. A. PRISMA2020: An R package and Shiny app for producing PRISMA 2020-compliant flow diagrams, with interactivity for optimised digital transparency and Open Synthesis. *Campbell Systematic Reviews* **18,** e1230 (2022).

233. Rohatgi, A. Webplotdigitizer: Version 4.6 2022.

234. Banakis Hartl, R. M. & Greene, N. T. Measurement and Mitigation of Intracochlear Pressure Transients During Cochlear Implant Electrode Insertion. *Otology & Neurotology* **43,** 174–182 (2022).

235. Greene, N. T., Mattingly, J. K., Banakis Hartl, R. M., Tollin, D. J. & Cass, S. P. Intracochlear Pressure Transients During Cochlear Implant Electrode Insertion. *Otology & Neurotology* **37,** 1541–1548 (2016).

236. Snels, C., Roland, J. T., Treaba, C., Jethanamest, D., Huinck, W., Friedmann, D. R., Dhooge, I. & Mylanus, E. Force and pressure measurements in temporal bones. *American Journal of Otolaryngology* **42,** 102859 (2021).

237. Ordonez, F., Riemann, C., Mueller, S., Sudhoff, H. & Todt, I. Dynamic intracochlear pressure measurement during cochlear implant electrode insertion. *Acta Oto-Laryngologica* **139,** 860–865 (2019).

238. Schurzig, D., Webster, R. J., Dietrich, M. S. & Labadie, R. F. Force of Cochlear Implant Electrode Insertion Performed by a Robotic Insertion Tool: Comparison of Traditional Versus Advance Off-Stylet Techniques. *Otology & Neurotology* **31,** 1207–1210 (2010).

239. Hügl, S., Scheper, V., Gepp, M. M., Lenarz, T., Rau, T. S. & Schwieger, J. Coating stability and insertion forces of an alginate-cell-based drug delivery implant system for the inner ear. *Journal of the Mechanical Behavior of Biomedical Materials* **97,** 90–98 (2019).

240. Dohr, D., Wulf, K., Grabow, N., Mlynski, R. & Schraven, S. P. A PLLA Coating Does Not Affect the Insertion Pressure or Frictional Behavior of a CI Electrode Array at Higher Insertion Speeds. *Materials* **15,** 3049 (2022).

241. Aebischer, P., Caversaccio, M. & Wimmer, W. Fabrication of human anatomy-based scala tympani models with a hydrophilic coating for cochlear implant insertion experiments. *Hearing Research* **404,** 108205 (2021).

242. Dhanasingh, A., Swords, C., Bance, M., Van Rompaey, V. & Van de Heyning, P. Cochlear Size Assessment Predicts Scala Tympani Volume and Electrode Insertion Force- Implications in Robotic Assisted Cochlear Implant Surgery. *Frontiers in Surgery* **8,** 723897 (2021).

243. Hügl, S., Blum, T., Lenarz, T., Majdani, O. & Rau, T. S. Impact of anatomical variations on insertion forces. *Current Directions in Biomedical Engineering* **4,** 509–512 (2018).

244. Miroir, M., Nguyen, Y., Kazmitcheff, G., Ferrary, E., Sterkers, O. & Grayeli, A. B. Friction Force Measurement During Cochlear Implant Insertion: Application to a Force-Controlled Insertion Tool Design. **33,** 9 (2012).

245. Mirsalehi, M., Rau, T. S., Harbach, L., Hügl, S., Mohebbi, S., Lenarz, T. & Majdani, O. Insertion forces and intracochlear trauma in temporal bone specimens implanted with a straight atraumatic electrode array. *European Archives of Oto-Rhino-Laryngology* **274,** 2131–2140 (2017).

246. Nguyen, Y., Kazmitcheff, G., De Seta, D., Miroir, M., Ferrary, E. & Sterkers, O. Definition of Metrics to Evaluate Cochlear Array Insertion Forces Performed with Forceps, Insertion Tool, or Motorized Tool in Temporal Bone Specimens. *BioMed Research International* **2014,** 1–9 (2014).

247. Radeloff, A., Unkelbach, M. H., Mack, M. G., Settevendemie, C., Helbig, S., Mueller, J., Hagen, R. & Mlynski, R. A coated electrode carrier for cochlear implantation reduces insertion forces: A Coated Electrode Carrier for Cochlear Implantation. *The Laryngoscope* **119,** 959–963 (2009).

248. Riojas, K. E., Tran, E. T., Freeman, M. H., Noble, J. H., Webster III, R. J. & Labadie, R. F. Clinical Translation of an Insertion Tool for Minimally Invasive Cochlear Implant Surgery. *Journal of Medical Devices* **15** (2021).

249. Rohani, P., Pile, J., Kahrs, L. A., Balachandran, R., Blachon, G. S., Simaan, N. & Labadie, R. F. Forces and Trauma Associated with Minimally Invasive Image-Guided Cochlear Implantation. *Otolaryngology–Head and Neck Surgery* **150,** 638–645 (2014).

250. Smetak, M. R., Riojas, K. E., Whittenbarger, N., Noble, J. H. & Labadie, R. F. Dynamic Behavior and Insertional Forces of a Precurved Electrode Using the Pull-Back Technique in a Fresh Microdissected Cochlea. **44** (2023).

251. Zuniga, M. G., Hügl, S., Engst, B. G., Lenarz, T. & Rau, T. S. The Effect of Ultra-slow Velocities on Insertion Forces: A Study Using a Highly Flexible Straight Electrode Array. *Otology & Neurotology* **42,** e1013–e1021 (2021).

252. Dohr, D., Fiedler, N., Schmidt, W., Grabow, N., Mlynski, R. & Schraven, S. P. Frictional Behavior of Cochlear Electrode Array Is Dictated by Insertion Speed and Impacts Insertion Force. *Applied Sciences* **11,** 5162 (2021).

253. Ishiyama, A., Ishiyama, G., Lopez, I. A. & Linthicum, F. H. Temporal Bone Histopathology of First-Generation Cochlear Implant Electrode Translocation. *Otology & Neurotology* **40,** e581–e591 (2019).

254. Fayad, J., Linthicum, F. H., Galey, F. R., Otto, S. R. & House, W. F. Cochlear Implants: Histopathologic Findings Related to Performance in 16 Human Temporal Bones. *Annals of Otology, Rhinology & Laryngology* **100,** 807–811 (1991).

255. Wanna, G. B., Noble, J. H., Carlson, M. L., Gifford, R. H., Dietrich, M. S., Haynes, D. S., Dawant, B. M. & Labadie, R. F. Impact of electrode design and surgical approach on scalar location and cochlear implant outcomes: Impact of Electrode Type and Approach on CI Outcome. *The Laryngoscope* **124,** S1–S7 (S6 2014).

256. Weng, Z., Zhou, Y., Lin, W., Senthil, T. & Wu, L. Structure-property relationship of nano enhanced stereolithography resin for desktop SLA 3D printer. *Composites Part A: Applied Science and Manufacturing* **88,** 234–242 (2016).

257. Borrello, J., Nasser, P., Iatridis, J. C. & Costa, K. D. 3D printing a mechanically-tunable acrylate resin on a commercial DLP-SLA printer. *Additive Manufacturing* **23,** 374–380 (2018).

258. Sarap, M., Kallaste, A., Shams Ghahfarokhi, P., Tiismus, H. & Vaimann, T. Utilization of Additive Manufacturing in the Thermal Design of Electrical Machines: A Review. *Machines* **10,** 251 (2022).

259. Luongo, A., Falster, V., Doest, M. B., Ribo, M. M., Eiriksson, E. R., Pedersen, D. B. & Frisvad, J. R. Microstructure Control in 3D Printing with Digital Light Processing. *Computer Graphics Forum* **39,** 347–359 (2020).

260. Compare Formlabs SLA 3D Printer Tech Specs Formlabs. https://formlabs.com/uk/3d-printers/form-3/tech-specs/ (2023).

261. Deafness & hearing loss facts Hearing Link Services. https://www.hearinglink.org/your-hearing/about-hearing/facts-about-deafness-hearing-loss/ (2022).

262. Vos, T. et al. Global, regional, and national incidence, prevalence, and years lived with disability for 310 diseases and injuries, 1990–2015: a systematic analysis for the Global Burden of Disease Study 2015. *The Lancet* **388,** 1545–1602 (2016).

263. Adigun, O. T. Depression and Individuals with Hearing Loss: A Systematic Review. *Journal of Psychology & Psychotherapy* **07** (2017).

264. Cosh, S., Carriere, I., Delcourt, C., Helmer, C. & Consortium, t. S.-C. A dimensional approach to understanding the relationship between self-reported hearing loss and depression over 12 years: the Three-City study. *Aging & Mental Health* **25,** 954–961 (2021).

265. Cosh, S., Carriere, I., Daien, V., Amieva, H., Tzourio, C., Delcourt, C., Helmer, C. & Consortium, t. S.-C. The relationship between hearing loss in older adults and depression over 12 years: Findings from the Three-City prospective cohort study. *International Journal of Geriatric Psychiatry* **33,** 1654–1661 (2018).

266. Ford, A. H., Hankey, G. J., Yeap, B. B., Golledge, J., Flicker, L. & Almeida, O. P. Hearing loss and the risk of dementia in later life. *Maturitas* **112,** 1–11 (2018).

267. Hardy, C. J. D., Marshall, C. R., Golden, H. L., Clark, C. N., Mummery, C. J., Griffiths, T. D., Bamiou, D.-E. & Warren, J. D. Hearing and dementia. *Journal of Neurology* **263,** 2339–2354 (2016).

268. Nadhimi, Y. & Llano, D. A. Does hearing loss lead to dementia? A review of the literature. *Hearing Research.* Special Issue on Presbycusis **402,** 108038 (2021).

269. Uhlmann, R. F., Larson, E. B., Rees, T. S., Koepsell, T. D. & Duckert, L. G. Relationship of Hearing Impairment to Dementia and Cognitive Dysfunction in Older Adults. *JAMA* **261,** 1916–1919 (1989).

270. Chen, D. S., Genther, D. J., Betz, J. & Lin, F. R. Association Between Hearing Impairment and Self-Reported Difficulty in Physical Functioning. *Journal of the American Geriatrics Society* **62,** 850–856 (2014).

271. Eriksson-Mangold, M. & Carlsson, S. G. Psychological and somatic distress in relation to perceived hearing disability, hearing handicap, and hearing measurements. *Journal of Psychosomatic Research* **35,** 729–740 (1991).

272. Yamada, M., Nishiwaki, Y., Michikawa, T. & Takebayashi, T. Impact of hearing difficulty on dependence in activities of daily living (ADL) and mortality: A 3-year cohort study of community-dwelling Japanese older adults. *Archives of Gerontology and Geriatrics* **52,** 245–249 (2011).

273. Jia, H., Wang, J., François, F., Uziel, A., Puel, J.-L. & Venail, F. Molecular and Cellular Mechanisms of Loss of Residual Hearing after Cochlear Implantation. *Annals of Otology, Rhinology & Laryngology* **122,** 33–39 (2013).

274. Zanetti, D., Nassif, N. & Redaelli De Zinis, L. Fattori influenzanti la conservazione dei residui uditivi negli impianti cocleari. *Acta Otorhinolaryngologica Italica* **35,** 433–441 (2015).

275. Eshraghi, A. A., Ahmed, J., Krysiak, E., Ila, K., Ashman, P., Telischi, F. F., Angeli, S., Prentiss, S., Martinez, D. & Valendia, S. Clinical, surgical, and electrical factors impacting residual hearing in cochlear implant surgery. *Acta Oto-Laryngologica* **137,** 384–388 (2017).

276. Hoskison, E., Mitchell, S. & Coulson, C. Systematic review: Radiological and histological evidence of cochlear implant insertion trauma in adult patients. *Cochlear Implants International* **18,** 192–197 (2017).

277. O'Leary, M. J., House, W. F., Fayad, J. & Linthicum, F. H. Electrode Insertion Trauma in Cochlear Implantation. *Annals of Otology, Rhinology & Laryngology* **100,** 695–699 (1991).

278. Zhou, L., Friedmann, D. R., Treaba, C., Peng, R. & Roland Jr., J. T. Does cochleostomy location influence electrode trajectory and intracochlear trauma? *The Laryngoscope* **125,** 966–971 (2015).

279. Shishodia, S. & Saurav, D. Round window versus conventional bony cochleostomy technique in pediatric cochlear implantation; A Randomized controlled double blinded trial. *International Journal of Otorhinolaryngology and Head and Neck Surgery* **7,** 1297 (2021).

280. Jiam, N. T. & Limb, C. J. The impact of round window vs cochleostomy surgical approaches on interscalar excursions in the cochlea: Preliminary results from a flat-panel computed tomography study. *World Journal of Otorhinolaryngology - Head and Neck Surgery* **2,** 142–147 (2016).

281. Demir, B., Yüksel, M., Atılgan, A., Ciprut, A. & Batman, C. Spectral resolution and speech perception after cochlear implantation using the round window versus cochleostomy technique. *The Journal of Laryngology & Otology* **135,** 513–517 (2021).

282. Carlson, M. L., O'Connell, B. P., Lohse, C. M., Driscoll, C. L. & Sweeney, A. D. Survey of the American Neurotology Society on Cochlear Implantation: Part 2, Surgical and Device-Related Practice Patterns. *Otology & Neurotology* **39,** e20 (2018).

283. Avasarala, V. S., Jinka, S. K. & Jeyakumar, A. Complications of Cochleostomy Versus Round Window Surgical Approaches: A Systematic Review and Meta-Analysis. *Cureus* **14** (2022).

284. Zhang, W., Kim, S. M., Wang, W., Cai, C., Feng, Y., Kong, W. & Lin, X. Cochlear Gene Therapy for Sensorineural Hearing Loss: Current Status and Major Remaining Hurdles for Translational Success. *Frontiers in Molecular Neuroscience* **11,** 221 (2018).

285. Boggess, W. J., Baker, J. E. & Balkany, T. J. Loss of residual hearing after cochlear implantation. *The Laryngoscope* **99,** 1002–1005 (1989).

286. Carlson, M. L., Driscoll, C. L. W., Gifford, R. H., Service, G. J., Tombers, N. M., Hughes-Borst, B. J., Neff, B. A. & Beatty, C. W. Implications of Minimizing Trauma During Conventional Cochlear Implantation. *Otology & Neurotology* **32,** 962–968 (2011).

287. Choong, J. K., Hampson, A. J., Brody, K. M., Lo, J., Bester, C. W., Gummer, A. W., Reynolds, N. P. & O'Leary, S. J. Nanomechanical mapping reveals localized stiffening of the basilar membrane after cochlear implantation. *Hearing Research* **385,** 107846 (2020).

288. Wilkening, P., Chien, W., Gonenc, B., Niparko, J., Kang, J. U., Iordachita, I. & Taylor, R. H. Evaluation of virtual fixtures for robot-assisted cochlear implant insertion. in. 5th IEEE RAS/EMBS International Conference on Biomedical Robotics and Biomechatronics (2014), 332–338.

289. Henslee, A. M., Kaufmann, C. R., Andrick, M. D., Reineke, P. T., Tejani, V. D. & Hansen, M. R. Development and Characterization of an Electrocochleography-Guided Robotics-Assisted Cochlear Implant Array Insertion System. *Otolaryngology–Head and Neck Surgery* **167,** 334–340 (2022).

290. Buchman, C. A., Dillon, M. T., King, E. R., Adunka, M. C., Adunka, O. F. & Pillsbury, H. C. Influence of Cochlear Implant Insertion Depth on Performance: A Prospective Randomized Trial. *Otology & Neurotology* **35,** 1773–1779 (2014).

291. Rebscher, S. J., Hetherington, A., Bonham, B., Wardrop, P. & Leake, P. A. Considerations for the design of future cochlear implant electrode arrays: Electrode array stiffness, size and depth of insertion, 25 (2008).

292. S Elgandy, M. & K Mobashir, M. What physicians and patients should know about different designs of cochlear implant electrodes? *Otorhinolaryngology-Head and Neck Surgery* **4** (2019).

293. Dhanasingh, A. & Jolly, C. An overview of cochlear implant electrode array designs. *Hearing Research* **356,** 93–103 (2017).

294. Jacobson, A. et al. gptoolbox: Geometry Processing Toolbox http://github.com/alecjacobson/gptoolbox.

295. geom3d https://www.mathworks.com/matlabcentral/fileexchange/24484-geom3d (2022).

296. Dang, K. Electrical conduction models for cochlear implant stimulation. Thesis (Université Côte d'Azur, 2017).

297. Cohen, L. T., Xu, J., Xu, S. A. & Clark, G. M. Improved and simplified methods for specifying positions of the electrode bands of a cochlear implant array. *The American Journal of Otology* **17,** 859–865 (1996).

298. Stuart, I. M. Capstan equation for strings with rigidity. *British Journal of Applied Physics* **12,** 559–562 (1961).

299. Ertas, Y. N., Ozpolat, D., Karasu, S. N. & Ashammakhi, N. Recent Advances in Cochlear Implant Electrode Array Design Parameters. *Micromachines* **13,** 1081 (2022).

Appendix A

Evaluation of Different 3D Printers for the Fabrication of Accurate Cochlea Model

A.1 Materials and methods

A.1.1 Preparation of 3D models

Cadaveric temporal bones were acquired from the Department of Physiology, Development and Neuroscience, University of Cambridge, UK. These temporal bones were scanned with micro-computed tomography (microCT) scanner Nikon XT 225 ST from the Cambridge Biotomography Centre. The acquisition parameters of the scans were as follow: the voltage was set to 125 kV; current was set to 120 µA; the number of projections was set to 1080; and the exposition time was 1000 ms.

Stradview 6.0 software (developed by Medical Imaging group at the Department of Engineering, University of Cambridge, UK, particularly Dr Andrew Gee and Dr Graham Treece) was exploited for the segmentation and 3D reconstruction of the cochlea shape from the scans. The threshold-based segmentation was used to obtain a rough set of cochlea contours. One example of the statistical shape model of the cochlea that best represented an average size and shape was used and saved as a PLY file. This statistical shape model was derived from the work of Dr Andrew Gee[87] using the manual registration and smoothing of the microCT scans of 18 human temporal bones that were collated in wxRegSurf software (developed by Medical Imaging group at the Department of Engineering, University of Cambridge, UK).

The 3D model files obtained from the microCT 3D reconstructions were subsequently manipulated in Meshmixer (Autodesk Research) computer-aided design (CAD) software. This allowed the production of various designs based on the original 3D model file and exporting the results to an STL file format. The designs produced include shell-like models, ‘open-top’ models, ‘block’ (negative) cochlea, and scaling of the cochlea model.

The STL files were prepared for printing using the various manufacturers’ software. This software generated support structures orientated the model at an angle for optimal printing and automatically optimised parameters for the chosen resin. Subsequently, the software slices the model and generates g-code (or equivalent), the computer numerical control language for the printer. For printing on the Formlabs Form 3, Preform software (Formlabs) was used to prepare the STL file that could be directly exported to the Form 3 printer.

A.1.2 Evaluation of different 3D printers

To evaluate the performance of different 3D printers, the same CAD file was printed consistently on all printers. This model consisted of a shell-like design with 300 µm-thick walls. The tested printers were: ProJet HD3500+ (3D Systems, Shapeways), Asiga MAX (Asiga), Micro Plus HD (EnvisionTEC), Cadworks3D M-50 (Cadworks3D) and Form 3 (Formlabs). In cases where the printers could not be directly accessed (all printers except the Asiga Max and Form 3 at that time), manufacturers were contacted and asked to print and deliver a transparent generic model to the lab for qualitative analysis. Note that 3D printed models shown in this section were printed on a Formlabs Form 3 unless otherwise stated.

All of the 3D printers tested used resin-based additive manufacturing techniques. The 3D Systems’ printer uses its proprietary multi-jet printing (MJP) technology which is an inkjet printing process that employs multiple printheads to deposit a photocurable resin. Cadworks3D and Asiga 3D printers use a digital light processing technology (DLP) that operates similarly to SLA as it exploits photopolymer reactions. However, instead of having one spot where the light hits the resin, the whole layer is formed at once by a projector or an LCD panel. EnvisionTEC utilises its patented continuous digital light processing technology (cDLP), which differs from classical DLP by allowing the build plate to move continuously during printing. The Form 3 exploits Formlabs’ developed Low Force Stereolithography (LFS) technology which utilises the manufacturer’s proprietary resins. LFS is an advanced form of SLA technology which uses a flexible tank and linear illumination to reduce the forces exerted on the parts during printing. This allows excellent print accuracy and surface finish. Furthermore, by decreasing these forces, smaller support contact points are required for successful printing. The print can then be easily released from the supportive scaffold, which results in shorter post-processing procedures and leaves fewer imperfections on the surface.

A.1.3 Formlabs Form 3 printing

The Formlabs Form 3 was used for the majority of 3D printing demonstrated in this appendix. The maximum building volume is 14.5 by 14.5 by 18.5 cm. Form 3 utilises a laser with 405 nm wavelength and 85 µm spot-size.

The printing layer height was set to 25 µm (the highest resolution). Two types of Formlabs' standard proprietary resins were used for our studies: Grey (V4) and Clear (V4). Grey resin delivers a smooth, matte finish with an opaque appearance, whereas Clear resin provides nearly optical transparency. Otherwise, all Formlabs' standard resins have the same material properties (tensile modulus, elongation at failure, flexural modulus, heat deflection at 264 and 66 psi). However, the chemical composition of these proprietary resins is not publicly available. Form 3 is only compatible with the proprietary resins supplied by Formlabs, and other resins cannot be used.

Following the printing process, all prints were thoroughly washed of residual resin in isopropanol (IPA) using Form Wash (Formlabs) device for 60 min. The Form Wash uses a large tank of IPA (8.6 L) and stirring mechanisms that provide optimal washing. After that, the prints were rewashed manually using IPA and a syringe to remove residuals of resin from hollow and unreachable places. Finally, samples were cured using Form Cure (Formlabs) device at 60 °C for 1 h. Form Cure uses 13 multi-directional LEDs light with 405 nm wavelength and rotating turntable, delivering continuous uniform exposure during post-curing.

Three shapes of the artificial cochlea were fabricated using Form 3 printer: 'shell', 'open-top', and 'block' (negative) cochlea (see Figure A.1). All printed models consisted of one lumen unifying all three scalae. In addition, 'shell' and 'block' models had a narrow 1 mm in diameter opening at the apex to flush out resin residues and fill the lumen with the saline solution. The prints' orientation toward the building platform was optimised to deliver an optimal surface finish. The 'shell' design was printed with a wall thickness of 300, 100, and 50 µm (see Figure A.10). The 'open-top' design consisted of 'shell' cochlea model partially embedded in a block with the removed top part of the lumen (see Figure A.11). 'Block' cochlea models were generated by fully embedding the reconstructed cochlea model in a block of material while making a Boolean difference of these structures using the Meshmixer software. The basal part of the cochlea at the beginning of the round was aligned with the edge of the block to produce an opening. The 'block' model was fabricated as 1 : 1, 1 : 0.75, 1 : 0.5 as well as 1 : 1.25 and 1 : 1.5 scale of the original model.

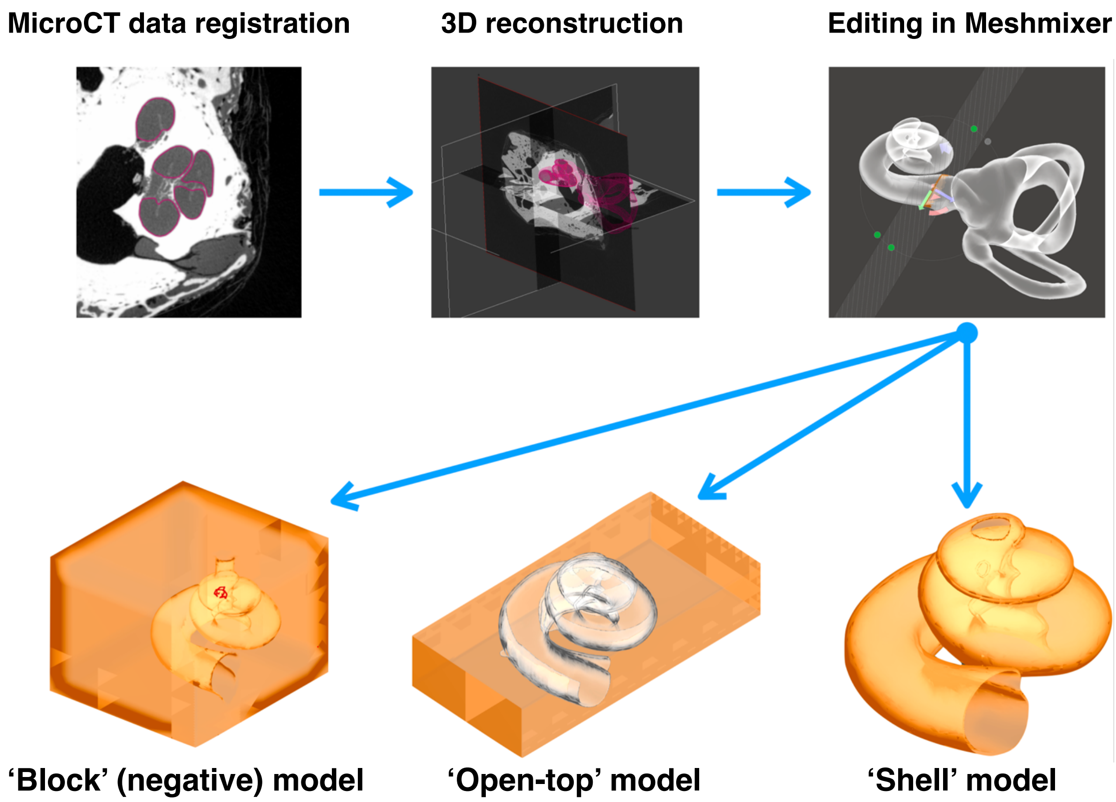

Figure A.1 The workflow of developing three cochlea models: 'shell', 'open-top', and 'block'. The cochlea shape was segmented from microCT scans and 3D reconstructed using Stradview software. The derived 3D object was subsequently edited in Meshmixer to create the three models.

A.1.4 Additional post-processing

The 'block' cochleae that were fabricated using the Clear resin were further optimised to deliver a nearly transparent appearance. This was achieved by coating the samples' surface with clear acrylic lacquer spray (Aerosol Solutions LTD). Any holes in the 'block' cochlea models were plugged up with Blue-Tack prior to placing the models on tissue paper in a chemical fume hood and spraying for approximately 1 s from approximately

10 cm away with the lacquer spray. This thin lacquer layer filled surface imperfections caused by the layer-by-layer process that scatter light and produced an even finish to improve the model transparency.

A surfactant Pluronic F-127 solution was used on the inner surface of cochlear models to improve transparency and reduce surface friction to aid the insertion of cochlear implants into the model. The surfactant solution was prepared by dissolving Pluronic F-127 powder (Sigma-Aldrich) in distilled water at room temperature overnight to produce 5 % solution.

A.1.5 Characterisation of printed models

3D printed models were imaged on a Leica M80 (Leica Microsystems) optical light microscope with Moticam 1080 BMH (Motic Instruments). This was used to evaluate the print quality and observe the implantation of cochlear implants into the model.

To evaluate the 3D printing accuracy, 3D printed models (specifically 300 µm 'shell' models) were analysed using Nikon XT 225 ST microrCT scanner. The acquisition parameters of the scans were as follows: the voltage was set to 145 kV; the current was set to 85 µA; the number of projections was 1080; and the voxel size was set to 20 µm. The stacks of images were subsequently reconstructed to form 3D models, which were compared to the original 3D object file used for the printing. This was executed by utilising Stradview 6.0 and wxRegSurf (for the comparison of the reconstructed 3D model and the original 3D object file) software. The comparison was performed using 100 'rigid' iteration registrations and illustrated using a Registration error heat map.

A.2 Results and discussion

A.2.1 Fabrication of artificial cochlea

Micro-computed tomography scans of cadaveric cochleae were used to produce geometrically and anatomically accurate 3D models. These 3D reconstructions were developed through segmentation in Stradview software, followed by further computer-aided design (CAD) software processing to produce 3D printable files (see Figure A.1).

The 'shell' model was developed by applying normal extrusion to the model's outer surface (initially 300 µm). The 'block' model was created using Boolean difference of the cochlea and cubic shape. The open-top model was developed by erasing the top part of 'shell' model lumen and encapsulating it in a cubic platform. The Boolean difference was used to subtract these two shapes and produce the 'open-top' model.

A.2.2 Evaluation of 3D printers

In order to investigate the performance of the tested 3D printers, a consistent CAD file of a cochlear 'shell' with a 300 μm wall thickness was printed on selected 3D printers. All printed models, either printed directly or by manufacturers, were evaluated through optical imaging.

Figure A.2 shows the specimens printed by 3D Systems. The printing quality was sub-optimal as the cochlea lumen was not fully developed, meaning that the lumen was blocked and could not be flushed with saline. This is likely attributed to the collapse of the inner structure during printing or insufficient post-processing. Additionally, the print's low quality might be due to MJP technology. MJP relies on using paraffin wax as a supporting material which is removed by placing the print into an oven and melting it. As the geometry of the cochlea lumen is very intricate, it might cause an insufficient release of the supporting material, which resulted in clogging the apex of the model.

Leon *et al.* utilised similar technology – polyjet printing (PJP) – for the development of artificial *scala tympani* model.[131] Using PJP, they observed excellent print quality with superior smoothness of the internal surface. However, the print was only semi-transparent, which limited application in observing the CI insertion into a model. Nevertheless, the surface finish and the internal smoothness produced by 3D Systems' printer were not adequate for printing artificial cochleae.

The print developed by Asiga demonstrated higher surface smoothness and improved geometric accuracy when compared to the 3D Systems (see Figure A.3) – looking at the Figure A.3 C, an inconsistent pattern can be seen within the model's lumen. This can be attributed to the angle of the print relative to the building platform. As the print rises from the bath, the residual resin remains in the lumen. If they are not removed thoroughly, the print's surface may manifest abnormalities. Asiga printer also supports third-party resins, which is advantageous in providing flexibility in printing material.

Although EnvisionTEC (cDLP) utilises similar technology as Asiga (DLP), its performance was superior (see Figure A.4). The analysed model exhibited remarkable geometric accuracy, positioning it as one of the superior performers within the examined group. The model's initial semi-transparency is promising, suggesting the potential to attain full transparency through additional post-processing procedures. It is vital to acknowledge, though, that this prospect remains speculative as it is yet to be empirically

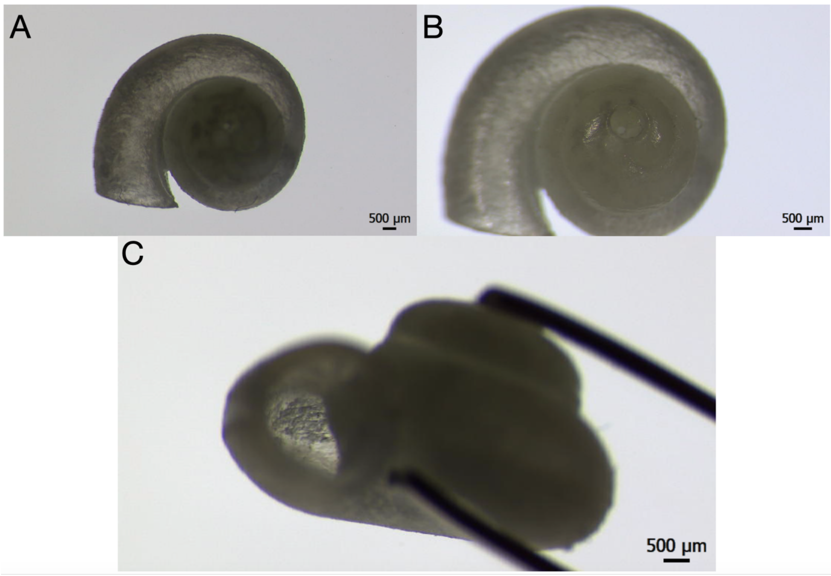

Figure A.2 Prints fabricated by 3D Systems demonstrated sub-optimal quality (A, B). (C) shows unsatisfactory smoothness of the internal lumen.

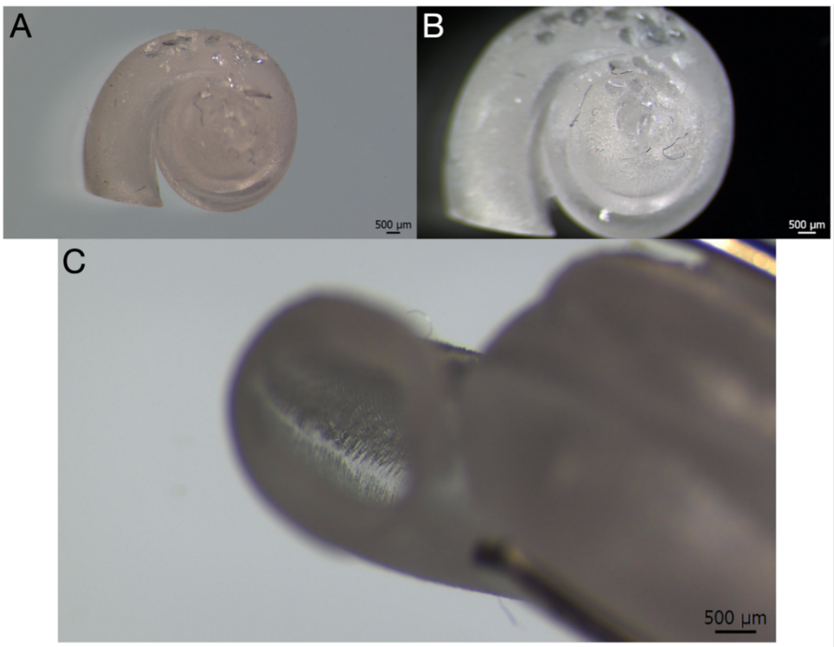

Figure A.3 Prints fabricated using Asiga 3D printer. (A) and (B) illustrate a good geometric accuracy. (C) depicts a very good smoothness of internal lumen with unrecognised pattern in the middle.

investigated. Notwithstanding, when gauging the surface smoothness, this model proved subpar in comparison to the other tested counterparts. Figure A.4 C illustrates voxel artefacts which may contribute to catching the tip of the array. Moreover, the rough surface cannot sufficiently mimic the smoothness of the cochlear lumen. Following this discovery, the EnvisionTEC's performance was not further investigated.

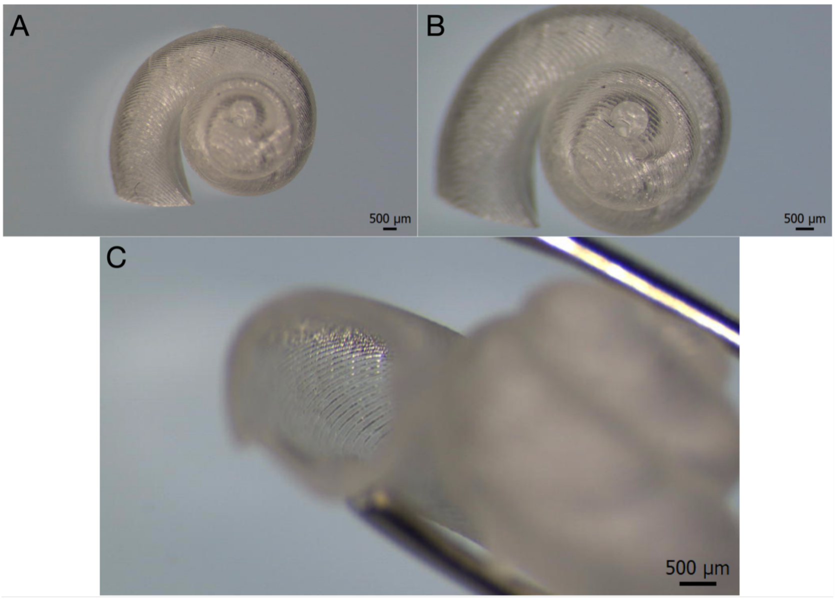

Figure A.4 Prints fabricated by EnvisionTEC. (A) and (B) demonstrate an excellent geometric accuracy, whereas (C) shows visible voxel artefacts.

Cadworks3D uses similar DLP technology as the abovementioned EnvisionTEC and Asiga. Its performance is excellent with regards to both surface smoothness and geometric accuracy (see Figure A.5). This can be assigned to a significantly lower layer height which contributes to the exceptional printing resolution. Hence, the smoothness of the internal structure is superior when comparing to EnvisionTEC's print. Moreover, the top view implies good initial transparency of the model, which might be further enhanced by post-processing. However, it should be noted that this requires further investigation. Finally, Cadworks3D supports the use of third-party resins which allows much flexibility in material choice.

Lastly, Figure A.6 depicts a sample fabricated by Formlabs' printer. Form 3 utilises LFS technology (enhanced SLA) which is slightly different from DLP technology. Instead of having a projector or LCD panel which cures the whole layer of resin at once, it focuses a laser on curing resin at one spot at a time. Hence, the SLA printer is significantly slower. However, this fact comes with an advantage of enhanced surface smoothness

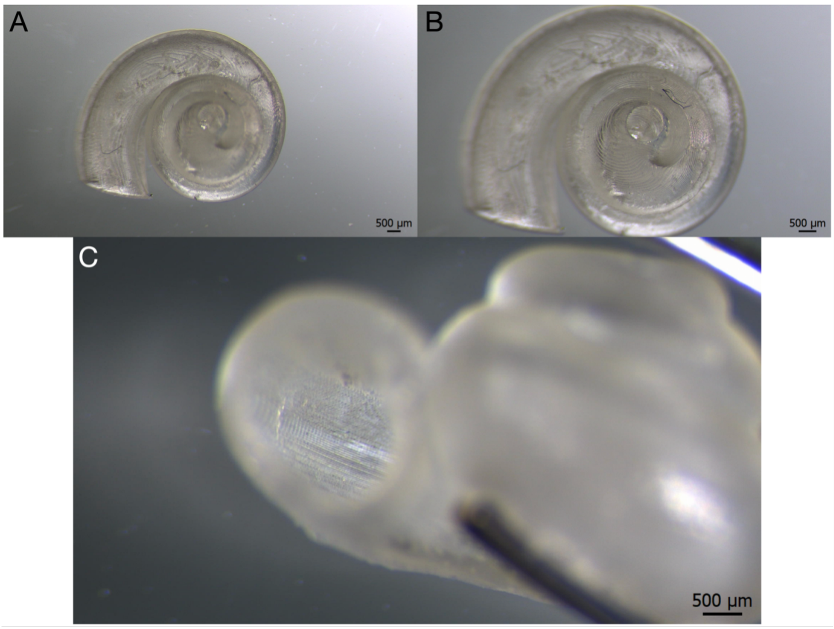

Figure A.5 Prints fabricated by Cadworks3D. (A) and (B) demonstrate good initial semi-transparency and excellent geometric accuracy. (C) illustrates a superb smoothness of the lumen.

(see Figure A.6 C) as curing the whole layer promotes 'stair-step' finish. Furthermore, LFS uses a flexible tank with linear illumination which drastically reduces the forces exerted on parts during printing and promote light-touch supports and excellent surface smoothness without visible layers. Form 3 provided the best surface smoothness and optimal geometric accuracy with a semi-transparent finish.

In summary, both Cadworks3D (DLP) and Formlabs (SLA) demonstrated superior inner lumen smoothness and geometric accuracy (refer to Figure A.7). Cadworks3D provides greater resin flexibility. Thus, Formlabs was used for cochlea model fabrication in the next section, with future research intending to utilise Cadworks3D (see Chapter 4). See Table A.1 for print analysis results.

Table A.1 Comparison of 3D printer's abilities and performance.

Manufacturer	**Printing Technology**	**Layer height [µm]***	**Surface Smoothness**	**Geometric Accuracy**	**Supports third party Resins**
3D Systems	MJP	16	inadequate	low	no
Asiga	DLP	25	moderate	good	yes
EnvisionTEC	cDLP	25	good	excellent	no
Cadworks3D	DLP	5	excellent	excellent	yes
Formlabs	SLA	25	excellent	excellent	no

*Numbers stated by manufacturer

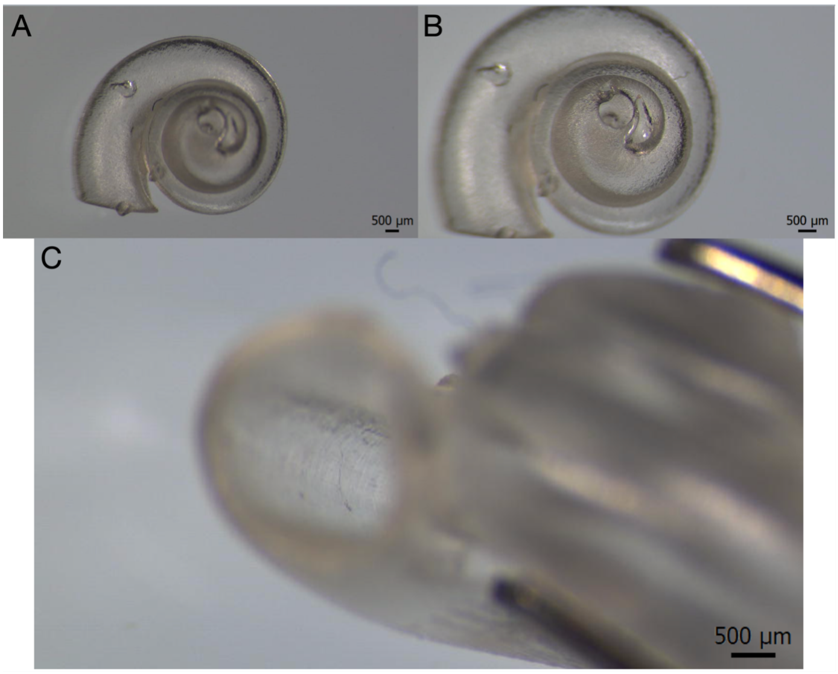

Figure A.6 Prints fabricated using Form 3. (A) and (B) show excellent geometric accuracy with a 'frosty-transparency'. (C) demonstrate the best internal smoothness of the model. The surface imperfections visible at (A, B) were developed due to the printing supports.

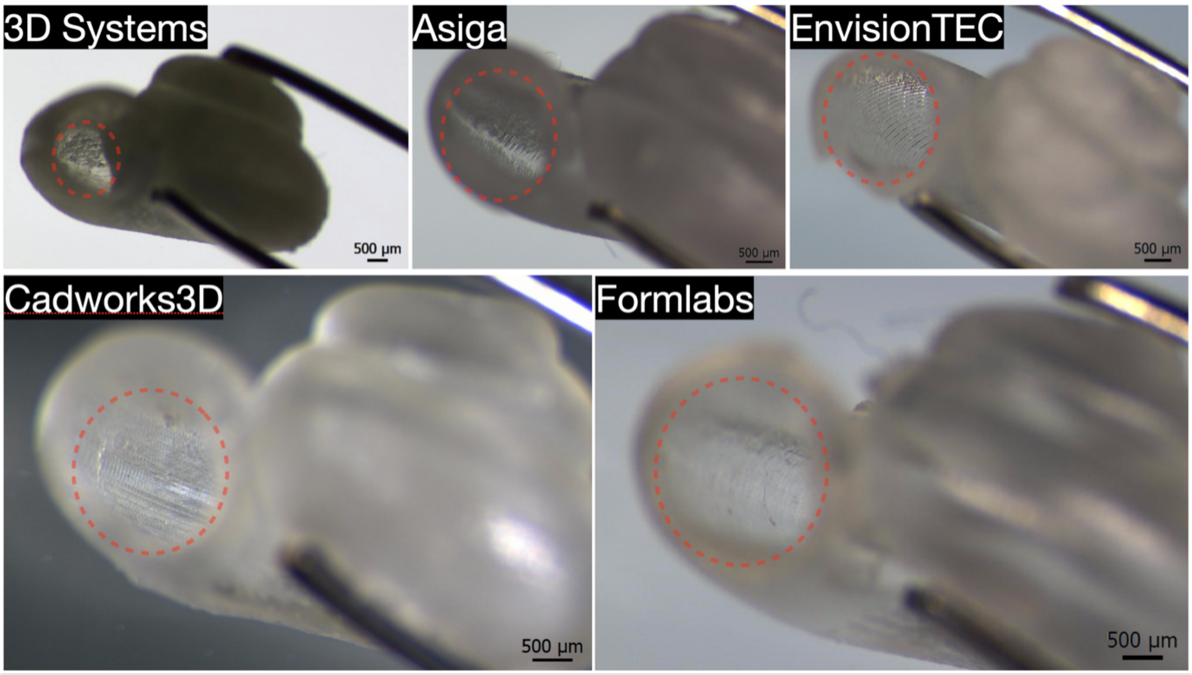

Figure A.7 Differences of performance among the tested 3D printers. Red circles depict the smoothness of the internal lumen. Cadworks3D and Formlabs produced the most optimal prints.

A.2.3 Design of cochlea model

The Form 3 printer was utilised for the fabrication of artificial cochlea model. Although this preliminary model combined all scalae as a single lumen and had an anatomically incorrect opening, it worked as a good demonstration of SLA technology and its application in the fabrication of artificial cochleae. Further work will consider 3D printing the *scala tympani* only (see Chapter 4).

Two types of resin were investigated on the Form 3 printer. At first, Grey resin was utilised for printing a 300 µm-thick 'shell' model (see Figure A.8).

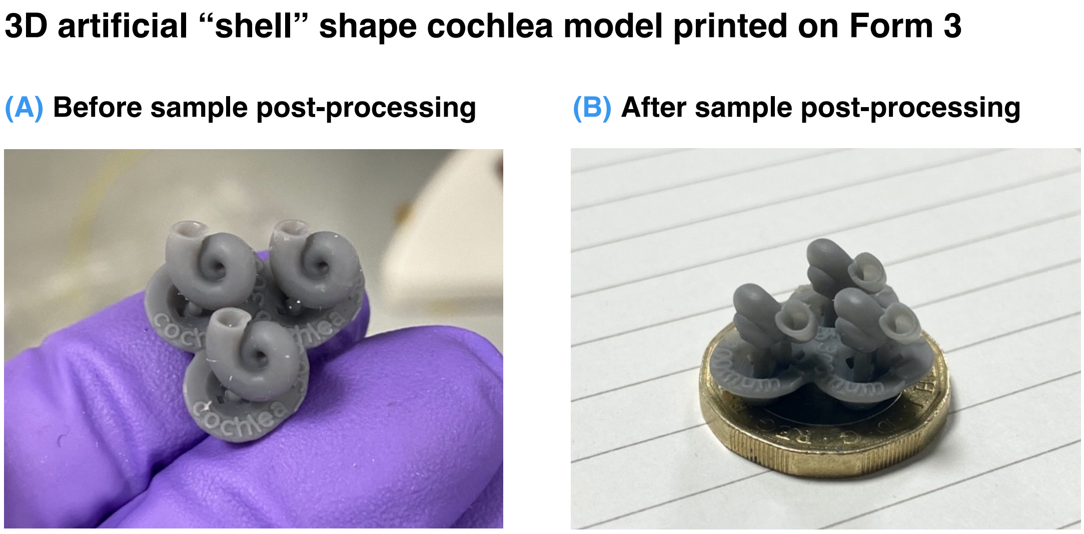

Figure A.8 3D artificial cochlea 'shell' produced with Form 3 using Grey resin. (A) - Image captured immediately after printing and (B) - Image captured following the post-processing curing phase, with a one-pound coin included for size comparison.

The fabricated models demonstrated good surface smoothness without any visible warping effect on the model's wall. The geometric accuracy of the print was examined by comparing the print to the original CAD model. Figure A.9 implies that Form 3 has good printing tolerance as the two objects overlay well. However, some differences are noticeable on the outer surface around the apex and in the inner lumen around 360° (angular depth). The cool colours illustrate a difference of 150 µm or more between the surfaces of the objects, whereas the hot ones depict good fit. The differences on the outer surface can be assigned to dust particles which might have been segmented with the cochlea shape. The prints were attached using tape in the microCT scanner which could potentially introduce dust particles to the sample. The variation in the inner lumen could be due to insufficient removal of resin or inappropriate fitting of the two 3D objects. The latter is a result of segmenting and aligning both outer and inner surface at once – wxRegSurf used rigid iteration registration which meant that no surface was deformed to align with the other. This resulted in preferable aligning of the outer surface (larger than inner) compared to the inner one.

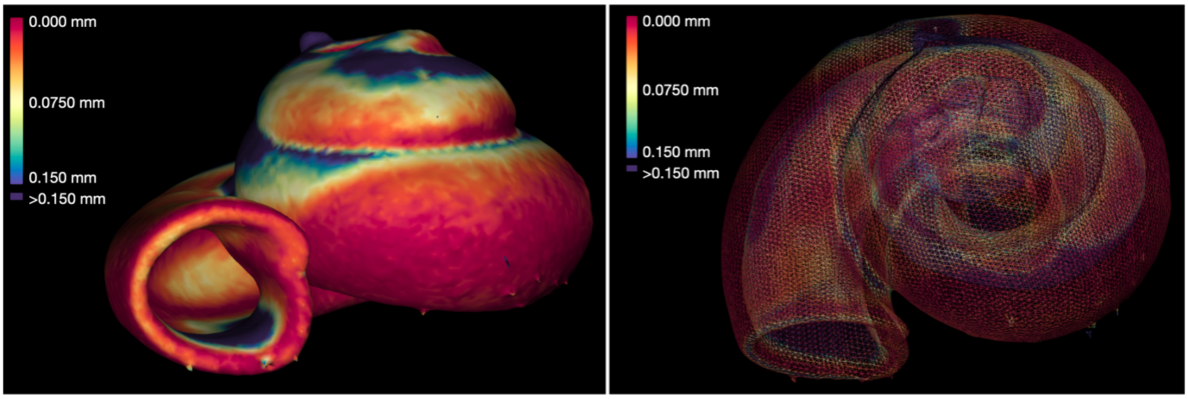

Figure A.9 A heat map depicting a comparison of the printed model and the original 3D object file using wxRegSurf. The differences are visible on the outer surface around apex (left) and in the inner lumen around 360° (right). The blueish colour depicts shape irregularities of 150 µm or more.

Following the success with Grey resin, Clear resin was evaluated as the transparency of the model is crucial for the insertion studies. In order to assess the printer's abilities, three wall thicknesses (300, 100, 50 µm) were printed. Figure A.9 depicts models with various thicknesses. Moreover, two printing angles (0° and 45°) towards the building platform were investigated. It was essential that the cochlea lumen was fully developed, meaning that it could be flushed with IPA to remove resin residuals, and subsequently with saline solution to mimic the real cochlea environment. These angles facilitated good allocation of supports that did not impair the geometry of the cochlea. Both 0° and 45° angles demonstrated successful development of the internal lumen from apex to the basal turn.

Both 300 and 100 µm demonstrated good consistency between prints and shape-accuracy to the CAD model used. However, 50 µm thick shell samples showed a 'warping' effect on the walls. This phenomenon is associated with uneven thermal contraction during printing, the resolution limits of the printer, properties of the resin, and generally a physical limitation as small perturbations will have a substantial effect on a thin structure of this size. The printing structure is not thick enough to support itself, so it collapses and thus changes the overall shape of the object (*e.g.* lumen). Hence, it was

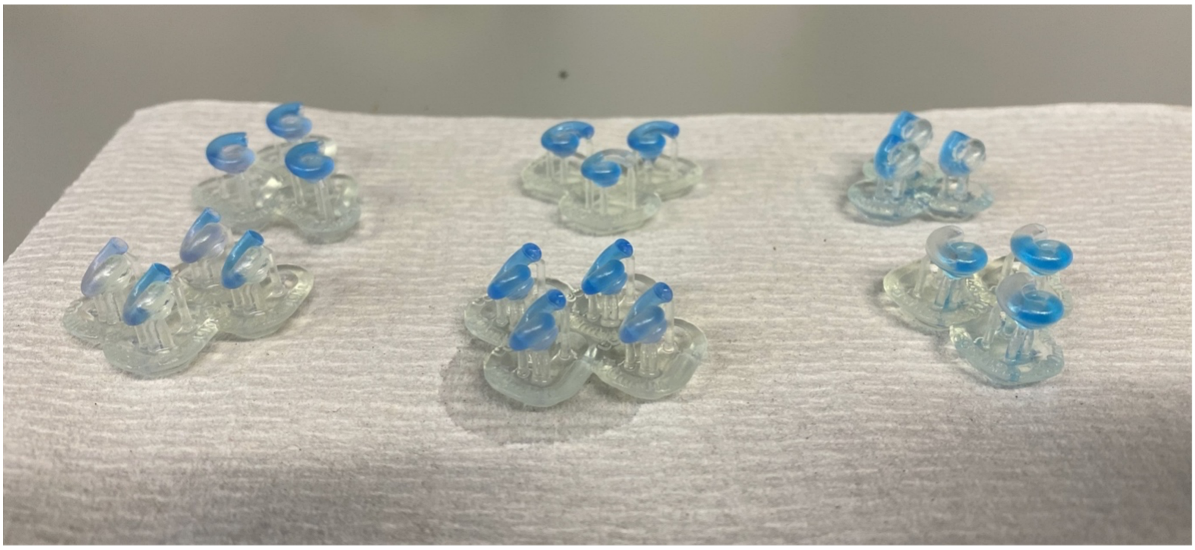

Figure A.10 3D printed artificial cochleae with 50 µm (left), 100 µm (middle), and 300 µm (right) wall thickness. Two angles towards the building platform were examined: 0° and 45°. Blue dye was used to demonstrate the full development (from apex to the basal turn) of the internal lumen.

assumed that the thickness of 100 µm was a good trade-off between the wall thickness and the quality of the printed object.

Although the 'shell' models were sufficient in terms of geometric accuracy and internal smoothness; their transparency was insufficient to image objects placed into the cochlea. Hence, the 'open-top' model was designed (see Figure A.11). Without the top part of the lumen, it is possible to observe implant behaviour during insertion. This is essential for the evaluation of insertion forces and trauma in particular locations such as the basal turn. However, the implants 'popped out' of the open-top model during insertion, which limited the model's application. Furthermore, Hartl *et al.* suggested that the measurement of the intracochlear pressure provides a direct projection of cochlear input energy and can more precisely quantify insertion trauma than the evaluation of insertion forces.[24] To solve these issues, a thin, transparent membrane could be placed on top of the model. Nonetheless, it would have to have a good seal with the model in order to be useful for intracochlear pressure studies.

One of the objectives of developing artificial cochlea was to obtain a transparent model which would be able to accommodate force sensors and recording devices in future; as a result, the 'block' model was fabricated. Its cubic shape provides good handling and can be utilised for the embedding of sensors by either drilling or printing channels within the structure to access the cochlea. Following that, the shape also promotes transparency

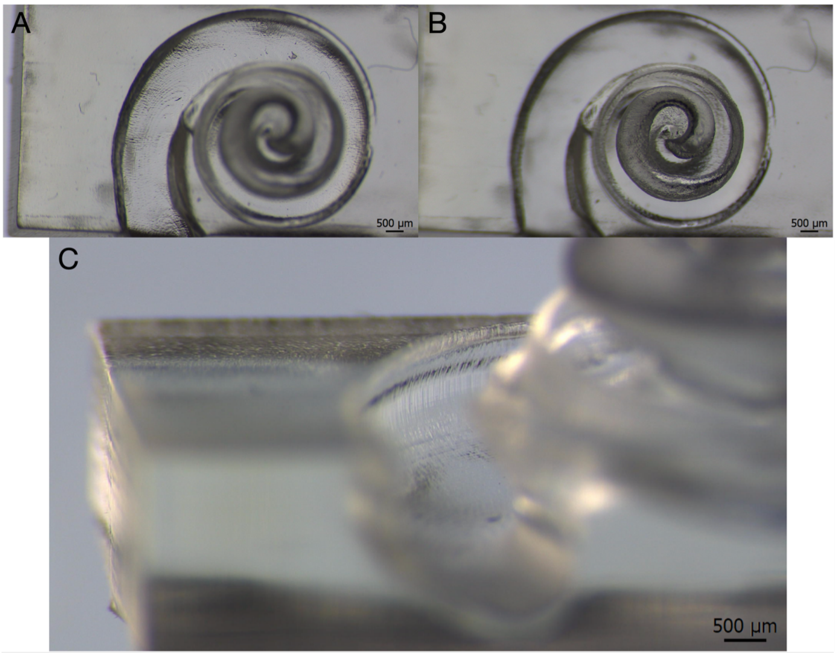

Figure A.11 'Open-top' prints developed using Form 3. (A) and (B) show the missing top part of the lumen. (C) demonstrates an excellent surface smoothness.

of the model as it has a flat surface as opposed to a curved one which is more likely to scatter light due to surface imperfections. The cochlea size within the block was produced at several scales: 1 : 0.5, 1 : 0.75, 1 : 1, 1 : 1.25 and 1 : 1.5, to evaluate the printer's abilities to deliver consistent results and maintain shape accuracy at different sizes. Furthermore, this capability will aid further studies in evaluating how cochlear size affects insertion (as discussed in Chapter 5). All samples were fabricated without failure and did not exhibit any geometric abnormalities.

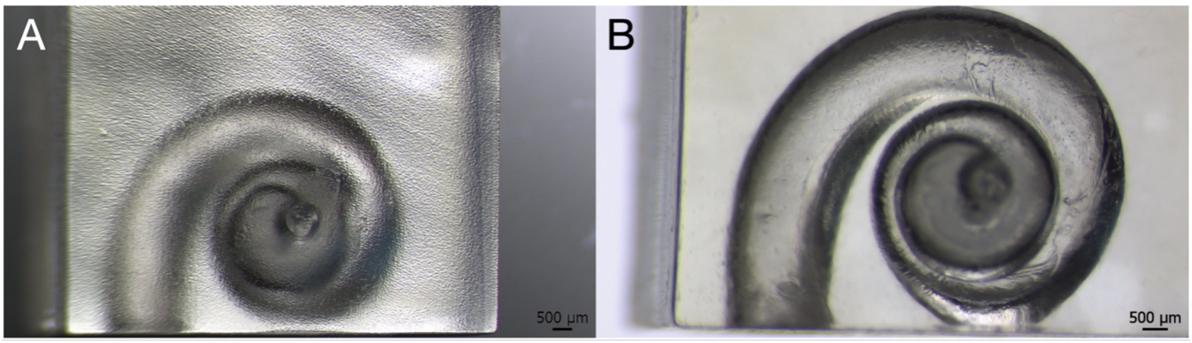

Figure A.12 'Block' model fabricated by Form 3 without any post-processing (A) and after our optimisation procedure (B).

Figure A.12 (A) illustrates the semi-transparent nature of the print after the UV curing process. The print surface exhibited ‘frosty’ finish due to the layering artefacts of the layer-by-layer printing process which is sub-optimal for the insertion studies. Hence, a new post-processing procedure was developed to optimise the model’s transparency. The deposition of an acrylic lacquer on the top part and a Pluronic solution in the inner lumen enhanced transparency significantly.

A.3 Conclusion

This study provides a description of the development and fabrication of an artificial cochlea for cochlear implant insertion studies with custom implant designs.

A 3D CAD model was successfully developed from microCT scans of cadaveric temporal bones and converted into printable files. This model constituted a generic model that was later exploited for the evaluation of 3D printers.

Five printers with different printing technologies were investigated for the production of the same cochlear model. Out of the tested group, Cadworks3D (DLP technology) and Form 3 (SLA technology) exhibited superior surface smoothness and geometric accuracy. Form 3 was used for developing artificial cochleae and Cadworks3D was recommended for future experiments.

Form 3 was utilised for the development of three distinctive designs of the artificial cochlea: ‘shell’, ‘open-top’, and ‘block’ model. The ‘shell’ model was printed with three different thicknesses of the lumen’s wall (50, 100, and 300 µm) to assess the printer’s abilities. The 100 µm-thickness was identified as an ideal trade-off between print’s quality and the size of the wall. Additionally, the ‘shell’ model was utilised for the evaluation of Form 3 printing accuracy. Comparing software wxRegSurf demonstrated good overall printing tolerance of Form 3. The ‘open-top’ model was successfully developed to achieve the best visualisation of inserted implants, although it had limitations of allowing the implant to ‘pop-out’ during insertion. The ‘block’ model was developed to address the issues with both ‘shell’ and ‘open-top’ models. Its cubic shape facilitated good handling of the model and provided a good base for the incorporation of sensors in future. This design was also successfully printed in several sizes of the cochlea to demonstrate the abilities of the printer. Lastly, the model’s transparency was significantly enhanced by developing a post-processing procedure which enabled direct observation of the implant’s behaviour during insertion.

This study shows that SLA and DLP printing technologies have considerable potential to drive the development of artificial cochlea and custom silicone arrays forward.